Magnetic skyrmions in GdCo ferrimagnetic thin-films

Léo Berges

université PARIS-SACLAY

Magnetic skyrmions in GdCo ferrimagnetic thin-films

Skyrmions magnétiques dans les couches minces ferrimagnétiques de GdCo

Thèse de doctorat de l'université Paris-Saclay

École doctorale n° 572, Ecole Doctorale Ondes et Matière (EDOM)
Spécialité de doctorat: Physique
Graduate School : Physique, Référent : Faculté des sciences d'Orsay

Thèse préparée au Laboratoire de Physique des Solides (Université Paris-Saclay, CNRS), sous la direction de Alexandra MOUGIN, directrice de recherche, et le co-encadrement de João SAMPAIO, chargé de recherche.

Thèse soutenue à Paris-Saclay, le 16 décembre 2022, par

Léo BERGES

Composition du jury

Membres du jury avec voix délibérative

Michel VIRET Directeur de recherche, Université Paris-Saclay	Président
Stefania PIZZINI Directrice de recherche, Université Grenoble Alpes	Rapporteure & Examinatrice
Juan-Carlos ROJAS-SANCHEZ Chargé de recherche, HDR, Université de Lorraine	Rapporteur & Examinateur
Anne BERNAND-MANTEL Chargée de recherche, Université Toulouse III - Paul Sabatier	Examinatrice
Olivier FRUCHART Directeur de recherche, Université Grenoble Alpes	Examinateur

THESE DE DOCTORAT
NNT : 2022UPASP161

université PARIS-SACLAY

ÉCOLE DOCTORALE
Ondes et matière
(EDOM)

Titre: Skyrmions magnétiques dans les couches minces ferrimagnétiques de GdCo.
Mots clés: Nanomagnetisme, Skyrmions, Electronique de Spin, Couches minces, Ferrimagnétiques, Chiral

Résumé: Les skyrmions magnétiques sont des textures magnétiques chirales topologiques décrites comme des particules magnétiques. Les skyrmions peuvent être déplacés efficacement par des courants polarisés en spins, ce qui, combinés avec leur taille nanométrique, en fait des objets prometteurs, par exemple pour des dispositifs de stockage d'information de faible consommation, haute densité et à encodage et lecture rapide. Leur découverte expérimentale dans les films minces magnétiques en 2011 a été suivie par de nombreuses études dans une grande variété de matériaux magnétiques, de couches uniques ou multiples de matériaux ferromagnétiques, à des matériaux possédant de multiples sous-réseaux magnétiques. Dans cette thèse, leurs propriétés statiques et dynamiques sont explorées dans une famille précise de composés à double réseau magnétique : les couches minces ferrimagnétiques de Terres-Rares et Métaux de Transition (TRMT). Cette recherche se concentre sur les alliages de Gd et Co qui constituent deux sous réseaux magnétiques couplés antiferromagnétiquement. La procédure de fabrication sous forme de couches minces de quelques nanomètres aux compositions contrôlées en Gd et Co est présentée. Leurs propriétés magnétiques sont caractérisées expérimentalement ce qui permet en regard de modèles théoriques d'explorer les propriétés statiques des skyrmions stabilisés dans ces films. Par exemple, la stabilité des skyrmions est largement déterminée par la compétition entre les interactions magnétiques dans le film, elles-mêmes très sensible à l'intensité de l'aimantation. Celle-ci varie rapidement en température dans les couches ferrimagnétiques de GdCo, et peut même être parfaitement compensée, comme dans les matériaux antiferromagnétiques, à la température de compensation magnétique. Cette grande sensibilité en température permet d'explorer la compétition entre les différentes interactions magnétiques qui favorisent la stabilité des skyrmions, et d'en extraire les paramètres clefs. Les skyrmions ainsi observés présentent des diamètres allant de 400 nm au micromètre. La comparaison des diagrammes de phases expérimentaux, en champ magnétiques et température, avec des simulations micromagnétiques ainsi que des modèles analytiques présente des accords quantitatifs. De plus, les propriétés dynamiques des skyrmions propagés par couple de spin-orbite induit par des couches adjacentes de matériaux lourds tels que le Pt ou le Ta sont présentées. Le résultat principal obtenu se trouve dans la démonstration de la dépendance en taille de la vitesse des skyrmions. A faible densité de courant, un régime de dépiégeage, caractérisé par de faibles vitesses est observé. Il est suivi par un régime ou la vitesse des skyrmions est linéaire avec la densité de courant, présentant une mobilité qui augmente avec leur diamètre. Un désavantage majeur pour les dispositifs à base de skyrmions se trouve dans leur trajectoire défléchie, causée par leur topologie, qui empêche un déplacement rectiligne. Le régime linéaire présente une déflexion constante des skyrmions avec la densité de courant (ou la vitesse). Ces observations dans le régime linéaire sont en accord quantitatif avec un modèle présenté de skyrmion rigide. De plus, le renversement de l'angle de déflexion est observé d'une part et d'autre de la température de compensation angulaire (lorsque la densité de moment angulaire est compensée). Cette observation est l'une des caractéristiques des matériaux ferrimagnétiques, attendue des propriétés dynamiques des skyrmions. Cela confirme l'efficacité de l'exploration des propriétés statiques et dynamiques des skyrmions que permettent les composés ferrimagnétiques TRMT grâce à leurs propriétés remarquablement ajustables. Finalement, l'irradiation par sonde ionique focalisée d'Helium a permis de modifier finement les propriétés magnétiques de ces films minces de façon à stabiliser des skyrmions, les nucléer, et permettre leur propagation confinée.

Title: Magnetic Skyrmions in GdCo ferrimagnetic thin-films
Keywords: Nanomagnetism, Skyrmions, Spintronics, Thin-films, Ferrimagnets, Chiral

Abstract: Magnetic skyrmions are chiral magnetic textures with topological properties that allow their description as particle like magnetic objects. Skyrmions can be displaced efficiently by spin polarised electrical currents, which combined to their nanometer scale, make them very promising objects for instance for low power, high density and fast reading and writing magnetic data storage devices. Their experimental discovery in magnetic thin-film in 2011 has been followed in recent years by their extensive study in many type of magnetic materials, from single or multi-layers of ferromagnetic materials to multi magnetic lattices materials. In this thesis their statics and dynamical properties are explored in a specific type of multi magnetic lattices materials, ferrimagnets of the Rare-Earth / Transition Metal family. Focus is made on ferrimagnets composed of Gd and Co, which constitute two magnetic lattices antiferromagnetically coupled. The fabrication process of thin films of few nanometers, with controlled composition of Gd and Co is described. Their magnetic properties are characterised experimentally and combined with theoretical models to explore the statics properties of skyrmions hosted in these films. For instance, the stability of skyrmions is greatly determined by the competition between magnetic interactions, where the strength of the magnetisation is a key parameter. The magnetisation in GdCo ferrimagnets varies rapidly with temperature and can even be completely compensated, as in antiferromagnets, at the magnetic compensation temperature. This great tunability allowed us to explore the competition between magnetic interactions that favours skyrmion stability and identify its key parameters. Skyrmions with sizes ranging from sub-400 nm to μm in diameters were observed. Micromagnetic simulations as well as analytical models are compared to the experimentally determined temperature and magnetic field phase diagrams of skyrmions, with quantitative agreement. The dynamical properties of skyrmions are studied when propagated by current induced spin orbit torques by adjacent heavy metal layers of Pt and Ta. The major result is the experimental evidence of the skyrmion velocity dependence with size. At low current density, a depinning regime characterised by low velocities is evidenced. It is followed by a regime where the skyrmion velocity is linear with current density and a mobility scaled by the skyrmion size. A major disadvantage for applications is the topologically induced deflected motion of skyrmions, which prevents their straight line displacement. The skyrmion deflection angle is observed to be constant with current density (or velocity) in the linear regime. Observations in the linear regime are accounted quantitatively by a rigid skyrmion model. Furthermore, the reversal of the skyrmion deflection angle was observed by crossing the angular compensation temperature (where the angular momentum density is compensated). This shows one of the key specificity of ferrimagnets for skyrmion dynamics. This further demonstrates the efficient exploration of static and dynamical properties of skyrmions enabled by the outstanding tunability of RETM ferrimagnets. Finally, using He-focused ion beam irradiation, a fine tuning of the thin films magnetic properties allowed for skyrmion stabilisation, nucleation and confined propagation.

Contents

List of Figures

List of Tables

Magnetic Parameters Table				
Name	Symbol	Formula	SI	Unit
Vacuum magnetic permeability	μ_0	4π x 10^{-7}	Hm^{-1}	$kgmC^{-2}$
Vacuum electric permittivity	ϵ_0	8.854 x 10^{-12}	Fm^{-1}	$kg^{-1}m^{-3}s^2C^2$
Speed of light	$c = \frac{1}{\sqrt{\epsilon_0 \mu_0}}$	299.792 x 10^6	ms^{-1}	ms^{-1}
Planck Constant	h , $\hbar = \frac{h}{2\pi}$	6.626 x 10^{-34}	Js	kgm^2s^{-1}
Boltzmann Constant	k_B	1.38 10^{-23}	JK^{-1}	$kgm^2s^{-2}K^{-1}$
Electron charge	e	1.603 x 10^{-19}	C	C
Electron mass	m_e	9.109 x 10^{-31}	kg	kg
Electron gyromagnetic ratio	$\gamma_e = \frac{e}{2m_e}$	1.761 x 10^{11}	Hz/T	$kg^{-1}C$
Bohr magneton	$\mu_B = \frac{e\hbar}{2m_e}$	9.274 x 10^{-24}	JT^{-1}	$m^2s^{-1}C$
Magnetic field	$\mathbf{B}$	B = μ_0(H+M)	T	$kgs^{-1}C^{-1}$
Electric field	$\mathbf{E}$	E = $\frac{1}{\epsilon_0}$(D-P)	Vm^{-1}	$kgms^{-2}C^{-1}$
Magnetic moment	μ	$\mu = \frac{g\mu_B J_a}{\hbar}$	JT^{-1}	$m^2s^{-1}C$
Total angular momentum	J_a	$J_a = L + S$ or $L - S$	Js	kgm^2s^{-1}
Gilbert Dissipation parameter	α			
Gyroscopic ratio	γ	$\gamma = \frac{M_s}{Ls}$	Hz/T	$kg^{-1}C$
Saturation magnetisation	M_s		Am^{-1}	$m^{-1}s^{-1}C$
Angular momentum density	L_s		Jsm^{-3}	$kgm^{-1}s^{-1}$
Dissipation rate density	L_α	$L_\alpha = \alpha L_s$	Jsm^{-3}	$kgm^{-1}s^{-1}$
Exchange parameter	J^{ex}		J	kgm^2s^{-2}
Exchange stiffness	A^{ex}	$A^{ex} = \frac{J^{ex}S^2}{a} c_{cryst}$	Jm^{-1}	$kgms^{-2}$
Interfacial Dzyaloshinskii-Moriya	D_s		Jm^{-1}	$kgms^{-2}$
Dzyaloshinskii-Moriya parameter	D_m	$D_m = \frac{D_s}{t}$	Jm^{-2}	kgs^{-2}
Interfacial magnetic anisotropy	K_s		Jm^{-2}	$kgms^{-2}$
Magnetic anisotropy constant	K_u	$K_u = \frac{K_s}{t}$	Jm^{-3}	$kgm^{-1}s^{-2}$
Effective Anisotropy	K_{eff}	$K_{eff} = K_u - \frac{\mu_0 M_s^2}{2}$	Jm^{-3}	$kgm^{-1}s^{-2}$
Simple Domain Wall Energy	σ_0	$\sigma_0 = 4\sqrt{AK_{eff}}$	Jm^{-2}	kgs^{-2}
Domain Wall Energy	σ	$\sigma = 4\sqrt{AK_{eff}} - \pi D_m$	Jm^{-2}	kgs^{-2}
Dipolar length	l_c	$l_C = \sigma/(\mu_0 M_s^2)$	m	m
Exchange length	l_{ex}	$l_{ex} = \sqrt{\frac{2A}{\mu_0 M_s^2}}$	m	m
Domain Wall Width Parameter	Δ	$\Delta = \sqrt{\frac{A}{K_{eff}}}$	m	m
Domain Wall moment	$\pi\Delta$	$\pi\Delta = \pi\sqrt{\frac{A}{K_{eff}}}$	m	m
Quality Factor	Q	$Q = \frac{2K_u}{\mu_0 M_s^2}$		
Anisotropy field	H_k	$H_k = \frac{2K_{eff}}{\mu_0 M_s}$	T	$kgs^{-1}C^{-1}$
Critical DMI	D_c	$D_c = \frac{\sigma_0}{\pi}$	Jm^{-2}	kgs^{-2}
Critical DMI ratio	κ	$\kappa = \frac{D_m}{D_c} = \frac{\pi D_m}{\sigma_0}$		
Skyrmionic factor	S_s	$S_s = -\frac{E_{ex}+E_{anis}+E_{DMI}}{E_{Dipolar}^{Longrange}}$		
Hamiltonian	$\mathcal{H}$		J	kgm^2s^{-2}
Volumic energy density	E		Jm^{-3}	$kgm^{-1}s^{-2}$
Skyrmion Energy	E_s		J	kgm^2s^{-2}
Thiele gyrotropic vector	$\mathbf{G}$		kgs^{-1}	kgs^{-1}
Thiele dissipation factor	$\mathcal{D}$		kgs^{-1}	kgs^{-1}

Table 1: Table of manuscript's important quantities.
Conversions: 1 erg = 10^{-7} J, 1 emu/cm^3 = 10^3 A/m, 1 G = 10^{-4} T and 1 Oe = $\frac{10^3}{4\pi}$ A/m.

Synthèse

Les skyrmions sont des objets originellement mathématiques, décris pour la première fois par Tony Skyrme [1, 2] dans les années 1960, pour obtenir une solution particulière de l'équation de champ du modèle standard des particules. Comme cela est succinctement développé au début du chapitre introductif 1, l'ajout d'un terme chiral dans l'équation du modèle standard permet d'y trouver des solutions très particulières, de solitons topologiques [3]. Les solitons sont des ondes solitaires capables de présenter une extension spatiale comparable à celle d'un paquet d'ondes, mais dont la forme se préserve dans le temps dans les milieux dispersifs [4, 5]. Cette étonnante classe de solution semble être commune à de nombreuses équations non-linéaires bien connues : Korteweg-de Vries, Sine-Gordon, Schrodinger-Non Linéaire, Sigma-Model, Ginzburg-Landau mais aussi Landau-Lifshitz qui décrit l'aimantation [6].
Dans le modèle de Skyrme, les solitons obtenus : les skyrmions, permettent de rendre compte de nombreuses propriétés des noyaux atomiques [7, 8], ce qui en fait un modèle effectif assez élégant des baryons dont le numéro est déterminé par le nombre topologique de la solution. On le calcul comme le nombre d'enroulements de la structure dans l'espace de solution du champ décrit. Dans le cas des skyrmions magnétiques [9], le nombre topologique est calculé comme le nombre d'enroulements sur la sphère unité, de l'aimantation de la structure de spin considérée.
Ces textures magnétiques sont observables dans des systèmes magnétiques chiraux et se décrivent comme une assemblée de spins à symétrie radiale, dont le cœur est orienté dans une direction opposée à sa bordure, avec un profil d'aimantation respectant une chiralité fixée par le signe de l'interaction chirale. Les skyrmions magnétiques possèdent de nombreuses similitudes avec le modèle bi-dimensionnel de Skyrme [10], de par leur profil ou leur structuration en réseaux par exemple.
Leur observation dans les matériaux magnétiques de bulk date de 2009 [11] dans des matériaux dont la maille unitaire ne possède pas de symétrie d'inversion, ce qui permet l'apparition de termes non-diagonaux à l'interaction d'échange. Cet échange antisymétrique, dit de Dzyaloshinskii-Moryia [12, 13] (DMI), est chiral et détermine une certaine hélicité et chiralité d'enroulement de la structure de spin [14, 15]. L'hélicité des skyrmions [16] est de type Bloch dans le cas de DMI de bulk, ou Néel, dans le cas de DMI d'interface. Cela détermine la direction de renversement de l'aimantation, qui peut être hélicoïdale, ou cycloïdale. Dans le cas de couches minces magnétiques, l'interaction de DMI est générée aux interfaces de métaux lourds, ce qui favorise la formation de skyrmion Néel.
Pour des empilements de couches sans symétrie d'inversion, l'intensité du DMI est suffisamment importante pour favoriser une chiralité unique du système. Sans chiralité fixe, comme dans les études des années 1970 sur les bulles magnétiques [17, 18, 19, 20], le manque de filtre autorise l'apparition de nombreuses solutions de topologies différentes, ce qui étend d'autant les modes d'excitations de ces objets, et les difficultés à les manipuler.
En 2011 [21], la première observation de skyrmions magnétiques dans des couches minces métalliques est obtenue, suivie rapidement de nombreuses observation à température ambiante, avec depuis la recherche sur ce sujet devenue très active.

Le travail de cette thèse consiste en l'étude d'alliage de Métaux de Transition et Terres-Rares aux propriétés ferrimagnétique dans lesquels des skyrmions ont été observés en 2018. Il s'agit de couches minces de GdCo, dont le couplage anti-ferromagnétique des sous-réseaux de chaque espèce, permet l'apparition de températures caractéristiques, dites de compensation magnétique et angulaire, auxquelles s'annulent l'aimantation du film mince pour l'une, et la densité de moment angulaire pour l'autre [22]. La fabrication des films minces étudiés dans cette thèse est menée par mes soins et celles de collaborateurs au laboratoire de Physique des Solides. Le détail de leur élaboration est présenté au chapitre 2, avec la discussion de nombreuses mesures de caractérisation permettant de déterminer l'évolution en température de leurs propriétés magnétiques. L'utilisation conjointe de magnétométrie SQUID, de magnéto-optique à effet Kerr (MOKE), de transport ou encore de Diffusion Inélastique Brillouin (BLS), permet d'obtenir une idée assez précise des propriétés de nos échantillons pour contraindre de façon pertinente les différents modèles utilisés pour reproduire leurs caractéristiques. Des études en empilement, épaisseur et composition de couches de Pt/GdCo/Ta sont présentées.

Les chapitres 3 et 4 se concentrent ensuite sur la présentation de deux échantillons caractéristiques des propriétés observées dans les différentes séries d'échantillon fabriqués pendant ces travaux.

Dans le chapitre 3, les propriétés statiques des skyrmions sont décrites. On y retrouve premièrement un récapitulatif des variations en température des différentes longueurs et énergies caractéristiques des interactions en jeu dans la stabilité des skyrmions. Je présente ensuite un modèle d'énergie des skyrmions appliqué au cas de systèmes ferrimagnétiques. Ce modèle est ensuite utilisé pour reproduire des diagrammes de phase expérimentaux obtenus dans mes échantillons de GdCo. Des skyrmions d'un diamètre de 300-800 nm sont observés, à température ambiante, et sous champ magnétique nul. Les conditions de stabilité des skyrmions dans les échantillons de GdCo et plus généralement des alliages de RETM sont précisément identifiés, ce qui permet en regard du chapitre 2 et du modèle détaillé de champ moyen de l'aimantation de ces couches, d'obtenir une méthode précise de controle de la stabilité des skyrmion en température.
Les échantillons ferrimagnétique montrent donc une ajustabilité des propriétés magnétiques, particulièrement intéressante pour explorer efficacement l'espace des paramètres magnétiques dans des échantillons uniques. Le chapitre est terminé par une étude du rayon des skyrmions en température et champ magnétique, qui sera utilisée dans le chapitre suivant pour étudier l'effet de la taille des skyrmions sur leur dynamique. On y compare des mesures réalisée en Microscopie à force magnétique (MFM) avec des images MOKE, qui permettent de valider nos protocoles de mesures de taille de skyrmions en MOKE. On observe une évolution de la taille moyenne d'équilibre des skyrmions en fonction de l'aimantation de la couche ferrimagnétique (en température) ainsi qu'une réduction de la taille par application d'un champ magnétique opposé au cœur des skyrmions.

Le chapitre 4 détaille lui les propriétés dynamiques des skyrmions déplacés par couple de spin orbite (SOT). De part la structure de nos empilements, les couches adjacentes de Pt et Ta génèrent par effet Hall de spin (SHE) un courant polarisé en spin transverse au courant appliqué. Ce courant de spin diffuse dans la couche magnétique adjacente et y applique un couple capable de déplacer les textures magnétiques [23, 24]. La propagation des skyrmions est étudiée dans des pistes magnétiques de 3 à 8 nm d'épaisseur, d'une largeur de 5-20 μm, sur une longueur typique de 100 μm.

Les mesures des propriétés dynamiques dépendent entièrement d'observation par microscope MOKE du déplacement de skyrmions individuels après des impulsions successive de 3-10 ns de tension électrique. Les images sont analysées principalement à l'aide de traitement d'image en python dans une interface que j'ai développée pour faciliter le traitement de mesures de trajectoire de skyrmions. La propagation en régime linéaire, de flow, des skyrmions est observée après un saut clair de dépiègeage à un courant critique J_c. La mobilité des skyrmions observés est très bonne comparée à la littérature actuelle. Cela nous a permis d'observer des vitesses de déplacement de 100 à 400 $\mathrm{m.s^{-1}}$ pour des densités de courant de 100 à 300 $\mathrm{GAm^{-2}}$. La mobilité des skyrmions est ensuite étudiée en fonction de leur taille, modulée par l'application d'un champ magnétique extérieur. Nos observations montrent une décroissance de la mobilité des skyrmions avec leur taille, ainsi qu'un accroissement de la densité de courant critique de dépiégeage.
Les propriétés de déflection des skyrmions sont étudiées à la fin du chapitre. Du fait de leur topologie non-triviale, ainsi que de la densité de moment angulaire du matériaux hôte, les skyrmions subissent une force gyrotropique pendant leur déplacement, qui induit une déflection de leur trajectoire. Cette déflection dite topologique, complexifie l'intégration de ces structures magnétiques dans des dispositifs industrialisables, et sa maîtrise est donc indispensable pour permettre leur utilisation concrète. Les propriétés ajustables des échantillons ferrimagnétiques sont une fois de plus utilisées, cette fois-ci pour ajuster la densité de moment angulaire de l'échantillon selon sa température. Mes mesures montrent de façon claire que l'angle de déflection des skyrmions s'inverse d'une part et d'autre de la compensation de moment angulaire des échantillons. En comparant des échantillons d'une part et d'autre de la compensation angulaire on observe effectivement une inversion du signe de la déflection topologique, mais cette inversion est aussi observable sur un unique échantillon en traversant la compensation angulaire en variant la température. Cette observation conforte la prédiction théorique d'une annulation de la déflection à la compensation angulaire, et permet d'imaginer, en regard des deux chapitres différents, une méthode d'optimisation des échantillons pour obtenir des skyrmions stable autour de la compensation angulaire, et de permettre donc une inhibition complète de la déflection de trajectoire des skyrmions. Ces mesures expérimentales sont reproduites avec un accord quantitatif très satisfaisant à l'aide d'un modèle de skyrmion rigide, développé dans le cadre de l'équation de Thiele. Notre modèle reproduit les propriétés de skyrmions isolés dans le régime linéaire de flow, avec un accord très bon lorqu'il est intégralement parametré par des mesures expérimentales. Ce très bon accord est vérifié dans différents échantillons, et aussi observé en regard de simulations micromagnétiques. Une grande partie de ces résultats est publiée dans l'article suivant [25].

Finalement, sont présentés dans le chapitre 5, des expériences d'irradiation par Faisceau d'ions focalisés (FIB) d'Helium de couches minces de GdCo [26, 27, 28, 29, 30]. On présente différents tests de dose d'irradiation, et leurs effets sur l'aimantation et l'anisotropie magnétique des échantillons. Ce travail préliminaire permet de modifier localement les propriétés magnétiques d'un échantillon, et de modifier, à une température donnée, le type de textures magnétiques observables entre la zone vierge et iradiée. Cette méthode autorise un ajustement fin des propriétés magnétiques d'une piste, que nous avons utilisé pour créer une zone de stabilité de skyrmions, obtenir de la propagation confinée, ou encore obtenir des zones de nucléation de skyrmion par impulsion de courant. Cette dernière partie présente donc des voies intéressantes pour permettre une manipulation précise de la trajectoire des skyrmions, mais aussi pour fonctionnaliser des pistes magnétiques permettant le développement de dispositif à texture magnétique plus complexes.

Remerciements

Le déroulement d'une thèse est une aventure pleine de rebondissements, un marathon d'ascenseurs émotionnels, que je recommande sans hésitations pour les joies immenses qu'il procure quand on résout enfin ces questions qui nous taraudent depuis des semaines. J'ai beaucoup de gratitude sur le cheminement qui m'a permis de réaliser cette expérience, et j'ai eu la chance de la vivre pleinement. Je tiens à remercier avant tous mes parents et mon frère qui m'ont tout appris, et que j'adore, mais aussi mes oncles, mes tantes et mes cousines, dont j'ai le plaisir de partager la vie et sans qui je n'aurais certainement jamais écrit ces mots. Je vous dois tous tellement, et j'espère garder toujours cette curiosité qui nous unit et que vous m'avez toujours partagé. Je remercie tout particulièrement mon grand-père, à qui je dois mes premiers livres de philosophie et de physique, et qui m'a nourri de son savoir encyclopédique toute ma jeunesse.

Je remercie tout le système éducatif français, pour m'avoir offert une éducation de qualité jusqu'aux études supérieures universitaires. Je remercie tous les professeurs que j'ai croisés, qui se donnaient pour leur cours et qui m'ont fait comprendre tellement. Tout particulièrement pour mes professeurs du Magistère d'Orsay et de master dont je garderai les enseignements précieusement et que remercie pour le travail magistral.

Dans cette thèse, j'ai eu le plaisir de découvrir un laboratoire d'excellence et d'y faire tellement de rencontres marquantes, dont la longue liste ne sera malheureusement toujours pas exhaustive.
Je voudrais remercier mes directeurs de thèse, Alexandra et João pour leur soutien et leur accompagnement tout au long de la thèse, et tout particulièrement pour la rédaction du manuscrit et les longues relectures. J'ai passé trois années tellement enrichissantes grâce à vous et je vous remercie de votre patience et de vos conseils. Je vais manquer les pauses-café du groupe qui étaient toujours un moment plaisant. Merci à André et Vincent pour toutes ces bonnes discussions et la compagnie charmante. Un grand merci à Stan pour le temps qu'il a pris à me former et me transmettre tant de son savoir, en plus du plaisir de fumer une clope avec toi ! Je veux aussi remercier Sujit, Banan, Sachin, Sougata et Eloi, qui ont partagé mes années de thèse, leur travail et leur bonne humeur, avec qui j'ai eu le plus grand plaisir de travailler. Un remerciement tout particulier pour Raphaël qui m'a énormément formé à ... à beaucoup de choses, de la salle blanche à python, à démonter des canons à plasma, je te suis vraiment reconnaissant de m'avoir accompagné pendant cette thèse et pour les cours que j'ai eu le plaisir de faire avec toi.

Je remercie aussi tous les gens du laboratoire, j'en ai croisé certain beaucoup et partagé au détour d'un couloir des rencontres et des discussions superbes. Je remercie déjà Véronique et Mélanie pour leur organisation et les services d'instrumentation et de mécanique avec qui j'ai eu le plaisir de partager, bricoler et apprendre beaucoup de savoir très utile.

Et pour terminer, je tiens à remercier tous mes amis. Ceux de Toulouse avec qui j'ai eu la meilleure des jeunesses et les discussions les plus folles ! Les potes de Paris aussi, c'était génial de faire ses études avec vous, avec une grande pensée aux Colocs, Julien, Hugo, Bol et Victor avec qui j'ai eu un quotidien des plus merveilleux, c'était vraiment un plaisir de partager tout ça. Pensée toute particulière au bricolocataire qui coupe des cartes !
Un plaisir aussi d'avoir rencontré pleins d'autres thésards et copains géniaux au labo, Mr Boury toujours vif, Sujit toujours marrant, Xavier toujours prêt à sortir sur la terrasse, Alice toujours la première le matin et la dernière à finir sa clope, Antoine pour les grandes discussion et pour le coup aussi Jules, le meilleur co-bureau. Et pour que la liste s'arrête, au plaisir d'avoir partagé de grands moments avec le docteur Ansgraf ! Et finalement, un énorme merci et beaucoup d'amour pour Helen, qui a su me supporter pendant ma rédaction de thèse ce qui lui vaut plus que ma gratitude.

Introduction

The amount of data stored at a global scale is increasing rapidly every year and seems to follow an exponential growth. For instance, the global datasphere was estimated at 25 ZB in 2018 and projected to reach 175 ZB by 2025 [31] and the power consumption of data centres is also expect to drastically increase [32]. Magnetic data storage with hard disk drives (HDD) is still dominating the market with a large share also taken by magnetic tapes. These two technologies offer very dense and robust data storage at low cost, but have the drawback to be rather slow to access. With the ever growing demand for real time access to data, with new generations of broadband cellular networks, for application to the internet of things (IoT) or for autonomous vehicles, a fast access to data becomes mandatory. On the other hand, the world is facing an unprecedented environmental crisis, where energy availability is contracting with the rapid depletion of the cheap fossil fuel reserves. This opens a growing interest for low power devices, where efforts to improve the energy efficiency of all appliances is slowly becoming a priority.

More than 30 years ago, a new path for data storage has been opened by the scientific community, who tried to tap into the second degree of freedom of electrons, by manipulating their spins. Flash memory, or solid state drives (SSD) only use the charge of electrons to store and access data, whereas solutions presented by the Spintronic community rely also on the electrons spins. This journey began with the discovery in 1988 of the Giant Magneto Resistance (GMR) by Albert Fert [33] and Peter Grünberg [34] for which they received the Nobel prize in 2007, that allowed the development of modern HDD. A recent realisation of this community can be found with MRAM and especially with STT-MRAM commercial devices that already reached an industrial level [35]. In these devices, nanopillars of magnetic material are switched between two states of magnetisation by spin transfer torque (STT) that relies on spin polarised electrical currents and allows for very dense data storage with low electrical consumption.

Another spintronic application is found in the racetrack technology [36], where the information is not stored on local nano-structures accessed by a complex wiring, but on magnetic objects that are dynamically displaced in magnetic tracks, from nucleation areas where they are created, to reading areas where they are accessed. Two types of magnetic objects have been proposed, magnetic domain wall (DW) on the one hand, that represent the area of reversal between two uniform magnetic domains of opposite orientation, and on the other hand skyrmions, round swirling magnetic domains with a core magnetisation pointing in the opposite direction from the surrounding uniform magnetic state, with a reversal of the magnetisation following an imposed chirality. Both of these objects are very promising for data storage application because of their small sizes (down to 30 nm for successive DWs, and 10 nm for skyrmions). Skyrmions present several advantages compared to DWs [37]. To list a few of them, skyrmions are more robust due to their non-trivial topology, they can be smaller than DWs, would present smaller error rate [38, 39] and very important, they are less sensitive to defects at magnetic tracks edges, that are known to inhibit DW propagation due to pinning effects. Skyrmions of different core polarity, or chirality would be used as carriers of information and displaced inside magnetic tracks by spin polarised currents [40].

This technology offers many advantages, with robust storage, information access time comparable to conventional electronics devices [38], but overall smaller energy consumption and also the possibility to develop complex 3D architectures to further increase storage density [41, 42]. Moreover, this type of technology can be extended to other devices than only data storage. It can be used for logical computing, with the realisation of skyrmion based logical gates [43, 44, 45]. Skyrmions can also be used to develop dedicated hardware for training neural networks, which is developed by the scientific community working on neuromorphic applications. Indeed, there is a huge increase in the use of artificial intelligence, and their very computationally demanding training can be optimised by using dedicated hardware instead of CPU or GPU. The use of skyrmion racetracks can be very easily converted to neuromorphic applications, using reshuffler [46], to mimic synapses transfer function for instance [47]. There are several other proposed applications for skyrmion devices [15], and this growing field of research is certainly going to find even more potential applications.

Since their discovery in magnetic thin films in 2011, the interest on skyrmions sky-rocketed (see skyrmion appearance in Google Ngram viewer for instance, or the number of related publications in Web of Science). In less than a decade, their stability mechanisms and dynamical properties have been largely explored in ferromagnetic materials, but have only been superficially described in other types of materials. There is for instance a major interest to study skyrmions in double magnetic lattices materials because it can tackle one of the major challenge with skyrmion manipulation which is their topologically induced deflection [48]. When displaced under current, they experience a transverse deflected motion which prevents their straight line motion along the current. Several mechanism have been explored to solve this issue, by confining effects of magnetic track edges for instance, but a more fundamental mechanism can prevent the deflection using the nature of double magnetic lattices materials. Indeed, because of the two lattices, the total angular momentum density of the system can be compensated, which inhibits the skyrmion deflections. One promising type of material to study this effect is found in the Rare-Earth/Transition Metal (RETM) ferrimagnets. Skyrmions have been observed in these materials only in 2018 [49, 50] and are now drawing much attention as they presented reduced deflection and extremely small size, down to 10 nm due to the RETM ferrimagnet particular properties.

In this thesis, I present an extensive study on the properties of RETM ferrimagnets [51] grown and characterised in our laboratory, and explore their interest to stabilise skyrmions and investigate their peculiar skyrmion dynamics.

In chapter 1, I introduce the state of the art on skyrmions static and dynamical properties. We begin by discussing the connections between magnetic skyrmions and skyrmions developed in the Skyrme model of the nucleus and then present all magnetic energies at play in our system. Afterwards, the basis of the theoretical description of skyrmions is introduced, in order to distinguish between their different types, and to lift potential ambiguities with magnetic bubbles or other resembling magnetic objects. We then present a timeline of skyrmion research, where we discuss the experimental observations of skyrmions in bulk and thin film materials. After, some general aspects on the skyrmion stability, the models developed to describe them are introduced. The different mechanisms to displace skyrmions, by magnetic field gradients and spin polarised currents are next presented. Their respective contributions are then compared using a Thiele based model of rigid magnetic textures. Finally, we present the experimental velocity and deflection curves obtained on skyrmions in different type of material to discuss the different regime expected for their dynamics.

In chapter 2, I discuss the properties of RETM ferrimagnetic alloys fabricated for this work. We focus first on the fabrication process of GdCo ferrimagnetic films with controlled thickness and composition, and then present some general aspects of these films, discussing the role of interfaces, the internal structure of the magnetic layer and their stability in time. We then examine the interactions between Gd and Co and the origin of their antiferromagnetic coupling. We next present and use mean field theory to describe the peculiar evolution in temperature of their magnetisation. The magnetic and angular momentum density compensation temperatures, characteristic of ferrimagnets, are then introduced. A quick description of the nano-fabrication process from plain thin film to functionalised magnetic track is presented afterwards. Finally, we present several experimental results on the determination of the magnetic properties of our film that will be used throughout this manuscript to parameterise our models.

In chapter 3, I explore the static properties of skyrmions in GdCo thin films. We start by discussing the temperature evolution of the sample magnetic properties, and focus on two samples that will be compared in this chapter and in the following one. We present the theoretical energy model we used to model our system, with its typical solutions in regard of the specificity of ferrimagnetic materials. The phase diagrams in temperature and magnetic field are then computed with the model and compared, with good qualitative agreement and arguable quantitative one, with experimental phase diagrams. Indeed, we observed skyrmions ranging from sub 400 nm to μm in many different samples, and were able to precisely understand the key parameters for their stability. Finally, we focus on the effect of magnetic field and temperature on the skyrmion radius, and compare micromagnetic simulations, theoretical model and experimental observations with good agreement.

In chapter 4, I present results on skyrmion dynamics, displaced by spin orbit torque, in the same samples explored in chapter 3. We begin by introducing our method for tracking skyrmions, that we used to measure their size, velocity and deflection angle. We then discuss in detail the observed effect of skyrmion size on the mobility of skyrmions. By using an external magnetic field to modify skyrmion size, we were able to observe a reduction of the skyrmion mobility with decreasing skyrmion size. We also observed the crossing from a pinning regime at low current density towards a linear regime at high current density. We were able to reproduce the linear regime observed using a Thiele based model of the skyrmion, which it very well constrained by experimental measurements of magnetic and skyrmion properties and yields very good quantitative agreement with our data. The model is also compared to micromagnetic simulations, again with a very good agreement. Different current induced parasitic effects that can bias our results are then discussed. Afterwards, a study on the reversal of the skyrmion deflection across the angular compensation temperature of the sample is presented. This effect has never been observed previously, and even though expected theoretically, its experimental demonstration is particularly important as it shows the interest of RETM ferrimagnets over conventional ferromagnets for controlled skyrmion dynamics.

Finally, in chapter 5, I describe my ongoing research on the manipulation of skyrmions. We present some of our trials for controlled skyrmion nucleation, and then focus on the more complete work we pursued using He-focused ion beam irradiation (FIB). He-FIB allowed us to precisely tune the properties of our ferrimagnetic samples. We realised several calibration tests for irradiation dosage, and disentangled the He-FIB effects on the magnetic anisotropy and magnetisation of the samples. We then present preliminary results on skyrmion stabilisation, controlled propagation and nucleation obtained on irradiated samples. This study is then concluded by a discussion on the optimisation of skyrmion properties in GdCo thin films.

Chapter 1

Skyrmions in magnetic materials: basis and state of the art

This manuscript studies topological solitons in magnetic media. More precisely, our focus is on magnetic skyrmions, named after skyrmions from the Skyrme model due to their numerous similarities that we will briefly present. There is a growing interest to study magnetic skyrmions due to their potential extremely small sizes, down to the nanometer scale and their particle like properties that offer promising and efficient manipulation capabilities by spin polarised electrical currents in magnetic tracks.
Many applications have been proposed to integrated magnetic skyrmions in information storage, logical computing or even neuromorphics devices [52, 53]. Our work focuses on the experimental study of theses magnetic objects in ferrimagnetic materials of the Rare-Earth/Transition Metal family .

In this chapter we will first present the connections between Skyrme atomic nucleus model and magnetic skyrmions. After introducing all magnetic energies relevant for their description, the main properties of magnetic skyrmions will be discussed, as well as the ones of resembling magnetic textures. Special attention is given to magnetic bubbles found in low chiral interaction environments.
We will discuss the skyrmion research timeline in order to introduce the state of the art on this broad research field. Some preliminary discussion will be made on the skyrmion statics properties as well as on the study of their dynamical properties by spin polarised electrical currents.

1.1 Connections to Skyrme's model

1.1.1 Skyrme model

Skyrmions were originally introduced as the solutions of the Skyrme model, developed by Tony Skyrme in the 1960s to describe atomic nucleus [1, 2]. In essence, the Skyrme model considers the interaction field of nucleus and extends its description with a non-linear term, which allows for a stabilising mechanism that yields soliton solutions. The non-linear term added to describe the pion field (interaction field of quarks) breaks the chirality of the system [7, 10] which favours a winding direction that stabilises topologically non-trivial solutions called skyrmions.
These solutions are far from being bizarre objects appearing in a complex nonlinear theory, but are actually a good description of the baryonic matter. As stated in [8]: *Suitably quantised, skyrmions are models for physical baryons.* Which is also stated in an extensive book on topological solitons [3] *"Thus a purely bosonic field theory could lead to spin 1/2 fermionic states, which could be identified as nucleons".*

Indeed, in this theory, the topological charge corresponds to the baryon number of nucleons. Later works have explored how these solutions can describe quantitatively the properties of nucleus [10, 54] and found a good quantitative performance as discussed in [6]: *"[The model] reproduces the properties of the nucleon to within an accuracy of around 30% [7]"*.
To conclude on the wide perspectives opened by the study of skyrmions, the quote from a large review on Skyrme solutions [55] highlights their great interest beyond nuclear physics *"[...] Skyrme's daring idea of 1960, originally conceived for nuclear physics, that fermions can arise from bosons via topological solitons, pervasively playing a powerful role in wide-ranging areas of physics, from nuclear/astrophysics, to particle physics, to string theory and to condensed matter physics. The skyrmion description, [...] offers solutions to some long-standing and extremely difficult problems at high baryonic density, inaccessible by QCD properly. It also offers explanations and makes startling predictions for fascinating new phenomena in condensed matter systems"*.
Fig. 1.1 shows some iso-densities map for skyrmions of different topological charges relating to different baryonic number.

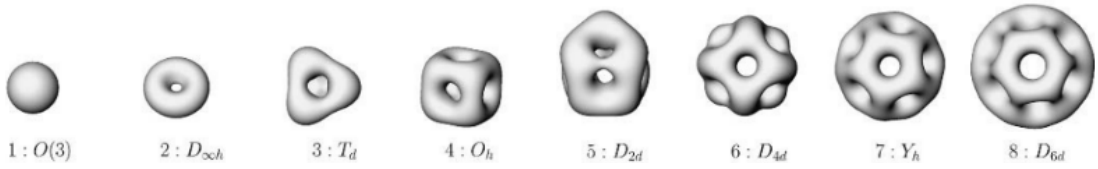

Figure 1.1: Skyrme solution illustration. Representation of baryon isodensity for n = 1 to 8 skyrmions and associated symmetry group of Skyrme model solutions. Extracted from [3].

1.1.2 Solitons

Solitons are a rather modern research topic (first description in 1834 by J.S Russell [4]) with major theoretical understanding developed in the first half of the 20^{th} century. Soliton solutions resemble the shape of wave-packets solutions of fields but possess the interesting property to be non-dispersive, which allows for the preservation of their shape in time even when displaced.
This type of solution is found in non-linear (NL) partial differential equations (PDE), which do not guarantee that the superposition of individual solutions of the equation are also valid solutions, whereas it is the case for linear equations. This opens a great deal of complexity along with a number of novel properties extensively studied in the domains of non-linear physics, a wide area of research as seen in the particularly rich *Encyclopedia of Nonlinear Science* [6]. There are three archetypal types of solitons: humps (bell shaped pulses), kinks (a constant amplitude that reverse gradually along a wall width) or breathers (which are periodic oscillating soliton structures that can take many shapes and decays exponentially with distance).
Solitons appear in many systems [4, 5]: from waves in shallow waters (described by the Korteweg-de Vries equation) and optical solitons, self-confining wave packets of light found in fiber optics (described by the Non-linear Schrödinger equation) to domain walls in magnetic materials (described by Sine-Gordon equation) only to name a few. The soliton solutions arise from non-linear terms that induces a retro-action on the system to prevent the dispersion of the excitation. This is for example the case of optical solitons, where a wave packet that should disperse can actually modify the refractive index of the material along its way which can prevent the diffusion when properly tuned. This is known as the Kerr effect (modification of the material refractive index by the light electric field which is then inherently non-linear), distinct from the Magneto-Optical Kerr effect, later discussed.

Solitons can be dynamical, preserving their shape only while moving, as discussed for optical solitons or water solitons like tidal bore, or they can be static with a preserved shape even at rest, which is the case of topological solitons such as magnetic domain walls or skyrmions of any kind.

Because solitons can be found as a way to obtain particle-like properties from fields they are very important to understand as they might allow for a more fundamental description of all physical phenomenon under the unifying notion of fields. Actually, the distinction between fields and particles has been puzzling physicists for a long time, and still continues today as one could see it in the unresolved issue of the wave-particle duality in Quantum Mechanics.
We might trace the modern debate (which otherwise can be found much sooner considering the nature of light between Newton and Huygens) to De Broglie's work who developed around the 1930s the pilot wave theory to describe a quantum particle coupled to its fields that follows trajectories in space [56, 57, 58, 59]. De Broglie itself traces his ideas back to Einstein who developed a precise intuition on the distinction of particle and field along its thorough study of Maxwell's equations or later general relativity, as seen in his statement [57]*: "A coherent field theory implies all its elements to be continuous not only in time but also in space, at any point. From which follows that the particle can not be a fundamental concept of a field theory."* Also one can read from de Broglie on Einstein: *" He (Einstein) have been led to conclude that all the physical world have to be entirely described with fields (or maybe a unique field), well defined in every point of space and time and following well determined propagation equations, probably nonlinear."*
Einstein ideas on the mater can even be found as soon as 1909 [60], which shows that he was looking, from a long time, for a special kind of field solution that can replicate particle like properties. The description of such a fundamental topic is far out of the scope of this manuscript, but it is noteworthy as it motivates the study of magnetic skyrmions that share many properties with the peculiar solitons found in the Skyrme model as we will present below.

1.1.3 Magnetic skyrmions and baby-skyrmions

The soliton structures found in the pion field by Skyrme require a chiral interaction to be stable. A chiral interaction is likewise at the root of the stability of magnetic skyrmions. Also, the Skyrme model is linked with magnetic materials by their common theoretical description in term of non-linear Sigma models [55, 62, 63, 16]. Moreover, the 2D version of the Skyrme model, usually described as the baby-Skyrmion model [10], shows a lot of similarities with the skyrmions observed in magnetic materials. In Fig. 1.2, arrows represent the vectors associated to the isospin of skyrmions (Skyrme model) and to the magnetic moments of magnetic skyrmions. Fig. 1.2 d) shows that the spatial representation of magnetic moments constituting a skyrmion paves fully the target space of magnetic moment orientation, i.e. the magnetic moments can be mapped onto a unit sphere, just like baby-skyrmions iso-spins also do, as seen in Fig. 1.2 a) . In b-e) we can see that they share the same shape of angle profile and in c-f) the same tendency to stabilise into skyrmion crystals, but also into tubular structures when non-zero thickness is considered [8, 64]. The common structures stabilised by these much different theories explain the naming of magnetic skyrmions as a 2D magnetic analogue of nuclear physics skyrmions. It seems that some more connections might be obtained considering the complex Ginzburg-Landau equation from which both the Skyrme Model and the Landau-Lifshitz equation (that describes magnetic materials) can be related in some specific cases [3, 65, 66, 6, 67, 68, 69].

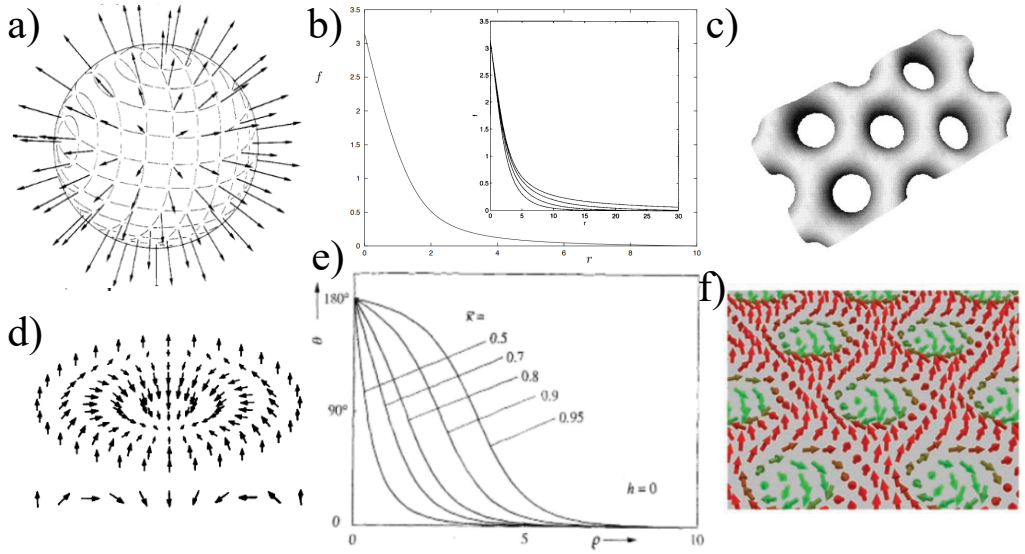

Figure 1.2: Baby skyrmion and magnetic skyrmion. a) Unit sphere paved by a baby-skyrmion iso-spin, from [10] b) Baby-skyrmion iso-spin profile, inset shows profile dependence with skyrmion angular momentum, from [3, 8] c) Baryon isodensity for baby-skyrmion model that present a lattice structure. Extracted from [10] d) Magnetic skyrmions representation that also paves the unit sphere, from [61]. e) Magnetic skyrmion profile for different ratio of chiral interaction in the domain wall energy, from [61] f) Representation of magnetic skyrmions in a lattice structure as observed by reciprocal space measurements [11].

These connections are not well described to my knowledge and some clear explanations might yield very interesting results. A broad discussion on the matter can be found in [70] and a more complete one in [71].

The magnetic skyrmions presented before, as a set of arrows pointing in different directions, is a peculiar kind of magnetic pattern, from a large zoology of what is usually referred as magnetic textures [72, 73]. The stability of a skyrmion as well as other magnetic textures, depends on the competition between multiple interactions that we introduce in the following part.

1.2 Magnetic interactions

First of all, magnetic moments $\vec{\boldsymbol{\mu}}$ arise from the angular momentum of charged particles and takes the following form when considering electrons: $\vec{\boldsymbol{\mu}} = -\gamma \vec{\boldsymbol{J}}_a$, with $\vec{\boldsymbol{J}}_a$ composed from the spin angular momentum S and the orbital angular momentum L. $\gamma = \frac{g_e \mu_B}{\hbar}$ is the gyromagnetic ratio and g_e the electron Landé factor, $\mu_B = \frac{e\hbar}{2m_e}$ the Bohr magnetron, with $\hbar$ the reduced Planck constant and m_e the electron mass. We will later use the denomination of spin in an abusive way, considering always the total angular momentum J_a as we will be sensitive in most of our experiments to the resulting magnetic moment and not to its individual contributions. If this can lead to any confusion, special care will be made to lift any ambiguity.
Spins experience the exchange interaction that can align or anti-align them locally. They also are sensitive to their local environment where spin-orbit coupling (SOC) related effects can create magneto-crystalline phenomena (anisotropy, magnetostriction), or also chiral interactions as DMI. Also, each spin corresponding magnetic moment, radiates a magnetic field called the dipolar field with effects on both short and long spatial scales. Then, spins are sensitive to external magnetic fields, as described considering the Zeeman energy. Let us now define all these interactions more rigorously.

1.2.1 Exchange Interaction

The exchange interaction describes the difference in energy for two neighbouring electron spins to be in a singlet (anti-symmetric) or triplet state (symmetric). Because electrons are fermions, their complete wave functions have to be anti-symmetric, and so the spatial symmetry of the wave function will be determined by the spin part. Considering only two electrons, in units of $\hbar$, a singlet wave function implies s = 0 and a symmetric spatial wave function whereas a triplet wave function implies s = 1 and an anti-symmetric spatial wave function [74, 75].

When computing the difference in energy between the singlet and triplet state one obtains an energy $J^{ex} = \frac{J^{ex}_{int} - CB^2}{1-B^4}$ where J^{ex}_{int} is the exchange integral, C the Coulomb integral and B the overlapping integral computed from the electron wave functions. The resulting energy J^{ex} can be positive and yields a ferromagnetic coupling or negative which yields an anti-ferromagnetic coupling [76].
One can for example consider the direct exchange for electrons on orthogonal orbitals (p_x, p_y, p_z, or s shell with any other orbital for example). In this case, the overlap integral $B = 0$ then $J^{ex} = J^{ex}_{int}$, and so the coupling is ferromagnetic, which gives a triplet state that reduces the coulombic repulsion thanks to the anti-symmetric spatial wave function. This is consistent with the first Hund rule. But in all other cases, for non-spherical orbitals of the same atom, or orbitals of different atoms, the exact determination of the sign of the exchange is far from being trivial [76].
Considering all pairs of neighbouring electrons $< i, j >$ with spin $\vec{\boldsymbol{S}}_i$ and $\vec{\boldsymbol{S}}_j$ [77], and a constant exchange J^{ex} for first neighbours and zero otherwise the total energy of the exchange is given by Eq. 1.1[1], where $s_i = \frac{S_i}{\hbar}$:

$$\mathcal{H}_{ex} = -J^{ex} \sum_{<i,j>} \vec{\boldsymbol{s}}_i \cdot \vec{\boldsymbol{s}}_j \tag{1.1}$$

The micromagnetic formalism considers the magnetisation at a mesoscopic scale (neglecting its discrete origin) and so all discrete energies can be derived in a continuous form. Eq. 1.2 gives the exchange interaction with $A^{ex} = \frac{2J^{ex}s^2}{a}c$ the exchange stiffness expressed with a the lattice constant and c a structural parameters given by the crystal symmetry (c= 1 for cubic, c= 2 for body centred cubic and c = 4 for face centred cubic lattices) [77]. With $\mathbf{m} = \frac{\mathbf{M}}{M_s}$, $\mathbf{M} = n < \boldsymbol{\mu} >$ with n the magnetic moment density.

$$\mathcal{H}_{ex} = A^{ex} \int dV[(\nabla m_x)^2 + (\nabla m_y)^2 + (\nabla m_z)^2] \tag{1.2}$$

The exchange interaction is usually stronger than all other interactions. The length scale of the interaction is given by the exchange length $l_{ex} = \sqrt{\frac{2A^{ex}}{\mu_0 M_s^2}}$, with M_s the saturation magnetisation of the material, μ_0 the vacuum magnetic permeability. The typical length scale of l_{ex} is in the tens of nanometers for the low magnetisation of ferrimagnets down to few nanometers for ferromagnets with larger magnetisation.

Exchange mechanisms

Most exchange interactions are very short range, confined to electrons in orbitals on the same atom (intra-atomic exchange) or between nearest neighbour atoms (direct exchange). However, long range interactions can occur via intermediary atoms, for example through oxygen atoms (superexchange) with special cases described by Goodenough-Kanamori [78, 79, 80].

[1] We use the convention of $\mathcal{H}^{spin}$=-2J$^{ex}\vec{\boldsymbol{s}}_1\vec{\boldsymbol{s}}_2$, see [77]p76-82.

The exchange interaction can also be mediated by conduction electrons, and then possesses the interesting property of oscillating between ferromagnetic and anti-ferromagnetic coupling depending on the distance between atoms, which is know as $RKKY$ coupling (Ruderman–Kittel–Kasuya–Yosida) [81, 82, 83]. This coupling is of great interest when considering multiple layers of magnetic material, where the precise determination of a spacer thickness between layers can allow for any kind of coupling [84]. This is the mechanism from which synthetic antiferromagnets are obtained for example. Also, it was believed for a long time that the coupling between 3d Transition Metals and 4f Rare-Earth was from RKKY origin, but later understood differently as discussed in [85]. The exchange coupling in ferrimagnets is discussed in section 2.2.

Metallic and magnetic materials

For materials with very large orbital hybridisation at the Fermi level, as in the case of metallic materials, the origin of magnetism has to consider the band structure in order to be consistent with experimental observations. The electronic bands can be separated between a majority and minority spin bands from which a more complex mechanism can favour ferromagnetic properties. This has to be considered using the Stoner criterion that consists in comparing the (kinetic) energy lost by stacking electrons from the minority to the majority spin band with the energy gained by the exchange [77]. This can be simply put as the fact that bands with large density of state (rather flat) implies a lower difference in energy between successive electron states and so will allow for more electrons to migrate from the minority to majority spin band for a given exchange interaction which results in spin polarised bands [77]. The Stoner criterion is only favourable for three pure atoms which are the Fe, Co and Ni, that are the only ferromagnetic pure materials above room temperature.

1.2.2 Dzyaloshinsky-Moriya Interaction

When considering large spin-orbit coupling (SOC) effects between two magnetic atoms and a third atom, like for superexchange, an interaction can arise between the neighbouring spins that will favour their canting. Because of the form of the interaction, it was referred as the antisymmetric exchange, but is nowadays named upon the two major contributors of its description, namely, Dzyaloshinsky [12] and Moriya [13]. The Dzyaloshinsky-Moriya interaction (DMI) can be found in non-centrosymmetric crystals, or at interfaces between magnetic and large spin-orbit coupling materials. The interaction $\mathcal{H}_{DM}$ for first neighbours takes the form given by Eq. 1.3:

$$\mathcal{H}_{DM} = \sum_{<i,j>} \vec{\boldsymbol{d}_{ij}} \cdot (\vec{\boldsymbol{s}_i} \times \vec{\boldsymbol{s}_j}) \tag{1.3}$$

Focusing on interfacial DMI, let us define $\vec{\boldsymbol{e}_z}$ as the normal to the interface. The continuous, micromagnetic, formulation of DMI [86] is given by Eq. 1.4:

$$\mathcal{H}_{DM} = D_m \int dV [m_z \cdot \nabla \vec{\boldsymbol{m}} - (\vec{\boldsymbol{m}} \cdot \vec{\boldsymbol{\nabla}}) m_z] \tag{1.4}$$

The volumic intensity of the DMI (in J/m^2) interaction is related to the strength of the DMI vector from Eq. 1.3 [87, 88]. D_m is referred as the DMI constant from which the sign determines the chirality ($D_m < 0$ favours clockwise winding [15], and inversely for $D_m > 0$). Fig. 1.3 a) presents a schematic picture of interfacial DMI vector. The volumic DMI can be related to the interfacial DMI D_s by $D_m = \frac{D_s}{t}$ where is t the magnetic layer thickness. D_s is better suited for comparisons as it considers the interfacial origin and not the resulting energy.

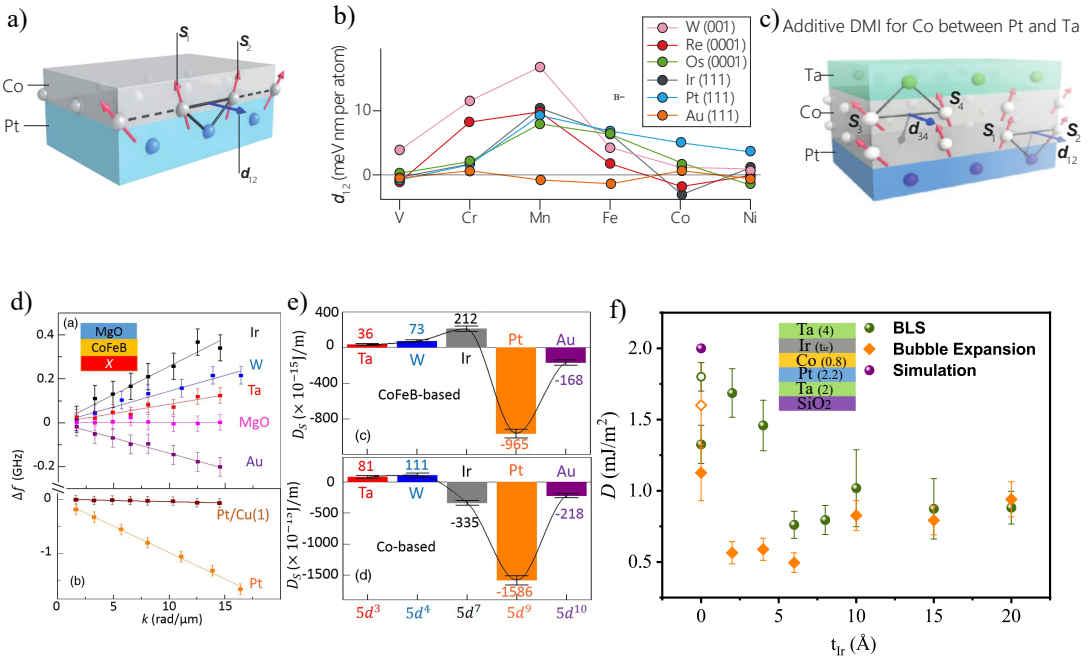

Figure 1.3: Interfacial DMI. a) Schematic principle of interfacial DMI and additive mechanism using opposite DMI constant adapted from [15] with c) DMI intensity computed theoretically (from [89]). d-e) CoFeB Interfacial DMI measured by BLS for several interfaces (from [90]). f) Focus on the DMI sign of Co-Ta interface measured by BLS and asymmetric magnetic domain expansion (from [91]).

Examples of DMI vector or DMI constant strength and signs for material couples are given in Fig. 1.3 b) and e), which show that the sign of the DMI is not the same for all interfaces.

Because of its interesting magnetic properties, Co is the material of choice in our research field, and will play a central role in the work presented in this thesis. For this reason we will see great interest in knowing its interfacial properties with other materials. The sign and intensity of DMI with Co (or CoFeB) from calculations is shown in b) and measured by Brillouin light scattering (BLS) in d,e), and both in f). As illustrated in Fig. 1.3 c), the interfaces should be chosen to allow for an additive effect of DMI. This can only be achieved using interfaces with opposite DMI, which is proven to be the case (e-f) for Pt and Ta. This choice of interface seems quite optimised to obtain large DMI acting on the magnetic layer.

1.2.3 Magnetic anisotropy

Magnetic anisotropy refers to the energetically favourable directions of the magnetisation. The anisotropy arises from the SOC of the magnetic orbitals with the surrounding environment. The microscopic mechanisms behind the anisotropy can be very intricate, because of hybridisation of orbitals that need to be considered with the example of Co with Pt or MgO for instance [92, 93]. On the other hand, the resulting effect is quite easy to model, using as an ansatz, a Taylor expansion of even powers of the reduced magnetisation $\vec{\boldsymbol{m}} = \frac{\vec{M}}{M_s}$.
In the case of multiple easy axis anisotropy along $\vec{\boldsymbol{u}}_i$, the energy is summed over the different directions:

$$\mathcal{H}_{Anis} = -\int dV \sum_i K_u(\vec{\boldsymbol{m}}.\vec{\boldsymbol{u}}_i)^2 + K'_u(\vec{\boldsymbol{m}}.\vec{\boldsymbol{u}}_i)^4 + ... \tag{1.5}$$

Where the $K_u^{'\cdots}$ are anisotropy constants for each order. For uniaxial anisotropy, the angle between the magnetisation and the single easy axis is θ. In the micromagnetic continuous formulation the interaction takes the form of Eq. 1.6:

$$\mathcal{H}_{\text{Anis}} = \int dV.K_u \sin^2(\theta) + K_u' \sin^4(\theta) + ... \tag{1.6}$$

We will usually simply consider the first order which gives $\mathcal{H}_{Anis} = K_u \sin^2(\theta)V$ where K_u is the total anisotropy that include terms from bulk and interfacial origin. So naturally, we can define Eq. 1.7:

$$K_u = K_v + \frac{K_s}{t} \tag{1.7}$$

K_v is the bulk contribution [94] that can have origin from anisotropic magnetic orbitals, stress or pairing with surrounding atoms and K_s the interfacial contribution [95, 96, 97]. Also K_u can be defined with $2K_s$ if one prefers to consider the two interfaces individually. The origin of the anisotropy in our films will be detailed in the next section 2.1.3.

Finally, because of the demagnetising effect of the dipolar field, a third origin of anisotropy can be taken into account, which is the shape anisotropy (see Eq. 1.10)

We will only study materials with an uniaxial anisotropy, with K_u either positive for out-of-plane, or negative for in-plane magnetic anisotropy. Major contributions are expected to arise from interface, and we can also note that the material that will be presented in our work (GdCo) should not present any in-plane easy axis anisotropy because of its amorphous nature.

1.2.4 Magnetic dipole-dipole interaction

The dipolar contribution to the total magnetic energy constitutes the most complex energy term to consider. Its complete formulation takes the following form:

$$\mathcal{H}_{sf} = \mu_0 \sum_{i,j} [\frac{\vec{\boldsymbol{\mu}}_i.\vec{\boldsymbol{\mu}}_j}{r_{ij}^3} - \frac{3(\vec{\boldsymbol{\mu}}_i.\vec{\boldsymbol{r}_{ij}})(\mu_j.\vec{\boldsymbol{r}_{ij}})}{r_{ij}^5}] \tag{1.8}$$

This term can seldom be analytically expressed, and is extremely computationally demanding because it has to be computed for each magnetic moment considering all other magnetic moments, and the distance between each magnetic moment r_{ij} dependence forbids any trivial simplification. However, for simple geometries, the dipolar field can be approximated by a constant field that depends only on the magnetisation orientation:

$$\mathcal{H}_{demag} = \frac{1}{2}\mu_0 \int dV.\vec{\boldsymbol{M}}^T N \vec{\boldsymbol{M}} \tag{1.9}$$

where N is the demagnetising tensor that depends on the shape of the system with its computation for arbitrary shapes discussed in details in [98].
For uniformly-magnetised ellipsoids and other simple shapes this approximation is accurate. In the case that we will be interested, very thin magnetic films, the best approximation for the demagnetising field is found to be an infinite magnetic film which yields a volumic energy of $K_d = \mu_0 M_s^2/2$ [99, 100, 101]. This yields the effective anisotropy [77]:

$$K_{\text{eff}} = K_u - K_d \tag{1.10}$$

The effect of the dipolar field can fortunately be separated in a long and short range contribution where the long range contribution can sometimes be neglected and the short range one computed accurately for simple geometries as a shape anisotropy, as seen in above.

1.2.5 Zeeman interaction

Finally, the effect of an external magnetic field acting on the magnetic moment of the material can be taken into account using the Zeeman energy which has the following form:

$$\mathcal{H}_{Zeeman} = -\mu_0 \sum_i \vec{\boldsymbol{\mu}}_i . \vec{\boldsymbol{H}} \tag{1.11}$$

Within the micromagnetic continuous formulation that reads:

$$\mathcal{H}_{Zeeman} = -\mu_0 \int dV \ \vec{\boldsymbol{M}} . \vec{\boldsymbol{H}} \tag{1.12}$$

Energetically speaking, the Zeeman energy simply favours the alignment of the magnetic moment with the applied magnetic field. Microscopically, it lowers the energy of electronic states with angular momentum in the direction favoured by the interaction of the field, which are then be preferentially populated. The application of a magnetic field is therefore the easiest experimental way to manipulate the magnetisation.

1.2.6 Bloch magnetic domain wall profile

Many magnetic systems show regions of uniform magnetisation stabilised by the exchange interaction and magnetic anisotropy called magnetic domains. Between these domains, thin regions of varying magnetic orientation appear: the domain walls (DW). Considering a system with uniaxial anisotropy, the domain walls follow the Bloch profile (Eq. 1.13):

$$\theta(x) = 2 \arctan(e^{\frac{x-x_0}{\Delta}}) \tag{1.13}$$

x_0 is the position of the DW and Δ the DW width parameter:

$$\Delta = \sqrt{\frac{A^{ex}}{K_{\text{eff}}}} \tag{1.14}$$

Typical profiles are plotted in Fig. 1.4 for several width parameters Δ. The DW presents two limit geometries of reversal.
The first one presented in Fig. 1.4 a) shows a cycloidal reversal and is referred as Néel DW. The second presented in Fig. 1.4 c) shows a helicoidal reversal and is referred as Bloch DW. The difference between the two DW is not seen in the reversal of the m_z component but in the direction of the spin reversing that can point along $\vec{\boldsymbol{e}}_x$ (Néel) ($\phi = 0$ or π) or $\vec{\boldsymbol{e}}_y$ (Bloch) ($\phi = \pi/2$ or $3\pi/2$).

Bloch DW are typically observed in thin magnetic films because they do not add surface magnetic charges (due to the dipolar field) as compared to Néel DW (see the direction of the central spin of the DW in white in both figures). In magnetic films with interfacial DMI, the Néel DW is promoted by the chiral interaction. These two geometries of reversal are limit cases, and magnetic system can present hybrid DW, or can even be shifted from Néel to Bloch by the action of spin polarised currents [86]. The complete reversal of the magnetic domains spreads on a region with a width typically of $\pi\Delta$ as seen in Fig. 1.4 b).

The DW can then be seen as an object with an energy cost given by Eq 1.15:

$$\sigma_0 = 4\sqrt{A^{ex} K_{eff}} \tag{1.15}$$

When considering DMI:

$$\sigma = \sigma_0 - \pi D_m \tag{1.16}$$

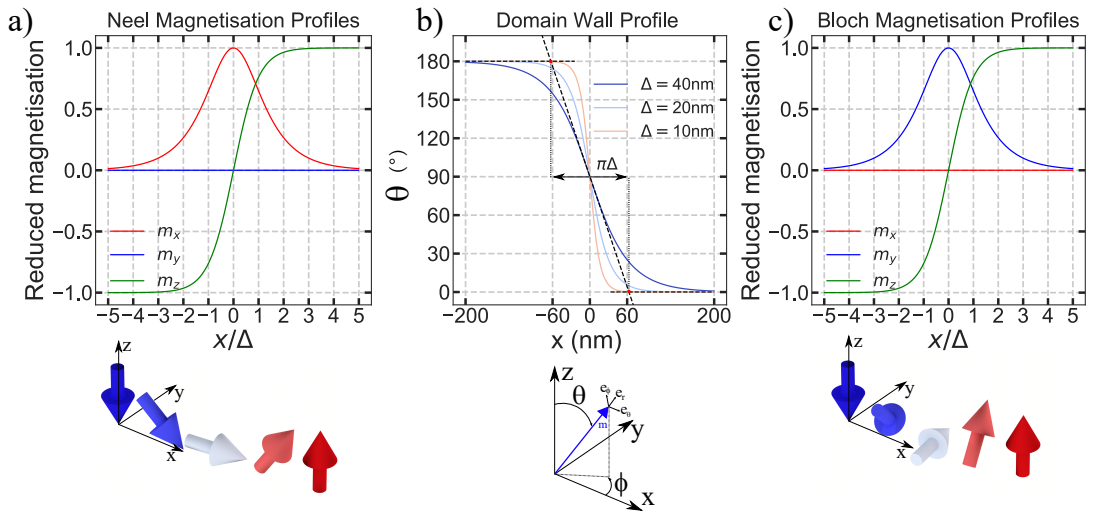

Figure 1.4: Bloch and Néel magnetic domain wall profiles. a) Néel domain wall normalised magnetisation following counter clockwise cycloidal reversal. b) General θ reversal profile with distance for several DW width parameters Δ. c) Bloch domain wall normalised magnetisation following clockwise helicoidal reversal.

The DW energy in J/m^2 gives a characteristic energy scale for magnetic textures. Indeed, in out-of-plane anisotropy magnetic systems, magnetic textures are separated by the reversal of their magnetisation, therefore greatly determined by the cost of the DW.

1.3 Magnetic Skyrmions theoretical foundation

Magnetic skyrmions were introduced by A.N. Bogdanov et al. in 1989 [9], refined a few years later [102, 61], at first as magnetic vortices, because of their resembling swirling magnetisation profile.
As explained before, the name skyrmion came from an analogy with the stabilising mechanism found by T. Skyrme to describe the stable soliton nature of atomic nucleus [2]. Bogdanov et al. showed that only non-centrosymmetric crystals (lacking inversion symmetry) may host stable skyrmions in bulk systems. Skyrmions can be seen as magnetic particle-like objects, topological structure of the magnetisation, with a core magnetisation pointing in a direction opposite to its surrounding. Its reversal profile follows a given chirality imposed by a chiral interaction such as DMI.

1.3.1 Néel and Bloch skyrmions

Because bulk or interfacial origins of the DMI lead to different symmetries of the chiral interaction [15], the resulting favoured magnetic textures are expected to differ in the two cases. For bulk origin of the DMI, the reversal profile of the skyrmion is expected to be helicoidal (like for Bloch domain wall) and cycloidal (like Néel domain wall) for interfacial origin of the DMI as shown in Fig. 1.5c-a). Both these skyrmions have the exact same topological properties, their magnetisation paves fully once the unit sphere of the magnetisation orientation space as illustrated in Fig. 1.5b). Other chiral effects can also stabilise skyrmions: dipolar, frustrated or higher order exchange interaction, for example [103, 104, 105].

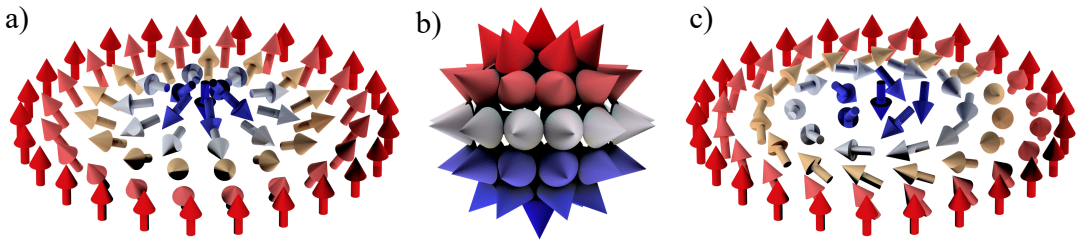

Figure 1.5: Bloch and Néel Skyrmions. a) CCW Néel skyrmion (interfacial DMI), with $P = -1$ $V = 1$ and $\phi = 0$ ($D < 0$). b) Fully paved unit sphere. c) CCW Bloch Skyrmion (bulk DMI) with $P = -1$ $V = 1$ and $\phi = \frac{3\pi}{2}$ ($D < 0$). P and V are defined in Eq. 1.20 and 1.21.

1.3.2 Topological properties of skyrmions

One of the main properties of skyrmions is their non-trivial topology, from which many of their interesting features arise. The topology is mathematically defined by the invariance of a property under continuous deformation, which can also be stated as the study of the deformation of spaces under continuous deformations. Topology is understood by looking at the winding in the solution space of the field. In the case of topological magnetism, the continuous field explored is the reduced magnetisation, the unit-vector space that describes the magnetic orientation. For skyrmions, the topological property of interest is the number of times the reduced magnetisation covers the unit sphere (see Fig. 1.2). If one follows the orientation of a 2D vector along a 1D line, like in the reversal of φ in Fig. 1.6, all possible orientations of the vector along the line cover a circle of 360° and so if one reverses the orientation of the vector from up to down, the path in solution space is covered once, following a given winding direction. This can be seen in Fig. 1.6, where the vector profile is plotted against its position, in real and target space. This winding can be integrated along a closed path and yields a topological charge that is quantified and conserved. An interesting introduction can be found in french in [62].

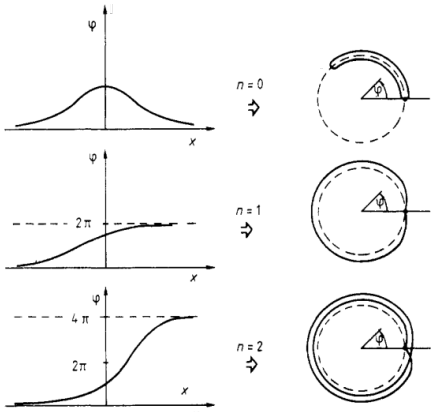

Figure 1.6: Example winding in solution space for n = 0,1,2. The angle versus position r is depicted on the left, and on the right, the position along the angle solution space (a circle for a 2D vector)[10].

Considering 2D skyrmions, the mathematical definition of the topology in magnetisation space is described by the winding number of the magnetisation that yields the magnetic texture topological charge as follows:

$$N_{sk} = \frac{1}{4\pi} \iint \vec{\boldsymbol{m}}. \left(\frac{\partial \vec{\boldsymbol{m}}}{\partial x} \times \frac{\partial \vec{\boldsymbol{m}}}{\partial y} \right) dxdy \tag{1.17}$$

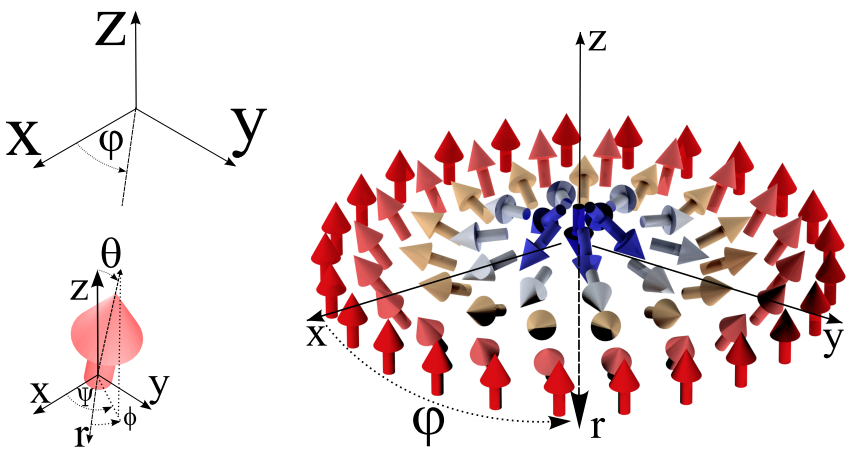

Figure 1.7: Schematic of the axis system.

We can express the last equation in polar coordinates (r, φ) with individual magnetic moment, described in a spherical coordinate system, of reduced magnetisation $\vec{\boldsymbol{m}} = \sin(\theta)\cos(\Psi)\vec{\boldsymbol{e}_x} + \sin(\theta)\sin(\Psi)\vec{\boldsymbol{e}_y} + \cos(\theta)\vec{\boldsymbol{e}_z}$ with the polar angle θ and the azimuthal angle Ψ. This allows us to separate the winding number in two contributions:

$$N_{sk} = \frac{1}{4\pi}\int_{r=0}^{\infty}\int_{\varphi=0}^{2\pi}\frac{\partial\theta}{\partial r}\sin\theta\frac{\partial\Psi}{\partial\varphi}drd\varphi \tag{1.18}$$

$$= \frac{1}{4\pi}[-\cos\theta(r)]_{r=0}^{r=\infty}[\Psi(\varphi)]_{\varphi=0}^{\varphi=2\pi} = PV \tag{1.19}$$

The skyrmion polarity number and the skyrmion vorticity number are given by:

$$P = [-\cos\theta(r)]_{r=0}^{r=\infty}/2 = [m_z(0) - m_z(\infty)]/2 \tag{1.20}$$

$$V = [\Psi(\varphi)]_{\varphi=0}^{\varphi=2\pi}/(2\pi). \tag{1.21}$$

It can be computed from the magnetisation texture as shown in Fig. 1.8 where the full unit sphere is covered by the magnetisation. This can also be directly observed by noticing that all directions of magnetisation are described along the reversal profile of skyrmions which possess axial symmetry.

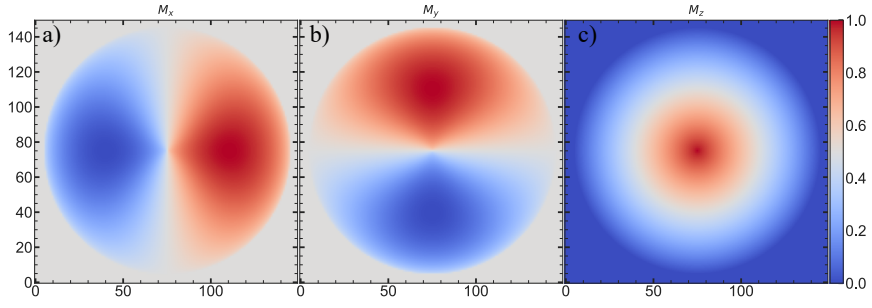

Figure 1.8: CW Néel skyrmion magnetisation. a-b-c) M_x, M_y, M_z components.

For a given form of profile, the previous integral can sometimes be computed analytically or can otherwise be integrated numerically, conventionally as done in the Fig. 1.8 that yields $N_{sk} = 0.999$, or exactly using a clever paving with triangles inside the numerical lattice [106]. This can be of importance when treating disorder, where the most straightforward computation of the topological charge can badly fail.

The topology of skyrmion is associated with an energy barrier necessary to break their topology. In a continuous space, the breaking of the topology if forbidden, however, in a real system the magnetisation has a discrete origin (spins) where a localised discontinuity is possible, and so a finite energy cost is associated to it. This finite cost has to be considered in order to account for the energy needed to collapse a skyrmion. In essence, just like a bowl that possesses no hole is topologically protected from a mug that possesses one (because no continuous transformation can change a bowl into a mug), the energy needed to punch a hole into a bowl is finite and depend on the stiffness of the links of the sources of the field from which the topology was computed. In the case of matter, the density can be described as a continuous field, but its source found in atom is itself discrete and can therefore only offer a finite energy protection. So conversely, for magnetic skyrmions the discrete sources of the magnetisation found in spins are linked by the exchange stiffness and therefore offer only a finite topological energy protection [107] . Simply put, topological protection (continuous field) is not the same as energetically protected by topology (discrete sources).

1.3.3 Types of skyrmion spin textures

Skyrmions have a vorticity $V = 1$ and depending on the core orientation of the skyrmion its polarity can be $P = \pm 1$. The type of Néel or Bloch skyrmion can be described by the definition of the helicity of skyrmion [16], i.e., the tilt angle ϕ of the magnetisation with respect to the radial axis. For Néel skyrmions $\phi = 0$ (*or* π) and for Bloch skyrmions $\phi = \frac{\pi}{2}$ (*or* $\frac{3\pi}{2}$).

Finally, the chirality, that directly refers to the reversal direction of the magnetisation along the radial axis, can be clockwise (CW), also called right-handed, or counter-clockwise (CCW), also called left-handed. For positive DMI interaction, the chirality is CCW and CCW for positive DMI interaction [15]. One can come up with a combination of the polarity P and azimuthal angle ϕ to determine the chirality of the skyrmion. For Néel skyrmion, if $P\cos(\phi) > 0$ the chirality is CW and CCW for $P\cos(\phi) < 0$. For Bloch skyrmion, if $P\sin(\phi) > 0$ the chirality is CW and CCW for $P\sin(\phi) < 0$.

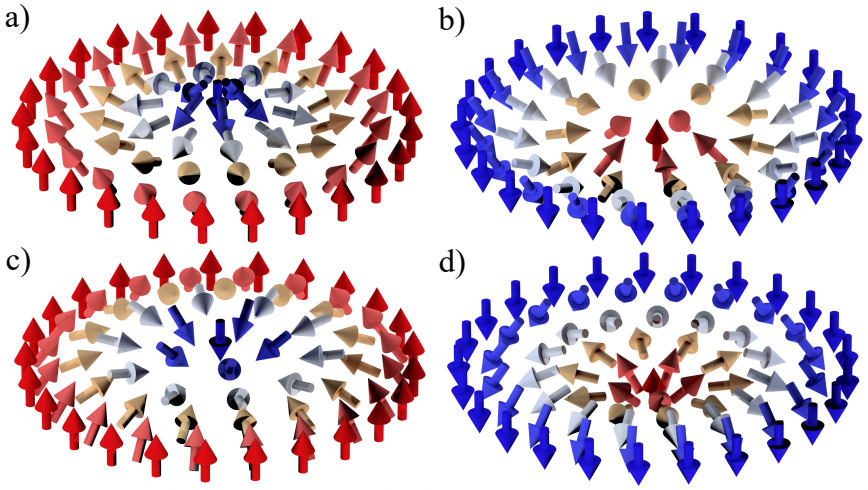

Figure 1.9: All Néel skyrmions configurations. a) CCW Down Néel skyrmion $P = -1$ $V = 1$ and $\phi = 0$ ($D < 0$). b) CCW Up Néel skyrmion $P = 1$ $V = 1$ and $\phi = \pi$ ($D < 0$). c) CW Down Néel skyrmion $P = -1$ $V = 1$ and $\phi = \pi$ ($D > 0$). d) CW Up Néel skyrmion $P = 1$ $V = 1$ and $\phi = 0$ ($D > 0$).

1.3.4 Other non-trivial topological spin textures

A complete description of the wide variety of skyrmion like textures can be found in [16]. Because there exist other kinds of swirling spin textures that can somehow resemble skyrmions we will briefly present them in order to avoid any confusion. For instance as illustrated in Fig. 1.10a), the second order skyrmions, which pave the unit sphere twice but that are not energetically favoured in strong chiral environment (also true for any higher order skyrmion) because of the chirality breaking they induce. Also potentially confusing, the anti-skyrmions (Fig. 1.10c), that possess an opposite vorticity. They are observed in anisotropic DMI [108, 109] materials like Heusler alloys [110]. This is also known to occur with higher order exchange interactions [104, 105] and can be probed with chiral sensitive experiments, for instance by measuring the dispersion of spin-waves by BLS [111].
It also worth describing vortex showed in Fig. 1.10d-g), which only cover half of the unit sphere and that can be observed in in-plane magnetised samples. Such magnetic texture have been extensively studied thanks to their interesting core precession motion which is of great interest for example for random number generation [112] or also neuromorphic application [113].

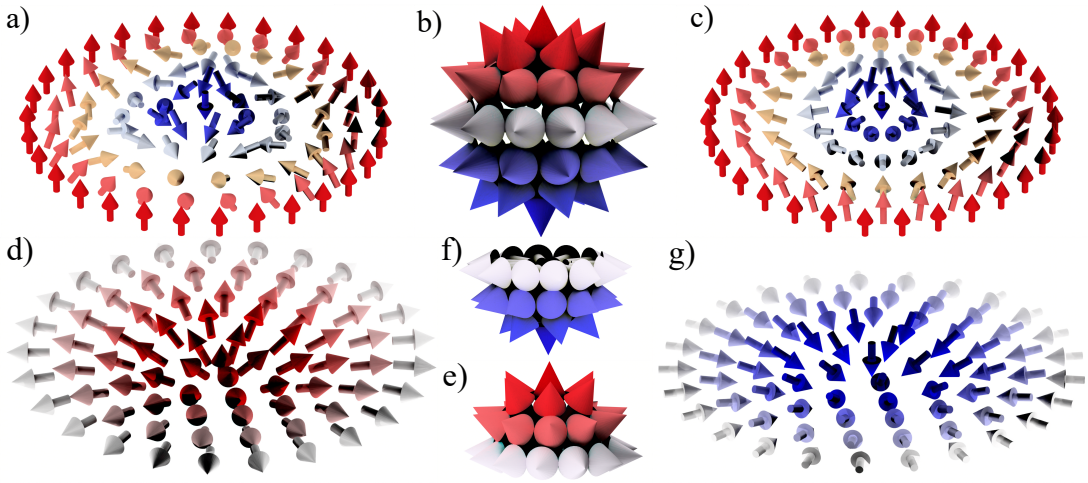

Figure 1.10: Other topological non-trivial spin texture. a) 2N skyrmion $P = 1$ $V = 2$b) The unit sphere is also paved at least once. c) Anti-Skyrmion $P = -1$ $V = -1$. d) Up Vortex $P = 1/2$ $V = 1$ and $\phi = 0$ e-f) The unit sphere is only half-paved g) Down Vortex $P = -1/2$ $V = 1$ and $\phi = \pi$.

Finally, one should be aware that skyrmions that would see their magnetisation reversing twice along the radial direction are called skyrmioniums. It can easily be seen that the polarity of such texture is 0 which makes them non-topological magnetic textures.

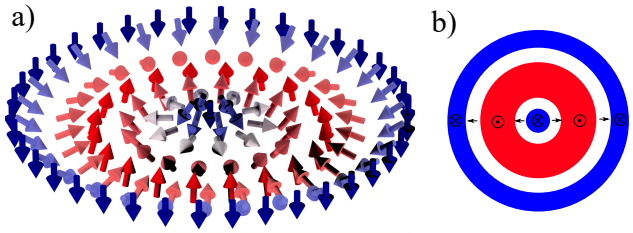

Figure 1.11: Topologicaly trivial texture Skyrmionium. a) Skyrmionium N=0. b) M_z component of the skyrmionium.

1.3.5 Magnetic bubbles

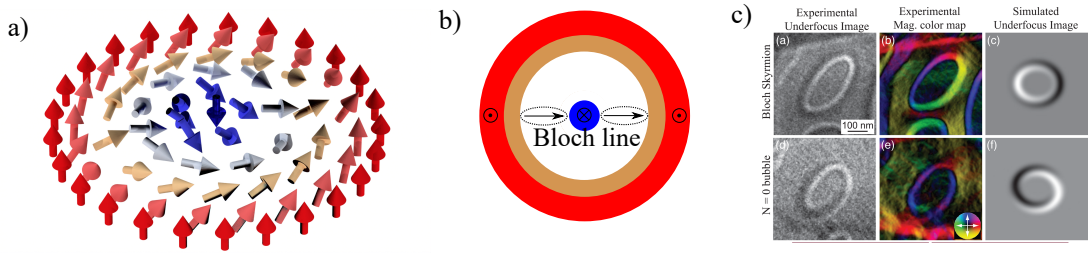

Figure 1.12: Magnetic bubbles. a) Magnetic bubble without unique chirality. b) M_z component of the bubble bubble,c) Lorentz transmission electron microscopy images (first and second column with artificial colors) and computed (third column) of Bloch skyrmions (first row) and magnetic bubbles (second row) in Ni_2MnGa [114].

Magnetic textures that resemble skyrmion can stabilise in environment without significant chiral interaction. For instance, take a conventional ferromagnetic thin film with PMA. Without chiral interaction, no winding handedness is preferred and so many kind of swirling textures can exist. This happens typically when the long range dipolar field has a sizeable effect compared to the DW energy cost. This idea is encapsulated in the dipolar characteristic length given by:

$$l_c = \sigma_0/(\mu_0 M_s^2) \tag{1.22}$$

l_c gives the magnetic thickness at which long range dipolar effects cannot be neglected. Then, for a given magnetic material with thickness t, when $l_c \leq t$ one can expect swirling magnetic textures to stabilise. In essence, one can think in terms of the dipolar field that favours larger bubble magnetic domains (to close more magnetic field lines) but because the growing bubble domain has a larger DW energy cost an equilibrium size is found by the competition. Also, considering the possibility that a single bubble fractures into multiple domains, other states can be favoured in this environment, such a bubble lattices, or stripes. This was observed in many systems, and even extensively studied around the 1970s in materials hosting magnetic bubbles [17, 18, 115, 19]. There was a great interest at the time for such magnetic textures as they were seen as potential candidates for information storage devices, before the transistors took over completely, with the most advanced architectures considering arrays of small antennas used to apply local magnetic field and move the bubbles [20]. Demonstration video is available at [116]. They were displaced with field gradients up to very fast velocities (10-100 m/s) [117, 118, 20]. The magnetic bubble possesses a trivial topology due to the creation of Bloch lines (see Fig. 1.12a-b) that present no chirality and breaks the topology of the texture. It can therefore be easily deformed of annihilated. Bloch lines would also be generated along the propagation of magnetic bubbles, which results in a saturating speed above a material dependant magnetic field gradient. Moreover, Bloch lines actually cost energy and can be seen as potential energy stored by the bubble which results in inertia in the bubble displacement, where the energy stored in Bloch lines continues the displacement after the excitation stopped [20].
Because of the absence of chiral interaction, bubbles with the two type of chirality can coexist. Also, bubbles with higher topological charge can be found which causes the deflection to present different orders (multiples of the N=1 deflection) [119, 20]. These were described at the time as bubble states and classified by their deflection order. Such higher order bubble can only be found in very low chirality systems because they break the chirality handedness. It seems to be the case in [120] where bi-skyrmions and also bubbles are observed.

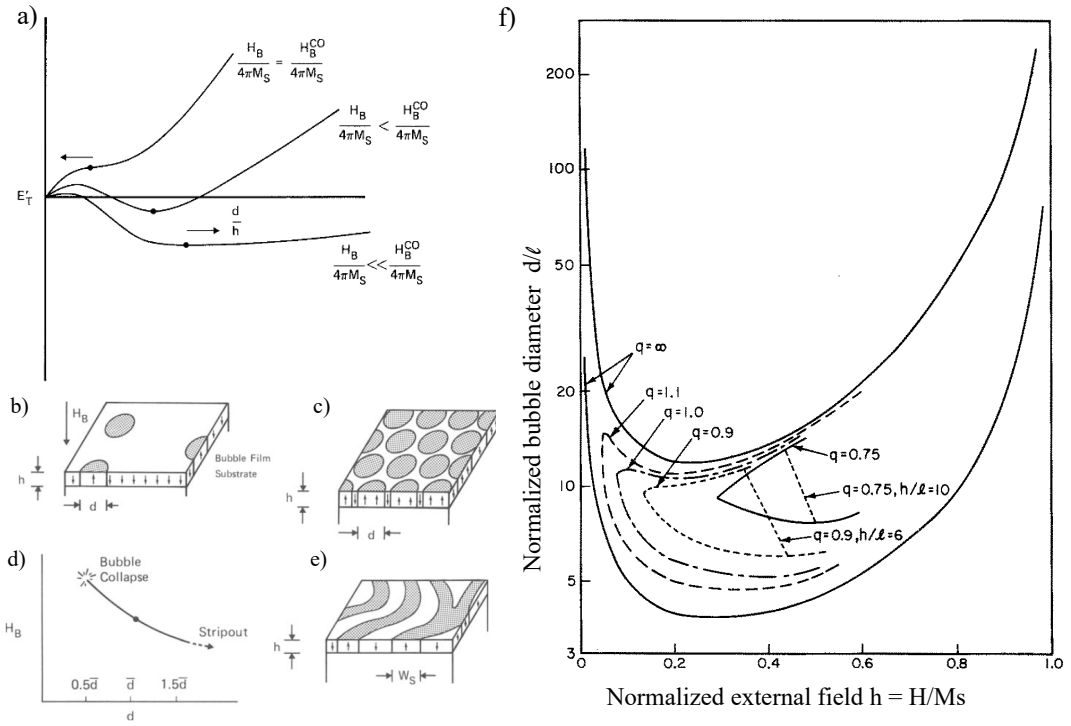

Figure 1.13: Magnetic bubble properties. a) Bubble energy versus diameter for several applied bias magnetic fields [20]. b) Isolated magnetic bubble c) Magnetic bubble lattice d) Magnetic bubble diameter with applied bias magnetic field, stripes are formed at low magnetic field, and isolated bubbles collapse at large magnetic field d) Striped magnetic textures [20] e) Magnetic bubble stable diameter versus magnetic field for several quality factor parameters (q) [121].

Finally, it is worth noting that one interesting way to distinguish between magnetic bubbles and skyrmions is found in the energy profile with radius of both solutions. One can see for example in Fig. 1.13 a) [20] or [122, 123] that bubbles present a positive $\frac{dE_{sk}}{dr}$ when $r \to 0$ whereas skyrmions present a negative $\frac{dE_{sk}}{dr}$ when $r \to 0$ as we will present latter in the manuscript. This means that when compressed (using magnetic field for example), bubbles would collapse, whereas skyrmions should survive and recover their initial radius when the magnetic field is removed (in a pinning free environment). Considering the DW energy without DMI, $\sigma_0 = 4\sqrt{(AK_{\text{eff}})}$ one can directly see that for $K_{\text{eff}} = 0$ the domain wall (DW) energy is 0. $K_{\text{eff}} = 0$ at the spin reorientation (SR) where the effective magnetic anisotropy is positive for out-of-plane magnetisation and negative for in-plane. This is often encapsulated in the quality factor Q (q in older publications) expressed in Eq. 1.23 because Q = 1 for $K_{\text{eff}} = 0$.

$$Q = \frac{2K_u}{\mu_0 M_s^2} \tag{1.23}$$

By getting close to the SR, the cost of the domain wall reduces and fractured magnetic textures, such as magnetic stripes or magnetic bubbles, can stabilise, as seen in [124] for instance. Also, from Fig. 1.13 f), one can see that there is no stable solution for magnetic bubbles at zero magnetic field (unless the q quality factor is increased towards infinity). This graphic is quite complete as it allows for a know M_s and K_u the computation of l_c (l in the figure) and Q (q) from which the field stability region and associated bubble size can be directly seen on the figure. As seen in figure Fig. 1.13 d), for large external magnetic field applied (against the bubble core) the bubble ends up collapsing, whereas for too low magnetic field, magnetic stripes will grow. In Fig. 1.13 b-c-e) are represented isolated magnetic bubbles, magnetic bubbles lattices and magnetic stripes.

Also, the long range dipolar field can induce chiral effects [103, 125] which means that some low strength chiral interaction can always be at play. This is for example the case in Ni_2MnGa as presented in Fig. 1.12c), where the low chirality of the material allows for the formation of both Bloch skyrmions (N=1) and magnetic bubbles (N=0). We can conclude that in low chiral environment, magnetic textures with the exact same profile as skyrmions can still stabilise, but the low chiral strength can allow many other kind of textures to stabilise as in [126]. Naming these objects as skyrmions in low anisotropy material is therefore coherent somehow only when taking a snapshot of the sample's magnetic textures, but there are then very little chances that such a texture behaves like the skyrmions found in strong chiral systems once displaced for instance. This means that even though very interesting to tune between different textures, the lack of strong chiral interaction do not select a single type of textures which would be very inconvenient for many applications. It should be noted that in low chiral environment, the nucleation procedure can actually favour either skyrmions profiles (nucleation by electrical current) or bubble (nucleation with in plane field) [127]. This can be understood because an applied magnetic field breaks the chirality of the system, and if low enough it can be sufficient to nucleate bubbles that will not relax into skyrmions once the field is removed. This can be checked following [127] approach by studying the asymmetrical behaviour of magnetic bubbles by current, that will collapse or elongate depending on its direction whereas skyrmion should simply be displaced symmetrically.

1.4 Skyrmions Statics in bulk and thin-film materials

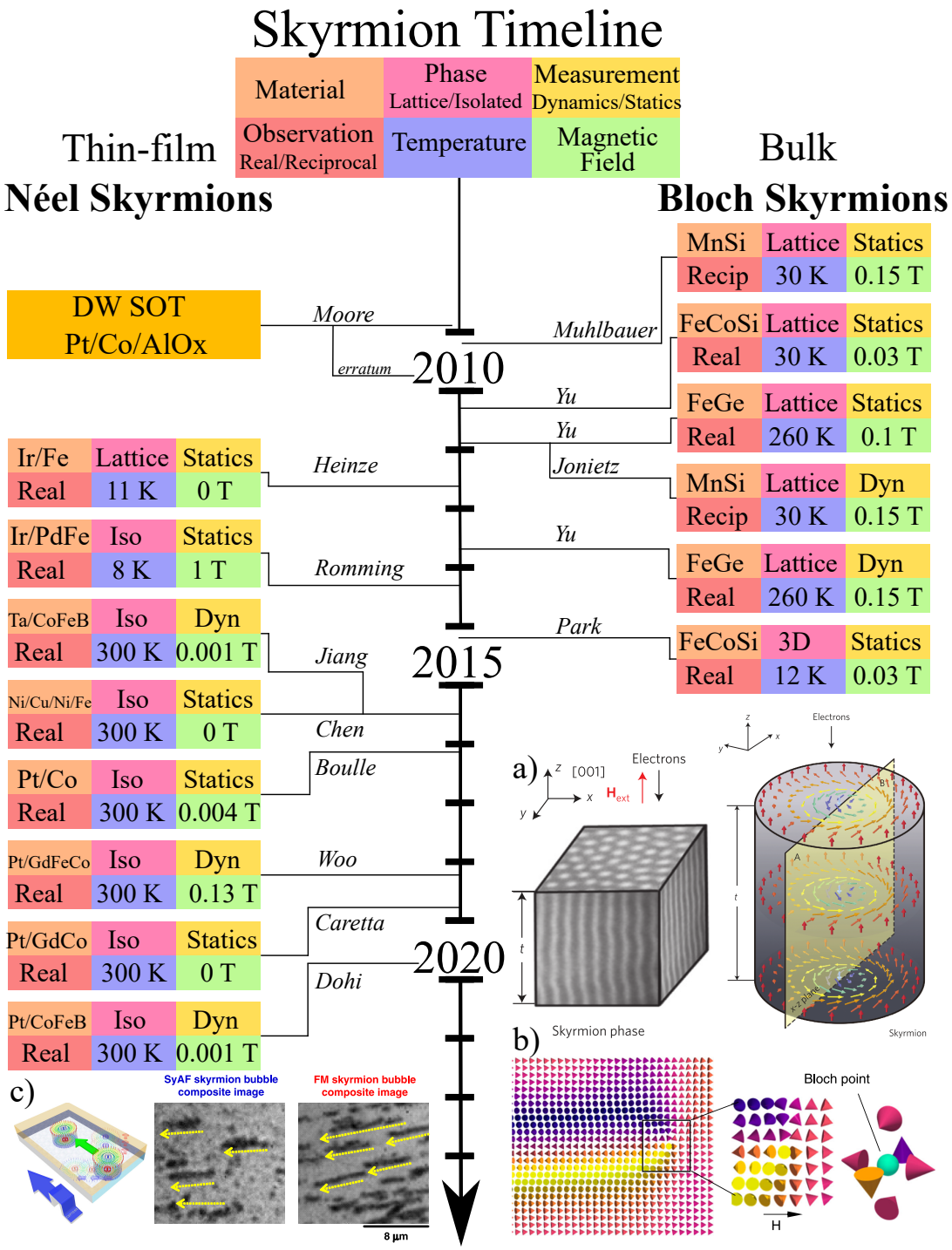

Figure 1.14: Timeline of some important contributions on skyrmions with bulk or interfacial DMI. For bulk skyrmion, in order: Muhlbauer [11], Yu [128], Yu [129], Jonietz [130],Yu [131], Park [132]. a) 3D skyrmions from [132]. b) Tubular skyrmions observed in FeGe and Bloch points observed micromagnetic simulation, from [133]. For thin film skyrmions, in order: Moore [134], Heinze [21], Romming [135], Jiang [127], Chen [136], Boulle [137], Woo [49], Caretta [50], Dohi [138]. c) Skyrmion topological deflection mitigated in SAF with MOKE images comparison with conventional ferromagnet from [138].

1.4.1 Bloch Skyrmions

After the theoretical description of skyrmions their experimental realisation took nearly 20 years, with their first observation in the isostructural B20 transition metal silicides TN (T= Fe,Co,Mn; N= Si,Ge). The discovery first happened at low temperature (below 30 K) with relatively important external magnetic field (40 to 200 mT) that stabilises the skyrmions out of a helical magnetic ground state.
They were first observed in reciprocal space by neutron scattering in MnSi [11] in 2009 with its phase diagram showed in Fig. 1.15a). and in $Fe_{0.8}Co_{0.2}Si$ in 2010 [139]. A few months later, the first real-space observation was obtained, by Lorentz transmission electron microscopy [128] in $Fe_{0.5}Co_{0.5}Si$ 20 nm thin film (with same properties as bulk material but optimised stability region in temperature and field thanks to the lowered thickness) as seen in Fig. 1.15b). Soon after, by optimisation of FeGe thickness, skyrmions could be stabilised at almost room temperature [129] with magnetic field around 100 mT as seen in the phase diagram in Fig. 1.15d).

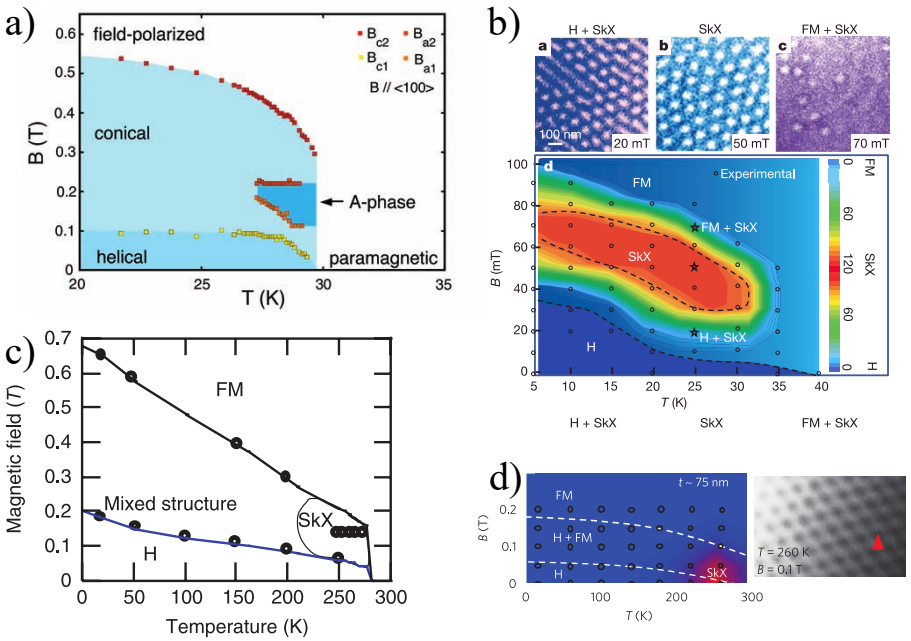

Figure 1.15: Founding publications on bulk skyrmions. a) First description of skyrmion lattice observed in reciprocal space on MnSi by [11]. b) First real space observation of skyrmions in FeCoSi by [128]. d) First skyrmions observed close to room temperature in FeGe by [129]. c) First real space observation of skyrmion lattice displace by electrical current in FeGe by [131].

Their observation by diffraction techniques pushed towards the study of the crystal lattice formation of skyrmions which reveals itself in reciprocal space. But we can also see in real space observations some isolated skyrmions in bulk material nearby the crystal lattice formation (see Fig. 1.15b) in the temperature and magnetic field parameter space but they have not been much explored in these materials. One other striking example of their interest is showed in the first study of the 3D nature of skyrmions in FeCoSi [132], with images showed in Fig. 1.14 a).
Their tubular shape has also been observed in another material, FeGe in [133]. Fig. 1.14 b shows the corresponding micromagnetic simulation of the measured tubular skyrmions that points to the presence of Bloch point at the end of the tubes. Such magnetic object is very interesting as it is the smallest magnetic object possible, a real point like defect that presents topological properties in all 3D directions. A complete review on these material can be found in [140] and a broader and recent review on skyrmions materials in [141].

1.4.2 Néel Skyrmions

1.4.2.1 Ferromagnetic skyrmions

Skyrmions stabilised by interfacial DMI, found in thin films, opened a new pathway for spintronic applications that became important for later stabilisation at convenient magnetic field and temperature. The theoretical description of such spin texture in ferromagnetic thin film was first realised by Bogdanov et al. in 2001 [14] and also took some time, 10 years, before its experimental realisation. This kind of skyrmions, because of their thin film hosting materials, are well suited for CMOS compatible applications.

Their first observation was obtained in 2011, where a skyrmion lattice was observed without external magnetic field on an atomic layer of Fe deposited on Ir(111) [21]. This was observed by spin-polarised scanning tunnelling microscope (SP-STM) still at low temperature (11K) because the Curie temperature of a single layer of Fe is very low by itself (around 30 K). The exotic 4-spin exchange of their material is at the core of the reason behind the stabilisation of the skyrmion lattice without any applied magnetic field. The image of the skyrmion lattice is presented in Fig. 1.16a).
The first isolated skyrmions were found in thin films, at high magnetic field (more than 1T) and low temperature (2-8K) in 2013 by Romming et al.[135] where the authors nucleated skyrmion using a SP-STM tip in a PdFe bi-layer on Ir(111) sample. An image is presented in Fig. 1.16b). In 2015 the same group [142] studied the effect of magnetic field on the skyrmion size and shape in the same system. The profile of these skyrmions was precisely explored in 2016 [143] also on PdFe bi-layer on Ir(111) and by SP-STM with again high magnetic-field needed to stabilise skyrmions out of spin-spiral ground states.

An important step in skyrmion stabilisation occurred in 2015 [136] with room temperature skyrmion in multi-layers thanks to inter-layer exchange coupling in Fe/Ni thin film with Cu spacer layer observed by spin polarised low-energy electron microscopy (SPLEEM). The use of a buried Ni layer offered an intrinsic magnetic field that stabilise skyrmions out of the stripe phase (in the above Fe/Ni layer) without an external magnetic field. This stack is presented in Fig. 1.16d. Even though very interesting, it means that the buried layer needs to remain magnetised, which otherwise reduces or cancels the intrinsic magnetic field.
At the same time, another step was achieved by Jiang et al. [127] that stabilised skyrmions at room temperature with little magnetic field in Ta/CoFeB sample with a skyrmion stability dependant on the nucleation mechanism by current or field. Monitored by Magneto-optical Kerr effect (MOKE), the authors used well designed constriction of magnetic tracks to nucleated skyrmions out of magnetic stripes using the current divergence of electrical pulses (see Fig. 1.16e).

An important conceptual step was achieved with the study of Pt/Co(1nm)/MgO thin film by Boulle et al. [137], where they studied the formation of skyrmion at room temperature and without any external magnetic field (or bias layer) using the strong DMI of the Pt/Co interface to lower the energetic cost of skyrmions. The skyrmion observed is reproduced in Fig. 1.16c. It was found that the long range dipolar field plays a major role in the stabilisation of skyrmion. even though it could be counter intuitive for thin films. Indeed, even in very thin films, were the dipolar strength could seem negligible, the strong effect of DMI on the reduction of DW energy lead to a potential important role of the dipolar field. They also observed strong effect on the stability due to confinement which was predicted a few years before [144].

Enlightening experimental evidence of the main ingredients necessary for skyrmion stabilisation in thin films, namely, the dipolar field, the magnetic anisotropy and the DMI, can be found in [145] where skyrmions were stabilised in IrMn thin film by exchange bias with fine tuning of the magnetic material thickness, and even more interestingly in wedged FeCoB thin film [146] that clearly demonstrate the combined role of all three interactions in the skyrmion stabilisation.

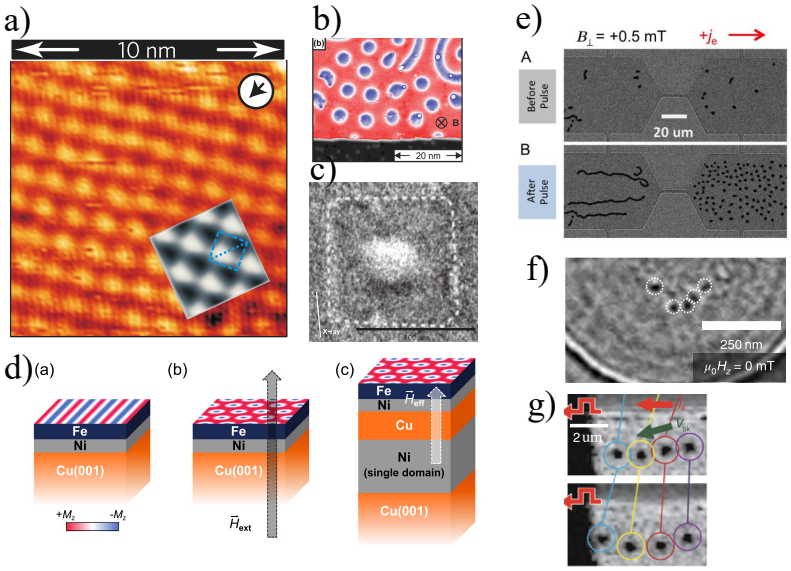

Figure 1.16: Founding publications on thin film skyrmions. a) First skyrmions observed in Ir/Fe thin film [21]. b) First isolated skyrmions observed in Ir/PdFe [135]. c) First isolated skyrmions observed in Pt/Co with clear description of the dipolar field effect by [137]. d) First use of a buried magnetic layer to stabilise skyrmions without magnetic field in Ni/Fe by [136]. e) First SOT dynamical experiment on skyrmions in Ta/CoFeB [127]. f) Smallest skyrmions observed at room temperature and zero field in ferrimagnetic sample of Pt/GdCo [50]. g) First SOT experiment in ferrimagnetic material of Pt/GdFeCo with low skyrmion deflection [49].

1.4.2.2 Double-magnetic lattices skyrmions

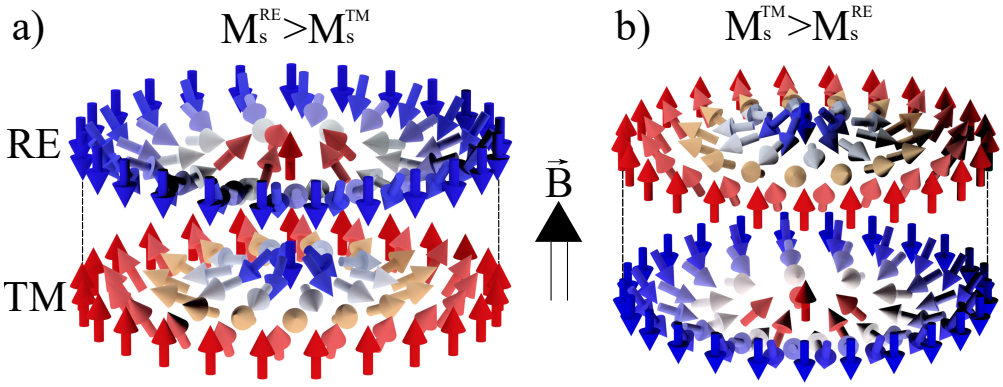

Figure 1.17: CCW coupled Néel Skyrmions in double magnetic lattices materials. Example given for a Rare-Earth (RE)/Transition Metal (TM) ferrimagnetic material, with one of the two sub-lattice with higher magnetisation that aligns with an external applied magnetic field. a) RE lattice dominates. b) TM lattice dominates.

The latest development for skyrmions can be found in multi-magnetic-lattices materials. Namely, antiferromagnets (AF), synthetic anti-ferromagnets (SAF) or ferrimagnets. Usually composed of only two antiferromagnetically coupled magnetic sublattices, these three types of materials share a lot of common properties. Antiferromagnets differ from ferrimagnets because both of their sub-lattices are from the same chemical nature when they are different for ferrimagnets. In the case of SAF, the two sub-lattices can be of the same or of different chemical nature, but are spatially separated by a spacing layer allowing for RKKY interaction. This oscillating interaction can be used to couple the separated layers ferromagnetically or antiferromagnetically, depending on their specific distance.
All these materials offer a wide variety of unique features that make them particularly interesting candidates for hosting skyrmions. One of the most straightforward interest, resides in their very low (to null) magnetisation that makes their magnetic textures less sensitive to external magnetic fields. Also, the low magnetisation of such materials favours a strong reduction of the skyrmions' size which is computed to be the lowest in zero magnetisation environment [147, 148, 149]. It is found that such material favour rapid dynamics of skyrmions [150, 138] but the actual reason behind this is not obviously connected to their low magnetisation or angular momentum density.
Finally, the double magnetic sub-lattices offers a way out of the most problematic issue with skyrmions which is their topological deflection that prevents their straight-line motion. The nature of this deflection is described later Sec.1.6.5. Indeed, the topological deflection direction depends on the polarity of the skyrmion, which is opposite between the two sub-lattices. This allows a reduction of the overall deflection (one lattice counter-acting the deflection of the other) up to a complete vanishing of the deflection when the angular momentum density in both sub-lattices perfectly cancels out. These points of interest will be refined in the next chapters as they are at the core of the motivation of our work.
There is little experimental literature on SAF skyrmions, and none on skyrmions in antiferromagnet to my knowledge. The study made by [138] in CoFeB layers coupled by RKKY interaction present a massively enhanced speed in the SAF material compared to the same conventional ferromagnetic one. Skyrmions were also observed in Pt/Co/Ru SAF in [151] with a complete study of thickness effects of each layer on the couplings and magnetic energy of the systems with accurate skyrmion profile measurements.

Finally, it is worth mentioning that the usual description of skyrmions as 2D objects is obviously a simplification of their 3D nature which follows in the simplest case a tubular shape as discussed for bulk skyrmions. The 3D nature of skyrmions has also been described in thin film multi-layers by [152] in hybrid ferromagnetic/ferrimagnetic structures. When studying very thin films, thinner than the exchange length, the 3D nature of the skyrmion seems quite irrelevant. But for thicker samples, and more especially for multi-layer materials like in the case of SAF, this 3D nature should be considered as it can drastically change the properties of the skyrmions. The work of W. Legrand [123], along with clear explanations of skyrmion properties, presents for instance very peculiar results on the internal structure of skyrmions. Indeed, in his rather thick multi-layer stack samples, the chirality of skyrmions from upper or lower layers is actually reversed due to flux closer effects of the dipolar field [153, 154]. The description of the complex phenomenon arising in these multi-layer material seems critical to understand how skyrmions can be efficiently displaced in such structures. For instance the reversal of the skyrmion chirality has dramatic effects on their dynamics (see Fig. 1.24 for instance), and the advantages of these thick magnetic systems for skyrmion stability (that somehow scales with the thickness of magnetic layer) have to be discussed in regard of the more complex dynamics they display.

1.4.2.3 Skyrmions in ferrimagnets

The experimental observation of skyrmions in ferrimagnetic systems is quite recent. It started in 2018 in a ferrimagnetic material of GdFeCo by Woo et al. [49] (Fig. 1.16g). This was quickly followed by interesting static observations of the smallest thin film skyrmions recorded in GdCo thin film by Caretta et al. [50] because of a favourable cancellation of the magnetisation of the two magnetic sub-lattices. These very small skyrmions are showed in Fig. 1.16f). Later, small skyrmions with typical size of 40 nm were observed in $DyCo_3$ with their magnetisation profile very well characterised by X-ray magnetic circular dichroism experiments by Chen et al. [155]. Also, a precise determination of the skyrmion radius evolution with magnetic field has been achieved in GdFeCo by scanning transmission X-ray microscopy by Wu et al. [156]. They have also shown, thanks to their sub-lattice sensitive the presence of a skyrmion in each of the lattice, as expected for ferrimagnetic skyrmions. Also in GdFeCo, Woo at al. [49] described the process of controlled nucleation of isolated skyrmions by electrical pulses and determined the interest of lowered magnetic anisotropy region as nucleation centres. There are also some studies on the stability of ferrimagnetic skyrmions in Fe/Gd multi-layer by Seaberg et al. [157] or for the size of confined ferrimagnetic skyrmions in micro-pillars of variable size in GdCo by Brandao et al. [158]. Finally, a very interesting study on the skyrmion stability in Pt/GdCo(t)/Pt as a function of the magnetic layer thickness is done by the same group [159].

1.5 Models of skyrmions stability

Let us introduce in the following paragraphs the main features to be described when discussing skyrmion statics in the micromagnetic framework. The method always follows the same procedure. Writing the energies at play, a variational approach is used to obtain a Euler-Lagrange equation on the magnetisation profile. The previous equation can be analytically computed in some specific cases, but is otherwise computed numerically in order to verify the validity of a skyrmion profile given as an ansatz. The explicit form of the energies can then be derived, and minimised according to the skyrmion radius. This yields an equilibrium radius which can then be studied by tuning magnetic parameters in order to explore the static properties of skyrmion.

Skyrmion profile

The skyrmion profile is usually considered to follow the 360° DW model [160]. In this framework, skyrmions of radius R can be described as a DW enclosed on itself with a reversal along r between its core and the surrounding on a length scale of the usual DW parameter width Δ which yields a the following profile (equivalent to eq. 1.13):

$$\theta(r) = 2\arctan\left(\frac{\sinh(R/\Delta)}{\sinh(r/\Delta)}\right) \tag{1.24}$$

An obvious limit between skyrmions with $R >> \Delta$ and skyrmions with $R \approx \Delta$ or lower appears in this formulation.
The profile of skyrmions can be precisely measured as observed by X-ray magnetic circular dichroism in Fig. 1.19 a) i). The image is deconvoluted from the experimental resolution and yields a very good agreement with the DW profile. The skyrmion profile is expected to change for different DMI ratio $\kappa = \frac{D_m}{D_c} = \frac{\pi D_m}{4\sqrt{AK_{\text{eff}}}}$ which defines the ratio of the DMI parameter D_m with the critical DMI D_c (above which cycloidal state is favoured). From this parameter, one can observe two types of profiles, one rather sharp, arrow like for compact skyrmions at smaller κ, and another profile at larger κ for bubble like skyrmions with a rather uniform core and a DW like reversal profile.

It should be noted that smallest skyrmion are expected to present a profile that differs from a DW due to a modification of Δ with the reduction of the radius. This lead [161] to propose a different ansatz for the skyrmion profile given by:

$$\theta(r) = 2\arctan\left(\frac{R}{r}e^{\frac{(R-r)}{\Delta}}\right) \tag{1.25}$$

Both equations yield the same profile for large skyrmion but indeed differ for small ones as seen in Fig. 1.18.

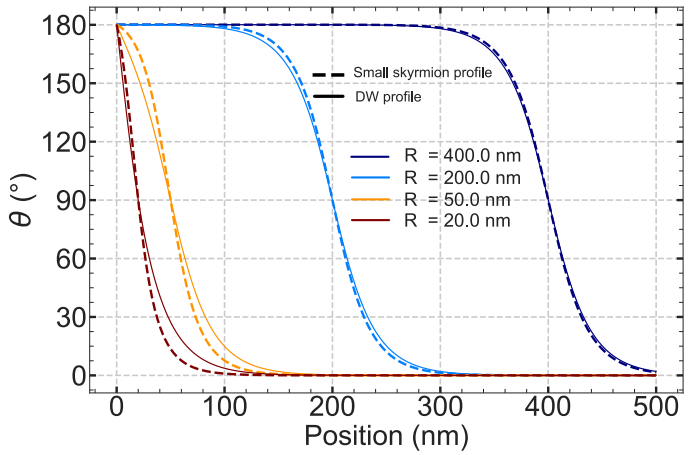

Figure 1.18: Skyrmion profile ansatz. Filled lines are plotted with Eq. 1.24 (DW profile) and dotted lines with Eq. 1.25 (Small skyrmion profile).

Large and small skyrmions

The very different sizes of skyrmions (from few nm to μms) that then present different profiles, found as well as in experimental than through theoretical or numerical works, points towards an obvious distinction between them. But it has been pointed to the fact that the profile in itself is not sufficient to distinguish a kind of skyrmion [147], but rather that the exact contribution from DMI and dipolar field should be weighted in order to distinguish them. This is done for example, in the pedagogical article of Bernand-Mantel et al. [148] reproduced in Fig. 1.19 b). The authors introduce a dimensionless factor that weights the contribution of the dipolar field with all the other micromagnetic energies to obtain the skyrmionic factor S_s. This factor shows that skyrmions dominated by exchange, anisotropy and DMI energy (with $S_s >> 1$), called compact skyrmion are usually smaller than skyrmions dominated by the dipolar energy with ($S_s << 1$) , called stray field, or bubble skyrmions.

We can see from Fig. 1.19 b i-iii) that an increasing D_m value increases the skyrmion equilibrium radius (<5 nm to > 100 nm). It should also be noticed that the magnetic field (applied against the skyrmion core) changes the skyrmion equilibrium radius. Indeed, we can see that between ii and iii) the D_m value is quite similar but in ii) with 0.28 mT the second solution yields a radius around 600 nm whereas in iii) with 2mT the radius is found to be around 100nm, which clearly shows the compressing effect of the magnetic field. As seen in Fig. 1.19 b ii), two equilibrium radius can coexisting for specific sets of parameters and corresponds to the compact and stray field skyrmions presented above. These two solutions have the exact same topology but can behave slightly differently due to their different sizes. For example, at low radius, the curvature energy of the exchange is not negligible which adds a restoring force against skyrmion deformation [162]. Also, the effect of magnetic field is skyrmion size dependant.

We will use this model for double magnetic sublattices material in Sec. 3.2 when discussing our results on skyrmion statics in ferrimagnetic materials.

Also, a limit is found in the only non-vanishing energy in the limit of $R \to 0$, which is the exchange energy that converges to a finite value. This was described by Belavin and Polyakov [163] who derived the topologically induced exchange energy limit $E(R=0) = E_0^{sk} = 8\pi A^{ex} t$ with t the magnetic film thickness. This finite energy at R = 0 is computed as the difference with the saturated state and is rather important for the statics properties of skyrmions as it makes negative the energy derivative with respect to radius at R = 0, which is one of the main difference with magnetic bubbles, and which implies that skyrmions should be compressible up to very low radius by magnetic field without inducing their annihilation whereas it induces the collapse of magnetic bubbles. Also, E_0^{sk} can be seen as the nucleation energy for skyrmions and is also related to the equilibrium of skyrmion because the annihilation energy $E_a = E_0^{sk} - E(R)$.

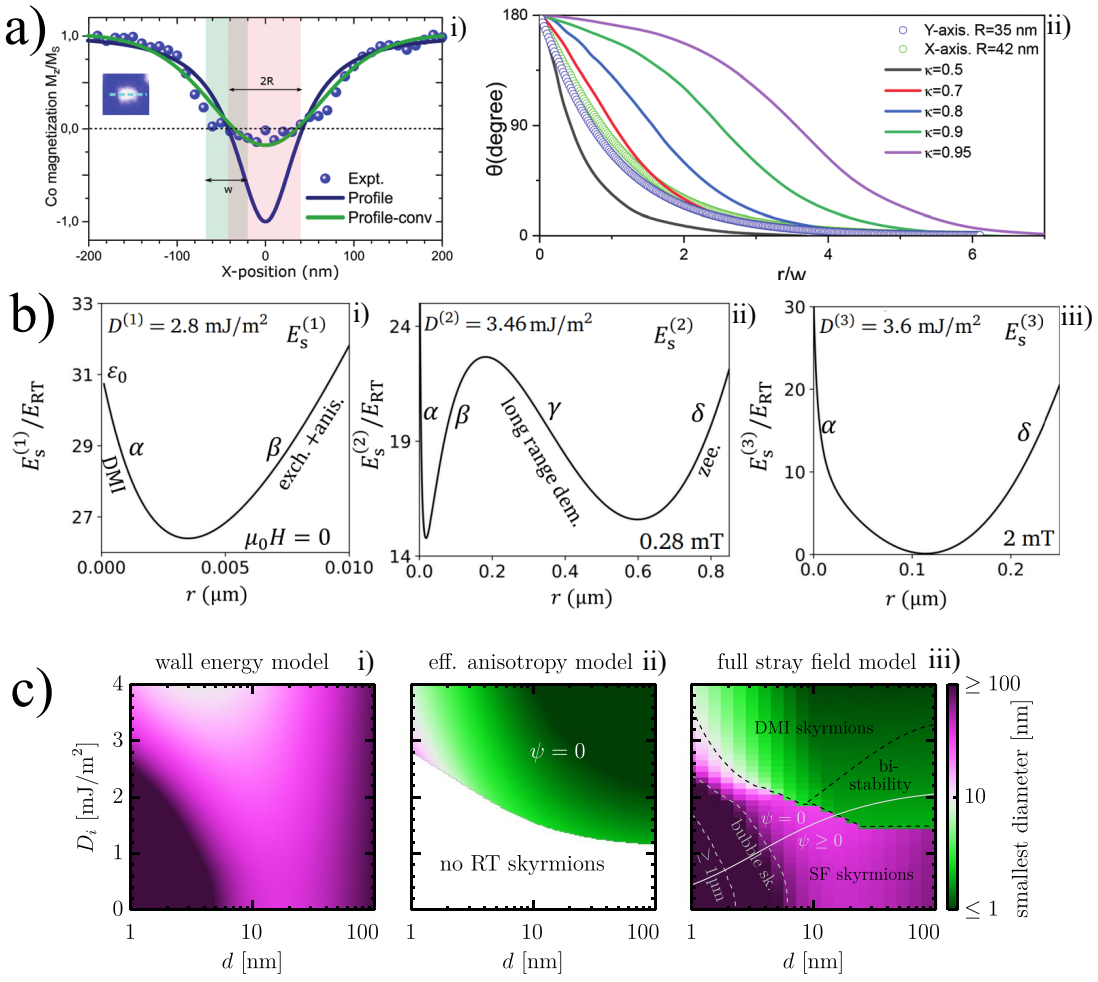

Figure 1.19: Multiple solution for Skyrmions. a) i) Skyrmion profile measured by X-ray magnetic circular dichroism and ii) deconvoluted profile super imposed with skyrmion profile for different DMI ratio from [155]. b) Skyrmion energy versus radius for the 3 different cases, i) single compact skyrmion solution, ii) Two skyrmions solutions, iii) Single bubble skyrmion solution from [148]. c) Skyrmion collapse radius for D_m versus magnetic film thickness phase diagram for three different models considering a stability criteria of $50k_BT$ from [147]. ψ defines the spin azimuthal angle (0 for Néel, $\pi/2$ for Bloch).

Different skyrmions energy models

Finally, we can describe the validity of three different models described by Büttner et al. [147] presented in Fig. 1.19 c). Model i) describes magnetic bubbles domains as known in the 1970s (without DMI) [164]. Model ii) describes skyrmion for ultra-thin film with DMI that only considers local demagnetising effects [102, 61]. And, finally, model iii) is the one developed by [147] which also considers the non-local effect of the dipolar field.
The simple DW model i) for magnetic bubbles present obvious different features (with the opposite energy derivative with R at R=0 for instance).
Models ii) and iii) give a very comparable separation line of the 10 nm skyrmion size. But ii) fails to find stable solutions (above $50k_BT$) for small DMI where both i and iii) does. The authors conclude that using model ii) whenever it yields a room temperature skyrmion is quite accurate, and that it could even be adapted otherwise with model i), where the superposition of both model seems to yield rather coherent results. Model iii) appears to be the more complete model and so points towards the importance of non-local effects of the stray-field in skyrmion stabilisation. This model clearly shows the two kind of compact and bubble skyrmions that are favoured by DMI and stray-field respectively, and also argues against the widely spread idea that compact skyrmions are necessarily smaller than bubble skyrmions and so that their profile can be a sufficient criteria for their distinction. This model seems very accurate and efficient to compute as they derived analytical functions to approximate all energy terms. Other models with similar developments and conclusions can be found in [165, 166, 143].
It should be noted that the boundary conditions of the system should not be neglected, as they have an effect on the skyrmion statics [144]. For instance, in confined environment like a nanodots of radius R_p , the borders will restrict the skyrmion size which can for example favour a unique skyrmion state when the skyrmion equilibrium radius R is greater than R_p (always the case for $\kappa \to 1$). But that was also observed experimentally on ferrimagnetic systems where isolated skyrmions would nucleate in small enough nanodots with stripes phase above a given nanodot diameter [158].

Metastability

The stability or metastability of skyrmions is apparently still subject to debate. It has been theoretically [167] shown that skyrmion lattice ground state is found in materials like MnSi near the Curie temperature of the material. This is reminiscent of the phase diagram of skyrmions in MnSi which shows skyrmions lattices and isolated skyrmions at the vicinity of the paramagnetic phase see Fig. 1.15a).
In thin films, Tomasello et al. discuss this question in [161]. The authors compare the skyrmion energy with the saturated state and find metastable skyrmion at low radius, far from SR, and stable ones closer to SR, which coincides with a fast skyrmion radius growth. It should be noted that the exploration of the phase space of the system is always restricted even in numerical experiments and so the absolute statement that a stable state is the ground state is very difficult to reach in practice. For instance, in [161], stripes or skyrmion lattice were not considered and could be the lower energy state of the real system compared to the isolated skyrmion one. There are no clear experimental evidences that can points towards ground state skyrmions over metastable skyrmion state. We will therefore consider in the later development that skyrmions are metastable, and compare their energy with the uniformly saturated state, seeking for local minima of their energy with radius. Such local minima yields the skyrmion equilibrium radius, and the energy barrier between the minima and $E(R = 0)$ will give the overall stability of such skyrmion when comparing to thermal fluctuations for instance.

1.6 Skyrmions Dynamics: Magnetic field and spin polarised currents

Spin textures can be manipulated by several way, that will always share the property of modifying the angular momentum of the texture, which correspond to transferring torque to the spin texture. This can be achieved by using magnetic field or electrical current. For both, several mechanism can be at play and are quickly described.

1.6.1 Magnetisation dynamics with field

The effect of a magnetic field on the magnetisation can be obtained from the fundamental Ehrenfest theorem that states for an observable A and an Hamiltonian $\mathcal{H}$ that: $\frac{d<A>}{dt} = \frac{1}{i\hbar} < [A, \mathcal{H}] > + < \frac{\partial A}{\partial t} >$ This gives the temporal evolution of an observable for given interactions describes in the Hamiltonian. If we then consider the spin as the observable, we can describe its temporal evolution in a magnetic field using the Zeeman Hamiltonian: $\mathcal{H} = -g\mu_0\mu_B\vec{\boldsymbol{S}}.\vec{\boldsymbol{H}}$ where $\vec{\boldsymbol{H}}$ is the applied magnetic field, S the spin, g the Landé factor. This yields: $\frac{d<\vec{\boldsymbol{S}}>}{dt} = \frac{g\mu_0\mu_B}{\hbar} < \vec{\boldsymbol{S}} > \times\vec{\boldsymbol{H}}$. Then because $< \vec{\boldsymbol{S}} >= \frac{\hbar}{g\mu_B}\vec{\boldsymbol{M}}$. One obtains the Landau-Lifshitz Equation:

$$\frac{d\vec{\boldsymbol{M}}}{dt} = -\mu_0\gamma\vec{\boldsymbol{M}} \times \vec{\boldsymbol{H}} \tag{1.26}$$

This equation describes that the evolution of a magnetic moment inside a magnetic field is a precessional motion around the field direction. This development is particularly interesting as it is fully general and can be used to derive the dynamical effect of all different interaction energies, directly from the Landau-Lifshitz Eq. 1.26 by replacing the excitation field $\vec{\boldsymbol{H}}$ by an effective field of the following form:

$$\vec{\boldsymbol{H}}_{\text{eff}} = -\frac{1}{\mu_0}\frac{\delta E}{\delta\vec{\boldsymbol{M}}} = -\frac{1}{\mu_0 M_s}\frac{\delta E}{\delta\vec{\boldsymbol{m}}} \tag{1.27}$$

where E is the volumic energy associated to an interaction by its Hamiltonian. By this mean, all previously introduced energies can be considered in this framework.

Landau-Lifshitz-Gilbert equation

Using the reduced magnetic moment $\vec{\boldsymbol{m}} = \frac{\vec{\boldsymbol{M}}}{M_s}$, with M_s the saturation magnetisation, α the Gilbert damping factor and $\gamma_0 = \mu_0\gamma$ the Landau-Lifshitz-Gilbert equation reads:

$$\frac{d\vec{\boldsymbol{m}}}{dt} = -\gamma_0\vec{\boldsymbol{m}} \times \vec{\boldsymbol{H}} + \alpha\vec{\boldsymbol{m}} \times \frac{d\vec{\boldsymbol{m}}}{dt} \tag{1.28}$$

$$= \vec{\boldsymbol{\Gamma}}_{FL} + \vec{\boldsymbol{\Gamma}}_{DL} \tag{1.29}$$

This equation first introduced by Landau and Lifshitz in 1935 [168] is the same as Eq. 1.26 with the addition of a damping term. Indeed, in real materials, dissipation processes damp the magnetic moment towards the field direction which is not described by the iso-energy precessionnal motion. To described this damped motion towards the field direction (second term), Gilbert introduced phenomenologicaly in 1955 a damping parameter, that has now been linked to a large variety of microscopic mechanism (of spins transferring angular momentum and energy to other degree of freedom, by emitting spin-waves, exciting electrons around the Fermi energy [169] or by coupling to the ionic lattices by phonons for instance [170, 171, 172]).

It it noteworthy to realise that the magnetisation needs to be non-collinear (because of the cross product) with the applied magnetic field in order to induce a torque. Also, the gyromagnetic ratio γ in Hz/T clearly appears here as the precession frequency of a magnetic moment in a magnetic field. This frequency is usually of great interest in order to obtain a characteristic time scale of the magnetisation dynamics. In Eq. 1.28, the first term can be associated to Γ_{FL} that makes the spin precesses and the second to Γ_{DL} the damping like torque that damps the spin towards the field as presented in Fig. 1.20.

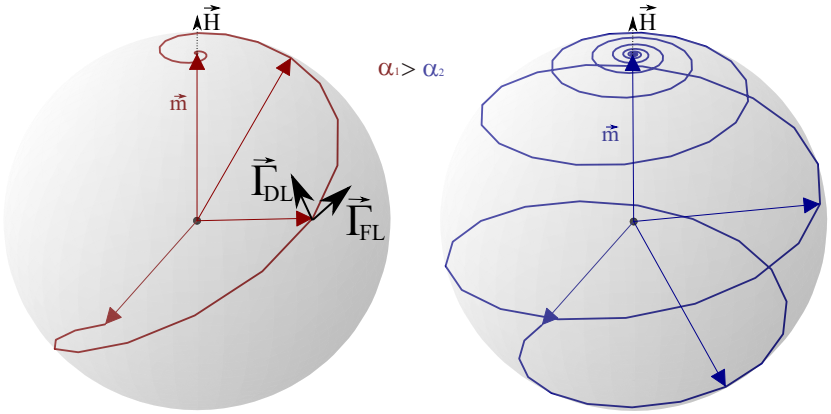

Figure 1.20: Field like and damping like torques. Schematic of the Field-Like (FL) and Damping-Like(DL) Torque on a magnetic moment for two the damping parameter.

Depending on the described geometry, this equation can lead to numerous soliton solutions with the most straightforward one being the domain wall, which is simply a kink soliton solution. But it can also gives breathers solutions [69] or humps [6]. It is noteworthy to remark that the LLG equation, without damping, can be reduced to a NLS equation for small angles of excitation [6, 68] which is a special case of the complex Ginzburg-Landau equation.

1.6.2 Skyrmion dynamics under magnetic field

It has been simulated and theorised [137, 161, 149] but also observed experimentally [26] that an external magnetic field oriented against its core magnetisation can compress the size of the skyrmion. We also measured this effect that we present in Sec. 3.4.3.

Moreover, it has been shown that an alternating magnetic field can excite internal modes of skyrmions, described as breathing modes [173, 174]. These breathing modes show that skyrmion possesses internal degree of freedom that are most often neglected (when considering a rigid texture approximation for instance) but that can indeed have effects on their dynamical properties. It was also shown that the internal modes of skyrmions can have effects on their stability, and can for instance favour their annihilation when excited, either for isolated skyrmions [175] or lattices [176]. The much larger entropy of skyrmions compared to the uniform state, due to their larger number of internal modes should also be explored for entropy driven stability [177, 175].

Magnetic field gradient

Magnetic domains aligned with a constant magnetic field are favoured energetically, which results in the displacement of the DW separating two domains. The DW is displaced over the magnetic domain opposed to the applied magnetic field, resulting in an increasing area of magnetic domain aligned with the external magnetic field.

In the case of skyrmions, a constant magnetic field can only change its size but not move its barycentre. On the other hand, a magnetic field gradient does induce a force on the skyrmion and can displace it, as it was well mastered with magnetic bubbles in the 1970s [116]. The force exerted on the skyrmion by a gradient of H_z along $\vec{e}_x$ is simply given by the following expression [19]:

$$F_H = -2\pi R^2 t M_s \frac{dH_z}{dx} \tag{1.30}$$

The in-plane components of the magnetic field do not result in a net force, but can impact the dynamics through deformation [162].

1.6.3 Dynamics by spin-transfer torque

The pioneering work of Berger on the effect of a spin-polarised current acting on magnetic textures opened a new pathway towards efficient magnetic texture displacement. First introduced in the late 1970s [178, 179] and observed experimentally a few year later in thin permalloy films [180] (that allowed to rule out the Hydrodynamic effect [181, 182, 180] arising in thick magnetic film submitted to electrical current), this mechanism relates to a transfer of angular momentum between s electrons (involved in the transport properties) to the d electrons (involved in the magnetic properties). The non-collinearity between the spin polarised current and magnetic moment induces a torque on the magnetic moment. Because the spin polarised current relaxes towards the local magnetisation direction, it can be understood by the angular momentum conservation law that the magnetic moment will themselves feel a torque proportional to the relaxed angular momentum of the incoming spin polarised current. This mechanism is referred as spin-transfer torque (STT) and have been largely explored since for magnetic textures dynamics. The first geometry explored, with a current in-plane of the magnetic film, described a relatively small force that did not bring much attention at first, until the independent description by Berger and Slonczewski [183, 184] that theorised the reversal of a magnetic layer by STT with a current applied perpendicular to the film plane. This mechanism then became the standard and for a long time, the most efficient way to displace magnetic textures. A clear review on the matter is presented in [185], which also describes the historical evolution of the mechanism broadening usage. Interestingly, this review was written slightly before the SOT mechanism was discovered. The STT is illustrated in Fig. 1.21.

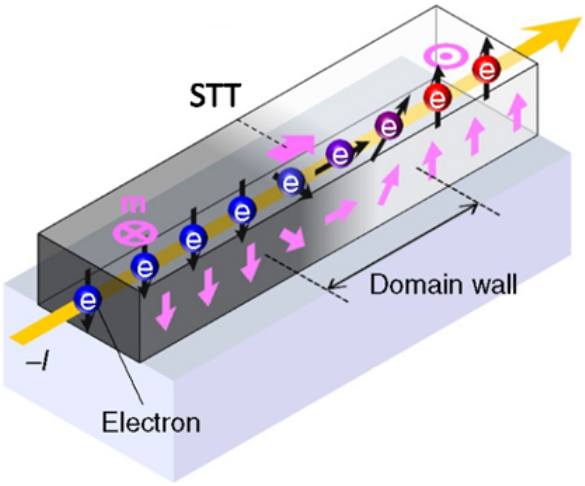

Figure 1.21: Spin Transfer Torque. Illustration of STT reproduced from [186].

The effect of STT has to be separated between two contributions, one is quite straightforward to understand with angular momentum conservation law as stated before, and is referred as adiabatic torque or Slonczewski term [187], and take the following form when applied to a magnetic moment:

$$\frac{d\vec{\boldsymbol{m}}}{dt} = -(\vec{\boldsymbol{u}}.\vec{\boldsymbol{\nabla}})\vec{\boldsymbol{m}} \tag{1.31}$$

with $u = j\frac{Pg\mu_B}{2eM_s} = j\frac{P\hbar}{2eL_s}$,P is the current spin polarisation.

If the spin polarised current relaxes completely and adiabatically follows the local magnetisation, this is the only term to consider. Otherwise, if the spin polarised current is not aligned with the local magnetisation, a second effect has to be considered. This is most often the case as the first term was not sufficient to describe experimental results.
It was shown phenomenologicaly that a supplementary Field-like term needed to be added [188]. One of its origin can be explained by hand considering that the dipolar field of the mis-aligned spins of the current acts on the local magnetisation and induces another torque, known as non-adiabatic which takes the following form [188]:

$$\frac{d\vec{\boldsymbol{m}}}{dt} = \beta\vec{\boldsymbol{m}} \times [(\vec{\boldsymbol{u}}.\vec{\boldsymbol{\nabla}})\vec{\boldsymbol{m}}] \tag{1.32}$$

Where β is a dimensionless coefficient of the torque efficiency.

It is interesting to note the correspondence between the adiabatic torque and the Damping-like (DL) term and the non-adiabatic torque and the Field-like (FL) term from the LLG Eq. 1.28. Indeed, only two type of symmetries of the torque are allowed, and so all torques acting on a magnetic texture have either from FL or DL symmetries. Also, just like charge current move spin textures, it was shown that moving spin textures generate an electric field which has an effect called spin motive force that is indeed observed [189].

1.6.4 Skyrmion STT experimental dynamics

Soon after the discovery of skyrmions in bulk materials, current induced motion of the skyrmions lattices by spin-transfer torque were performed. The first one on MnSi in 2010 [130] monitored in reciprocal space the rotation of the diffraction pattern from neutron-scattering and revealed an effect of the current at extremely low current densities (some $10^6 \mathrm{A/m^2}$) compared to what was known in the more conventional dynamics of magnetic domain walls (usually around the $10^{12} \mathrm{A/m^2}$). This was confirmed by real space observation in 2012 by [131] on FeGe samples by Lorrentz TEM and also monitored by the changes on electrical resistivity in MnSi by [190] and also described an interesting emergent phenomena related to skyrmions, which is the induction of an electric field (by Faraday's Law) due to the displacement of skyrmions as magnetic charges, corresponding to the reciprocal effect that moving electric charges induces a magnetic field.
An interesting review on these dynamical measurement can be found in [191]. Because of the almost conjoint discovery of skyrmions in magnetic thin films with adjacent heavy metal layers like Pt, and the very efficient torque that such heavy metal can generated on magnetic texture as presented below, there are no experimental results focusing on STT dynamics in thin films to my knowledge.

1.6.5 Spin-orbit torque and spin Hall effect

In 2009, magnetic textures moving against the flow of electron [134] pointed to a new spin torque mechanism as this is not expected in STT dynamics. This new mechanism is now known as spin-orbit-torque (SOT)[23] with several microscopic mechanisms at its origin [24]. The most important one considered for our specific material is found in the generation of a spin polarised current transverse to the charge current by Spin Hall effect (SHE) in an adjacent layer to the magnetic layer with large SOC [192]. The spin accumulation at the interface with the large SOC layer then diffuses into the magnetic layer and induce a torque through the relaxation of the spins towards the local magnetisation. This mechanism is usually observed with adjacent heavy metal layers that can present sizeable SHE like Pt, W or Ta for instance. Other mechanisms of SOT can also be present due to interface oxidation or spin-dependent scattering of the spin polarised current flowing in the ferromagnet [24]. Finally, another effect can be present conjointly to the SHE SOT which appears with the accumulation of spins at the interface. The accumulated electrons induce an electric field that has mostly a FL effect on the moving electrons in the magnetic layer. The effect is can also present DL symmetry with more complete description [24]. Several name can be found in the literature to describe this effect, Rashba-Edelstein [193] or inverse spin galvanic effect [194]. Harmonic Hall voltage measurements (presented later) can not disentangle the SHE and Rashba-Edelstein effects that both exert FL and DL torques on magnetic textures. The large review on SOT found in [24] present exhaustively the details of these complex mechanisms. We can also point to these other reviews that give a clear description of the Rashba effect [195], SOC effects in magnetic materials [196] or more broadly interfacial induced effects [197]. The SHE SOT is illustrated in Fig. 1.22.

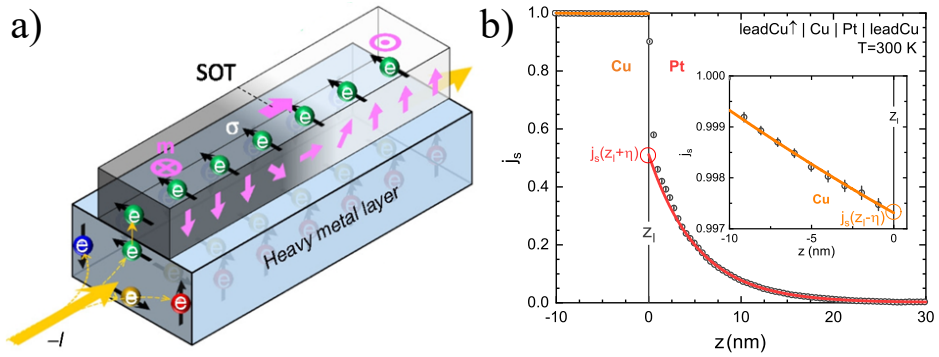

Figure 1.22: Spin Orbit Torque. a) Illustration of SOT reproduced from [186]. b) Computed interfacial effect of spin memory loss for Cu/Py interface from [198] where fully spin polarised current from Cu flows along $\vec{e}_z$.

Because heavy metals develop large SOC, they are well suited to favour SHE, but also strong interfacial interaction like DMI. This makes them very suitable to stabilise skyrmions, and so this type of mechanism rapidly imposed as the standard for skyrmion dynamics in thin films. This is typically observed in Pt for instance, where a current injected in the layer will be converted by SHE into transverse spin-polarised current. The spin polarised current is very sensitive to the interface. Due to spin-memory loss, a large amount of the polarised current depolarises at the interface as computed for Cu/Pt in Fig. 1.22b). This figure shows a 100% spin polarised current going from Cu to Pt and the discontinuity of the polarisation at the interface. It can then be expected that spin polarised current generated by Pt suffers the same effect when diffusing into an adjacent layer. Other studies discuss this effect for Co/Pt interface as in [199], and we only present it to stress the fact the SHE efficiency can vary greatly depending on the transmission of interface.

The spin polarised current generated by Pt takes the following form [200]:

$$\boldsymbol{J}_{SHE} = \frac{\hbar}{2e}\theta_{SHE}(\boldsymbol{J}_c \times \boldsymbol{\sigma}) \tag{1.33}$$

with θ_{SHE} the spin Hall angle that quantify the SHE conversion efficiency of the current charge J_c injected in the large SOC layer, into spin polarised current J_{SHE} of polarisation σ. This torque offers the possibility to decouple the materials used for spin polarised current generation from the one hosting the magnetic properties, which allows for better optimisation of each. The spin polarised current generated then accumulates at the interface and its diffusion exerts torques on the magnetic layer. As well as in the case of STT, two torques can be found, one with DL effects, and the second with FL effects. The two torques take the following form [24]:

$$\frac{d\vec{\boldsymbol{m}}}{dt} = \tau_{FL}(\vec{\boldsymbol{m}} \times \vec{\boldsymbol{\sigma}}) + \tau_{DL}\vec{\boldsymbol{m}} \times (\vec{\boldsymbol{m}} \times \vec{\boldsymbol{\sigma}}) = \boldsymbol{\Gamma_{FL}} + \boldsymbol{\Gamma_{DL}} \tag{1.34}$$

with t the magnetic layer thickness τ_{DL} and τ_{FL} coefficients for the efficiency of the DL and FL torques. In a phenomenological description, the effect of the torques can be ascribed to the effective field $H_{DL} = \tau_{DL}$ and $H_{FL} = \tau_{FL}$ with the comparison to the LGG Eq. 1.28. For H_{DL} arising from SHE SOT, the ratio of the effective spin current absorbed by the ferromagnet relative to the charge current injected in the nonmagnetic metal layer can thus be considered as an effective spin Hall angle [24]:

$$\theta_{SHE} = \mu_0 H_{DL} \frac{2e}{\hbar} \frac{M_s t}{J} \tag{1.35}$$

Considering that the H_{FL} is induced by Rashba like torque, the efficiency of the effect is given by [201]:

$$\alpha_R P = -\mu_0 H_{FL} \frac{2e}{\hbar} \frac{M_s}{J m_e} \tag{1.36}$$

We indeed expect that SHE in our sample of Pt/GdCo/Ta mostly exert DL torque, and that FL torque should be attributed to Rashba effects [201].

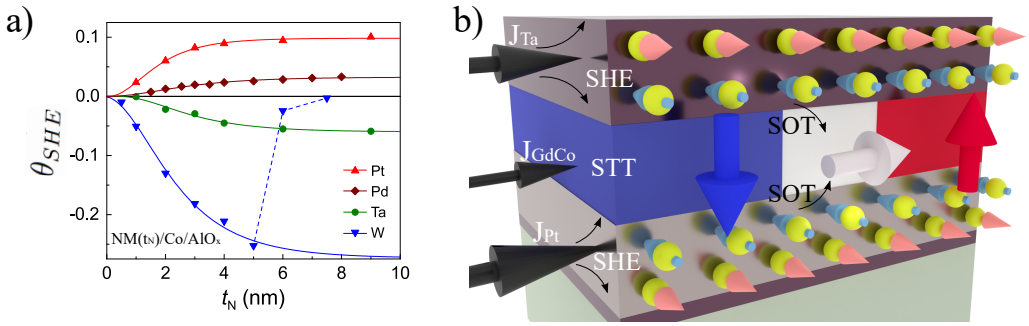

Figure 1.23: SHE in Pt and Ta. a) θ_{SHE} measured in NM(t_N)/Co/AlO$_x$ samples with various non-magnetic metals from [24]. b) Illustration of the resulting SHE and SOT on one of our typical sample of Si/Ta/Pt/GdCo/Ta. SHE is inverted between Pt and Ta layers inducing SOT on the GdCO layer, which also present some STT.

As it is seen in Fig. 1.23 a), the spin hall angle of Pt and Ta is opposite. This is quite interesting as it means that the SHE SOT effects of each layer will add up as it is sketched in Fig. 1.23 b). We can also notice that W could replace Ta as it shows a stronger effect, and also an opposite θ_{SHE} compared to Pt (with also opposite DMI constant Fig. 1.3). Fig. 1.23 a) shows saturating efficiency of SHE for both Pt and Ta with layer thickness around 5 nm.

Finally, very recent studies suggest a two-fold effect of the SHE. One originates from the spin polarised current, as described above, but a second effect due to orbital current should also be considered. As described in [202], the orbital current cannot directly exert a torque on a ferromagnet, but necessitate a conversion process from orbital current to spin current before having a net effect. Such conversion is possible by SOC, and expected to be efficiently obtained using Pt or Gd for instance. It is shown that such orbital current can be order of magnitude larger than simple spin polarised ones, which can results in strong torque if efficiently converted. A particularly complete article computing the contribution of both types of current for almost all material of interest can be found in [203]. In this work, it for instance showed that the observed SHE of Ta or W would be mostly due to orbital current later converted into spin polarised current, whereas Pt shows strong contribution from both. Such mechanism could be used to enhance the efficiency of SOT, for instance by simply adding a Cu layer on top of a strong SOC material adjacent to a magnetic layer. This emphasise once more the importance of material choice their order for the optimisation of dynamical properties of magnetic textures.

1.6.6 Thiele equation for skyrmion dynamics

The simplest theoretical model to describe this effect is found using the Thiele equation that uses the solitonic nature of skyrmions to simplify its description. Indeed, the Thiele formalism focuses on a rigid approximation, considering that the skyrmion profile remains unchanged along its displacement, where the geometrical aspects of the texture can be computed simply once. This offers a much simpler description than if one used the LLG equation directly for instance. The Thiele formalism [204, 205] is derived by integrating the LLG equation Eq. 1.28 in the volume and is an exact description of the texture (also used for DWs, vortices or others). Under the hypothesis of a rigid (or stationary) profile $\vec{\boldsymbol{m}}(\vec{\boldsymbol{r}}, t)$ equals $\vec{\boldsymbol{m}}_0(\vec{\boldsymbol{r}} - \vec{\boldsymbol{v}}t)$, where $\vec{\boldsymbol{m}}_0(\vec{\boldsymbol{r}})$ is the rigid texture and $\vec{\boldsymbol{v}}$ its velocity.

For a circular skyrmion, the Thiele equation reads [206, 207, 147]:

$$\vec{\boldsymbol{G}} \times \vec{\boldsymbol{v}} - \alpha D \vec{\boldsymbol{v}} + \vec{\boldsymbol{F}} = 0 \tag{1.37}$$

where $\vec{\boldsymbol{G}} = L_S t n \vec{\boldsymbol{e}}_z$, $\alpha D = L_\alpha t d$ ($\alpha = L_\alpha / L_S$ is Gilbert's damping constant) and $\vec{\boldsymbol{F}}$ is the total force. The three terms in eq. 1.37 respectively arise from the precessional, damping and other torques in the LLG equations. Note that in the general case D is a tensor $\mathcal{D}$ but because of the symmetry of skyrmion it is diagonal such that $\mathcal{D}_{xx} = \mathcal{D}_{yy} = D$.

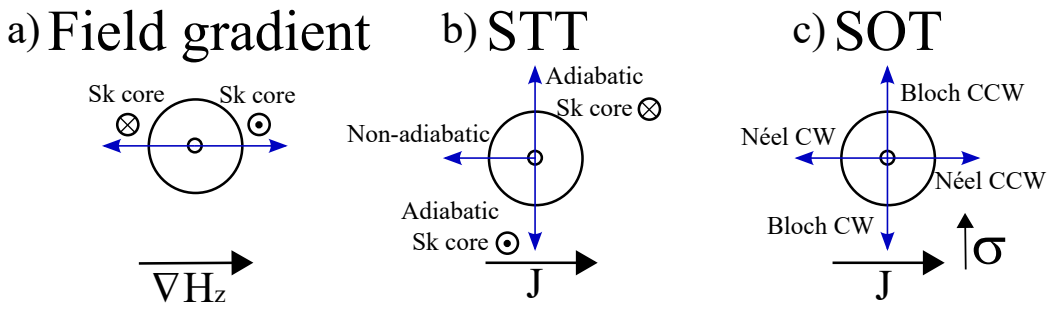

Figure 1.24: Force directions on skyrmion from field gradients, STT and SOT. Forces (blue arrows) acting on a skyrmion submitted to (a) a magnetic field gradient, (b) adiabatic and non-adiabatic STT, and (c) damping-like SOT . Inspired from [24].

As one can see in Fig. 1.24, the forces acting on skyrmions are very different depending on the type of excitation. When submitted to a magnetic field gradient (a), the force reverses with skyrmion core magnetisation only. When submitted to STT (b), the non-adiabatic (FL) force is constant in direction but the adiabatic (DL) one depends on the skyrmion core polarity (P, Eq. 1.20). Finally, when the skyrmion is submitted to DL SOT (c), the force does not change with skyrmion core polarity but reverses with CW or CCW chirality. It is also dependant on the Néel or Bloch nature of the skyrmion with 90° difference between the two types.
We can quickly remark that in our films of Pt/GdCo/Ta, the DMI is expected to be negative and strong enough to favour Néel skyrmions, with CCW chirality. Skyrmions displaced by SOT in our system should therefore move along the current direction. Finally, the FL SOT does not add any force on the skyrmion and acts like a constant in-plane field [24]. The dynamics experienced by skyrmions is actually more complex than the simple description of forces directions. Indeed, due to its topological nature, a force arises when skyrmions are displaced (the first term in Eq. 1.37). This force is called the gyrotropic force (or Skyrmion Hall effect) and adds a transverse contribution to the skyrmion displacement.

For a skyrmion driven by SOT, $\vec{\boldsymbol{F}} = -\frac{\hbar}{2e}\theta_{SHE}\vec{\boldsymbol{J}}f$. The parameters n, d and f characterise the texture geometry $\vec{\boldsymbol{m}}_0(\vec{\boldsymbol{r}})$ and are given by

$$n = \iint \left(\frac{\partial \vec{\boldsymbol{m}}_0}{\partial x} \times \frac{\partial \vec{\boldsymbol{m}}_0}{\partial y}\right) \cdot \vec{\boldsymbol{m}}_0 d^2r \tag{1.38a}$$

$$d = \iint \left(\frac{\partial \vec{\boldsymbol{m}}_0}{\partial x}\right)^2 d^2r \tag{1.38b}$$

$$f = \iint \left(m_{0,x}\frac{\partial m_{0,z}}{\partial x} - m_{0,z}\frac{\partial m_{0,x}}{\partial x}\right) d^2r \tag{1.38c}$$

They correspond, respectively, to the texture topology ($n = \pm 4\pi$, depending on the skyrmion core polarity), to the magnetisation rotation length-scale, and to the texture chirality. They are shown as a function of skyrmion radius in Fig. 4.6. The solution of Eq. 1.37 is

$$v = v_0/\sqrt{1+\rho^2} \tag{1.39a}$$

$$v_y/v_x = \rho \tag{1.39b}$$

with

$$v_0 = \frac{F}{\alpha D} = -\frac{\hbar j \theta_{SHE}}{2e\alpha L_s\, t}\frac{f}{d} \tag{1.40a}$$

$$\rho = \frac{G}{\alpha D} = \frac{1}{\alpha}\frac{n}{d} \tag{1.40b}$$

where v_0 and ρ correspond, respectively, to the velocity in the case without deflection (i.e., the velocity when $v_y = 0$), and to the deflection of the skyrmion.

In the case of STT with torques expressed in Eq. 1.31 and Eq. 1.32 [208]:

$$v_x = u\frac{\frac{\beta}{\alpha}+\rho^2}{1+\rho^2} \quad \text{and} \quad v_y = u\rho\frac{\frac{\beta}{\alpha}-1}{1+\rho^2} \tag{1.41}$$

1.7 Driving by STT and SOT

We present in Fig. 1.25 the contributions for v_x, v_y and v from the STT and SOT considering reasonable values for all parameters using equations Eq. 1.39b and Eq. 1.41.

The comparison between SOT and the effect of field gradients is presented in the chapter on skyrmion dynamics.

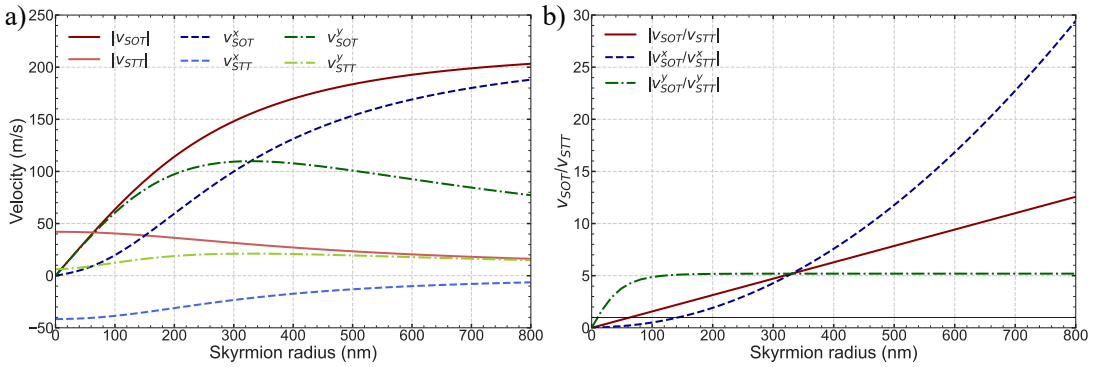

Figure 1.25: SOT vs STT contribution, a) $|v|$, v_x and v_y computed for SOT and STT using Eq. 1.39b and Eq. 1.41 with parameter described below for various skyrmion radius. b) Ratio between SOT and STT induced velocities obtained from a).

In order to compute velocities presented in Fig. 1.25 we used typical parameters comparable with the experiments we realised (presented in Tab. 2.2 for the RE-dominated sample). For STT, we used parameters from [209] which are $\beta = 0.01$ and $P = 0.3$.

We can see in Fig. 1.25a) that the typical effect of the SOT is much larger than STT for large skyrmions but, at small skyrmion size, the STT present larger effect due to its non-vanishing contribution. Interestingly, the ratio between the two effects, presented in Fig. 1.25b) shows a saturating constant ratio for v_y with a linear ratio increase with skyrmion radius (for these parameters, $\frac{|v_{SOT}|}{|v_{STT}|} = 1$ at around $R = 60$ nm). The contribution of the SOT then linearly increases (about 4 times the one of STT for $R = 250$ nm).

1.8 Experimental skyrmion SOT dynamics

This area of research being still rather new, the literature on the subject is quite limited. We attempt here to make a complete review to best of our knowledge. First, we present skyrmion velocity curves versus current density in Fig. 1.26 and then skyrmion deflection curves versus current density or skyrmion velocity in Fig. 1.27. We only present here articles where velocity curves were reported. In chapter 4 section 4.9, articles where the mobility can be extracted are also included.

We propose here a first description of the reported results on SOT driven skyrmions dynamics in magnetic thin films. All studies presented in Fig. 1.26 use current pulses to displace skyrmions with pulse width ranging from μs to few ns. The first striking difference between these studies is presented in the figure where we separated low maximum velocities below 10 m/s from high velocities that range from 50 to 120 m/s. The extremely low speeds from Fig. 1.26a) are rather surprising and might be due to the peculiar geometry of the experiment which has been designed to blow magnetic skyrmions through a constriction and not to move them efficiently. This might be the reason for the very low current density they explored (some 0.45GA/m^2) where typical experiments are obtained from some 10s to 100s up to 1000s GA/m^2 (only reached in Fig. 1.26 c)).

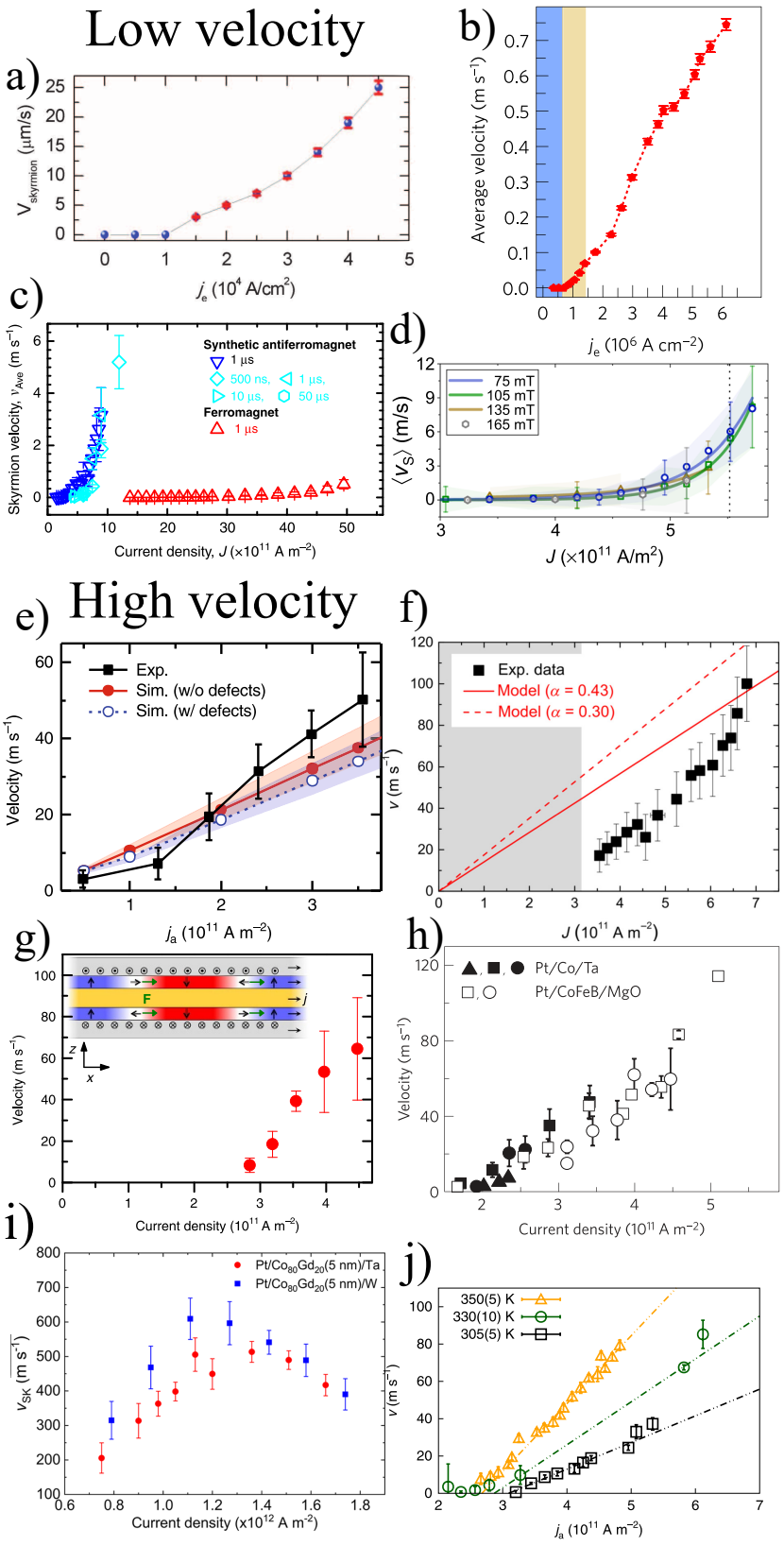

Figure 1.26: Skyrmion dynamics experimental results. Low velocity: a) [127] in CoFeB, b) [48] in CoFeB, c) [138] in CoFeB, d) [210] in Co. High velocity: e) [49] in GdFeCo, f) [211] in Co, g) [125] in Ni/Co, h) [212] in Co and CoFeB, i) [213] in GdCo, j) [162] in CoFeB.

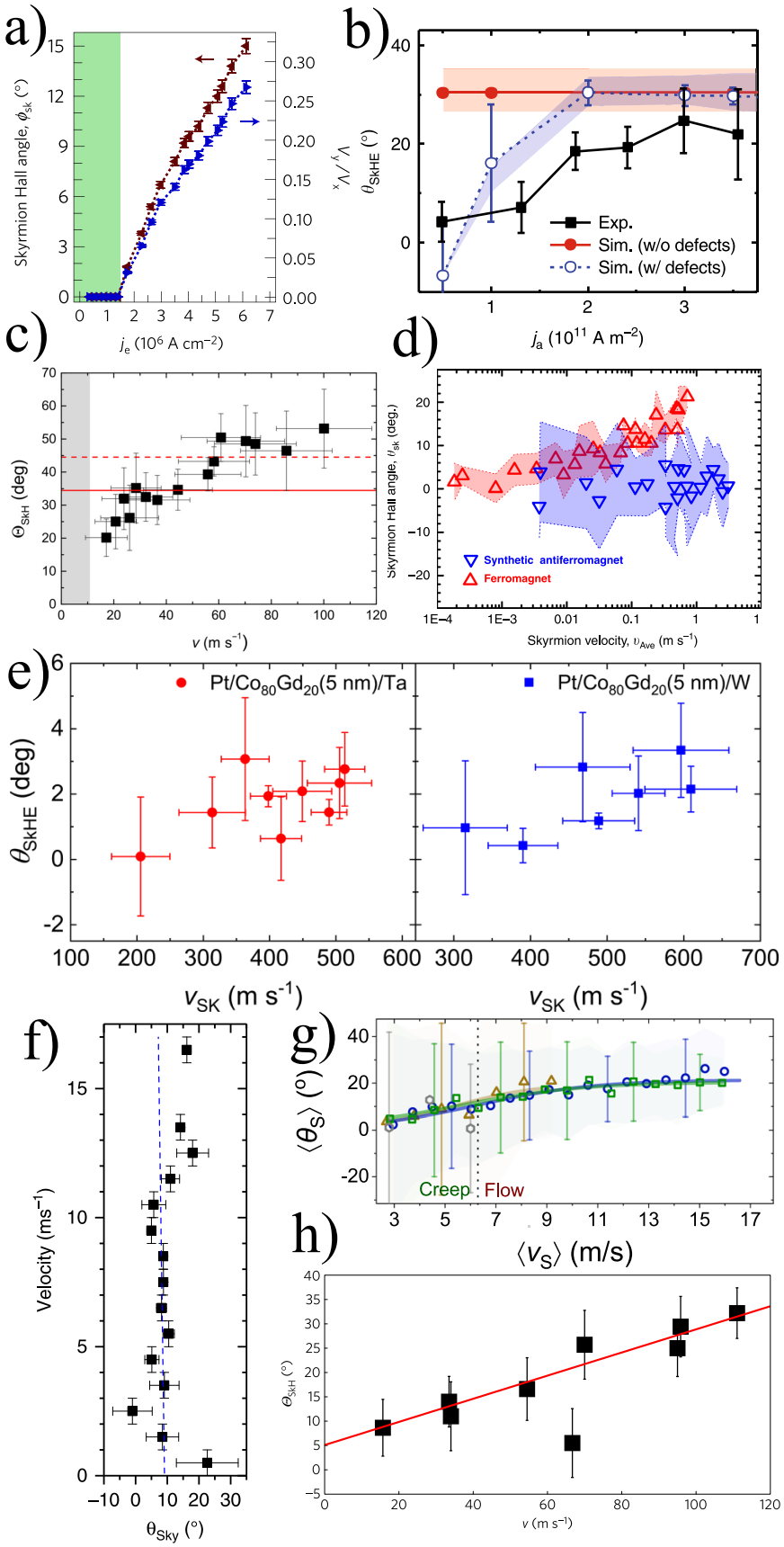

Figure 1.27: Skyrmion deflection experimental results. a) [48] in CoFeB, b) [49] in GdFeCo, c) [211] in Co, d) [138] in CoFeB, e) [213] in GdCo, f) [214] in CoB, g) citeTan2021 in Co, h) [215] in CoFeB.

As discussed in [216], the typically expected skyrmion regimes are, at non-zero temperature, a creep [2] regime with extremely low velocity. This regime has never been evidenced for skyrmion dynamics. Afterwards, a depinning regime is expected with increasing speed (that could be the case in a-b-c-d) with small velocities again. This is then followed by a linear, flow regime, at higher current density that seems to be attained at largest current densities for all other velocity curves presented (e-f-g-h-j). This transition from pinned to linear regime can be understood with the effect of a pinning potential [216] that prevents the texture from being displaced below a threshold driving force. We can note that, in this theory, the flow regime is expected to present a linear variation with the driving force that extrapolates to zero. It is then quite surprising to see most of the velocity curves from Fig. 1.26 presenting a shifted linear regime. This might simply be due to the fact that in most figures presented the skyrmions are barely entering the flow regime at highest current density, which is for instance quite probable in Fig. 1.26 f). It seems that only Fig. 1.26 e) presents a clear linear regime starting around $250\mathrm{GA/m^2}$ and maybe g) around $400\mathrm{GA/m^2}$ and h-j) around $450\mathrm{GA/m^2}$ or i) at $1100\mathrm{GA/m^2}$. We can regret velocity plots that do not start at $j = 0$ as it obscures the potential linearity of the attained regime. We can only observe that many velocity curves present large velocity, suggesting a flow regime, but shifted in current density (g-h-i-j). There might be some physical mechanism explaining why a flow regime could be shifted, and so could not extrapolate to zero, but no explanation is given in these references nor any clues on the matter can be found, to my knowledge, in the literature.

It can be seen in the expression given in Eq. 1.39b for skyrmion driven by SOT that the velocity is indeed expected to increase linearly with the driving force (with j). It can also be seen that the deflection angle is expected to be independent on the driving force. Therefore, any deflection angle curve with skyrmion velocity, or current density that does not show a saturation would be evidence for creep or depinning regime instead of flow. Such non-saturating deflection angle are observed in Fig. 1.27a), b) for the ferromagnet case or g) for instance. Much care should be taken with this last consideration. Indeed, in the case of compensated materials (SAF or ferrimagnets) the deflection can be reduced down to zero as seen in Fig. 1.27 d) for instance, which then shows a rather constant deflection angle with skyrmion velocity but that is not equivalent as the saturating skyrmion deflection discussed above. Quite similarly, the effect of confinement by edges on the skyrmion dynamics is also to compensate the deflection. For instance, skyrmions that are stable enough to be displaced along track edges will present a constant zero deflection angle with driving force, again not comparable to the deflection saturation discussed previously.

Finally, it has been discussed theoretically and numerically that the deformation of skyrmions, either due to the strength of disorder [218], anisotropic interactions [219] or driving force induced distortion [162] can drastically modify their dynamical properties. The effect of the pinning strength on the crossover between different regimes seems to be rather determinant as discussed in [218]. These effects are discussed in more details in the conclusion of chapter 4 in section 4.9.

[2] The denomination of creep is ascribed to a special type of dynamics, where elastic properties of magnetic textures implies universal law of motion shared by many other systems than purely magnetic ones (see [217] for a general review).

Chapter 2

GdCo ferrimagnetic thin films

In this chapter we first discuss the fabrication process of rare earth/ transition metal (RETM) ferrimagnetic thin films with controlled thicknesses and composition in section 2.1. These materials present numerous interesting properties to explore. For instance due to their antiferromagnetic coupling, these materials present very low magnetisation and angular momentum density as compared to conventional ferromagnets (Co, Fe...) which has major impact on the statics and dynamical properties of these films.

We will focus on the properties of ferrimagnets composed of Gd and Co. We describe the interactions between the two sub-lattices in section 2.1.3 with the lattice dependant sensitivity of certain effects. We will complete our description of ferrimagnets with an introduction to mean field theory in section 2.3.2 from which we can compute effective parameters to describe both sub-lattices as an effective single lattice. The nano-fabrication process of plain films into functionalized magnetic track devices will then be addressed in section 2.4.

Finally, we will focus on the experimental determination of magnetic parameters and present most of the relevant techniques used throughout this work to characterise our thin films in section 2.5. We mostly present results obtained by SQUID magnetometry, electrical transport and Brillouin light scattering spectroscopy. The chapter ends with a summary, in section 2.6,of the magnetic parameters measured for two samples that will be studied in chapter 3 and chapter4.

2.1 Rare-Earth /Transition Metal ferrimagnets thin film fabrication

We fabricate samples in a molecular beam epitaxy (MBE) ultra-high-vacuum (UHV) chamber. The chamber is kept at very low pressure around 10^{-10} mbar with a turbo-molecular and ionic pumps. The deposition is obtained by the sublimation or evaporation of target materials by electron guns. The chamber possesses two electron guns that allows for controlled co-deposition of materials. Each gun can be independently controlled to sublimate one of its seven available materials, that we specifically select to construct complex stacking of layers of different materials without breaking the vacuum. Figure 2.1 shows the MBE which is composed of a main chamber and a load lock in which several sample holders are installed. They are individually transferred into the main chamber on the manipulation arm. The sample holder is rotated during deposition to increase homogeneity and can be heated or cooled, but all sample presented later will be deposited at room temperature.

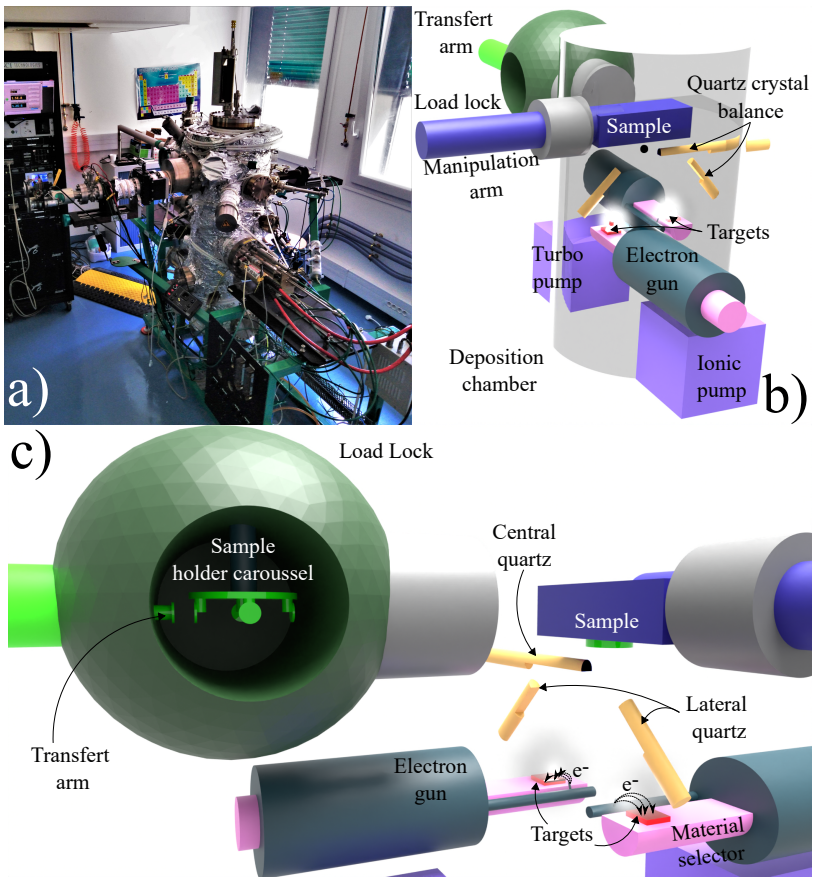

Figure 2.1: Molecular beam epitaxy UHV Deposition chamber. a) Photography and sketch b-c) of the MBE with most important parts being the two targets with their associated electron gun and the multiple quartz balances.

2.1.1 Composition and thickness control

The deposition rate is monitored in real time by three calibrated quartz balances: one ('central') near the sample and two others ('lateral') near each evaporation gun. During deposition, the quartz mass increases slightly, which reduces its resonance frequency. The known density of deposited materials allows to compute the deposition rate from the quartz resonance frequency shift over time. The rate is integrated to obtain the total thickness deposited. Tooling factors, which are the ratio between the deposition rate on the sample and on the quartz balance, are taken into account. These tooling factors can be verified by measuring the thickness after deposition by several ways, using AFM or profilometry for fast verification, or by X-ray reflectometry, or TEM cut, for precise determination. Regular calibration is needed to ensure reproducibility. This MBE setup has been developed to obtain a controlled composition of co-deposited materials. This is quite a difficult matter as the typical aimed deposition rate of 0.1 to 0.5 Å/s is very sensitive to the e-beam location on the target. The deposition rate of each electron gun is monitored by its associated lateral quartz balance as seen in figure 2.1. Due to the chamber geometry, each lateral quartz sees a different deposition rate compared to the central quartz. The total thickness is measured by the central quartz, but the deposition rate by the lateral ones, which implies another calibration between lateral and central quartzes. A real time PID regulation of individual e-guns current ensures a constant ratio of deposition rate between the guns, determined to obtain a given composition. The composition can be checked by Rutherford back scattering spectroscopy (RBS), a technique sensitive to the atomic number, to control nominal versus real composition which is found within 0.5% [220, 221].

The reproducibility of the composition can also be assessed by measuring the T_{mc} of the film, which varies by $\approx$ 30 K per % of Gd (Fig. 2.10). Samples with the same nominal composition typically show T_{mc} within 30 K of each other, which indicates an error around 1% on the composition. This shows how precise the composition has to be in order to obtain reproducible recipes. The compositions measured by RBS and by T_{mc} differ as the two techniques are sensitive to different properties of the sample. The RBS integrates all Gd atoms (across the depth), whereas the T_{mc} depends only on the Gd that is in the magnetically-polarised material (and thus is sensitive to the oxidation of Gd). This is seen, for instance, in GdCo films below 5 nm of thickness, where the Gd sub-lattice exhibits very low magnetisation [222], with most of the Gd passivated by migration to interfaces. The larger dispersion observed by monitoring T_{mc} points to the larger variability of the oxidation process as compared to the deposition composition. This underlines the importance of the buffer and capping layers, as they affect the proportion of active Gd, an effect that is describe later in section 2.1.3. We present in figure 2.2 the typical architecture of our thin film stacks. They are composed of a primary seed layer (e.g. Ta, Ti), which favours the growth of the upper layers and the adhesion on the substrate, and then a first buffer layer (e.g. Pt). Next, the magnetic layer is deposited (GdCo) and covered by a second buffer (e.g. Ta) and a final capping layer to passivate the surface (e.g. Al, Pt).

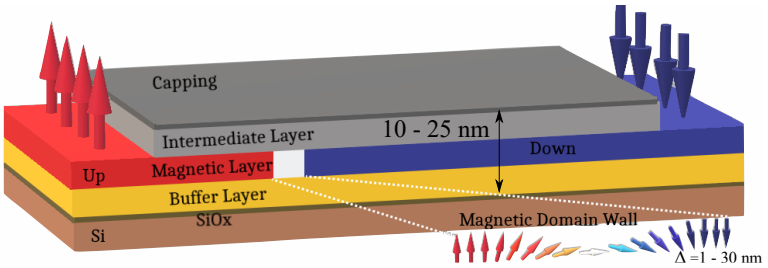

Figure 2.2: Typical thin film stack. Thin film layers thicknesses ranging from 1 to 10 nm.

2.1.2 Seed and buffer layers

The order of the layers in the stack is critical as it can modify the growth conditions of the upper layers. For example, when Pt is deposited directly on SiO_x (100) it does not crystallise properly (with multiple crystallites), due to the large lattice constant mismatch, which does not results in the interfacial properties we are looking for. On the contrary, when grown on a 1 to 3 nm thick Ta buffer layer, the Pt film is crystalline and presents the interfacial qualities we are looking for as described in section 2.5.2. Therefore, we obtain very different properties for a Ta/GdCo/Pt sample compared to a Ta/Pt/GdCo/Ta sample.

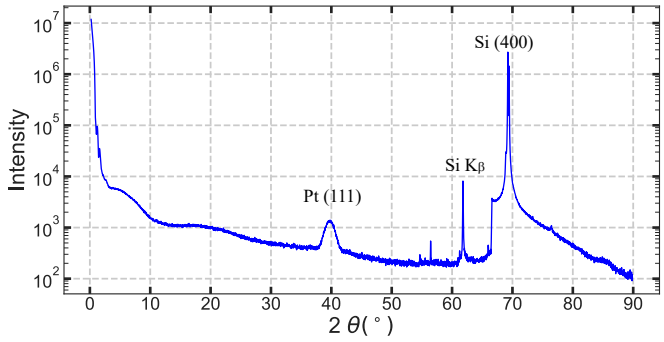

Figure 2.3: X-ray diffraction in Si/SiO$_x$/Ta/Pt/GdCo/Ta. X-ray diffraction $\theta - 2\theta$ on Si/SiO$_x$/Ta/Pt/GdCo/Ta sample with clear peak for Pt (111) and Si (400).

Figure 2.3 shows the $\theta - 2\theta$ X-ray diffraction of a Ta(1)/Pt(5)/GdCo(10)/Ta(5) (nm) sample, with the characteristic peaks of crystalline Pt (111) and Si (400) (lower order are forbidden by extinction rules)[223]. On the other hand, no diffraction peak is observed for the Ta [224] and GdCo [225] layers that should otherwise appear around 30°. The absence of these peaks is not enough to assure the amorphous nature of these layers, although transmission electron microscopy (TEM) cross-sectional imaging (on other stacks) does show the clear amorphous nature of the ferrimagnetic layer (figure 2.4). Because the ferrimagnetic layer is thin (3-8nm), its properties are greatly affected by its two interfaces. Ta is used as a buffer layer to grow crystalline Pt. The crystalline (111) Pt induces a large interfacial out of plane anisotropy in Co [95], but the origin of this anisotropy is not straightforward, as both the oxygen content and Pt-Co intermixing seem to play an important role, with, for example, an increase of anisotropy with annealing for Pt/Co/AlO_x due to Co-O-Al bonds [96], but a decrease of anisotropy due to thermally-activated intermixing [226, 227]. Also, due to the large magnetisation of Co and interfacial nature of the Pt/Co anisotropy, only thin-enough Co films display perpendicular magnetic anisotropy (PMA), with a transition to in-plane magnetic anisotropy (IPA) at around 1.4 nm of Co, where demagnetising effects overcome the interfacially induced PMA [227].

The interface with Pt is also used for the effects related to spin-orbit coupling (SOC) that this heavy material can develop, such as interfacial DMI [15, 89, 90] necessary for skyrmion stabilisation. The Co/Ta interface also contributes to DMI, as it has the opposite sign as Co/Pt [228, 91] (see 1.2.2).
Finally, both Pt and Ta are used to obtain spin currents through the spin Hall effect (SHE) (see 1.6.5), which are used to drive magnetic textures by Spin Orbit Torque (SOT) [186]. Again, Ta and Pt show an additive effect due to the opposite signs of the SHE in these materials [229]. These buffer layers are then very interesting to functionalise the stack, with a magnetic layer optimised for its magnetic properties and adjacent layers optimised for their transport, thermal or passivating properties. The interest of Ta and Pt is further discussed in the introductory section 1.2.

2.1.3 GdCo magnetic layer

The exact structure of the amorphous ferrimagnetic layer is far from trivial as Gd is very sensitive to oxidation, and present internal chemical potential gradients that favour the migration of Gd towards the interfaces. This makes the assumption of a uniform GdCo layer rather incorrect, as Gd migration modifies the interfaces with surrounding layers and changes the effective composition through Gd oxidation at the interfaces.

Another enigmatic aspect of GdCo thin films is the origin of their intrinsic anisotropy [230, 231, 232, 233, 234, 235, 236]. The intrinsic anisotropy contribution of the magnetic layer was suggested to come from various mechanisms: magnetostriction, anisotropic pair correlation, dipolar effects, and bond-orientation anisotropy, as is well summarised in [237]. Latest research on the matter concluded on a dominant effect of the pair-pair correlation [237], but this still remains to be fully demonstrated.
Let us finally briefly describe the difference between crystalline an amorphous GdCo material. There is more literature on crystalline GdCo compounds than on amorphous ones, which cannot be compared directly [238, 239]. Amorphous structures tend to crystallise over time which, being a thermally-activated process, varies according to the temperature cycles of a sample. It was observed that 100 nm thick GdCo films [240] present PMA which reduces with annealing from 50 to 200 °C, from which the lifetime of GdCo films was extrapolated to be 100 years at 373 K but only 22 days at 473 K[241]. This shows how sensitive to temperature these films are.

The same effect was also observed in [237] with a shift from PMA to in-plane anisotropy once reaching 573 K. There, X-ray diffraction on annealed samples ruled out the crystallisation of the GdCo layer, and the PMA drop is understood as resulting from an inter-mixing of layers which reduces anisotropic pair-pair correlations responsible for the PMA [237, 240].

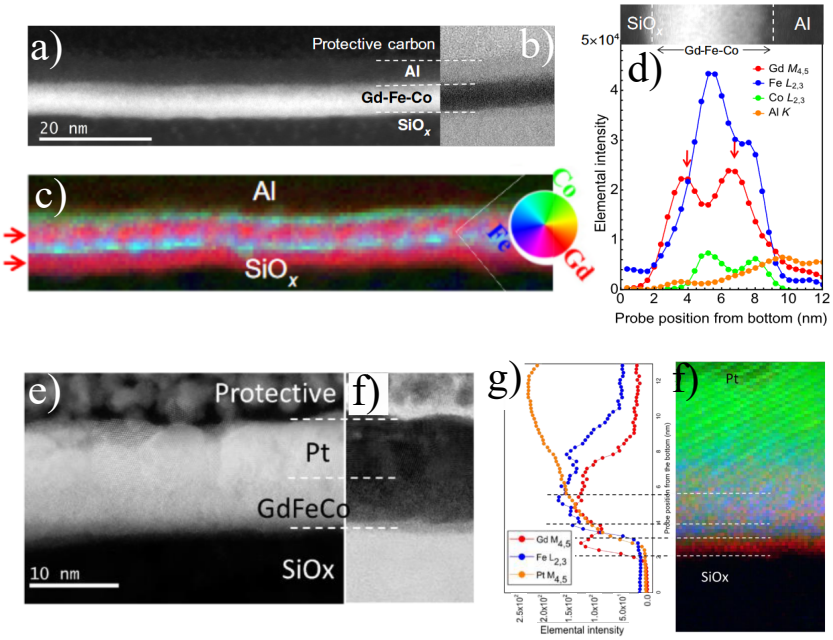

Figure 2.4: TEM cut on SiO_x/GdFeCo/Al and SiO_x/GdFeCo/Pt, a-e) HAADF and b-f) BF STEM images of sample cross section. c-h) Superimposed contributions with false colours of elemental maps (element, edge and colour): Gd $M_{4,5}$ in red,Fe $L_{2,3}$ in blue, Co $L_{2,3}$ in green, (Pt $M_{4,5}$ in green). d) Laterally integrated line profiles intensity over a length of 12 nm, same edges and colours with Al on K edge in orange (Pt in orange).

Figure 2.4, published in [201], shows a TEM cross-section image obtained for two samples of SiOx/$Gd_{0.35}(Fe_{0.85}Co_{0.15})_{0.65}$ (5 nm capped with either Pt or Al). These films, which contain Fe and have a different layer stack, are not directly comparable with the typical GdCo stacks analysed in the following chapters, but we can expect that they show a similar structure to some extent. The cross section high-angle annular dark-field (HAADF) images show the continuity of the films, their amorphous nature and the expected thicknesses of the layers (Fig. 2.4a-e). The chemical analysis obtained by electron energy-loss spectroscopy (EELS), Fig. 2.4 d-h), shows that, in both films, the Gd composition varies along the thickness, and is greater near the interfaces, probably due to migration. These richer Gd layers are presented by red arrows in figure 2.4 c). These raw results points towards very large composition differences (more than 10%) between the interfaces and the centre of the magnetic layer. One can also see that Pt diffused into the GdFeCo layer, which blurs its interface. Finally, both samples show Fe-Co rich clusters separated regularly by 2.8 ± 0.4 nm in the FeCo-rich section. Sub-structures inside the magnetic film have been described in amorphous ferrimagnetic thin films [233, 242], where two different kinds of structures are discussed. The first one take the form of growth-induced parallel columnar shapes, oriented with relation of the deposition incidence angle, with typical sizes around 20 nm, that originate from self-shadowing of material resulting in density modulations[233, 242]. This effect should be negligible for few nanometer-thick films. The second type, the one we observed, are compositional Co-rich clusters [201, 220, 243] with no clear origin, that are perhap due to complex chemical potential effects.

These internal structures may have a large impact on the properties of the material. The large modulation of Gd content suggests a better description of the GdCo layer should consider at least three layers of ferrimagnetic alloys of different compositions. Also, due to expected the Pt-Co origin of the interfacial anisotropy, the cluster structures may induce some modulations of the interfacial anisotropy field, which may pin magnetic textures.

2.1.4 Composition drift

Ensuring the stability of ferrimagnetic thin film is quite challenging, with notorious drift of the effective Gd composition, probably due to thermally-activated diffusion/oxidation, which may be accelerated in some of the sample fabrication process steps. The thermal history of the sample must, therefore, be carefully tracked, in order to avoid confusions arising from measurements separated by significant heating of the sample. To understand better this phenomenon, we tracked over three months the T_{MC} (and, thus, the effective Gd composition) of samples with different structures, thermal histories (annealed/non-annealed) and stored in different conditions (vacuum/air), shown in figure 2.5. The samples structure are SiOx/Ta (3)/Pt (5)/GdCo (5)/Ta (3-5) (nm) and an additional 1-2 nm Pt cap for the two indicated cases. In general, we observe that the drift rate is not constant, being faster at the beginning and then saturating, or at least largely slowing down, after a few months. The largest difference was found between annealed and non-annealed samples. The annealing consisted in a 10 min heating on a hot plate at 150° C. The non-annealed sample continuously drifted in T_{mc} for months, at a rate around 3K/month, whereas the annealed sample was quite stable, after a a drop induced by annealing (20-50 K). Finally, the sample stored in vacuum showed the same drift as the one stored in air after 3 months, although it showed a more gradual drift. In order to reduce such effect, diffusion barrier of Vanadium has been explored to prevent RE migration towards Al capped sample [220], but did not presented any sizeable effects. It was also proposed that a thin Pt cover [237] could mitigate quite efficiently this issue. We could indeed observe a better stability over time of Pt-capped samples, but we observe that the films were still sensitive to the temperature history. For example, after etching in an argon ion beam etching (IBE) as part of the fabrication process, the Pt-capped samples would still show a shift in T_{mc}, only slightly smaller than that of the uncapped ones [1].

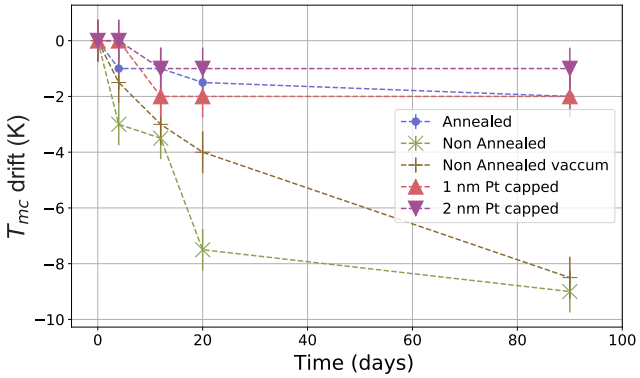

Figure 2.5: GdCo thin film aging. Shift over time of the T_{MC} for samples with different cappings (with or without Pt), annealed or non-annealed, stored in vacuum or in air.

[1] We measured the heating during IBE to occur at a rate of 5K/s by exposing a metallic track to IBE for 30s, measuring its resistivity right after while the sample cools down to room temperature and calibrating its resistivity versus temperature afterwards.

2.1.5 Degradation of patterned samples

The samples show degradation effects that evolve in time, spreading from the borders inwards (for a few μm), Fig 2.6. This effect appeared in Ta-capped samples erratically after multiple washes in acetone and isopropanol. For Pt-capped samples, the degradation was not observed. However, for both caps, washing in a (basic) soap solution induced a clear degradation of the magnetic properties. Bubbles of gas where observed under microscope when such solution was poured on patterned samples, and the effects of degradation seems to preferentially infiltrate in the edges of the sample up to the removal of the capping layer and then inducing a complete degradation of the magnetic properties. As seen in Fig 2.6 d), the degraded zone shows little to no magnetic signal in MOKE, and a clear drift of T_{mc} is also observed around the degraded zones (consistent with a large Gd oxidation) with a μm wide spreading that grows with time. As observed in the image 2.6 f), obtained with scanning electron microscope (SEM) on a Ta(3)/Pt(5)/GdCo(5)/Ta(5)/Pt(2nm) sample exposed to soap solution, the degraded region is located in the middle of a sample. The energy dispersive X-ray spectroscopy (EDX) measurement obtained along the line drawn in f) is presented in e). It shows a reducing of the Pt and Ta content on the degraded region, consistent with the removal of the two top layers. This phenomenon shortens the lifetime of samples drastically but, because it only appeared erratically (in some samples) it was not very limiting in practice. It suggests that edges can also be a source of Gd oxidation, which combines with the internal migration of Gd. The sample stability could perhaps be enhanced by a passivating encapsulation after the fabrication process to cover edges, which could prevent chemical sensitivity as well as further reducing Gd oxidation.

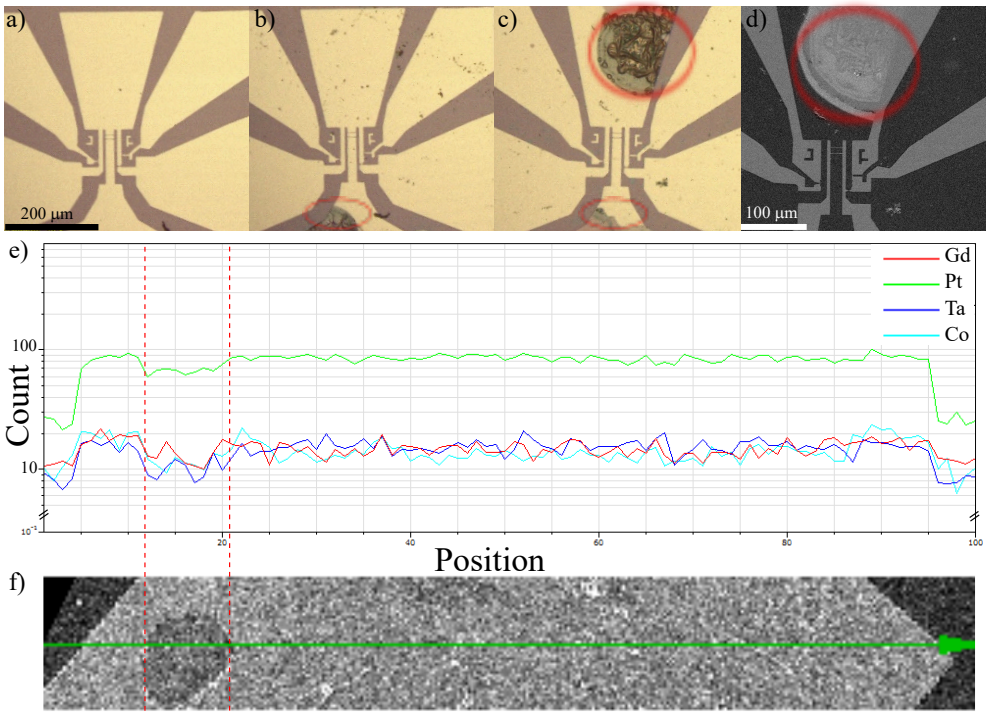

Figure 2.6: Sample chemical degradation . a) Original sample Ta(3)/Pt(5)/GdCo(5)/Ta(5) (nm). b) After multiple washing in acetone and IPA, one zone highlighted in red degraded. c) Sample washed in soap shows a spreading of the initial degraded zone and a large new one at the top. d) Large degraded zone observed by MOKE. e) EDX cut along a degraded zone of a Ta(3)/Pt(5)/GdCo(5)/Ta(5)/Pt(2) (nm) sample. f) SEM image of a degraded zone with the line cut where e) was obtained.

2.2 Gd-Co couplings and sub-lattice sensitivity

The very different electronic structures of Gd([Xe] $4f^7 5d^1 6s^2$) and Co ([Ar]$3d^7 4s^2$) leads to two different origins of magnetic properties. The magnetic moments of Gd are considered to be local, as the 4f orbital is shielded by higher orbitals and thus shows a reduced hybridisation with the atomic environment. On the other hand, metals present band magnetism due to the large hybridisation of 3d orbitals [77]. This d band actively interacts with the s - p bands that drive the electronic transport properties. This different nature of magnetism is also quite interesting to study in ferrimagnetic alloys, as both sublattices interact differently with the local environment, which implies sublattice sensitivity for most type of experiments.
Results from crystalline GdCo can be looked at in order to obtain some insights on amorphous GdCo. Buschow et al. [239] show that amorphous GdCo and their comparable crystalline compounds (e.g., $GdCo_2$ and $Gd_{0.33}Co_{0.66}$), although not equivalent, present a magnetisation of the same order of magnitude and share some of the same trends (lowering of magnetic moment per unit cell with increasing Co content, for example). It is then informative to look at theoretical predictions for crystalline GdCo, which are more easily derived than those for amorphous materials.

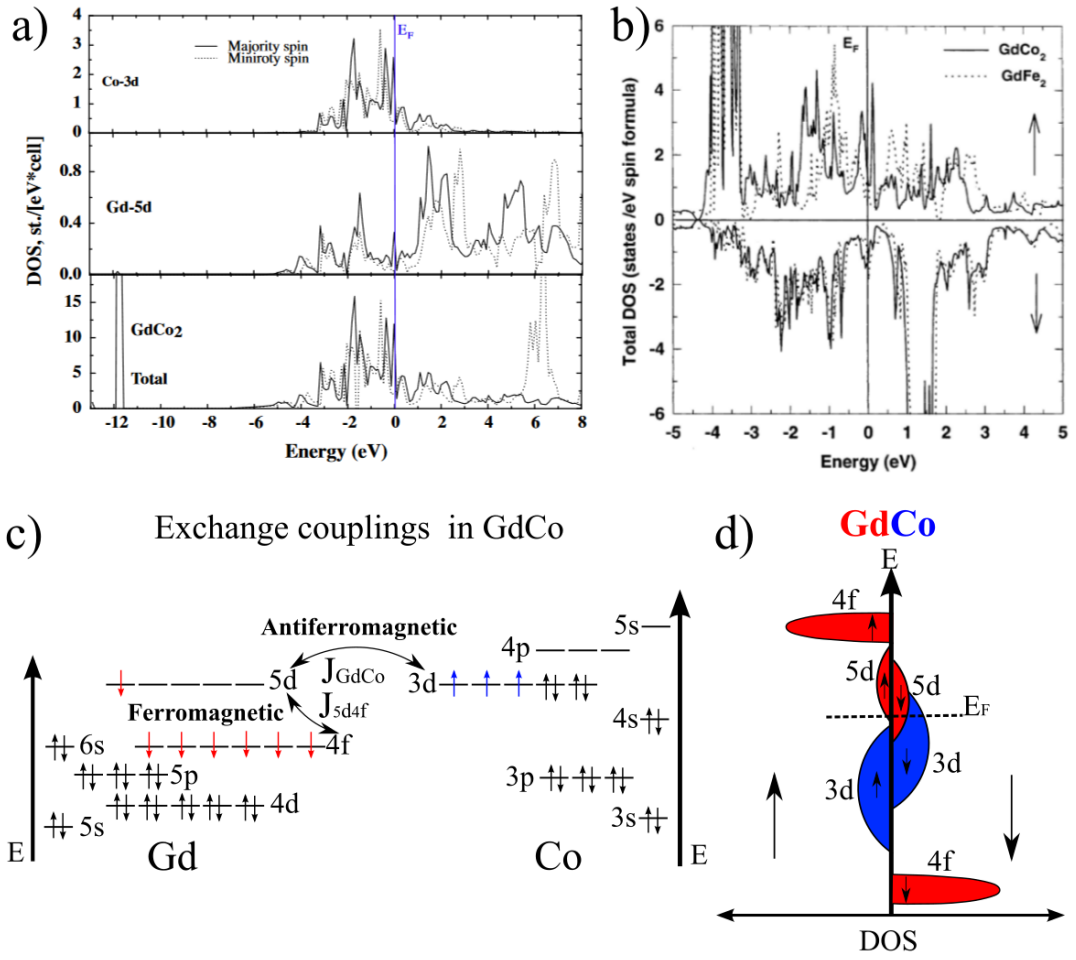

Figure 2.7: Band structure and Exchange Interactions in GdCo. a) Spin DOS for $GdCo_2$ using Hubbard corrected Generalised Gradient Approximation (within DFT theory) from [244]. b) Spin DOS for $GdCo_2$ computed with tight-binding linear muffin-tin orbital method from [245]. c) Schematic of exchange interaction between Gd and Co (considering [85]. d) Schematic illustration of spin DOS for amorphous GdCo considering results on $GdCo_2$ for Co dominated sample. A better schematic DOS can be found in [51].

The theoretical spin resolved electronic band structure of $GdCo_2$ is presented in fig 2.7 for different computational techniques. Considering the density of states (DOS) presented in figure 2.7 a-b), some general features stand out. The two computational techniques show some discrepancies, predicting peaks for the majority and minority spins at different positions, -2 and $+2$ eV for one model and -4 and $+6$ eV for the second model (with also different computed DOS), which emphasises that these theoretical computations are not exact determinations of the DoS. Nonetheless, these theoretical computations show us that the large peaks of the Gd 4f orbitals are indeed expected to present larger DOS compared to the Co 3d band (2.7 c).
It appears that the exchange splitting between up and down d states is rather small (close to the Fermi energy of 2.7 a)), with a larger contribution from Co and a residual one from Gd. Also, the single 5d electron of Gd should be filling the 3d Co band when hybridised [246, 247]. This hybridisation is known to yield an strong antiferromagnetic coupling between the 5d and 3d band of Gd and Co [85, 244]. This points to the fact that the composition has a very important effect on the magnetic properties of the Co sub-lattice which is filled by Gd 5d electrons, and one could expect from simplistic atomistic considerations that the d band is completely filled for $Gd_{0.75}Co_{0.25}$ which would have dramatically effects on the magnetic properties of the material.

The antiferromagnetic interaction between the Gd 4f and Co 3d electrons of is then mediated by the Gd 5d electrons (ferromagnetically coupled with the 4f), which can have some effects on the magnetic properties of Gd [85]. Indeed, one would expect that the magnetic properties of Gd are free of spin-orbit coupling due to the $L = 0$ state of the 4f levels, but the coupling with the 5d band can then indirectly induce some spin-orbit effects on the magnetic orbitals of Gd. This half-filled 4f orbital is nonetheless an important feature of Gd alloys, as it implies a much lower sensitivity to the local atomic environment than is the case of other rare earths. This can be compared for instance with Tb (with $L \neq 0$), which is known to present a large magneto-crystalline anisotropy, expected from the very anisotropic 4f orbitals [248].

Also, one can directly understand from the presented pictures that Gd and Co magnetic states will not be sensitive to the same range of energy when probed by electromagnetic waves, as higher energy is needed to access Gd magnetic states compared to Co ones. Also, the transport properties of GdCo should be mainly dominated by the effect of the d band interacting with the delocalised s and p electrons in the vicinity of the Fermi level [189]. This implies that transport properties will be sensitive to the Co magnetic sublattice, as well as the MOKE signal at the wavelength typically used in our experiments.
We can note that the position of the large Gd 4f peak below the Fermi energy is in the majority spin band when the sample is Gd dominated (as it would be for a-b) and in the minority spin band when the sample is Co dominated (as represented in d).

2.3 Mean field and effective parameters

2.3.1 Ferrimagnetic effective parameters

In a ferrimagnet where the coupling between sublattices is strong, a perfect antiparallel alignment of the two sublattices can be assumed: $\vec{\boldsymbol{m}} = \vec{\boldsymbol{m}}^{\mathrm{Co}} = -\vec{\boldsymbol{m}}^{\mathrm{Gd}}$. To keep track of the material parameters, one has to choose a reference direction of magnetisation from one of the sub-lattices. We will always use in this manuscript the historical convention [249] that considers the Co lattice as the reference which implies that M_s and L_s are now either positive or negative quantities according to the sample domination.

When considering infinite antiferromagnetic exchange, the ferrimagnet can be precisely treated as a ferromagnet with effective parameters calculated from the parameters of the two sublattices [249, 250]:

$$\begin{aligned} M_S &= (|M_{Co}| - |M_{Gd}|) \\ L_S &= (|L_{Co}| - |L_{Gd}|) \\ L_\alpha &= (\alpha_{Co}|L_{Co}| + \alpha_{Gd}|L_{Gd}|) \\ \gamma &= \frac{M_s}{L_s} \\ \alpha &= \frac{L_\alpha}{L_s} \end{aligned} \tag{2.1}$$

where we define the saturation magnetisation M_s, the angular momentum density L_s, the energy dissipation density L_α, the gyromagnetic ratio γ and Gilbert damping parameter α. Also, the typical variation of these parameters with the temperature in a ferrimagnet is presented in Fig 2.9.

Other effective parameters, defined for single lattices in chapter 1, are given for the two lattices by [250]:

$$\begin{aligned} A^{ex} &= (A^{ex}_{Co} + A^{ex}_{Gd}) \\ K &= (K_{Co} + K_{Gd}) \\ D_m &= (D_{Co} + D_{Gd}) \\ P &= (P_{Co} - P_{Gd}) \\ u &= \frac{\hbar/2}{L_S}\frac{PJ}{e} \\ \beta &= (\beta_1 P_{Co} + \beta_2 P_{Gd})/P \\ \tau_{FL} &= (\tau_{FL_{Co}} - \tau_{FL_{Gd}}) \\ \tau_{DL} &= (\tau_{DL_{Co}} + \tau_{DL_{Gd}}) \\ \theta_{\mathrm{SHE}} &= \theta_{\mathrm{SHE_{Co}}} + \theta_{\mathrm{SHE_{Gd}}} \end{aligned} \tag{2.2}$$

Ferrimagnet magnetisation versus temperature

We present in figure 2.8 the peculiar magnetisation dependence with temperature of a GdFeCo ferrimagnet measured by SQUID. The sample displays a rapidly varying magnetisation. with temperature. At low temperature it reaches 150 kA/m, and drops to 0 around 130 K before increasing again up to 270 K where it then reduces up to the Curie temperature estimated slightly below 400 K. The blue curve is obtained by a temperature sweep at zero field, with preliminary saturation with positive field at low temperature. It shows a negative magnetisation after the compensation of the magnetisation of the purple curve, which can appear to be rather surprising. This very specific feature of the ferrimagnets is explained in section 2.3.5, but we prefer first to introduce in details the description of the couple lattices of ferrimagnets to allow later, for a more precise description of this behaviour.

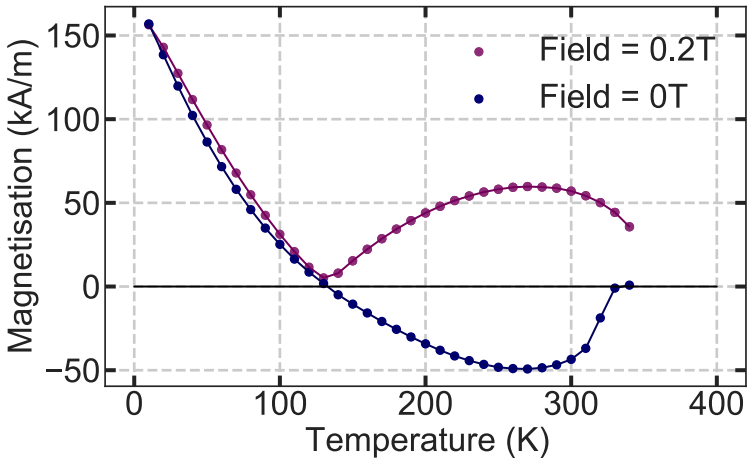

Figure 2.8: SQUID magnetometry temperature sweep measurement of $Gd_{0.35}FeCo_{0.65}(4)/Al(5)$ (nm) sample with 0.2 T applied or 0 T applied after saturation at low temperature.

2.3.2 Single-lattice mean field

Considering the thermal occupancy of spin states following Maxwell-Boltzmann statistics, the averaged magnetisation of a large assembly of magnetic moments in a paramagnetic material can be computed for arbitrary angular momentum J_a using Brillouin function $B_{J_a}(y)$ and yields [77]:

$$M = ng\mu_B J_a B_{J_a}(\frac{g\mu_B J_a B}{k_B T}) \tag{2.3}$$

with the Brillouin function

$$B_{J_a}(y) = \frac{2J_a+1}{2J_a}\coth\left(\frac{2J_a+1}{2J_a}y\right) - \frac{1}{2J_a}\coth\left(\frac{y}{2J_a}\right) \tag{2.4}$$

n is the density of atoms. The susceptibility, for small B, can then be obtained $\chi_{para} = \frac{n\mu_0 g^2\mu_B^2 J_a(J_a+1)}{3k_B T} = \frac{C_{Curie}}{T}$ with C_{Curie} the Curie constant. This describes paramagnetic materials, with a characteristic susceptibility $\chi_{para} \propto 1/T$.

This formalism can be extended to ferromagnetic materials by including the exchange interaction as an effective field B_m. This effective field is understood in the framework of the Weiss molecular field theory [251, 252, 253] that considers the crystal/ molecular environment to act on the energy of a magnetic moment as a Zeeman energy. For the exchange interaction of one spin $\mathcal{H}_{ex} = -2J^{ex}\sum_j \vec{\boldsymbol{S}}_i\vec{\boldsymbol{S}}_j$ the expression is re-arranged to reveal B_m as follows: $\mathcal{H}_{ex} = -2J^{ex}\frac{\vec{\mu}_i}{g\mu_B}\sum_j \vec{\boldsymbol{S}}_j = -\vec{\boldsymbol{\mu}}_i.\vec{\boldsymbol{B}}_m$.
Considering z neighbours for each spin, and the mean value of the spins (the root hypothesis of mean field theory), the molecular field is given by:

$$B_m = \frac{-2zJ^{ex}}{g\mu_B} < S >= \frac{-2zJ^{ex}}{g\mu_B}\frac{-M}{ng\mu_B}.$$

The effective molecular field parameter $\Lambda = -\frac{2zJ^{ex}}{ng^2\mu_B^2}$ is defined by $\vec{\boldsymbol{B}}_m = \Lambda\vec{\boldsymbol{M}}$. The complete effective field is therefore given by $B_{\text{eff}} = B + B_m$ so, $M = \chi_{para}\frac{B_{\text{eff}}}{\mu_0}$.

This finally yields: $M = ng\mu_B J_a B_{J_a}(\frac{g\mu_B J_a(B+\Lambda M)}{k_B T})$.
This is then used to obtain the ferromagnetic susceptibility $\chi_{ferro} = \frac{C_{Curie}}{T-T_c}$ with the Curie temperature $T_c = \frac{\Lambda C_{Curie}}{\mu_0} = \frac{2zJ^{ex}J_a(J_a+1)}{3k_B}$.

2.3.3 Double-lattice mean field

To reproduce the magnetisation of a ferrimagnetic alloy, the antiferromagnetic coupling is simply added as an effective field, which yields a system of two coupled equations for the magnetisation of the two sub-lattices. The complexity of the double-lattice mean field is not mathematical but rather practical, due to the large number of parameters it leaves to be defined. Moreover, these parameters can change with temperature, and with composition, and these dependencies can only be taken into account with a limited precision, either because of simplistic models, or also lack of experimental data to verify predictions. We present below the choices made for our mean field approach. We consider the Co lattice with number 1 and Gd with number 2. The magnetisation temperature dependence of each lattice is described using Brillouin functions and a molecular field B_{mi} that acts on each i lattice:

$$M_{Co}(T) = n_{Co}\mu_{Co}B_{J_{Co}}(\frac{\mu_{Co}B_{m1}}{k_BT}) \tag{2.5}$$

$$M_{Gd}(T) = n_{Gd}\mu_{Gd}B_{J_{Gd}}(\frac{\mu_{Gd}B_{m2}}{k_BT}) \tag{2.6}$$

where

$$B_{mi} = \sum_j \Lambda_{j-i}M_j$$

This gives for the Co and Gd lattices the following molecular fields:

$$B_{m1} = \Lambda_{Co-Co}M_{Co} - \Lambda_{Gd-Co}M_{Gd} \tag{2.7}$$

$$B_{m2} = \Lambda_{Gd-Gd}M_{Gd} - \Lambda_{Co-Gd}M_{Co} \tag{2.8}$$

The expression for the mean field parameter is generalised as follows [254]:

$$\Lambda_{ij} = -\frac{2z_{ij}J_{ij}^{ex}}{\mu_B^2 g_i g_j n_j} \tag{2.9}$$

It is common to neglect the exchange coupling of the Gd lattice because $\Lambda_{Gd-Gd} << \Lambda_{Co-Co}$ [255] so $B_{m2} = -\Lambda_{Co-Gd}M_{Co}$.

This approximation translates to the fact that the ordering of the Gd sublattice is only due to the coupled ordered Co layer.

Because of their coupling, both lattices present a common T_c. The major approximation we consider is to neglect the variation with temperature of the model parameters, as discussed in Sec. 2.6. This can be completely inappropriate when parameters rapidly vary with temperature. In our systems, the variation of these parameters is nonetheless neglected since such approximation still yields quite qualitative and quantitative agreements with experimental data.

2.3.4 Parameters evolution with composition

We will rather focus on the effects of composition which are more important as they directly change the ratio between the two chemically different materials. We consider 4 parameters: $J_{Co}, n_{Gd,Co}, z_{Gd,Co}, J_{Gd,Co}^{ex}$ and search in the literature the best values to parameterise the mean field.

Because the orbital moment of transition metal is mostly quenched in a real material we cannot use the atomic expectations (S = 3/2 and L =3) so experimentally determined values for $J_{Co} = 0.84$ [256] is preferred ([22] gives 0.75). Also, adding Gd modifies the 3d band filling (one e- in the minority d band per Gd atom) so the J_{Co} will change with composition accordingly [22].

The typical density for the alloy can be computed from the average distance between Gd and Co atoms. It is found to lay between 1.96-3.1 Å from X ray diffraction [239] and analysis from Extended X-ray Absorption Fine Structure (EXAFS) found 2.43 Å for Co-Co, 2.9 Å for Gd-Co and 3.6 Å for Gd-Gd [243], with these distances sometimes called metallic radius. One can use these distances to compute the expected density for hard spheres of two different radius with $n = \frac{1}{\sum_n (4\pi r_n^3/3) x_n}$. This gives a density around 254 atoms/nm^3 for a distance of 1.96 Å and 64 atoms/nm^3 for 3.1 Å . When considering both lattice sizes, it yields around 85 atoms/nm^3 for 25% Gd content. The density of the material will then change with composition and can be simply linearly interpolated, as described in [239, 257]. We observed that the obtained density is too large to fit with our measurements of $M_s(T \to 0) = n(x g_{Co} J_{Co} \mu B - (1-x) g_{Gd} J_{Gd} \mu B)$ with x the Co composition. The factor is around two, and so we take the linear interpolation of [239, 257] but halve it.
Then, unlike in the case of a single sized compact stack of hard spheres that possesses 12 neighbours, the difference in size of Gd and Co atoms implies that Gd atoms have a maximum of 18 neighbours (12 if only Gd and 18 if only Co) where Co atoms have a maximum of 12 neighbours (6 if only Gd and 12 if only Co)[238]. This can be approximated by $Z_{Co} = 6 + 6x$ and $Z_{Gd} = 12 + 6x$ (where a more complex function with $Z'(x = 0 \text{ and} x = 1) = 0$ would be better suited). Considering that $Z_{Co} = Z_{CoCo} + Z_{CoGd}$, $Z_{Gd} = Z_{GdGd} + Z_{GdCo}$ and the neighbour pair equality $x Z_{CoGd} = (1-x) Z_{GdCo}$ [238, 256] (we do not use the rest of their expressions) we obtain a system of two equations but three variables.
We decide to fix $Z_{GdCo} = x(6 + 12x^2)$ so $Z_{CoGd} = (1-x)(6 + 12x^2)$ because it gives the correct limits for x=0 and x=1 and can deduce Z_{CoCo} and Z_{GdGd} from the above equations. This could be refined to have better behaviour of the derivatives of the number of neighbours at x=0 and x=1. Because we have no interest to computed mean field at such extreme compositions these expression are sufficient.
Duc et al [238] studied the exchange J^{ex}_{GdCo} with composition, and compared results between amorphous and crystalline samples. As we neglect the J^{ex}_{GdGd}, and that J^{ex}_{CoCo} varies around 1% per %Co [258], we will make the assumption that J^{ex}_{GdCo} is the only exchange interaction that evolves with composition following the measurement of [256]. Also, to obtain a variation of T_{mc} with composition consistent with our measurements (see Fig. 2.10), the antiferromagnetic exchange between Gd and Co is increased by a factor of 1.3. This is rather consistent with our experimental determination of this interaction as presented in section 2.5.4.

As we already discussed the complex internal structure of ferrimagnetic thin films, it seems important to note that the mean field we use is a crude model of the reality of our samples. We will show that this model nonetheless presents rather satisfactory results. We discuss the limits of this model in section 2.3.6. We sum up the chosen parameters models and values in the table 2.1 considering a composition x for $Gd_{1-x}Co_x$.

	Gd (1-x)	Co (x)	Ref
J_a ($\hbar$)	3.5	$0.84 * \sum_{k=l}^{n} \frac{n!}{k!(n-k)!} x^k (1-x)^{n-k}$	[22], [256]
g	2	2.22	[22]
J^{ex}_{Co-} (J)	$(-3.25x + 3.5).10^{-22} \times 1.3$	11.10^{-22}	[238]
J^{ex}_{Gd-} (J)	0 (0.2-0.5.10^{-22})	$(-3.25x + 3.5).10^{-22} \times 1.3$	[259][256]
N (atoms/m^3)	$(1-x)(73x + 9).10^{27}/2$	$x(73x + 9).10^{27}/2$	$M_s(T \to 0)$,[239]
Z_{Co-}	(6+12x^2)(1-x)	12x(1-x+x^2)	[256]
Z_{Gd-}	12(1-x^3)	(6+12x^2)x	[256]

Table 2.1: Mean field parameters for coupled GdCo.

2.3.5 Ferrimagnetic compensations: observations and implications

In Fig 2.9 we present the typical magnetisation obtained by this mean field theory. We can see on the figure that for a composition of 25% of Gd, the overall magnetisation is zero around 300 K. This temperature is called the magnetisation compensation temperature T_{mc}, because both sub-lattices magnetisation cancel each other. Below this temperature, the Gd sub-lattice possesses the larger magnetisation and the sample is described as RE dominated. Above this temperature the Co sub-lattice possesses the larger magnetisation and the sample is described as TM dominated. Also, considering the angular momentum density L_s of the alloy, we can see that it present the same general shape as the magnetisation, but it reaches zero at a slightly higher temperature defined as the angular compensation temperature T_{ac}.

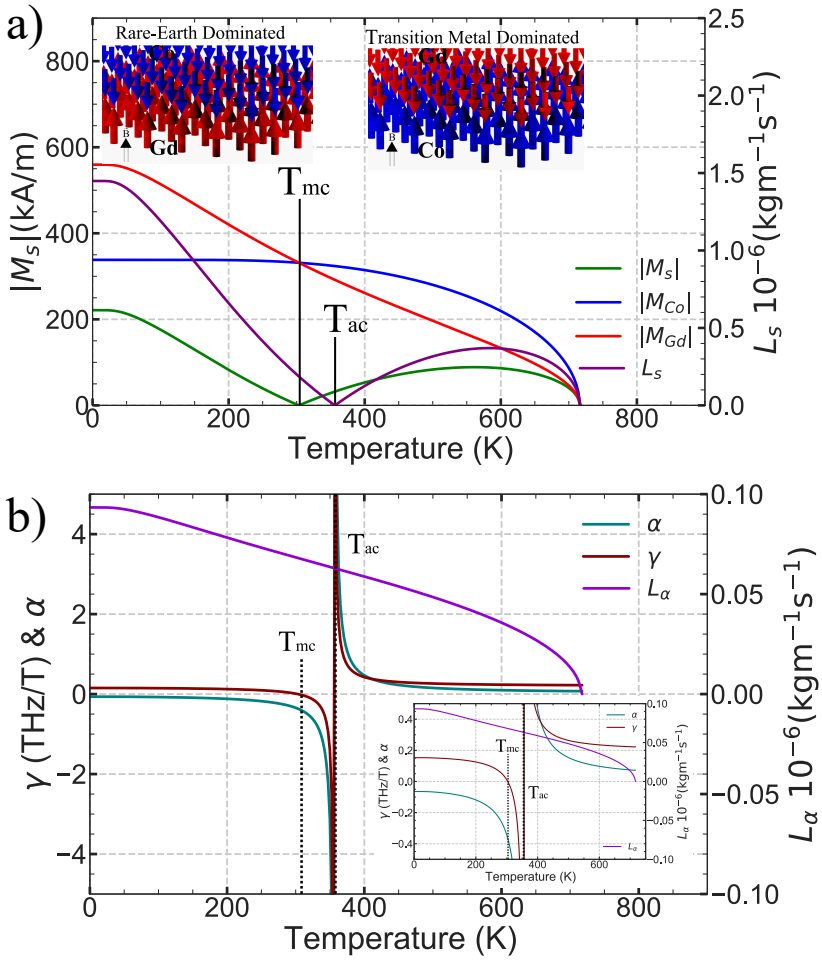

Figure 2.9: GdCo mean field, compensation temperatures and effective parameters evolution. a) Example of mean field for $Gd_0.25Co_0.75$ and parameters of 2.1. Insets shows the RE domination before T_{mc} or TM domination after. The angular compensation T_{ac} can be observed above T_{mc}. b) Evolution of γ, α and L_α for the same composition as a).

From this typical behaviour of two coupled magnetic lattices, we can now understand the measurement from fig. 2.8, where the magnetisation curve displays a magnetic compensation around 130 K. The measurement at zero magnetic field simply shows the reversal of the dominant sub-lattice. When no magnetic field is applied, the full magnetisation change direction when crossing the T_{mc} but because the sub-lattices do not reverse the signal measured is negative. If a magnetic field is applied, the measured magnetisation will remain positive on the whole temperature range because the new dominant lattices reverses along the field.

Magnetic Compensation

When no T_{mc} is observable on the whole temperature scale, the sample is either TM or RE dominated which happens respectively for low (below 20%) or high (above 40%) Gd content. We also see that the Curie temperature T_c evolves with composition. The larger the Gd content, the lower the T_c becomes, acting as a temperature cut-off for the T_{mc} at high Gd content. This is clearly understandable due to the lower exchange interaction of the Gd, which cannot sustain a magnetic order at as high temperature as the Co can. This shows how tunable the magnetisation of RETM material is, either by changing the composition or by working at different temperatures. At the T_{mc} the zero magnetisation implies that the system is no longer sensitive to external magnetic field (in the limit of spin flop see Sec. 2.5.4.1).

Also, as we will see later, it has major effects on the statics of the system, with already an important effect due to the vanishing of stray-field related effects. The magnetic compensation can be measured by several ways, either sensitive to the full magnetisation (like in SQUID magnetometry, or VSM or MFM...), but also with techniques sensitive to only one magnetic sublattice (usually Co by transport of magneto-optics measurements) that will see a reversal of their signal when a magnetic field is applied and the compensation crossed. These techniques shows more difficulties to precisely define the T_{mc} in the sense that the sample has to be far enough of the compensation so its magnetisation can be reversed by a given applied magnetic field.

Angular Compensation

The angular momentum L_s follows a comparable, shifted thermal variation compared to M_s as can be seen in 2.9 a), where the compensation temperature T_{ac} is observed above T_{mc}. This behaviour is due to the difference in gyromagnetic ratio of the two sublattices. Indeed, at T_{ac}: $L_s = 0 = |L_{Co}| - |L_{Gd}| = \frac{|M_{Co}|}{\gamma_{Co}} - \frac{|M_{Gd}|}{\gamma_{Gd}} = \frac{|M_{Co}|}{\gamma_{Co}}(1 - \frac{|M_{Gd}|}{|M_{Co}|}\frac{\gamma_{Co}}{\gamma_{Gd}})$, which leads to $\frac{M_{Gd}}{M_{Co}}\frac{\gamma_{Co}}{\gamma_{Gd}} = 1$ at T_{ac}. As $\gamma_{Co} > \gamma_{Gd}$, this only happens if $|M_{Co}| > |M_{Gd}|$, and so $T_{ac} > T_{mc}$.

A more complete description of the relation between T_{mc} and T_{ac} can be found is the series of experimental determinations of both compensations temperature of GdFeCo sample in [260]. The authors give an experimentally determined relation to link the two compensation temperatures:

$$T_{ac} = 0.87 T_{mc} + 101K \tag{2.10}$$

We can otherwise use the mean field (parameterised to fit a given magnetisation curve) in order to compute the location of T_{ac}. This indeed shows that the distance between the two compensations is greatly determined by the ratio between the gyromagnetic ratio of both sub-lattices.

This temperature has a major effect on the dynamical properties of the system. Indeed, when the angular momentum density vanishes, precessional effects are cancelled. This means that for DW displaced by magnetic field, the walker breakdown field, where the mean velocity is reduced by the precessional motion of the DW, should vanish at T_{ac} [261]. In the case of chiral Néel DW driven by SOT, the saturation of the velocity at high current can be suppressed [262]. This is usually observed as a peak in mobility of magnetic textures at T_{ac}. Finally it was observed that the current-induced deflection of finger-like chiral Néel DWs is reversed when crossing T_{ac} [263], a direct evidence of the effect of T_{ac} on the precessional degree of freedom of magnetic textures.

Effective parameters evolution

The effective damping parameter α and gyrotropic ratio γ are expected to diverge and to change sign at T_{ac} as they vary with $1/L_s$ (eq. 2.2) with γ already changing sign at T_{mc}. Experimentally, the sign of α can not be directly measured. On the other hand some techniques using circularly polarised electromagnetic waves (in Ferromagnetic resonance for instance) can distinguish the gyration direction. Also, divergence obtained with the model are softened in real materials due to the finite coupling between the two sub-lattices and also to the inhomogeneity of the sample properties. This is seen by the increasing but non-divergent α and γ in [264].

Finally, the evolution of L_α is quite important to describe, as this parameter determines the rate of dissipation of the system. We can see in Fig. 2.9b) that the closer to T_c the smaller L_α becomes, with an approximately linear decrease through the whole temperature range. Dynamical experiments at low and high temperature, obtained in a same sample, are presented in chapter 4 in section 4.8 and will highlight the importance of this parameter.

It should be noted that the effective parameter model cannot be used in all situations. For example, the finite coupling between lattices implies an antiferromagnetic mode. This has been extensively studied in GdFeCo in [265], where it was observed that data could only be described by considering a complete model of the two sublattices. The developed model showed very good quantitative agreement with the spin-wave frequency dependence with temperature across the compensation points of the ferrimagnet.

2.3.6 Mean field and effective GdCo composition

The magnetisation measured for a series of comparable samples, where only the composition varies (SiO_x/Ta(1)/Pt(5)Gd_xCo_{1-x}(8)/Ta(5)/Pt(1) (nm)) is presented in figure 2.10. It shows an increasing T_{mc} with Gd content, as expected from mean field. The magnetisation at low temperature reduces with a lower content of Gd, which is expected due to the higher magnetisation of Gd compared to Co. We parameterised the mean field with values from Table 2.1 and only let the composition as a fitting parameter, with the resulting magnetisation curves presented in Fig. 2.10 a) as dashed lines.
We can observe an overall satisfactory fit of the mean field for this composition series. The discrepancies may be attributed to an imperfect modelling of the mean parameters with temperature and composition and to the complexity of the internal structure of GdCo thin films. Nonetheless, it shows that this simple mean field theory gives a good approximation of the magnetisation dependence with temperature. From the measurements of figure 2.10 a) we obtain the variation of T_{mc} with Gd content: $\frac{\partial T_{mc}}{\partial x} = 31\text{K}/\%\text{Gd}$. Comparing with the mean field in Fig. 2.10 b), the nominal composition is shifted by $\approx 5\%$.

This shows that, when modelling $M_S(T)$ for a real sample, the composition used in the mean field composition must not be the nominal composition at deposition, as it would not yield the correct T_{mc}. The composition of the model will remain as a free parameter that we will tune to obtain the best agreement with the experimental $M_S(T)$, with the other parameters listed in table 2.1.

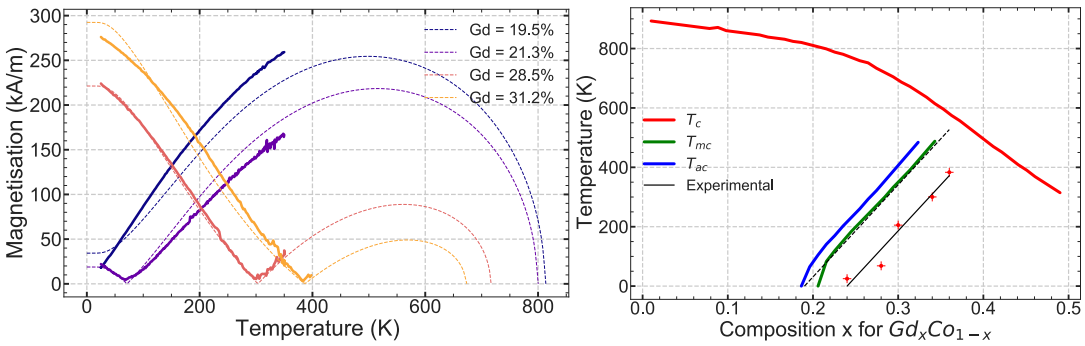

Figure 2.10: Compositions study. a) SQUID magnetometry measurement on SiO_x/Ta(1)/Pt(5)Gd_xCo_{1-x}(8)/Ta(5)/Pt(1) (nm) thin films and magnetic compensation T_{mc} evolution with temperature . Fitted data by mean field with only composition adjustment. b) Experimental T_{mc} dependence with composition (red crosses). The dotted line is shifted by 5% less of gadolinium. Other quantities are computed by mean field.

The exchange interaction between the Co moments, J_{CoCo}, can be determined from the spin wave stiffness measured by BLS, as presented in section 2.5.4.2. BLS can also be used to determine J_{CoGd} by studying the antiferromagnetic mode [265]. The J_{CoGd} can also be determined from the spin-flop field, the field needed to break the antiferromagnetic coupling between both sub-lattices, accessible with magnetisation measurements [266, 255], which we also studied, or by inelastic neutron scattering [267]. The density is hard to measure in thin films. It would be easier to measure the density of orders-of-magnitude thicker films, although the density would be perhaps very different.

2.3.7 Validity of the mean field parameters

There are many articles that use the mean field approach to describe GdCo films properties which use different values for the parameters and different approximations to their compositional and thermal variation [268, 269, 270, 259, 22, 271, 238, 272]. A thorough discussion can be found in [268]. The parameters that show the larger differences in the literature are the strength of the exchange interactions, the Landé factor/ the total angular momentum, with the two latter being the hardest to measure experimentally. The diversity of parameter values found in literature may come from the different properties of films deposited with different techniques, from the different thicknesses, or from different interfaces. Whatever the cause, an exact parameterisation of the mean field is difficult, and we could not find in literature the parameters to satisfactorily constrain fully the mean field. As a consequence, some properties, either measured or deduced from mean field models, can show large differences in different reports. For example, the evolution of T_{mc} with composition of GdCo is found to be 70 K/% Gd in [22] (measured in very thick films) but around 40 K/% Gd in [272] (from mean field analysis).

Although a perfect parameterisation seems out of reach, the use of the mean field model for our films allow us to disentangle the magnetisations of the two sublattices and, therefore, to calculate the thermal and compositional variation of the effective parameters. We use the parameters in table 2.1, usually slightly adjusted to better fit the magnetisation curve, by changing the exchange couplings, or the composition by some % of the nominal values. This procedure weakens the comparability between samples, however, it can be justified in cases where the stack was changed. For this reason, when studying a series of samples, we used a single set of mean field parameters (as in the previously presented composition series, Fig. 2.10).

This concludes our description of the ferrimagnets by a mean field approach. We observe that the mean field captures quite precisely the properties of the ferrimagnets, but the exact parameterisation of the model remains challenging, where only very broad systematic studies would allow a clearer view on the parameters dependencies with temperature, composition, thickness and interfaces.

2.4 Nanofabrication of functionalised magnetic tracks

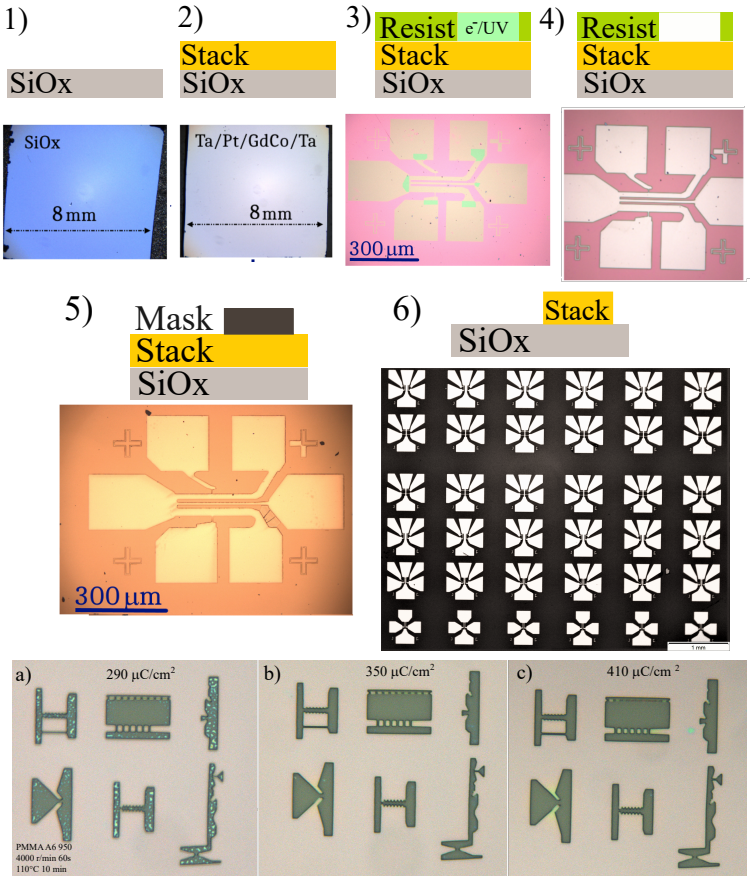

Figure 2.11: Nano patterning of micrometric magnetic tracks. 1) Substrate cleaning, 2) plain film deposition, 3) resist exposure, 4) resist development, 5) mask deposition, 6) mask etching and final array of magnetic tracks. Images below (a,b,c) present a SEM lithography test dose for our resist (PMMA 950k 6% in anisol). a) Under-dosed, b) perfect dose, c) overdosed.

The samples are fabricated following the different steps sketched in Fig. 2.11. Once the magnetic film is deposited on the silicon substrate (2), the film is characterised using MOKE or transport measurements to assess its magnetic properties. Samples with interesting magnetic properties are selected and patterned into magnetic tracks to create desired geometries.

The fabrication procedure is quite standard, but the sensitivity of these films to temperature (Sect. 2.1.4) demands some care. The sample is cleaned in acetone and rinsed with isopropanol. Then, a controlled thickness of electro-sensitive resist, PMMA (typical concentration 6% in anisol, chain length 950k), is applied on the sample in a spin-coater (2-3) and polymerised at 110°C for 10 min. The resist is then exposed, in a scanning electron microscope. The resist is developed in chemical solution (MIBK:IPA solution) (4). A metallic mask (typically Al 40 nm) is then deposited. The resist is removed in acetone bath, which lifts off the mask material on the un-exposed areas.

After this step, we obtain a mask with the desired geometry on top of the film (5). The film is then etched using Ion Beam Etching which removes the film unprotected by the mask (6). The etching time is controlled by using control samples of mask material for reference. The complete etching of the film can be verified by a measuring the resistance between unconnected devices. The rest of the mask can be removed by chemical etch.

PMMA is an interesting resist for several reasons. First, it can be used with a baking temperature of only around 110 ° C (after the spin-coating process), which is convenient to avoid a large drift in effective T_{mc} (sect. 2.1.4). Also, because it allows for a large degree of overdosage, it simplifies the stitching of large lithography patterns. Indeed in fig 2.11a-c) we can see that the overdosed sample is well developed, with only a small rounding of the features. Stitching allows to expose different parts of the pattern with different conditions (large current to expose large contact pads, small apertures for the small tracks) and garantee that the structures remain continuous. Double exposed PMMA (stitching) areas are visible in fig 2.11 3), but disappear once the resist is developed.

2.4.1 Typical geometry for magnetic tracks

The typical devices we study are presented in figure 2.12. We can sum up the most important devices as the one used for Hall bars, for skyrmion nucleation or for skyrmion dynamics measurements. All these designs are made to be quite versatile and to allow for several measurements. This is also very convenient to have multiple kinds of devices on the same sample, to be able to safely compare different measurement quantities obtained on the same (homogeneous) film.

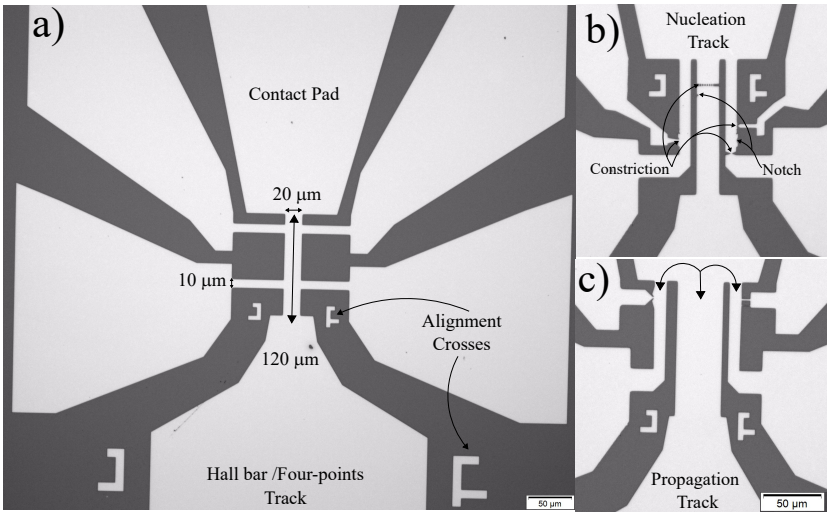

Figure 2.12: Different magnetic tracks geometries. a) Hall bar and four points measurement tracks b) Skyrmion nucleation tracks c) Skyrmion propagation tracks.

The geometry of magnetic tracks is guided by several considerations. One is the electrical resistance of the track. We can shorten the magnetic track to reduce its resistance, and enable higher current densities. This can also allow to improve impedance matching to the 50 Ω impedance circuit used to send short electrical pulses. The requirement of low resistance (for higher currents and better impedance matching) must be balanced with the second consideration, to have a sufficiently long and wide track to be able to observe the skyrmion trajectories.

The typical resistivity of our films is $100 \cdot 10^{-8}\Omega$m (Ta(1)/Pt(5)/GdCo(5)/Ta(5) (nm)), which yields a sheet resistance $R_{\square} = 62.5\Omega$. Because we know the typical interesting range of current densities to lay around 10^9 to 10^{12} A/m^2, we choose the track width and length necessary to reach such current densities, given the accessible voltage applications of our experiments (50 V), while being able to comfortably observe skyrmion trajectories. The compromise is found in 10 to 20 μm wide track of 50 to 100 μm length. In the next section, we will present many measurements made on the first kind of devices, which are the one used for transport measurements. In the chapter 4 and 5, we will use sample designed for propagation and nucleation.

2.5 Measuring magnetic properties

The magnetisation of ferrimagnets varies strongly with temperature as do many other of their magnetic properties. We will briefly discuss in this section the measurement of the following parameters: M_s, H_k, K_u, θ_{SHE}, D_m, A^{ex}_{Co-Co}, J^{ex}_{Gd-Co}, α, γ. The experimental techniques used in this work to obtain these parameters are the anomalous Hall effect (AHE), SQUID magnetometry, second harmonic torque measurement and BLS. In chapter 3 we will also present results obtained by Magneto-Optical Kerr Effect (MOKE).

2.5.1 Magnetic field hysteresis loop configurations

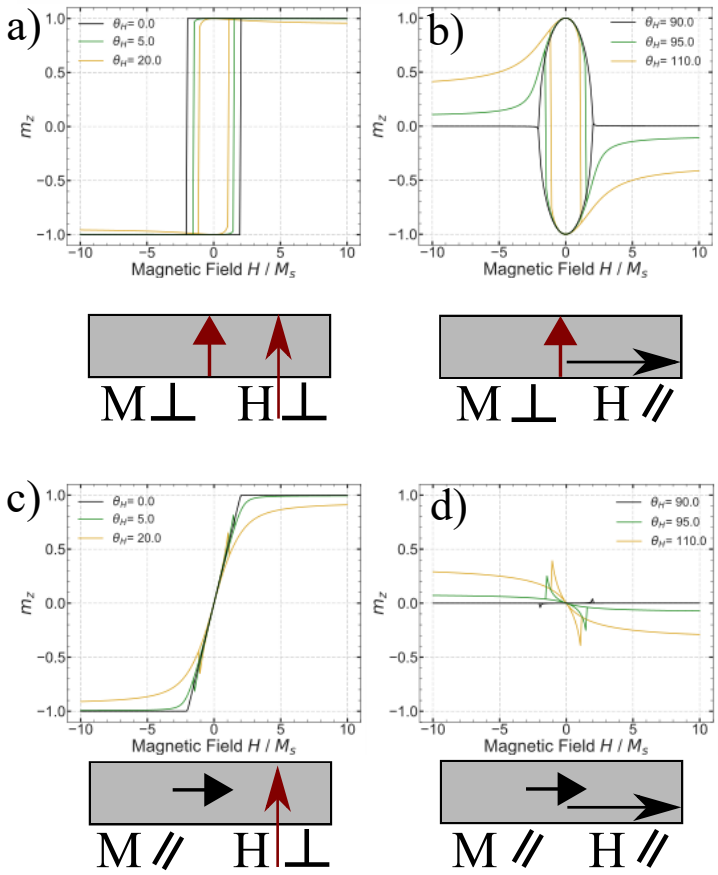

Figure 2.13: Magnetic field hysteresis loop schematic relative configurations between M and H. a-b) **M** Out of plane (OP) and **H** OP, **M** OP and **H** In Plane (IP) c-d) **M** IP **H** OP, **M** IP **H** IP. In all cases, figure above is m_z for an hysteresis loop from $-H$, computed from Stoner model of a macrospin for misalignment of 0, 5 or 20°.

Hysteresis loop refers to the sweeping of a parameter while monitoring a system's physical quantity in order to observe its response depending on the direction of the sweep (low to high or high to low). The sweeping parameter can be the temperature or the magnetic field for example, and hysteretic behaviour appears as an opening of the observable path between the two sweeping directions. Only magnetic field sweep hysteresis loops are described here. They are studied by transport measurements, of the AHE and later also by MOKE. As described previously, the AHE or MOKE in polar configuration are both sensitive to the m_z component the Co lattice magnetisation. The four different configurations of the relative orientation between the magnetisation and applied field are presented in figure 2.13.

In figure 2.13 we observe in a-b) the typically observed signal for a macrospin in a magnetic field applied perpendicular or along the sample plane for a OP anisotropy. In c-d) the same model describes the case of a magnetic field applied perpendicular or along the sample plane for an IP anisotropy. Each configuration is presented for the related angle θ of the magnetic field, which is zero when applied along $\vec{e_z}$. When the field is along the magnetic anisotropy preferred direction, the hysteresis loop is referred as easy-axis a-d) and when transverse to the magnetic anisotropy as hard-axis loop b-c).

2.5.1.1 PMA and IPA samples AHE hysteresis loop

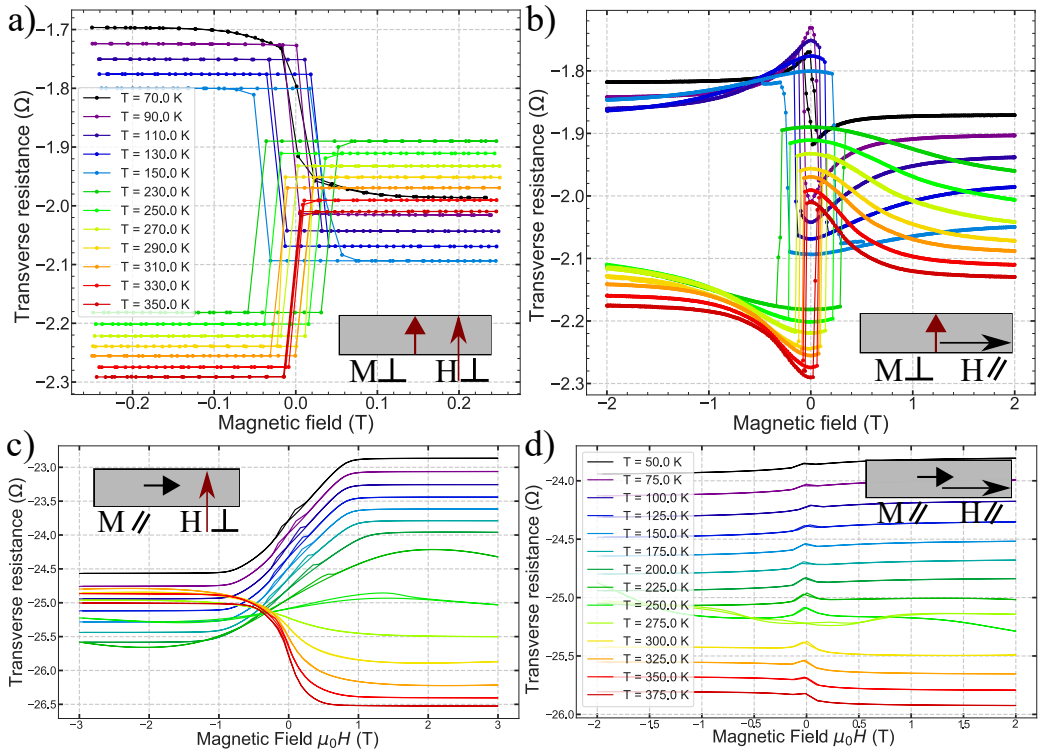

Figure 2.14: AHE Easy and Hard axis hysteresis loops in PMA or IPA GdCo thin film. a) AHE measured in configuration 2.13a) (easy-axis). b) AHE measured in configuration 2.13b) (hard-axis). c) AHE in with IP magnetisation, measured in configuration 2.13c) (hard-axis). d) measured in configuration 2.13d) (easy-axis).

AHE measurements presented in this work are mostly obtained in a commercial cryostat PPMS (Physical properties measurement system from Quantum Design) with a current source of 300 μA using a rotatable cane. The PPMS allows for large temperature range from 5 to 400 K and large magnetic field up to 9 T. The sample presented in figure 2.14a-b) is a Ta(3)/Pt(5)/GdCo(8)/Ta(5)/Pt(1) with a T_{mc} around 180 K.

In figure 2.14c-d) a Ta(3)/Pt(5)/GdCo(10)/Ta(5) sample with T_{mc} around 260 K is presented. The curves close to T_{mc} are removed from the plot to improve readability due to their noisy nature [2]. AHE hysteresis loops are presented in figure 2.14a) for easy-axis and in b) for hard axis configuration. The sample presents a PMA and so the magnetic field is along the sample surface normal in a) and along the surface in b). We see in 2.14a-b) the AHE reverses sign between low and high temperature. The change in sign is observed to coincide with T_{mc} measured with SQUID. This observation is very consistent with the expected AHE Co lattice sensitivity, and so, is due to the reversal of the Co sub-lattice response at T_{mc}, which is positive above T_{mc} and negative below [3]. The AHE depends on many properties of the material, with a clear relation with its resistivity for instance [273]. We neglect such effects in this explanation, which is a way to consider the Hall resistance to be directly proportional to the magnetisation of the Co lattice. We can note that the AHE signal is not centred at zero for zero field, which is due to a contribution of R_{xx}. Also, the evolution of the baseline is directly related to the resistivity variation with temperature of the sample. The resistivity is expected to vary around 5% on the whole temperature range for GdCo, with the specificity of the amorphous material to present a higher resistivity at lower temperature [274, 275]. Our measurements shows a domination of the Pt/Ta resistances.

The hard axis measurement of IPA sample presented in figure 2.14 c) also shows a reversal of the saturation at T_{mc} as in the other configurations. The magnetisation present the typical linear variation with field before saturation at high field. Measurements from 2.14 d) are not useful as the reversal of the magnetisation happens in the plane of the sample whereas the AHE is sensitive to the out of plane magnetisation. We will not be interested in sample that only present IP magnetic anisotropy on the whole temperature range, because they will not present the magnetic textures we are interested in. AHE measurements are very convenient to determine precisely T_{mc}, by measuring the temperature where the saturation sign reverses. This can be done in any configuration but easy-axis measurement is preferred as it can exert larger magnetic field and so reveal the hysteresis closer to T_{mc}.

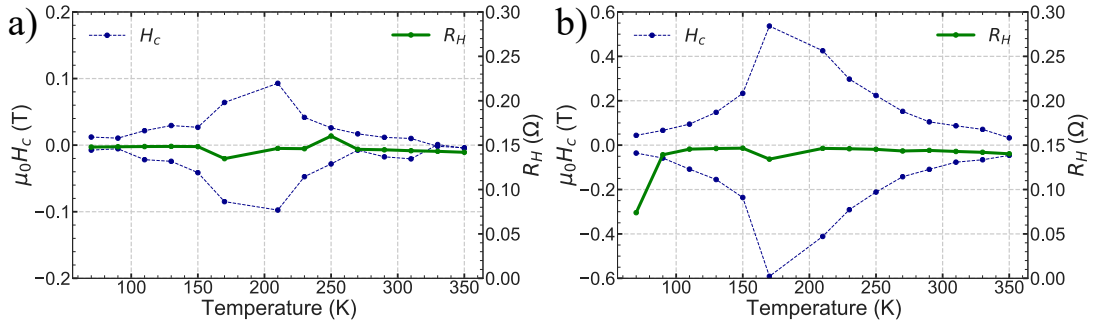

Figure 2.15: AHE hysteresis loops H_c and R_H a-b) Coercive field H_c and Hall resistance R_H measured from 2.14a-b).

We present the analysis of H_c and AHE signal amplitude (from figure 2.14 a-b) in figure 2.15. We can see in 2.15a-b) that $R_H = V_y/I_x$ remains constant on the whole temperature range. From the mean field, we expect that the magnetisation of the Co to change little far from T_c (see Fig.2.9), which suggests that the AHE is indeed mostly sensitive to the Co lattice.

[2] Near T_{mc}, only some parts of the sample reverses during the loop, which blurs the signal.

[3] The AHE signal depends on the convention on the hall measurement. Our convention is, counting clockwise, $I^+V^+I^-V^-$ which gives a positive signal for TM dom. at positive magnetic field. This sign reverses for the other convention $I^+V^-I^-V^+$ that is often used in the literature.

The coercive field H_c is the field at which the magnetisation is zero (half of the sample is reversed). It is found to increase close to T_{mc} due to the lowering of the magnetisation as seen in figure 2.15a-b). At T_{mc} the sample is no longer sensitive to external magnetic and so it takes an infinite field to reverse the magnetic domains (when considering an infinite coupling between the two sublattices). At large magnetisation, H_c tends to zero as the magnetisation of the system becomes increasingly sensitive to the external magnetic field. The magnetisation reversal is a thermally activated process, and so H_c will depend on the temperature and field rate, which makes it an ambiguous quantity. We will prefer to measure the effective anisotropy field H_k, which is the field necessary to force the magnetisation along its hard axis. This quantity is measured from Fig. 2.14b-c) and will be presented in detail in the next section.
Finally, it can be seen in Fig. 2.14 b) (or Fig. 2.15b) at 70 K that R_H drops, which is due to the unsaturated sample at zero field, itself due to the dipolar effect increasing with the magnetisation that favours fractured magnetic domains. It is also seen in 2.14a) at high temperature with the reversal of domains happening before the reversal of the magnetic field.

2.5.2 GdCo PMA dependence with stack

The fabrication of GdCo samples with OP magnetic anisotropy is the very first investigation we had to initiate because skyrmions can only be found in such thin films.

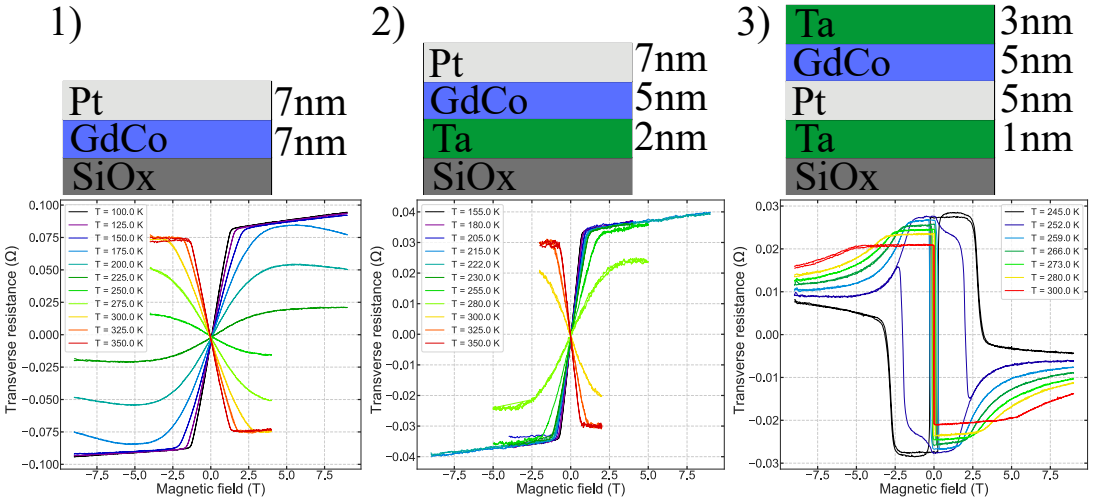

Figure 2.16: Stack optimisation. AHE hysteresis loops with field perpendicular to the plane for several temperatures for different thin film stacks. Gd composition is 27% for all samples.

Each interface contributes to the final properties of the film, but even the deposition order of the layers affects greatly the properties. We show in figure 2.161) that GdCo deposited directly on SiO_x substrate does not present PMA, with typical IP loops, even with a 7 nm Pt capping layer, which should favour an interfacial anisotropy by interacting with the Co [95]. When deposited on a Ta buffer 2), the sample still presents an IP anisotropy, with again a Pt interface that does not induce a strong enough PMA. In 1) and 2), even close to T_{mc}, the signal shows IP anisotropy, which rules out the effect of demagnetising field that could be the cause of the observed IP anisotropy at large magnetisation. Finally in 3) while keeping the same interface, but reversing the order of the stack, the sample finally presents PMA. This can be understood by the fact that in 3), the Pt is crystalline (fig. 2.3), which is necessary to favour interfacial anisotropy with the Co [226].

The proper growth of Pt is obtained by the Ta buffer layer below the Pt. Moreover, we saw in fig 2.4 that Pt deposited on top of the ferrimagnet presented a large inter-diffusion, which we might expect to be less pronounced for a ferrimagnet deposited on an already crystallised Pt layer [227, 276]. The stack 3) is close to the standard stack we will use all along this work. Our optimised stack was chosen to be composed of a 3 nm Ta buffer layer, 5 nm Pt layer, 5-8 nm GdCo and 5 nm Ta layer, with a 1nm Pt capping layer.

2.5.3 GdCo thickness dependant magnetic anisotropy

In order to stabilise skyrmions we need a precise control of the magnetic anisotropy K_u. We can measure the effective anisotropy field H_k that relates to the effective magnetic anisotropy $K_{\text{eff}} = \frac{M_s \mu_0 H_k}{2} = K_u - \frac{\mu_0 M_s^2}{2}$, with the second term being the contribution from the dipolar field. H_k is measured in hard-axis configuration 2.13 a-c) for PMA or IPA samples. K_u can then be computed by removing the demagnetising field contribution.

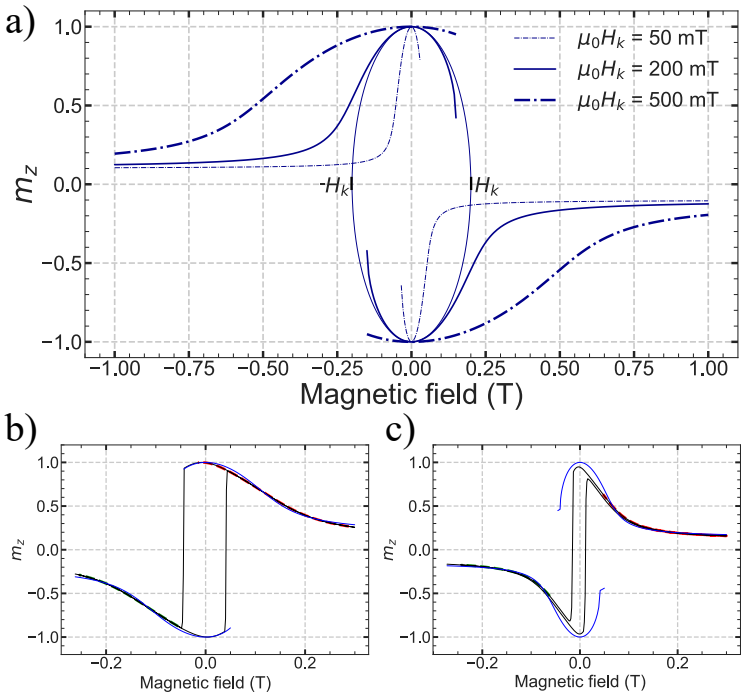

Figure 2.17: Effective anisotropy field determination. a) Model of [277] that describes the orientation of magnetisation in a magnetic field. Presented for several value of effective anisotropy field. Stoner-Wohlfarth ellipse drawn for $\mu_0 H_k$ = 200mT. b) Example of fit far from T_R. c) Example of fit close to T_R.

The AHE signal is normalised with the saturation magnetisation and can be directly reproduced by a macrospin energy minimisation in a Stoner-Wohlfarth model [228], or otherwise fitted by an analytical derivation obtained from the model of Wood et al. [277]. These solutions are constructed as branches. The effective anisotropy field can be directly seen at the crossing of the adjusted Stoner-Wohlfarth ellipse with the abscissa (for zero misalignment) that the model from Wood et al. indeed reproduces.

We present in Fig. 2.17 the model solutions for several anisotropy field and a fixed misalignment of 6°. Typical fittings obtained on a sample at two different temperatures are presented. Samples with a low effective magnetic anisotropy, for instance close to the spin reorientation temperature T_R where the magnetic anisotropy changes from PMA to IPA, present demagnetised states (fractured magnetic textures) at zero field. This makes measurements close to T_R quite complex because of the indeterminacy of

the saturation needed to normalise the signal. The normalising factor can be obtained in such scenario with data at higher or lower temperature, with remnant magnetisation at zero field. This allows a proper normalisation of demagnetised samples. This is the case in Fig. 2.17b)-c), where the measurement in b) is obtained at 290 K, far from T_R and c) at 350 K, close to T_R. Data presented in c) are then normalised using the saturated signal of b). Also, at high magnetic field, the two lattices can start to Spin-Flop, which results in a signal increasing instead of lowering. This means that in practice, the data should be fitted only on a high enough field to ensure saturated state, but low enough to prevent spin-flop. Close to T_{mc} the spin-flop is minimum which further limits the accessible field range (see Sec. 2.5.4.1).

PMA versus thickness We realised a thickness series of Ta(3)/Pt(5)/GdCo(t)/Ta(5) (nm) in order to investigate the nature of the anisotropy in these films. The main measurements are presented in Fig. 2.18.

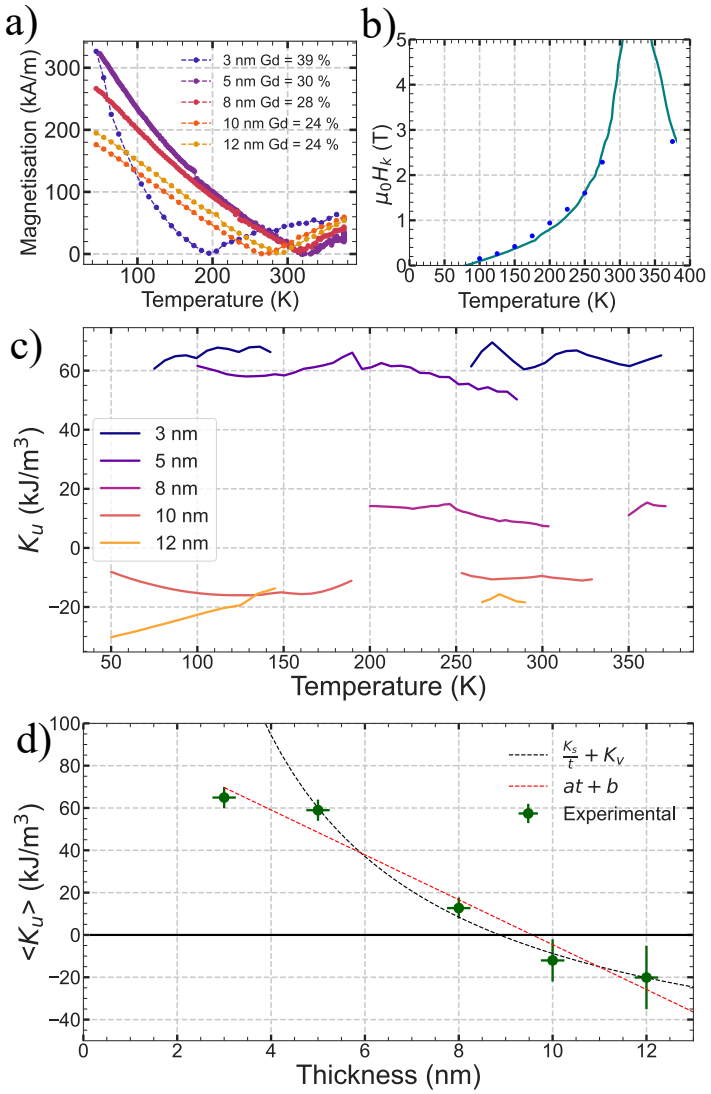

Figure 2.18: Magnetic anisotropy determination Pt/GdCo(t)/Ta series. a) Saturation magnetisation. b) Effective anisotropy field measured and fitted with $H_k = 2K_{\text{eff}}/(\mu_0 M_s)$ for $K_u = 60$ kJ/m^3 and magnetisation from a) at $t = 5$ nm. c) Magnetic anisotropy versus temperature for several GdCo thicknesses, from the interpolation of M_s and H_k given $K_u = \frac{\mu_0 M_s}{2}(H_k + M_s)$ d) Averaged K_u versus GdCo thickness. Inset shows the magnetisation curves of all samples with associated nominal composition.

We decided to increase the Gd composition in thinner films so they all present a T_{mc} around room temperature, as thinner films present a stronger reduction of the effective composition (sect. 2.1.4). This choice was made in order to see if it is possible to modify the magnetic anisotropy while preserving the same magnetisation and effective composition (and so obtain overall comparable magnetic properties). We can see in the inset of Fig. 2.18 that our strategy worked up to the 3 nm thickness, where we under-estimated the shift.
For each sample, the effective anisotropy field H_k is measured with temperature (an example is given in Fig. 2.18 b for a 5nm GdCo thickness) as well as its magnetisation (presented in Fig. 2.18 a). Both magnetisation and anisotropy field are interpolated to compute the magnetic anisotropy K_u with temperature in figure 2.18 c). K_u is observed to be rather constant with temperature for all samples except for the 12 nm one. The data close to T_{mc} are notoriously noisy in this situation, as any slight shift in temperature between the superposition of H_k and M_s will induce a very large deviation near T_{mc} as the two quantities diverge to opposite limits. We could not precisely determine K_u close to T_{mc} in most cases, but we do not believe this to be necessary for comparisons. In figure 2.18 d) is presented the magnetic anisotropy average for all different thicknesses. We can check the consistency of the obtained K_u by fitting H_k with $H_k = 2K_{\text{eff}}/(\mu_0 M_s)$ as shown in figure 2.18.

The dependence of K_u with GdCo thickness from Fig. 2.18 d) shows a decreasing K_u with increasing thickness, which is quite consistent with an interfacial contribution to the magnetic anisotropy, but a negative volumic term K_v is needed to fit these measurements. The fit of $K_u = \frac{K_s}{t} + K_v$ shown in Fig. 2.18 d) in black yields K_s =0.69mJ/m^2 and K_v = -77.5 kJ/m^3 (these parameters are reduced by almost half if the point at 3 nm is included in the fit; it was not included as it is clearly an outlier and its composition is very different from the other films).

The negative K_v can have different origins, a potential internal in-plane anisotropy, discussed for very thick samples in [22] (which would be quite surprising in these very thin films), or an additional contribution of the demagnetising field. Considering the internal structure of the GdCo layer, that presents composition gradients (see Fig. 2.4), it is quite reasonable to expect that our simple approximation of the dipolar field of a uniform film is limited. At the length scale of the magnetic layer, a composition gradient implies an always finite magnetisation inside the layer, which results in a demagnetising-field-induced shape anisotropy, even when the total M_s is zero (at T_{MC}). Indeed, SQUID measures the total moment, and so the deduced M_s corresponds to an averaged value. Evaluating precisely this effect would require a chemical analysis by EELS on TEM cross-sections, possibly for all samples, which we have not done. From the composition thickness profile, we would model the thickness profile of M_s and from that the dipolar energy, using the same approach as in [278].

The typical interfacial anisotropy found for Pt/Co interface is given around 1mJ/m^2 [279, 280]. Although GdCo is significantly different from the Co in those systems (e.g., it is amorphous), we do observe that our samples with 70% of Co present around 70% of the Pt/Co magnetic anisotropy. This suggests a major contribution of Pt/Co interfacial anisotropy. The composition is then expected to change slightly the anisotropy, as less Co at the interface means a reduced Pt/Co interfacial anisotropy. We can clearly see from the figure that the effect of composition is much weaker than the effect of magnetic layer thickness variation. This study should be followed by a second one with a series of samples with different GdCo thicknesses but equivalent composition.
Nonetheless, this study shows us that between 8 and 10 nm the anisotropy changes sign, where 10 and 12 nm thick samples presented an IP anisotropy on the whole temperature range. For practical purposes, we can use the linear law in red (shown in Fig. 2.18 d), that yields $K_u(t) = -10.6\ t \times \frac{kJ}{m^3}/nm + 101.5 \times 10^3 \frac{J}{m^3}$ for t in nanometers.

Comparing with results from [159] on multi-layers of GdCo of thickness ranging from 0.6 to 2.3 nm, the linear law we obtained would break at very small thickness, as they observed a linear law with a very different slope around -47 kJ/m^3/ nm of GdCo.
This study allows us to utilise the GdCo thickness to obtain the desired magnetic anisotropy. We can conclude that samples around 5 to 8 nm seem interesting as they possess a large enough anisotropy to ensure PMA on a rather large temperature range. Indeed, it was in this thickness range that we observed a reorientation temperature T_R, i.e., a transition from PMA to in-plane magnetisation. We could expect a different result for Tb films for example, because Tb possesses a large internal anisotropy [248] which could then rather display a bulk evolution, constant anisotropy with thickness despite its amorphous nature. Note that this expectation is not straightforward as seen in [197, 281, 282] where growth induced origin of the anisotropy is also observed as well as clear reduction of anisotropy with annealing.

2.5.4 Exchange coupling

The intensity of the exchange couplings is a key parameter to reproduce the ferrimagnet properties. There are two distinct exchange couplings to be measured, one is the antiferromagnetic coupling between Gd and Co, and the second is the exchange between Co and Co (Gd-Gd coupling is neglected). We will describe in this section how to measure these couplings.

2.5.4.1 Antiferromagnetic exchange coupling from spin-flop

We can deduce the exchange coupling between the Gd and Co lattice from the spin-flop field, by comparing the measured hysteresis loop with a double macrospin model. To do this model, we take as the energy of the system the Zeeman, anisotropy and antiferromagnetic coupling energies. Considering the sublattice magnetisations $\vec{\boldsymbol{M}}_i = M_i \vec{\boldsymbol{m}}_i$ (i=Gd or Co) and θ_{Co} and θ_{Gd} their polar angles (from the normal to the surface, $\vec{\boldsymbol{e}_z}$), with an applied field H (with θ_H its polar angle), and uniaxial anisotropies K_{Co} and K_{Gd} (perpendicular to the film) and an exchange coupling J^{ex}_{GdCo}, we obtain the following energy [283, 284, 285, 286]:

$$\begin{aligned} E(\theta_{Co}, \theta_{Gd}) = & - \mu_0 H M_{Co} \cos(\theta_{Co} - \theta_H) + K_{Co} \sin^2(\theta_{Co}) \\ & - \mu_0 H M_{Gd} \cos(\theta_{Gd} - \theta_H) + K_{Gd} \sin^2(\theta_{Gd}) \\ & + 2 J_{GdCo} \cos(\theta_{Co} - \theta_{Gd}) \end{aligned} \tag{2.11}$$

Figure 2.19 a-b) shows hysteresis loops obtained from this double-macrospin model. We obtain the equilibrium position of each lattice magnetisation by minimising the energy from 2.12 with respect to θ_{Co} and θ_{Gd}. At low field, the magnetisation of the dominating sublattice is fully along the easy axis and reverses normally with field, which gives square shape loops, with opposite magnetisation direction compared to the other lattice.
At higher magnetic field, the dominating lattice tilts, which lowers its amplitude, while the coupled lattice starts to tilt towards the magnetic field. It will reverse sign at some field to finally reach saturation along the applied magnetic field.
This is due to the competition between the antiferromagnetic exchange coupling and the Zeeman energy. Indeed, the antiferromagnetically coupled lattice is opposite to the applied field, and so a large Zeeman energy cost is associated to this configuration. One can understand here that the ratio between the magnetisations is going to drastically change the balance of the Zeeman energy. Once the Zeeman energy is large enough to equal the exchange energy, there is no net gain in energy for the system to stay perfectly anti-aligned, and so the spins tilt.

This is observed in the effective magnetisation that only increases during spin-flop (which could be seen in SQUID for instance). At very high field, both lattices will simply align with the field. Depending on the anisotropies of the two lattices, the misalignment angle may not be the same in the two lattices.

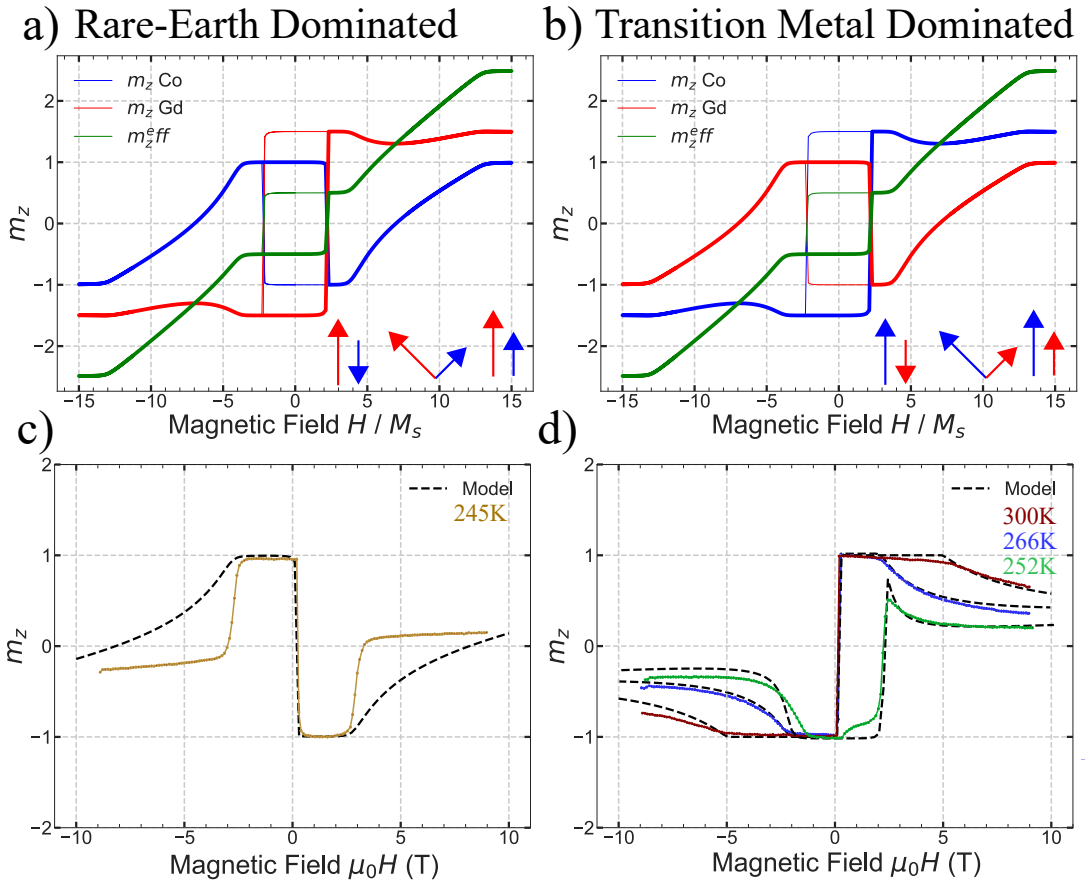

Figure 2.19: Spin-flop. a)-b) Gd (Co) sub-lattice dominating situation of spin-flop. Computed by two-coupled-macrospin model. Figure below are comparisons between experimental data and model with experimentally constrained parameters.

In figure 2.19 we fit our experimental data on AHE measurements obtained up to large magnetic field on a Ta(1)/Pt(5)$Gd_{0.27}Co_{0.73}$(5)/Ta(3) (nm) sample. One can see that the reversal changes sign when crossing the T_{mc} which is expected by our model. It fits poorly the Rare earth dominated case, but quite precisely the TM dominated ones. This can be due to the parameterisation of the model which is quite sensitive to the apportionment of the anisotropy between lattices. Furthermore, as it was shown that the anisotropy from the Gd 4f orbital is negligible [286] (and the contribution from the 5d much lower than from the Co 3d orbitals [247]) we observe a good fitting when applying all the magnetic anisotropy to the Co lattice.

The sample magnetisation is measured by SQUID and the magnetisations of the two lattices are deduced using the mean field model. This measurement also allows the determination of the T_{mc} around 250 K consistent with the measurements presented in Fig. 2.19c-d). Moreover, hard axis loops with magnetic field, measured by AHE, determined the anisotropy field of the film. Both parameters give us a good estimate of the sample properties and so values input in the model are well constrained.

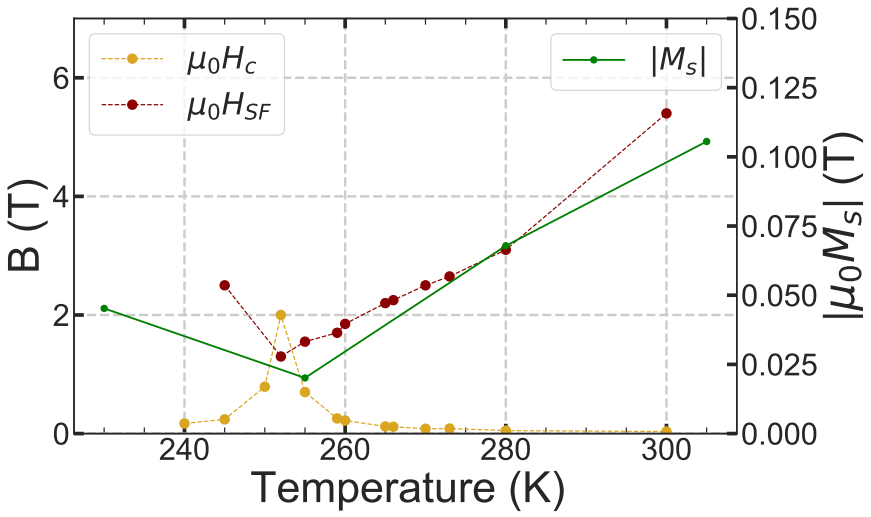

Figure 2.20: Spin-flop and effective anisotropy. Spin-flop field and coercive field versus temperature for Ta(1)/Pt(5)/$Gd_{0.27}Co_{0.73}$(5)/Ta(3) (nm).

It can be shown that, when neglecting the anisotropy, the spin-flop field takes a very simple form $2\mu_0 H_{sf} = \Lambda_{GdCo}(M_{Co} - M_{Gd})$ [287], and the saturation of the magnetisation takes place at $2\mu_0 H_{sf2} = \Lambda_{GdCo}(M_{Co} + M_{Gd})$. So one can expect that the spin-flop field varies with the magnetic properties of the sample, and indeed, one can observe in fig 2.19 that the spin-flop field is smallest when the coercive field is maximum, which coincides with T_{mc}. The previous development shows the spin-flop field to be zero at T_{mc} for zero anisotropy [287], and so the analysis of the spin-flop field can be related to the anisotropy of the system as well as to the antiferromagnetic exchange.

With the minimisation of our model energy, we can extract the volumic antiferromagnetic coupling of J^{vol}_{GdCo} = 14-15.5 MJ/m^3. This volumic energy density is converted to J^{ex}_{GdCo} by considering the average density of Co and its coordination number with Gd at the corresponding composition (that yields the same results for Gd average density and coordination with Co). Doing so, we obtain the exchange interaction energy $J^{ex}_{GdCo} \approx 1.9 \times 10^{-22}$ J. When considering the approximation that neglects the anisotropy, we can directly compute Λ_{GdCo} from the values of figure 2.20, with the ratio $H_{sf}/M_s \approx 55 - 60$, so $J^{ex}_{GdCo} = \frac{n_{Co} g_{Co} g_{Gd} \mu_0 \mu_B^2 \Lambda_{GdCo}}{2 z_{GdCo}} \approx 1.5$ - 1.8×10^{-22} J which is quite comparable with the value obtained by the fitting model.
There are some studies on the spin-flop transition in RETM in the literature. One on GdCo in [288] that focused on the transport properties in the spin-flop regime. Another study on GdFe [289] observed spin-flop near the magnetic compensation, and studied the competing anisotropy contributions on a wide range of Gd composition, which pointed to the complex internal structure of the magnetic layer with phase segregation. Then, the study on GdFeCo from [290] shows a very similar figure as the one presented in Fig. 2.20 and then focuses on the femtosecond laser excitation response of the system across the spin flop transition and shows a large increase of the decay time (to restore equilibrium) after the pump pulse close to the spin flop, for a sample studied above and below T_{mc}.

2.5.4.2 Brillouin light scattering experiments

Brillouin light scattering (BLS) allows a precise determination of many parameters of magnetic films, with the ones studied here being: H_k, J^{ex}, γ, α, and D_m. This technique consists in the study of thermal spin-waves (magnons) by the spectroscopy analysis of back-scattered polarised light (used to remove the contribution of phonons).

The sample is installed on heating or cooling sample holder that allows measurements at controlled temperatures. The incoming photon will generate or absorb a magnon that is observed in the spectrum as a lowered or increased energy of the back-scattered photon (Stokes or anti-Stokes peaks). Thus, by analysing the frequency of the Stokes and anti-Stokes peak the spin-wave frequency can be determined. In the Damon-Eshbach geometry, for a ferromagnet with in-plane magnetisation (or aligned in-plane by an external magnetic field), the frequency of the spin-wave is given by [228]:

$$\begin{aligned} f &= f_0 \pm f_{DMI} \\ &= \frac{\mu_0\gamma}{2\pi}\sqrt{[H + J^{ex}k_{sw}^2 + P(k_{sw}t)M_s][H + J^{ex}k_{sw}^2 - P(k_{sw}t)M_s - H_k]} \pm \frac{\gamma}{\pi M_s} D_m k_{sw} \end{aligned} \tag{2.12}$$

where $P(k_{sw}t) = 1 - \frac{1-\exp(-|k_{sw}|t)}{|k_{sw}|t}$ and $k_{sw} = 4\pi\frac{\sin(\theta_{inc})}{\lambda}$ is the spin-wave wave-vector.

Using eq 2.12, it can be seen that measuring the Stokes and anti-Stokes peak frequencies at various incidence angles and values of field, all previously stated parameters can be determined.

A more complete framework considering the two magnetic sub-lattices can also describe the antiferromagnetic coupling between the two lattices. This is accessible through the study of spin-wave modes present at high frequency, that only drop to accessible range of some 100s of GHz close enough to the T_{ac}. A careful study in [265] could access and describe these modes with a model of the ferrimagnetic system considering two coupled Landau-Lifshitz-Gilbert (LLG) equations and two magnetisation vector fields, corresponding to the RE and TM moments, following an approach used to analyse the ferromagnetic resonance. It was shown that such a complete model is necessary to fully describe the complex behaviour of spin-waves observed in ferrimagnets. The analysis of the antiferromagnetic modes allowed to compute the antiferromagnetic coupling of GdFeCo films which gave $J_{GdCo} = 20$ MJ/m^3 so $J^{ex}_{GdCo} = 2.7\text{e}^{-22}$J. This value is around 35% higher than the one obtained on GdCo thin films with the study of spin-flop.

We performed BLS measurements at 285 K on Ta(1)/Pt(5)$Gd_{0.32}Co_{0.68}$(5)/Ta(3) (nm), versus field and wave vector as presented in figure 2.21 a-b. We determined the material parameters, by the analysis of the measured spectrum following procedure explained in [265]. In this sample, with T_{mc} around 360 K and measurement at room temperature, the high frequency antiferromagnetic modes could not be measured (because too far away from T_{ac}). Because this sample is RE dominated at room temperature, we will name it the **RE dom. sample** from now on.
The measurement of the mean frequency of Stokes an anti-Stokes frequency versus wave vector (see Fig. 2.21 c) allows the determination of the exchange stiffness of the Co lattice (to which the spin-waves are expected to couple). It yields $A^{ex} = 4.6$ pJ/m which can be converted to $J^{ex}_{CoCo} \approx 8-10\ 10^{-22}J$ (for $S_{Co} = 0.75-0.84$) using a lattice parameter of 2.5 Å and c=1 (like for a simple cubic because for this composition of Co we find $z_{Co-Co} \approx 6$) .
The measurements of the exchange by Spin flop and BLS, are comforting our standard choices for the mean field for the Co-Co exchange coupling as well as for the correcting factor of Gd-Co exchange coupling.
Other parameter are determined at the same temperature: $\gamma/2\pi = 18.3$ GHz/T, $D_m = -0.22$ mJ/m^2 and $\alpha = 0.15$, with respective measurements presented Fig. 2.21 d-e-f).

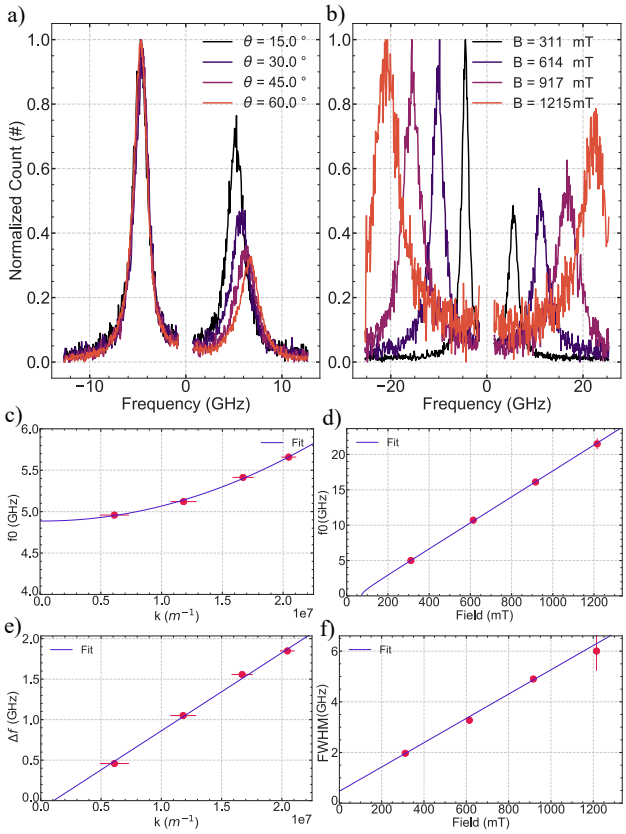

Figure 2.21: Brillouin Light Scattering measurement of Ta(1)/Pt(5)$Gd_{0.32}Co_{0.68}$(5)/Ta(3) (nm)thin film magnetic properties. a) BLS spectra, normalised to their maximum, for various light incidence angles (311 mT). b) Normalised BLS spectra for various fields (incidence angle of 30°). c) Stokes/anti-Stokes mean frequency versus wave vector, fitted to extract A^{ex}. d) Stokes/anti-Stokes mean frequency versus field, fitted to extract γ. e) Stokes/anti-Stokes frequency difference versus incident light wave vector, fitted to extract D_m. f) Full width at half maximum of the peak versus magnetic field, fitted to extract α.

Similar measurements, realised only at fixed wave vector were obtained on a sample composed of Ta(3)/Pt(5)$Gd_{0.3}Co_{0.7}$(5)/Ta(5)/Pt(1) (nm) at 355 K. This sample present a T_{mc} at 200 K. Because this sample is TM dominated at room temperature, we will name it the **TM dom. sample** from now on. It allowed us to extract $\gamma/2\pi = 40.8$ GHz/T, $\alpha = 0.175$ and with less precision than for the previous sample (because no wave vector dependence) $D_m = -0.14$ mJ/m^2). We also measured at fixed wave vector and magnetic field the mean Stokes and anti-Stokes frequency and peak width to extract α of γ vs with temperature, presented in Fig. 2.22.

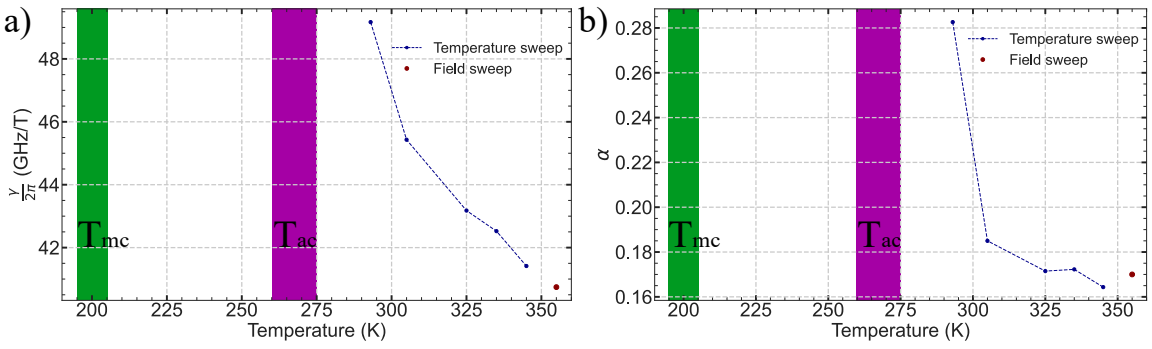

Figure 2.22: α and γ versus temperature in Ta(3)/Pt(5)$Gd_{0.3}Co_{0.7}$(5)/Ta(5)/Pt(1) (nm). a),b) Evolution of γ, α versus temperature, in blue extracted from a single measurement of average peak frequency, in red from fitting of field sweep. Green (purple) band shows $T_{mc}(T_{ac})$.

The measurements presented in Fig. 2.22 show the expected diverging α and γ close to T_{ac}. The T_{ac} is determined using Eq. 2.10 (see Sec. 2.6). The measurement procedure is not as precise as the one presented in Fig. 2.21 for all points in blue. Indeed, these points are obtained from a single BLS spectrum, and so we directly compute γ and α without fitting it over a field sweep. The points in red follow the same procedure as presented in Fig. 2.21, and it is very satisfying to see an overall good consistency with the measurements obtained with the less precise procedure. We used measurements of H_k obtained by AHE hard axis loops, and a parameter (of the anisotropy distribution) obtained from the field sweep to compute blue points.

2.5.5 Damping-like and field-Like torque measurements

The measurement technique described in this section aims to measure the effect of spin polarised current on a saturated magnetic state. As explained previously, there are two different possible orientations for the torque: Damping like (DL) or Field like (FL). The measurement of the torques is very important as it allows to quantify the conversion efficiency of current to spin current.

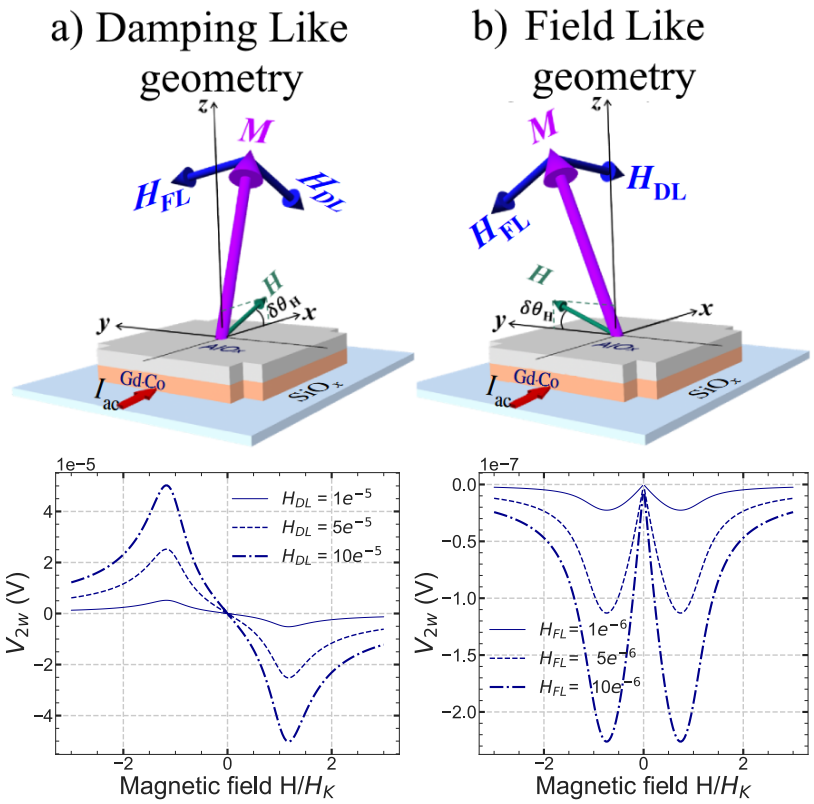

Figure 2.23: DL and FL SOT Torque. Schematic and calculated 2nd-harmonic signal in the DL a) and FL geometry b).

We need an expression that links the effect of these torques with the magnetisation of the saturated state described as a macrospin with two angles θ and φ.

The energy of the system is defined for a macrospin description as:

$$E = -K_{\text{eff}} \cos^2(\theta) - K_l \sin^2(\varphi) \sin^2(\theta) - \vec{\boldsymbol{M}}.\vec{\boldsymbol{H}} \tag{2.13}$$

Where K_l is the in-plane magnetic anisotropy and K_{eff} the effective out of plane anisotropy. In order to find the equilibrium position of the macrospin we minimise the energy with respect to θ and ϕ.

The expression is then used, as developed in [291], to isolate $\frac{\partial\theta}{\partial H}$ and $\frac{\partial\varphi}{\partial H}$. Several assumptions have to be made in order to simplified the obtained expressions. First we consider the in-plane anisotropy to be much smaller than the applied magnetic field, which ensure that only θ can be misaligned with the field direction. Then, we consider an applied magnetic field along $\vec{e_x}$ or $\vec{e_y}$. This gives the variation of θ and φ with magnetic field.

Now, neglecting the normal Hall effect, we consider the voltage $V_{xy} = \frac{R_{xy}}{I_{xx}}$ for a current I along $\vec{e}_x$ to be generated by Anomalous Hall Effect (AHE) R_{AHE} and Planar Hall Effect (PHE) R_{PHE}. Considering a small variation around the equilibrium position of the magnetisation $\theta = \theta_0 + \Delta\theta$ and $\varphi = \varphi + \Delta\varphi$ in the case of PMA samples excited by an oscillating current $I = \Delta I \sin(wt)$ the signal measured at the first harmonic ω or second harmonic 2ω can be separated as follows:

$$V_{xy} = V_{DC} + V_\omega \sin(\omega t) + V_{2\omega}\cos(2\omega t) \tag{2.14}$$

$$V_\omega = [\frac{1}{2}\Delta R_{AHE}\cos(\theta_0) + \frac{1}{2}R_{PHE}\sin^2(\theta_0)\sin(2\phi_0)]\Delta I \tag{2.15}$$

$$\begin{aligned} V_{2\omega} = {} & [-\frac{1}{2h}(\Delta R_{PHE}\cos(2\varphi_0)\mathrm{cosec}(\theta_h)\sin^2(\theta_0)(\Delta h_y\cos(\varphi_h) - \Delta h_x\sin(\varphi_h))) \\ & -\frac{1}{4(\cos(2\theta_0) + h\cos(\theta_0 - \theta_h))}(\Delta R_{AHE}\sin(\theta_0) - R_{PHE}\sin(2\theta_0)\sin(2\varphi_0)) \\ & (\Delta h_z\sin(\theta_0) - \cos(\theta_0)(\Delta h_x\cos(\varphi_h) + \Delta h_y\sin(\varphi_h))]\Delta I \end{aligned} \tag{2.16}$$

Where the expressions of the V_ω and $V_{2\omega}$ are normalised by the effective anisotropy field H_k so $h = \frac{H}{H_k}$.

These expressions can now be directly used for the two different experimental configurations, one for DL with $\varphi_h = 0$ or π and the other for FL with $\varphi_h = \pi/2$ or $3\pi/2$, with θ_0 that will change depending to the applied magnetic field from 0 to π. The effect of the DL torque is found in the Δh_x term, whereas the effect of the FL torque is found in the Δh_y term. The fitting procedure can then be explained as follows. First, by analysing the V_ω signal, we obtain the equilibrium position of the magnetisation along the field sweep. Indeed V_ω simply gives the same signal as the one obtained in DC measurements of the AHE in hard-axis configuration. The most critical step here is to correctly normalise the signal by ensuring that the sample is saturated at H = 0; otherwise, it is necessary to obtain a correct value of the saturated sample signal from another measurement, at a different temperature for example. Also, if the angle of the field is well known, we can obtain the signal value at H = 0 from the signal at high magnetic field because $V_{H_0}\cos(\theta_H) = V_{H_{max}}$ considering a large enough field H_{max} so the magnetisation is perfectly aligned with it. So from V_ω we obtain R_{AHE}, H_k and so the equilibrium magnetisation angle θ_0 at any given field.
Then, by plugging these values into the equation for $V_2\omega$ we can fit the effective field corresponding effect of the spin polarised current. For example for the DL measurement geometry (field applied along the current), we obtain:

$$V_\omega = [\frac{1}{2}\Delta R_{AHE}\cos(\theta_0)]\Delta I \tag{2.17}$$

$$\begin{aligned} V_{2\omega} = {} & [-\frac{(\Delta R_{PHE}\Delta h_y)\rfloor\wr\int\rceil\rfloor(\theta_h)\sin^2(\theta_0)}{2h} \\ & -\frac{(\Delta R_{AHE}\Delta h_x)\sin(\theta_0)(\Delta h_z\sin(\theta_0) - \cos(\theta_0))}{4(\cos(2\theta_0) + h\cos(\theta_0 - \theta_h))}]\Delta I \end{aligned} \tag{2.18}$$

We see from this expression that the scaling factor for each torque is associated with R_{PHE} for the FL one and with R_{AHE} for the DL one. Also, we see that in DL geometry, the signal is sensitive to the FL field (and conversely if in FL geometry). This means that for consistency, we usually fit the data with both FL and DL, and then compare it with only DL in order to assess correctly the contribution of both fields that can sometimes be mixed by the fitting algorithms. By following the same approach for measurements in FL geometry, the FL and DL fields can be disentangled. At last, we obtain the value for $\Delta h_x = H_{DL}/H_k$ and for $\Delta h_y = H_{FL}/H_k$, that are used to obtain the Spin Hall effect (SHE) conversion efficiency θ_{SHE} from the DL field and the Rashba parameter and current polarisation $\alpha_R P$ from the FL field. Using expressions from eqs. 1.35 and 1.36, which assume the DL and FL torques to be respectively only due to the SHE and Rashba effects, we can explore the efficiency of the torques in our samples. We did not explore FL geometries much, and the few data points taken pointed towards a small contribution, and therefore this torque is not discussed further.
We present results from DL geometry in fig 2.24. The signal at 2ω measured for two temperatures of two sample is presented with the extracted θ_{SHE}.

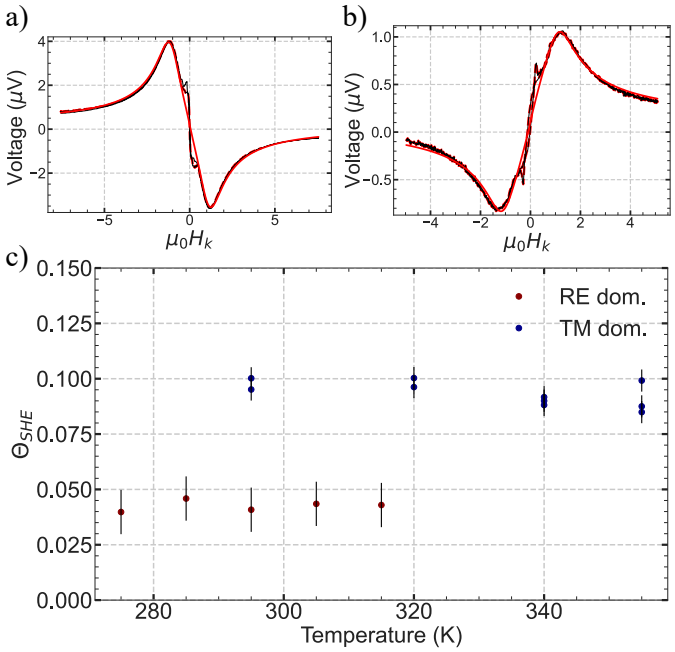

Figure 2.24: Harmonic Hall voltage measurements in GdCo. a) Example of second harmonic signal in RE dom. sample at 285K (black) and fit with only DL torque (red). b) Example of second harmonic signal in MT dom. sample at 355K (black) and fit with only DL torque (red). c) θ_{SHE} vs temperature obtained for both samples.

We focus on the effect of the DL torque in our samples as it is observed to be the major contribution. We realised torque measurements in several GdCo thin film samples to study the variation of the θ_{SHE} with temperature. There are several limitations to these measurements. First, close to T_{mc} the signal is usually not clear because of issues to drive the magnetisation in plane with the external magnetic field. Indeed, once the magnetisation is in-plane due to the external field, the DL torque can slightly drive the magnetisation out of the plane which is then measured with the synchronous detection of the lock-in amplifier at twice the exciting frequency and yield the characteristic peak of this signal that is indeed observe to lay close to H = H_k. Also, close to the the spin reorientation T_R, the measurement is quite tedious because of the usually non-saturated state at H=0, a state that is also favoured by the applied in-plane field.

Special care has to be made to ensure proper measurements, for instance, it becomes very important to keep some out of plane component of the applied magnetic field to favour the saturation of the sample. Also, it appears that close to T_R the Slonczweski-Berger coefficient (a_j, b_j see [291] section C) describing the effect of the torque vary from their usual values which could imply a temperature dependant efficiency of the Torque in our system. The analysis of these measurements can therefore be quite complex. For instance, we do not have a strong confidence in the measurements of the RE. dom. sample because of clear evidences of non-saturated state from the signal at the first harmonic. We have stronger confidence on the measurements of the TM dom. sample. These measurement show us a clear increase of the θ_{SHE} between the two samples, with the average around 0.04 for the RE dom. and 0.09 for the TM dom. sample. The exact explanation for this large difference is not obvious to us. The main reason is to be found in the difference between both sample structures. Because the RE dom. is only capped by 3 nm of Ta, we can expect the Pt to be the only source of SOT, whereas for the TM dom. sample, there is a 5 nm Ta capping, itself protected by 1 nm of Pt. But on the other hand the TM dom. sample has a 8 nm thick GdCo layer compared to 5 nm for the other one which is expected to reduce the θ_{SHE}.
Indeed, it is important to note that we do not have access to the "real" θ_{SHE} with this technique, because we compute it from its effect on the magnetisation of the sample, the θ_{SHE} obtained is an effective one. Nonetheless, it appears that the 5 nm Ta capping indeed increase largely the SOT, and we can only speculate on the effect of the 1 nm Pt layer supplementary to the passivation of the Ta. The effect of interface on the SOT is very subtle (see for instance [292]) and driving much interest lately, therefore we can hope that future experiments will allow us to better interpret these results.

2.5.6 RETM self-torque and DMI

We realised a comparative study of the torques and DMI published in [201] between GdFeCo samples capped with heavy metal (Pt) or light one (Al). The Al capped sample of interest is: $SiO_x/Gd_{0.35}(Fe_{0.85}Co_{0.15})_{0.65}(t)/Al0_x(5)$ whereas the stack of the control sample of Pt is $SiO_x/Gd_{0.35}(Fe_{0.85}Co_{0.15})(5)/Pt(7)$ (nm) with the same composition. In this study, a sample of $SiO_x/GdFeCo(5)/Al0_x(5)$ is measured by photo-emission electron microscopy combined with X-ray magnetic circular dichroism (X-PEEM), and electron energy-loss spectroscopy (EELS) of cross section of the sample combined obtained with a scanning transmission electron microscope (STEM). Cross sections of the control sample have also been observed by STEM and characterised by EELS. These two measurements are presented in section 2.4.

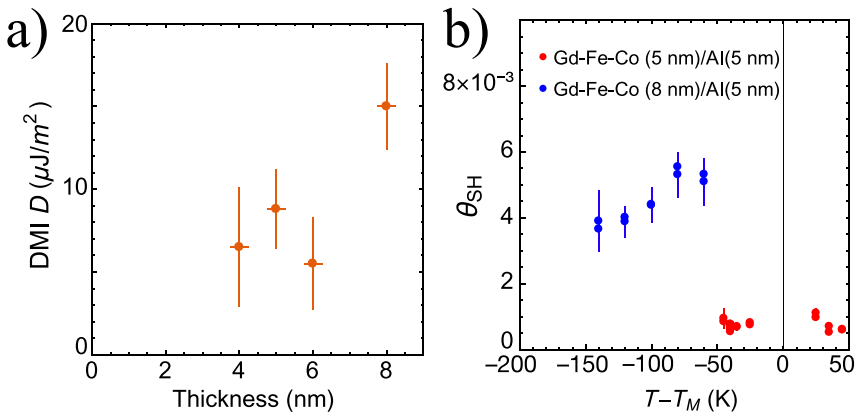

Figure 2.25: Self-torque and DMI in $SiO_x/Gd(FeCo(t)/Al0_x$. a) DMI from BLS. b) Extracted Θ_{SHE} from torque measurements for t = 5 and 8 nm.

The 5nm Al capped sample and others with different thicknesses are also measured by BLS and Harmonic Torque measurements with D_m and θ_{SHE} values obtained shown in Fig 2.25 a-b). BLS measurements realised on the control sample yield a $D_s = 0.163$ pJ/m which can be compared with $D_s = 1.72$ pJ/m measured in simple Pt/Co interface [228]. This control GdFeCo sample possesses 9.75% of Co which points towards a DMI due to the Co/Pt interface as it scales with the Co content ($1.72 \times 0.0975 = 0.167$). As precisely explained in [201], the results obtained in this study could be at first glance surprising because we observe typical effects of heavy metal adjacent layer in a sample without such adjacent layer. First of all, XMCD PEEM measurement resolved a Néel profile of the DW, which is only possible in thin magnetic film when a sizeable chiral interaction is at play. This is indeed the case as showed in Fig. 2.25a) where a DMI around $9\mu J/m^2$ is measured by BLS, and confirmed for several other thicknesses. This DMI value is above the computed D_{th} which explains this observation of Néel DW. Also, the evolution in thickness of the DMI is observed to be rather constant, possibly increasing at 8 nm, which rules out an interfacial origin of the DMI and points towards an effect of the magnetic layer itself. The measurements of DL torque in second harmonic torque measurement, presented in Fig. 2.25b) shows small but clearly measured spin conversion inside of the ferrimagnetic layer, around 0.45% for the 8 nm sample and 0.1% for the 5 nm one. The TEM cuts and EELS chemical analysis revealed an inhomogeneous composition across the GdFeCo thickness which is determinant to obtain a breaking of the inversion symmetry necessary to explain the observed DMI or torque inside of the layer. This might also be the reason for the higher DMI and Θ_{SHE} on the 8 nm sample (for which we do not have TEM cuts), as we can speculate that the larger the thickness, the stronger the thickness inhomogeneities and so the stronger DMI and self-torque. This is indeed the trend observed for thicker samples of the same material in [293] that also observed a bulk origin of DMI (with interfacial DMI symmetry) without heavy metal adjacent layer and attributed it to the composition gradient along the thickness direction. It should be noted that the self DMI and torque are relatively small compared to the effect from a Pt interface for instance. As we showed previously, we can expect for a 5 nm GdCo $D_m \approx 220\ \mu J/m^2$ (so 25 times the one measured for the 5 nm Al capped sample here) and $\theta_{SHE} \approx 4\%$, so 40 times the one measured for self-torque here. Nonetheless, this effect is certainly very sensitive to the exact internal structure of the layer and should therefore be understood precisely to either cancelling or enhancing it.

2.6 Samples parameters used for skyrmion studies

Several measurements made on multiple samples have been presented along the previous sections. We want to focus now on the measurements obtained one the **RE dom. sample**: Ta(1)/Pt(5)/$Gd_{0.32}Co_{0.68}$(5)/Ta(3) (nm) and on the **TM dom. sample**: Ta(3)/Pt(5)/$Gd_{0.3}Co_{0.7}$(8)/Ta(5)/Pt(1) (nm). They are studied in details for skyrmion statics in Chap. 3 and skyrmion dynamics in Chap. 4. For clarity, we present in Tab. 2.2 all parameters of interest for these two samples only.

Sample	T_{mc} (K)	T_{ac} (K)	K_u ($\frac{kJ}{m^3}$)	D_m ($\frac{mJ}{m^2}$)	D_s ($\frac{pJ}{m}$)	A^{ex} ($\frac{pJ}{m}$)	θ_{SHE}	α	$\frac{\gamma}{2\pi}$ ($\frac{GHz}{T}$)
RE dom.	360	416	11.5	-0.22	-1.1	4.6	0.04	0.015	18.3
TM dom.	200	260	11	-0.14	-1.1	.	0.09	0.0175	40.8

Table 2.2: Magnetic parameters of RE and TM dominated samples. Note that the damping α and the gyromagnetic ratio γ are given for T=285 K for the RE dom. sample and T=355 K for the TM dom. sample.

Let us make some initial comparisons between the two samples. The RE dom. sample has a 32% Gd nominal composition, with a T_{mc} around 360 K. It is RE dominated at room-temperature as indicated by its name. The TM dom. sample has a 30% Gd nominal composition, with a T_{mc} around 200 K, TM dominated at room temperature. We can already note a larger difference in T_{mc} of 160 K than expected for the small nominal composition difference (2%) which we expect to produce a difference of T_{mc} of 60 to 80 K. This may be attributed to the large sensitivity to the capping and GdCo thickness for the real composition of a sample. We can presume a composition difference around 5% when considering the T_{mc} difference of the two samples. In order to infer on the location of T_{ac} of each sample, we computed it using their respective mean field fitting. This yields $T_{ac} = 416$ K for the RE dom. sample and $T_{ac} = 260$ K for the TM dom. one. Using expression from Eq. 2.10 we obtained $T_{ac} = 414$ K and $T_{ac} = 275$ K respectively, which comforts our expectations.
The anisotropy constant K_u for both sample is obtained using their respective M_s and H_k, measured by SQUID magnetometry and hard-axis AHE hysteresis loops(see Fig. 3.1 c-d,i-j). We find similar $K_u = 11.5$ kJ/m^3 values for both samples which is surprising considering the thickness difference. It is known that annealing GdCo samples lowers K_s and that thermal history also impacts magnetic anisotropy, that can superimpose on the T_{mc} drift towards low temperature over time due to Gd oxidation [220, 237, 231, 233, 294, 240]. This combination might explain the rather low K_u of the RE dom. sample that has been submitted to much more measurements at rather high temperatures (around 350 K) with extensive studies spread over a long period of time.

We measured DMI constants in BLS (see Fig. 2.21): $D_m = -0.22$ mJ/m^2 on the RE dom. sample and $D_m =$ - 0.14 mJ/m^2 the TM dom. sample. When renormalized by the thickness, because $D_m(8nm).t(8\times10^{-9}) \simeq D_m(5nm)/5\times10^{-9}$ one can consider that both samples are described with the same $D_s \approx D_m.t$, with $D_s = -1.18$ pJ/m which we consider as a standard values for our films with Pt/GdCo/Ta interfaces for later discussion on sample optimisation in Sec. 5.3.
We measured θ_{SHE} by second harmonic hall measurements that yields $\theta_{SHE} = 0.04$ and $\theta_{SHE} = 0.09$ for the RE and TM dom. samples respectively.

Measurements of DMI and θ_{SHE} are rather consistent with literature on GdCo, as seen in [295], where the authors found on Pt(5)/$Gd_{0.23-0.27}Co_{0.77-0.73}$(5)/Ta(3)/Pt(2) $D_m \approx 0.32$ mJ/m^2, $\theta_{SHE} \approx 0.07$ and $K_u \approx 10 - 20$ kJ/m^3. Considering the RE dom. sample with potentially oxidised Ta, and the active 5 nm compared to 3 nm Ta in the TM dom. sample, their value of θ_{SHE} is very consistent with our own observations.
The exchange was measured in BLS as well in the RE dom. sample $A^{ex} = 4.6$ pJ/m
The exchange stiffness $A^{ex} = 4.6$ pJ/m is in agreement with values reported in [296, 294]. The value of γ is much lower than the value of pure Co [297], as expected from Wangsness formula. We expect the measured effective α to be larger than the α of the Co sublattice, which is indeed the case [298].
All parameters but α and γ (measured at T=285 K and T=355 K for RE and TM dom. samples respectively) vary with temperature. All other parameters are considered to remain relatively constant over a large temperature range. We could verify this for θ_{SHE} (see Fig. 2.24c) and for K_u (see Fig.2.18). We could not find reliable experimental data concerning the evolution in temperature of A^{ex} and D_m. Therefore we made the rough simplification of considering A^{ex} and D_m constant with temperature to avoid to input a bias in our results that we can not properly justify. We are aware of tentative experiments from literature [88, 299, 259] and performed preliminary BLS measurements temperature sweep (not shown) without being able to assert that both are constant far from T_C.

Chapter 3

Magnetic Skyrmions Statics

The stability of skyrmions in GdCo ferrimagnetic thin films is described in this chapter. Section 3.1 is focused on the evolution in temperature of parameters relevant to skyrmions stability in ferrimagnets and in our GdCo thin films (section 3.1.2). Using an analytical model of skyrmion statics, we explore the magnetic field and temperature phase diagram of skyrmions in ferrimagnetic films (section 3.2). Experimental phase diagrams of GdCo thin films are then presented in section 3.3 and compared with the analytical model and micromagnetic simulations. They all show a clear qualitative agreement and, an arguable quantitative one. We also present experimental measurements of skyrmion radius, and its variation with magnetic field and temperature in section 3.4.3. Finally, we compare our results with the literature in section 3.23.

3.1 Thermal evolution of skyrmion stability parameters

3.1.1 Definition of useful parameters

Micromagnetic parameters

Considering a thin film of thickness t smaller than λ_{ex} to ensure homogeneous magnetisation along z, both ideal, cylindrical shaped, magnetic bubbles and skyrmions can be described as a 360° domain wall (DW) [160]. The size of the skyrmions, but also that of magnetic domains in general is found in the balance between dipolar interactions, that favours small fractured domains (reducing emitted stray field) and exchange and anisotropy that favour collinear uniform magnetic domains. This is encapsulated in the energy of a magnetic domain wall σ previously discussed (See Eq. 1.15). Let us remind $\sigma = \sigma_0 - \pi D_m$ with D_m the DMI constant, $\sigma_0 = 4\sqrt{A^{ex} K_{\text{eff}}}$, where $K_{\text{eff}} = K_u - K_d = K_u - \frac{\mu_0 M_s^2}{2}$. This expression shows that both magnetic anisotropy and exchange increase the DW energy, whereas the shape anisotropy due to dipolar effects reduces it. Also, the DMI interaction that favours non-collinear magnetic textures is found to reduce the DW energy cost. One can expect that very large DW energy cost favours large uniform texture whereas low DW energy cost favours fractured magnetic textures. The characteristic length scale of magnetic textures is imposed by the DW width parameter Δ (Eq. 1.14). Other important parameters to describe skyrmion stability are the quality factor $Q = \frac{2K_u}{\mu_0 M_s^2}$ (Eq. 1.23), the dipolar length $l_c = \frac{\sigma}{\mu_0 M_s^2}$ [17] and the critical DMI $D_c = \frac{\sigma_0}{\pi}$. The quality factor represents the ratio between the magnetic anisotropy and the shape anisotropy, the dipolar length the ratio between the DW energy and the dipolar effects, and the critical DMI the balance between the simple DW energy and DMI. Q and l_c have been used to describe the stability of magnetic bubble [17, 19, 300], which can be adapted to skyrmions by including the effect of DMI [137].

Néel to Bloch profile transition: threshold DMI D_{th}

In thin magnetic films, the dipolar interaction favours Bloch DWs while interfacial DMI favours chiral Néel DWs (see Sec. 1.2.6). This is a continuous transition as a function of D_m, leading to a limit value D_{th} at which the azimuthal angle $\psi = 0$ and the DW is purely Néel. This has been strikingly presented in [301] where a wedge Ta capping on CoFeB shows a reversal of the chirality of DW depending on its oxidation state, that is also demonstrated to be controlled with gate voltage pulses. One can find an expression (Eq. 3.1) for D_{th} in [101] (or an equivalent approximation for thin films in [86])

$$D_{th} = \frac{2\ln(2)t}{\pi^2}\mu_0 M_s^2 \tag{3.1}$$

For typical parameters in our films (M_s = 0-200 kA/m, K_u = 5 to 20 kJ/m^3, A^{ex} = 4-5 pJ/m and t = 5-8 nm), it yields D_{th} = 0-0.05 mJ/m^2. D_{th} value is quite small and so Néel configuration should be satisfied with typical D_m values in our film of 0.14-0.25 mJ/m^2. We can be rather confident that our films with a sizeable DMI favour Néel profile. Indeed, we could observe experimentally by photoemission electron microscopy combined with x-ray magnetic circular dichroism (XMCD PEEM) a Néel DW profile in similar ferrimagnetic films without any SOC layer, i.e., only due to intrinsic DMI of the ferrimagnetic sample [201].

It was shown in [302] that Eq. 3.1 (determined for DW and so valid for large skyrmions compared to Δ) underestimates D_{th} in the case of small skyrmions (compared to Δ) by a factor of ≈ 3. As we will see later, our skyrmions are in the large skyrmion limit, but we can see that, even for small skyrmions, D_{th} is largely surpassed in almost all conditions, and so there is no reason to consider skyrmion profiles other than pure Néel. Only in the case of thicker samples (8 nm) and the highest magnetisation (200 kA/m), may the smallest skyrmion profile start to deviate from pure Néel. This shows that the transition towards hybrid skyrmions may be engineered in ferrimagnetic samples for skyrmions with sizes comparable to the domain wall width.

3.1.2 Skyrmion stability parameters in GdCo films

The varying magnetisation with temperature of GdCo entails an evolution of many parameters of interest which needs to be taken into account. In order to shed some light on their evolution, we compute Δ, Q, D_c, l_c and other parameters for the two GdCo samples with 32% (RE dom.) and 30% Gd (TM dom.) described in section 2.6. All quantities are computed with experimentally determined values of exchange, DMI, magnetic anisotropy and magnetisation (see Fig. 3.1 and Tab. 2.2).

The saturation magnetisation M_s and effective anisotropy field H_k are presented in Figure 3.1 c-i) and d-j) versus temperature for the two samples in which skyrmions were stabilised and studied in the following chapters. As described in section 2.3.6, for a known T_{mc} and sample composition, the mean field theory can be used to extrapolate the magnetisation profile with temperature. These samples present T_{mc} far above or below room temperature, chosen so their magnetostatic properties allow to obtain stable skyrmions at experimentally convenient temperatures.

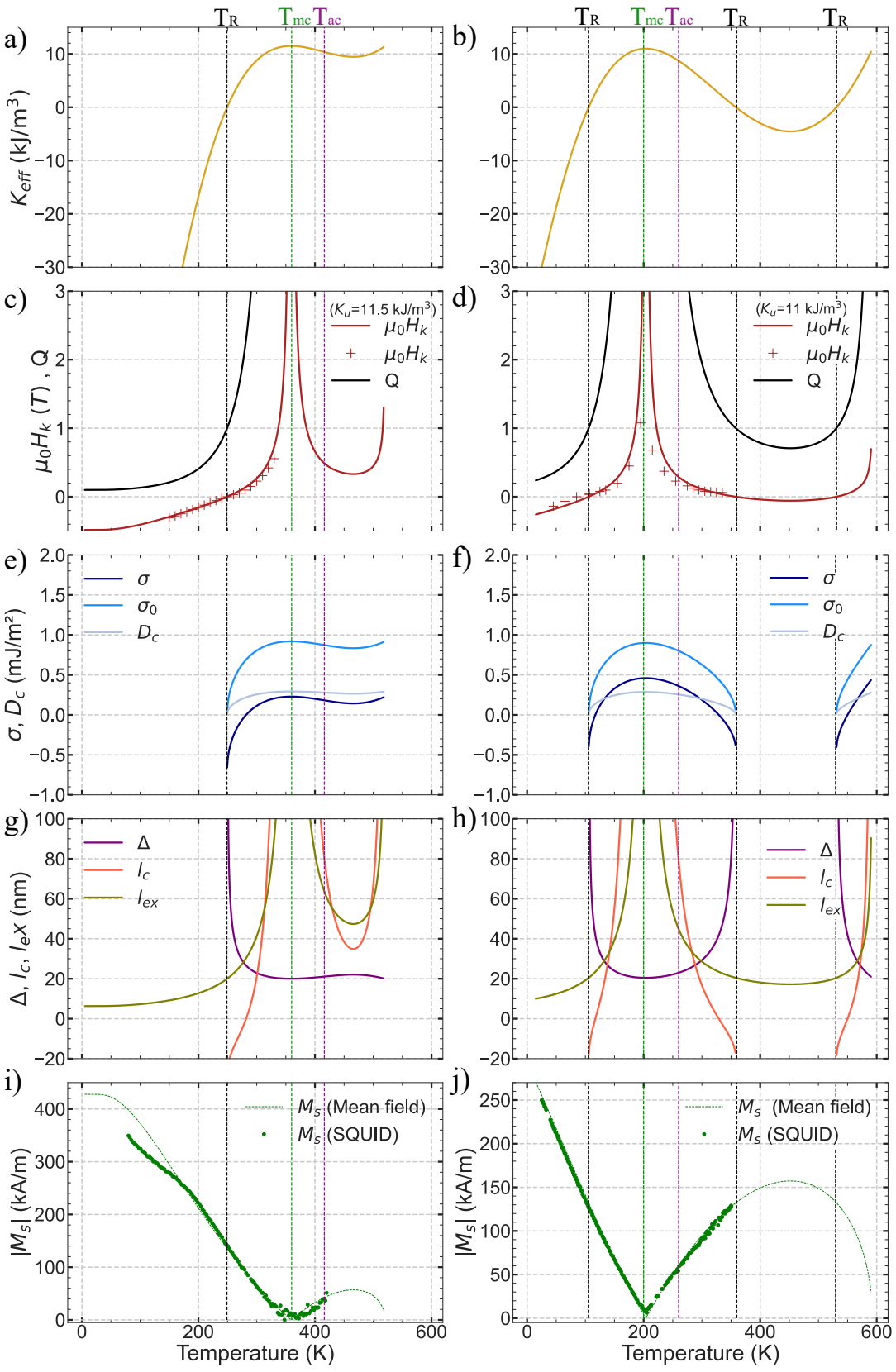

Figure 3.1: Evolution of characteristic parameters with temperature. a-c-e-g-i) Ta(1)/Pt(5)/$Gd_{0.32}Co_{0.68}$(5)/Ta(3) (nm) later referred as RE dominated sample. b-d-f-h-j) Ta(3)/Pt(5)/$Gd_{0.3}Co_{0.7}$(8)/Ta(5)/Pt(1) (nm) later referred as TM dominated sample. Presented parameters are from top to bottom: K_{eff}, H_k and Q, σ_0 and σ and D_c, Δ and l_c and l_{ex}, M_s.

RE dom. sample

Let us first comment on the magnetisation behaviour of the RE dominated sample at 300 K (Fig. 3.1 i). Its T_{mc} is 360 K and the Curie temperature T_c is between 500 and 550 K from mean-field extrapolation. This implies a rather low magnetisation between T_{mc} and T_c in this sample. Below compensation, the magnetisation increases rapidly when lowering temperature and reaches around 400 kA/m at lowest temperature. The SQUID measurement exhibits an inflection point, attributed to the in-plane demagnetising energy $K_d = \mu_0 M_s^2/2$ overcoming the Zeeman energy (due to the applied field of 200 mT) and the perpendicular anisotropy. At the inflection we can directly see that $\mu_0 H_k \approx -200$ mT.

This sample undergoes a spin reorientation at $T_R = 250$ K. T_R describes the temperature at which the effective anisotropy changes from perpendicular to in-plane. It can be seen in Fig. 3.1a) where $K_{\text{eff}} = 0$. It is also observed in Fig. 3.1c) where $H_k = 0$. The red line in this figure is obtained by fitting the measured H_k with $H_k = \frac{2K_{eff}}{\mu_0 M_s}$ with $K_u = 11.5$ kJ/m^3. One can see on the same graph that Q equals 1 at T_R, and that both Q and H_K diverge at T_{mc}.

In Fig. 3.1e), the simple domain wall energy σ_0 is estimated to be zero at T_R. The domain wall energy $\sigma = \sigma_0 - \pi D_m$ is even negative at T_R due to the contribution of DMI. Then σ reaches zero at a certain temperature T_{Dc} (when $D_m = D_c = \frac{4\sqrt{A^{ex} K_{\text{eff}}}}{\pi}$) before T_R. T_{Dc} is around 280 K here. This is quite interesting because between T_{Dc} and T_R the domain wall cost is negative but there is still non-zero PMA. In this region, one would expect stripes to stabilise when no external magnetic field is applied [144, 15].

Finally, in figure 3.1g), the divergence of the DW width parameter Δ is observed at T_R. This divergence can be understood by the fact that the DW width is obtained by the competition of the exchange interaction that favours a gradual reversal (to reduce adjacent spin non-collinearity) whereas all spins misaligned with the magnetic anisotropy have an increased energy cost that can be reduced with an abrupt reversal. Therefore, for vanishing magnetic anisotropy at T_R the reversal of the DW is favoured to extend spatially to satisfy the exchange energy. The exact divergence might be softened in real materials due to internal demagnetising effects of the DW, because of the approximation made for the demagnetising anisotropy that breaks for DW width much larger than the magnetic film thickness [100]. Also one can see on the same figure the lowering of l_c close to T_R up to $l_c \simeq t$ around 280 K. This implies that long range dipolar effect should no longer be neglected as the DW and dipolar energies become comparable. We can also see that l_{ex} is greater than the sample thickness in all the sample PMA region.

From these graphs, one can consider that for a given $K_u(t)$, D_s and A^{ex} the thickness has to be tuned as well as the GdCo composition in order to obtain a combination of magnetisation and anisotropy that yields a low effective anisotropy where the effects of the DMI and dipolar field become large enough to favour low DW energy and so skyrmions.

TM dom. sample

The parameters of the second sample (Figure 3.1, right column) follow the same trends as those of the first, but with the added complexity arising from the different location of the magnetic compensation ($T_{mc} = 200$ K) that duplicates regions of reorientation. It implies a lower content of Gd than previously, and so higher T_c, around 600 K.

A steeper increase of magnetisation is therefore observed after T_{mc} (Fig. 3.1j). The magnetisation increases enough below and above T_{mc} to induce the crossing of T_R (Fig. 3.1b-d). A triple crossing of T_R is observed in this sample, one below T_{mc} around 100 K and two above T_{mc}, around 350 and 530 K. This triple crossing of T_R imprints in all the parameters that behave as described for the first sample. One can see three crossing of σ with zero (Fig. 3.1f) as well as three temperatures of divergence of Δ (Fig. 3.1h). Finally, the divergence of H_k, Q, l_c or l_{ex} at high temperature is due to the lowering of the magnetisation close to T_c, although the model used has not been verified at these high temperatures and reserves have to be made (see 3.1).

3.2 Skyrmion energy model for ferrimagnets

Using the energy model described in this section, we can predict that both GdCo films should host skyrmions, around 280 K for the RE dominated one and around 100 and 350 K for the TM dominated one. We follow the model presented by A. Bernand-Mantel in [148]. Another model, developed by Büttner [147], uses a more elaborated model for the long range dipolar field. The two models differ in the choice of analytical developments. In [148] specific approximations are made that we also followed to obtain analytical formulations of all energies at play. In [147] a different approach is used that relies on interpolations of all energy terms by analytical functions, where physical meaning is blurred, but that allows for a very efficient exploration of the phase diagram with little error on each term. In this section we first present the minimal model to account for skyrmion profile, we present solutions of profile valid for large and small skyrmions, and then complete the energy model to obtain an analytical formulation of the skyrmions energy compared to the saturated state. The different solutions of the model are discussed and it is finally applied with our sample parameters.

3.2.1 Skyrmion energy and profile

Using the micromagnetic energies described in section 1.2, the energy of the skyrmion are computed once defining its profile. We can then determine if it is stable and in the affirmative, its corresponding equilibrium size, depending on the micromagnetic parameters. The effect of magnetic field is also considered and so (H,T) phase diagram computed with parameters relevant to our samples are drawn. We also explore the different contribution of each energy terms to pinpoint to the key ingredients of skyrmion stabilisation

Minimal theoretical model

Considering a radially-symmetric skyrmion with, at first, only exchange, anisotropy and DMI energies, the total energy is given by:

$$E[\theta(r)] = 2\pi t \int_0^\infty \left[A^{ex} \left[\left(\frac{\partial \theta}{\partial r} \right)^2 + \frac{\sin^2 \theta}{r^2} \right] + K_u \sin^2 \theta - D_m \left(\frac{\partial \theta}{\partial r} + \frac{\cos\theta \sin\theta}{r} \right) \right] r dr \quad (3.2)$$

where the magnetisation profile is described with the cylindrical coordinates defined in section 1.3 (and Fig. 1.7). The first term accounts for the exchange energy E_{Ex}, the second term for the uniaxial magnetic anisotropy E_{Anis}, and the third for the DMI energy E_{DMI}, all three described using the expressions given in section 1.2. Both the exchange and DMI energies present a term in $1/r^2$ and in $1/r$ (respectively) that account for the effect of curvature. These terms are important for textures with very small radius [163], and will add a contribution to the energy of the simple DW also for large skyrmions [144].

There is no general solution for this energy functional, and the magnetisation profile $\theta(r)$ that minimises it is not analytical. We can compare the energy of different profiles, for instance with the saturated state found for $\theta(r) = 0$. A variational approach [143] consists in finding the equation satisfied by θ such that an infinitesimal variation yields the same energy (so an extremum), i.e., $\Delta E = E(\theta + \epsilon) - E(\theta) = 0$. This yields the following Euler-Lagrange equation:

$$A^{ex}\left(\frac{d^2\theta}{dr^2} + \frac{1}{r}\frac{d\theta}{dr} - \frac{\sin(2\theta)}{2r^2}\right) + D\frac{\sin^2(\theta)}{r} - K_u\frac{\sin(2\theta)}{2} = 0 \tag{3.3}$$

From Eq. 3.3, one can consider boundary condition, for example $\theta(r = 0) = \pi$ and $\theta(r = \infty) = 0$, with $\frac{\partial\theta}{\partial r}(r = 0)$ chosen to correspond to the sign of the DMI [144]. The shooting method can then be used to find a profile $\theta(r)$ that minimises Eq. 3.2 [148, 144, 303]. This procedure leads to a profile that can be well approximated by a DW profile, from which the 360° DW model for the skyrmion finds its roots [155, 302, 144, 160]. The skyrmion profile is expressed as:

$$\theta(r) = 2\arctan\left(e^{\frac{(R-r)}{\Delta}}\right) = 2\arctan\left(\frac{\sinh(R/\Delta)}{\sinh(r/\Delta)}\right) \tag{3.4}$$

As described in section 1.5, a different ansatz for the skyrmion profile could have been chosen. In order to obtain analytical solutions of the magnetic energies, we next focus on two limiting cases: large skyrmions (R>> Δ) and small skyrmions (R<< Δ).

3.2.1.1 Large skyrmion limit

As demonstrated in [144], using a conventional variational approach from Equation 3.3, the energy of large skyrmions is obtained. In the large skyrmion approximation, Equation 3.3 coincides with the 1D DW model equation, with a supplementary term arising from the curvature of the skyrmion border. This supplementary term is obtained through the approximation that the profile shows a large variation of θ only around r$\simeq R$. The skyrmion energy (Eq. 3.5) is then simply the sum of the energy of the 1D DW model with the supplementary curvature term.

$$E_s = 2\pi Rt\sigma + \frac{4\pi A^{ex} t\Delta}{R} \tag{3.5}$$

The result can be separated in two ranges. For $D_m < D_c$, the solution is either uniform, a domain wall, or a metastable skyrmion solution of the saturated state. With no magnetic field, the skyrmion radius R is then:

$$R = \frac{\Delta}{\sqrt{2(1 - D_m/D_c)}} \tag{3.6}$$

For $D_m > D_c$ the solution is a cycloid state with a periodicity of $\xi = 2A^{ex}/D_m$, in which skyrmions are metastable solutions exisiting only when a magnetic field is applied against their core to stabilise them out of the stripe phase. The profile for large skyrmions has been verified numerically to coincide very well with the DW profile (Eq. 3.4), which confirms the pertinence of the ansatz.

A complete study on the skyrmion radius compared with micromagnetic simulations can be found in [149]. It yields the following formula and gives better results than Eq. 3.6 at small radius and also a better behaviour at large A^{ex}.

$$R = \Delta\frac{D_m/D_c}{\sqrt{1 - (\frac{D_m}{D_c})^2}} \tag{3.7}$$

3.2.1.2 Small skyrmion limit

Considering small skyrmions, i.e., R<< Δ, all terms but the exchange converge to zero, and the curvature term in E_{Ex} becomes sizeable, which yields the following equation:

$$E = 2\pi t \int_0^\infty \left[A^{ex} \left(\frac{\partial \theta}{\partial r} \right)^2 + \frac{\sin^2(\theta)}{r^2} \right] r dr \tag{3.8}$$

Using again a variational approach with θ deviated by ϵ, one can find ΔE that must be 0 whatever ϵ:

$$\Delta E = -4\pi A^{ex} \int_0^\infty \epsilon \Big[\frac{\partial \theta}{\partial r} + r \frac{\partial^2 \theta}{\partial r^2} \Big] dr \quad \text{then} \quad \frac{\partial^2 \theta}{\partial r^2} = -\frac{1}{r} \frac{\partial \theta}{\partial r} \tag{3.9}$$

From Eq. 3.9, one can recognise the equation found by Belavin and Poliakov [163] that yields a limit energy due to the exchange curvature term for cylindrical texture with radius $R \to 0$ found to be $E_0^{ex} = 8\pi A^{ex} t$. With this small skyrmion limit, Equation 3.9 gives a simple analytical solution for the skyrmion profile [163]:

$$\theta(r) = 2 \arctan \left(\frac{R}{r} \right) \tag{3.10}$$

The analysis made in [161] (see also its supplementary material) proposes another ansatz for the skyrmion profile which interpolates very well between the Belavin and Poliakov soliton profile and the large skyrmion profile of the 360° DW profile defined by Eq. 3.4.

3.2.1.3 General solution

Using analytical expressions of the energies known to hold for the small and large skyrmion limits, we can then define an interpolation between them. This can be done using an expression for the curvature energy that satisfies both limits [1]:

$$E_{curve}(R) = \frac{8\pi A^{ex} t}{\frac{2R}{\Delta} + 1} \tag{3.11}$$

$$E_{curve}(R \to 0) = 8\pi A^{ex} t \tag{3.12}$$

$$E_{curve}(R \gg \Delta) = \frac{4\pi A^{ex} t \Delta}{R} \tag{3.13}$$

Then, considering the local effect of the dipolar field, we replace K_u by $K_{eff} = K_u - K_d$ where $K_d = \frac{\mu_0 M_s^2}{2}$ is the usual approximation of the local effects of the dipolar field [99, 100, 101]. Also, in order to take into account the long range effect of the dipolar field, we use the same analytical approximation as in [148, 72] that considers:

$$E_{dem}^{\text{long range}} = -\mu_0 M_s^2 I(d) 2\pi R t^2 \tag{3.14}$$

with $I(d) = \frac{-2}{3\pi}[d^2 + (1-d^2)E(u^2)/u - K(u^2)/u$, $d = 2R/t$, $u^2 = d^2/(1+d^2)$, and $K(u)$ and $E(u)$ the complete elliptic integrals of the first and second kind. As described in [148], this formula is a very good approximation of the surface demagnetising energy for skyrmion radius large compared to the domain wall width parameter. For $R \sim \Delta$ it leads to an overestimation of the dipolar energy which is quantified in [148]. This is not a problem for this work, as in our experiments $R >> \Delta$.

[1] The derivative of this expression is not satisfactory for $R \to 0$ when compared with numerical integration, and so over-estimates the energy barrier of small skyrmions. A better suited expression for the exchange curvature energy of small skyrmions can be found for instance in [302].

Finally, considering the Zeeman term, the complete energy of the skyrmion is:

$$\begin{aligned} E_s = & \quad E_{Ex} + E_{Anis} + E_{DMI} + E_{Dip} + E_{Zee} \\ = & \quad \frac{8\pi A^{ex} t}{\frac{2R}{\Delta}+1} + 2\sqrt{A^{ex}K_{\text{eff}}}2\pi Rt + 2\sqrt{A^{ex}K_{\text{eff}}}2\pi Rt \\ - & \quad \pi D_m 2\pi Rt - \mu_0 M_s^2 I(d) 2\pi R t^2 + 2\mu_0 M_s H \pi R^2 t \\ = & \quad E_{curve} + \sigma 2\pi Rt + E_{Dip} + E_{Zee} \end{aligned} \tag{3.15}$$

Using this expression, we can explore the energy of the skyrmion versus its radius and search for local minima that are associated to the skyrmion equilibrium radius. The only specificity of ferrimagnets is found in the definition of effective parameters, such as M_s (see Eq. 2.2) that considers the resulting magnetisation of both sub-lattices. Indeed, because we will only explore the low field range, the spin-flop can be ruled out and an infinite antiferromagnetic coupling can be considered, therefore the system is precisely described by the effective parameters.

3.2.2 Energy versus radius

Let us present the different contributions of each term depending on the skyrmion radius, with the only non-vanishing energy at $R = 0$ for the exchange energy that converges towards E_0^{ex}. In Figure 3.2 we compute the previously described terms using the measured values of the RE dominated sample at 290 K (Table 2.2). In figure 3.2 a), we observe that the exchange, anisotropy and Zeeman terms increase the energy of skyrmions whereas the DMI and long range dipolar terms lower it. One can also observe that the Zeeman and long range dipolar energy only have noticeable effects compared to other energies for large enough skyrmion between 10 to 100 nm.

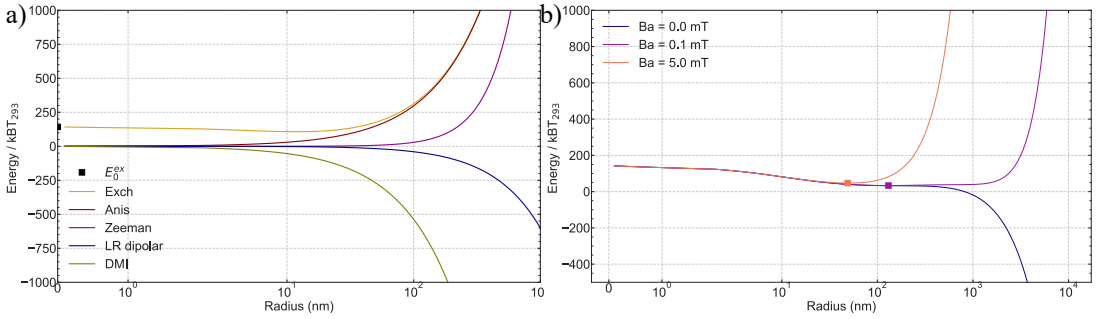

Figure 3.2: All energies contributions and typical solution for skyrmion theoretical model. a) All different energies with skyrmion radius considered for parameters of RE dom. sample, M_s = 75 kA/m and B_a = 5mT. b) Three typical solutions for $D_m > D_c$ obtained for different applied magnetic field.

Skyrmion annihilation energy

The difference between the energy at $R = 0$ and $R = R_{eq}$ defines the energy E_a needed to collapse a skyrmion following a path of isocompression of the skyrmion diameter. This energy can then be compared to k_BT in order to define a threshold criteria for stability, that can be for example $E_a > 50k_B300$K that ensure a 10 years stability considering a standard Arhenius law [147, 177, 304]. We will compare the energies with room temperature that is preferably defined at 20° C, so at 293 K. From now on, k_BT will refer to k_BT at 293K. Other annihilation paths can be found [107] and the skyrmion can disappear by other means than collapsing, due to instabilities of its shape, for example. This was also discussed in the case of magnetic bubbles that can present the same type of elliptic instabilities [19]. In this case the skyrmion will be transformed into stripes, but the present model does not account for this mechanism.

Typical model solutions

Let us explore the model solutions at different fields always for parameters computed using Tab. 2.2. One can see in Figure 3.2 b) that three typical solution curves (E vs radius) can be found. The first one (5 mT in the figure) shows a rather well defined equilibrium radius around 70 nm. A second one can be found at very low magnetic field (0.1 mT), with an equilibrium radius around 200 nm. This solution presents a very shallow energy minimum, which makes the equilibrium radius badly defined.

Finally, the third case occurs when no magnetic field is applied, and no equilibrium radius is found, due to the negative DW energy (with the considered parameters). Note that a solution at very small radius is always found if we consider only the exchange and anisotropy energy. This solution appears typically below 10 nm, but presents a low stability with thermal fluctuations (around $10k_BT$ with our set of parameters). We will see this in more detail in Sec. 3.2.4.1, but we can already state that increasing DMI pushes this solution towards larger radius (with larger stability), whereas the long range dipolar field creates a second solution of larger radius.

Two equilibrium radius solution

Skyrmions can present two equilibrium radius solutions, as described by A. Bernand-Mantel [148] and others [147]. These two solutions arise from the two mechanisms of skyrmion stabilisation. One is driven by the DMI and the second by the long-range dipolar field [302].

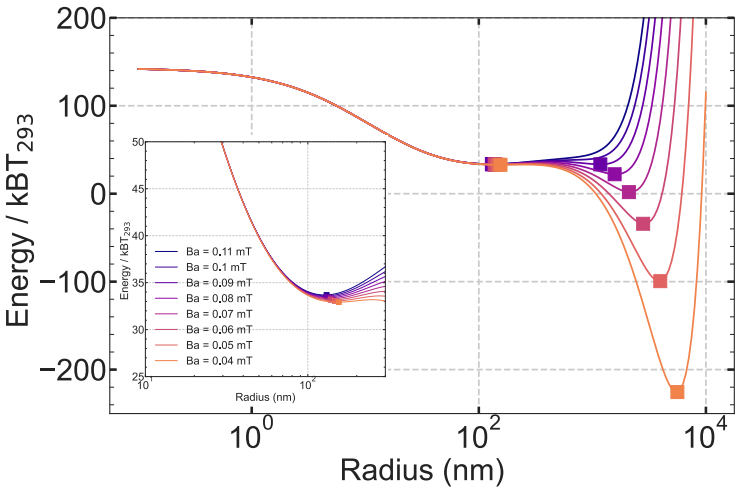

Figure 3.3: Two skyrmion equilibrium radius solutions slightly above T_{Dc}. The energies are computed for various magnetic field at a temperature of 292 K that correspond to a magnetisation of 75 kA/m with all other parameters from RE dom. sample. The inset shows a zoomed region around the small radius solution.

We compute the skyrmion energy at T= 292 K in Figure 3.3 with parameters from the RE dom. sample found in table 2.2. The temperature is chosen slightly above T_{Dc}, when $D_m \lesssim D_c$. As it will be clearly seen in the phase diagrams 3.7 and 3.5, the double solutions appear for T slightly above T_{Dc}, when $D_m < D_c$. One can see in Figure 3.3 that two equilibrium radius are found on a small range of magnetic field in the conditions described before. One solution appears at a radius around 200 nm and the other at few μm. The solutions found for highest radius may convert into stripes before being reached in a real material. It is also important to note that the magnetic field has a much larger effect on large skyrmions and so on the equilibrium solutions at larger radius. This is striking where a small magnetic field change affects strongly the large radius solution compared to the negligible effect on the solution at small radius.

One can see that the energy profile is very shallow around 0.1 mT, where a slightly higher magnetic field will collapse the large radius solution to the small one. Once again, skyrmions with large radius are found to be more stable than the small ones.

3.2.3 Compact and stray field skyrmions

General discussion

One solution is always found at small radius below few 100s of nm, stabilised mostly by the DMI, and can be referred to as compact skyrmion [147]. The second solution can be found at larger radius up to few μm, but can also be compressed with a magnetic field to a radius comparable to the first solution. This solution is stabilised by long-range dipolar effects and so is denoted as bubble skyrmions (or stray-field skyrmions). The two types of skyrmions are often distinguished [155] with the parameter $\kappa = \frac{D_m}{D_c} = \frac{\pi D_m}{\sigma_0}$ which can be related to the skyrmion profile. For $\kappa \to 1$ the profile is bubble-like, whereas it is compact, arrow-like, for $\kappa \to 1$, as seen in Figure 1.19. However, as explained in section 1.5, the correspondence of κ with profile is not so straightforward and has been shown to be abusive [147]. This further shows the difficulty to distinguish these two solutions other than by a precise comparison of the magnetic energies at play. As proposed by [148], the distinction can be better obtained by defining the skyrmionic factor that weights the contribution of the dipolar energy with the total energy.

In the rest of the manuscript, we will not distinguish these two kinds of solutions, as both present the same topology and therefore share the same general properties. It is still noteworthy to realise that both solutions exist, because they showcase the two mechanisms at play in skyrmion stabilisation [302]. More importantly, this analysis is useful because the region of coexistence is related to the very shallow radius energy landscape. In a shallow energy profile, small anisotropy inhomogeneities present in a real sample induce various local minima for the radius, and thus the coexistence of skyrmions very different sizes. Indeed, in the observations of the RE dom. sample around this specific region, skyrmions with sizes ranging from sub 300 nm to μm were observed. A precise analysis on the evolution of size distribution with magnetic field and temperature in this region would have been interesting to be able to confirm the origin of the observed large skyrmion size distribution.

Large skyrmions at T_R and small skyrmions at T_{mc}

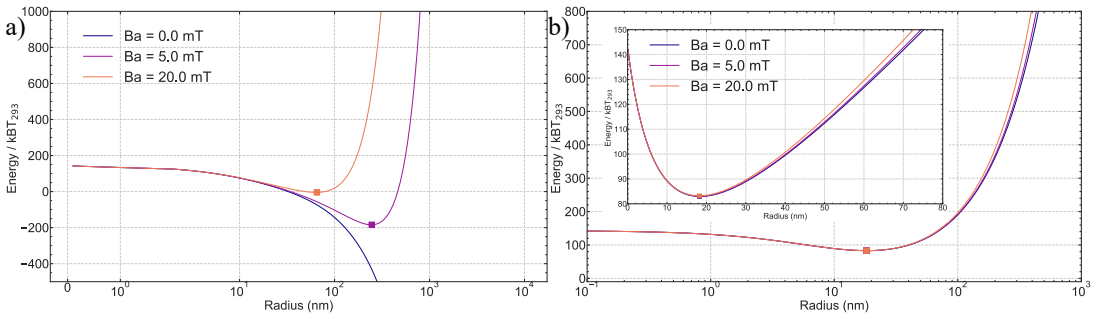

Figure 3.4: Skyrmion large radius solution close to T_R and small radius solution close to T_{mc}, calculated using the parameters of the RE dom. sample (Table 2.2), with magnetisation corresponding to temperatures of interest. a) Energy computed for 270 K ($M_s = 130$ kA/m), close to T_R. b) Energy computed for 355 K ($M_s = 5$ kA/m), close to T_{mc}. The inset shows a zoom of the same plot without the logarithmic scale.

Solutions of this model are also presented in the two limiting cases, close to T_R and close to T_{mc}, in Fig. 3.4. With a temperature close to T_R (Fig. 3.4a), the solutions are found at higher radius than previously, for the same magnetic field, with also a much higher stability ($> 200k_BT$). The equilibrium radius solution is also found to reduce with increasing magnetic field. With a temperature close to T_{mc} (Fig. 3.4b), the solutions are found for smaller radius, below 5 nm, where the effect of the magnetic field, even though still reducing the radius, is much less pronounced. Also, these skyrmions present a much lower stability. These typical solutions allow us to draw general considerations. Stable skyrmions should be observed with large radius close to T_R when applying magnetic field. On the other hand, much smaller skyrmions, quite insensitive to magnetic field and with lower stability (around $55k_BT$) should be observed close to T_{mc}. It should be noted that skyrmion solution close to T_{mc} even though comparable in size with the "artificial" solution found when considering only exchange and anisotropy are themselves "real" solutions as the stability they present is still rather large.

3.2.4 GdCo theoretical phase diagram (H,T)

3.2.4.1 RE dom. sample

Figure 3.5 shows the phase diagram in temperature and magnetic field for the RE dom. sample (obtained with parameters in Tab. 2.2 and considering the $M_S(T)$ shown in Fig. 3.1 i).

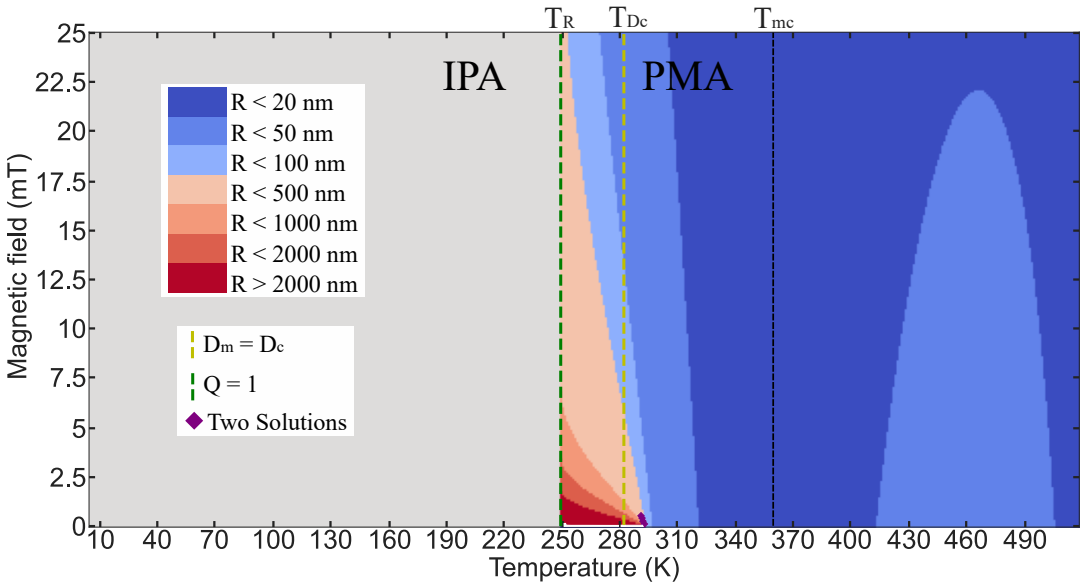

Figure 3.5: RE dominated sample theoretical phase diagram. Temperature and magnetic field phase diagram computed for parameters of RE dom. sample, with magnetisation following its experimentally measured magnetisation. Local minimum of the energy profile are computed for each pair of magnetic field and magnetisation and coloured accordingly to the equilibrium radius found. D_m=D_c corresponds to T_{Dc}, Q=1 corresponds to T_R, and T_{mc}=360 K.

We observe in figure 3.5 large skyrmions close to T_R and small ones close to T_{mc}. The skyrmion equilibrium radius diverges close to T_R, and lowers with increasing magnetic field, with a dependence that is not easy to observe for very small skyrmions found at low M_s, i.e., close to T_{mc}. We do see that the solution vanishes below $Q = 1$, where we could expect with more elaborated model that allows for continuous transition from PMA to IPA, some solutions at large enough magnetic field even for $Q < 1$, as it was usually discussed in the case of magnetic bubbles [19, 305].

These results are completely consistent with the DW model of magnetic bubbles adapted with DMI of the previous section (Sec. 3.1.2), where the simple analysis of the DW energy indeed pointed towards stable skyrmions between T_R and T_{Dc}. The present model is nonetheless much richer in physical insights as it yields the radius and stability of skyrmions and their evolution with magnetic field and temperature.

The model can therefore be used to better explore the roles of each interaction. For example, one could be quite surprised to see large skyrmions stable even for $D_m < D_c$. This can be understood better by computing the same phase diagram, and by switching off either the long range dipolar or the DMI contribution as presented in Figure 3.6.

DMI and dipolar field contributions

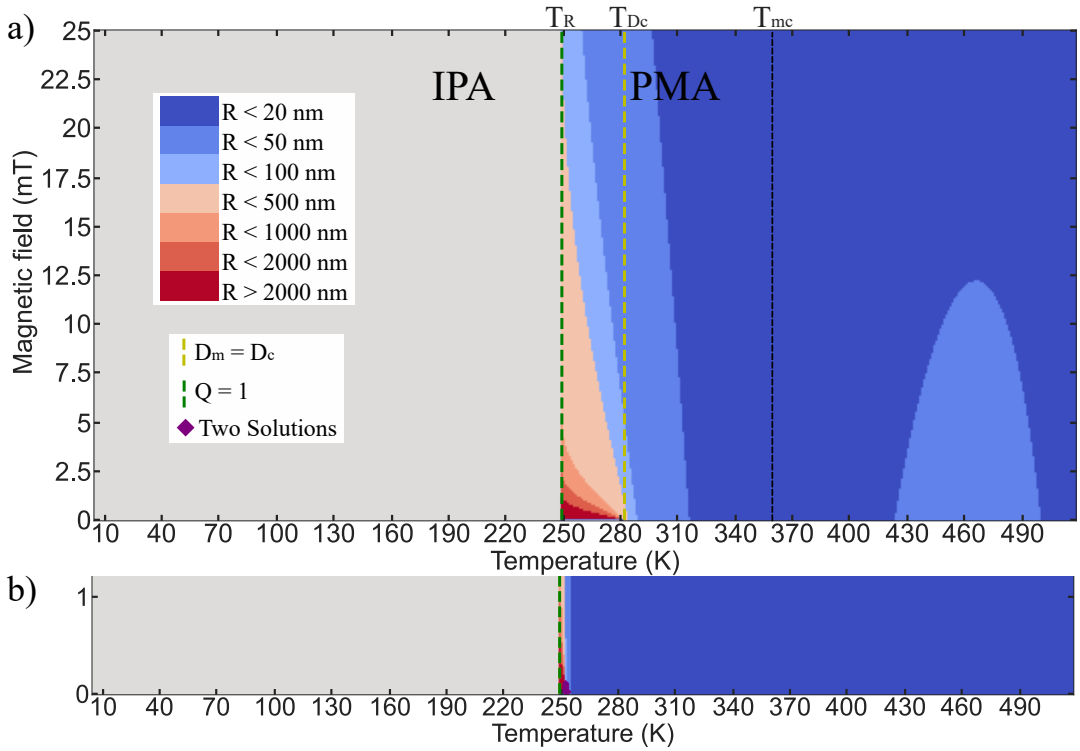

Figure 3.6: Effects of DMI and long range dipolar field on skyrmion phase diagram. The phase diagrams are computed with the parameters of RE dom. sample. a) The long range dipolar field term is removed. b) The DMI term is removed.

Figure 3.6a) shows the phase diagram computed with the same parameters than Fig. 3.5, but by removing the long range dipolar term. We observe that skyrmions radius steep growth only begins at temperatures for which $D_m > D_c$, with the radius that diverges at B_a=0. In Figure 3.6 b), we zoomed in on the low range field phase diagram, computed with the same parameters, but without the effect of DMI this time. We observe that large skyrmions can be found, but only much closer to T_R.

This phase diagram is quite comparable with the one expected in the physics of magnetic bubbles [19] as it is composed of the exact same interactions, because we removed the DMI. Both of these phase diagrams are quite interesting to point to the joint effect of DMI and long range dipolar field that allows for the stabilisation of large skyrmions in low enough magnetic anisotropy systems.

Indeed, we can now understand that in Figure 3.5, skyrmions could stabilise for $D_m < D_c$ because of the effect of long range dipolar field, that opens a new region where skyrmions are stable even at zero magnetic which is not possible when $D_m > D_c$ because of a negative DW energy that favours stripes textures. This region coincides with the the first large increase in temperature of skyrmion radius (R > 500 nm). This is also where the energy profile can be very shallow and present two local equilibrium solutions. This also explains why such double solution if found in the region slightly above D_c, because both the contribution of DMI and long range dipolar field contribute comparably in this already reduced anisotropy environment and can then draw a peculiar energy profile with radius in which both solutions are found.

3.2.4.2 TM dom. sample

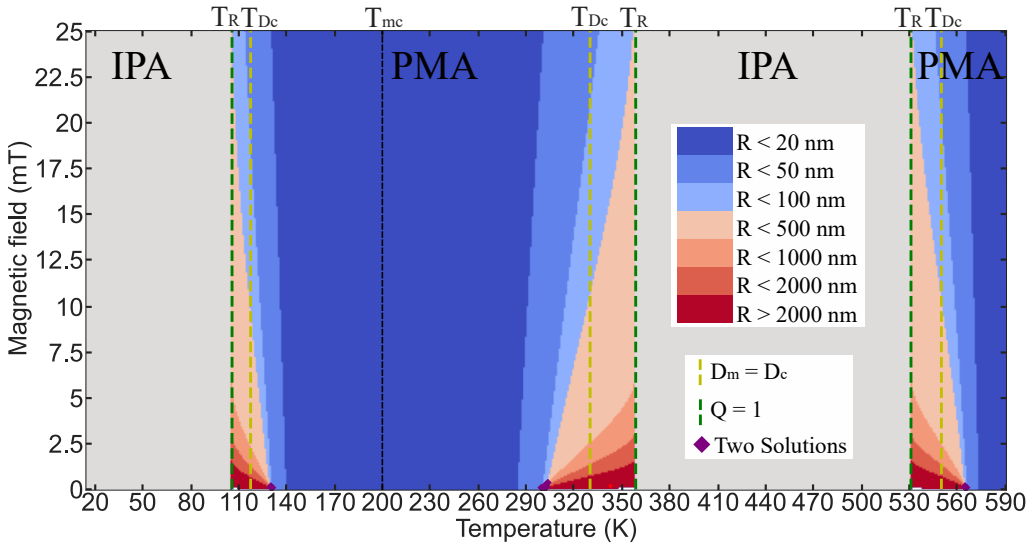

Figure 3.7: TM dominated sample theoretical phase diagram. Temperature and magnetic field phase diagram computed for parameters of TM dom. sample, with magnetisation following its experimentally measured magnetisation. Local minimum of the energy profile are computed for each pair of magnetic field and magnetisation and coloured accordingly to the equilibrium radius found. D_m=D_c corresponds to T_{Dc}, Q=1 corresponds to T_R, and T_{mc}=200 K.

In Figure 3.7 we compute the phase diagram of the TM dom. sample, with parameters of table 2.2 and the same $A^{ex} = 4.6$ pJ/m as the RE dom. sample. In Figure 3.7, the same behaviour as the one described for the RE dom sample is observed. Due to the existence of three T_R, the phase diagram presents three regions with rapidly growing skyrmions radius with temperature. We can see that the region were skyrmions are growing is larger above T_{mc} than below, which we simply attribute to a steeper magnetisation variation at low temperature compared to the one at higher temperature. This is quite interesting to notice, because the magnetisation of ferrimagnets, even though varying rapidly on the whole temperature range, is quite flat around the magnetisation maximum above T_{mc}. This region, with a lower dependence of the magnetisation with temperature, would be quite suitable for applications as the lower dependence would mitigate the effects of slight temperature variations. The magnetic anisotropy of the sample should then be chosen precisely to satisfy the stabilisation of skyrmions on this magnetisation range. In this specific sample, with $M_s = 160$ kA/m at the maximum of the dome (see Fig. 3.1i), the magnetic anisotropy K_u should be larger to allow for PMA even with this magnetisation. This would be achieved with a slight decrease of the sample magnetic thickness to increase the magnetic anisotropy up to $K_u = 16.1$ kJ/m^3 (by less than 1 nm from the linear relation obtained in Fig.2.18)

In this sample, the skyrmions are found at higher temperature. This model does not consider the effects of the temperature on the skyrmion stability. We will present our experimental results on this sample in the later section 3.3.2.2, but we can already state that the thermal fluctuation did not have a major impact on the properties of the skyrmions observed. Their stability remained unchanged in the limit of the time scale of our experiments, and even though thermal fluctuation could have favoured other magnetic states (due to increased energy of the system), the expected skyrmion state indeed appeared. Also, skyrmions can be stabilised at low temperature (around 110 K) which is very interesting as it can allow for a direct comparison of the properties of skyrmions when crossing T_{mc} and T_{ac} as discussed in section 4.8.1.

3.2.4.3 Energy barrier versus temperature and thickness

In order to sum up the important properties found in the previous phase diagrams, some cuts at fixed magnetic field of the energy barrier E_a, that describes the stability of skyrmion, found for both samples are presented versus temperature in Figure 3.8.

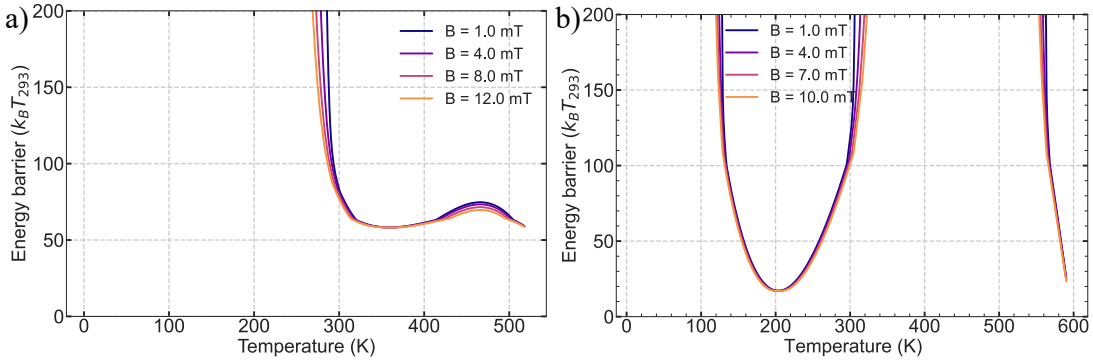

Figure 3.8: Energy barrier vs temperature for RE and TM dom. samples. c-d) Energy barrier E_a versus temperature of the RE dom. sample (TM dom. sample) for several magnetic fields.

As presented in Figure 3.8 a,b), the energy barrier scales with the skyrmion radius. So, the most stable skyrmions are found close to T_R, and the least stable skyrmions are found at T_{mc} (360 and 200 K for a and b).

At T_{mc}, increasing D_s increases the skyrmion energy barrier, whereas increasing K_s lowers it. The energy barrier increases with E_0^{ex} which is proportional to the magnetic layer thickness. The skyrmion DMI energy (after integration) is independent of the sample thickness, but the exchange and magnetic anisotropy increase with sample thickness. This opens an interesting evolution of the energy barrier by varying the thickness that we analyse using parameters of the RE dom. sample.
Considering $D_m = D_s/t$ and $K_u = K_s/t$, we can see an increase of the skyrmion energy barrier with increasing thickness conjointly with a skyrmion radius reduction. This behaviour holds down to 4nm. But below 4nm, the energy barrier actually increases when reducing thickness. This is accompanied with a fast increase of the skyrmion diameter. Because Zeeman and long range dipolar energies are negligible for very small skyrmions, especially close to T_{mc} with little magnetisation, we look closely at the three energy contributions at play here. We can see that this shift in behaviour is due to the ever lowering contribution of the anisotropy and exchange, while the constant DMI contribution become sufficiently large to increase skyrmion diameter and rapidly lower the energy of the equilibrium radius. Then, even though E_0^{ex} decreases with small thickness, the energy barrier ends up increasing. We present this interesting effect in Fig.3.9.

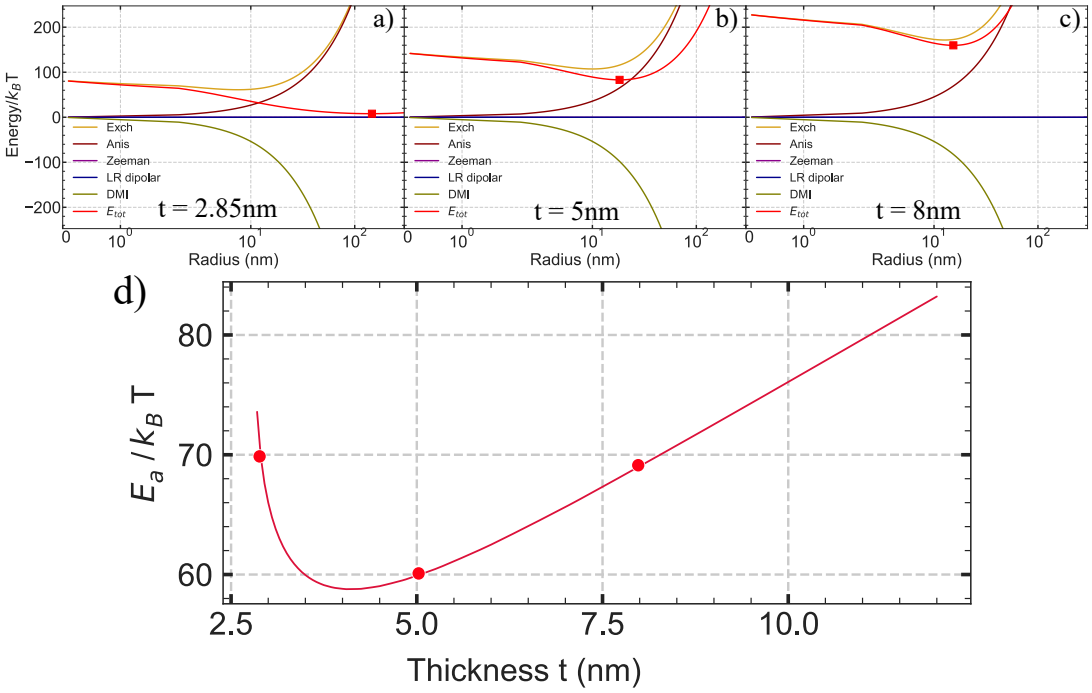

Figure 3.9: Skyrmion energy barrier vs sample thickness. a,b,c) All magnetic energies vs skyrmion radius computed with RE dom. parameters presented for t= 2.85nm, 5nm and 8nm respectively. Red square is the equilibrium skyrmion radius. d) Skyrmion energy barrier E_a versus sample thickness. Red points correspond to thickness presented above.

The evolution of the skyrmion energy barrier E_a with thickness shows that there is actually a minimum of stability found at a certain thickness. Then below this thickness, the stability increases but skyrmion becomes larger. Above this thickness, skyrmion radius decreases, but the energy barrier becomes larger. It should be noted that for very large thickness the radius begins to increase. In Fig. 3.8, the barrier energy is found to be larger for the RE dom. sample compared to the TM. dom one which can appear quite surprising, considering that the RE dom. sample is thinner than the TM dom. one. This can be explained because both sample present the same D_s (see Tab. 2.2) but a very different K_s. Therefore, the lowered interfacial anisotropy of the RE dom. sample grants it with a larger skyrmion stability than for the TM dom. one.

3.3 Skyrmion observation in GdCo ferrimagnets

Now that we explored the characteristic parameters for skyrmion stability and the theoretical phase diagrams for two chosen samples, we will describe their respective experimental phases diagrams and compare them with the results of the previous sections. A discussion on subtleties of MOKE with ferrimagnets is first discussed, as well as considerations on its resolution. We then present our image analysis protocol and finally the phase diagram of the two samples.

3.3.1 Observing skyrmions by MOKE microscopy

Using MOKE microscopy, we observed the skyrmion stabilised in the films. The MOKE signal depends on the scalar product of the incident wavevector with the magnetisation. The incident light of the microscope is selected with a diaphragm to be mostly at normal incidence, denoted as polar MOKE configuration, which results in a m_z sensitivity of the magnetisation.

MOKE contrast and Co lattice orientation

It is also important to remember (see Sec. 2.2) that due to the different energies of the magnetic orbitals of RE and TM materials, the MOKE is sub-lattice sensitive [22] and so the wavelength should be chosen to probe the desired sub-lattice. In our setup, with white light, with peak intensity in the red spectrum, the signal is observed to be mostly sensitive to the Co sub-lattice.
This is best observed by looking at the domain contrast (black or white) favoured by a given orientation of the applied magnetic field. For a sample before T_{mc} (RE dom.) the Gd lattice has a higher magnetisation and therefore aligns with the field (so the growing magnetic domain present a Co lattice pointing down).
Above T_{mc} (TM dom.) the Co lattice is dominant (so the growing domains present a Co lattice pointing up).
The MOKE contrast can be reversed depending on the angle between the polariser and analyser. We made the choice to keep this angle the same throughout our measurements to avoid confusion. In our conditions, a positive magnetic field favours the growth of black domains when the sample is RE dom. and conversely of white domains when the sample is TM dominated. With this choice, a black domain corresponds to a down Co moment and, conversely, a white domain corresponds to an up Co moment.

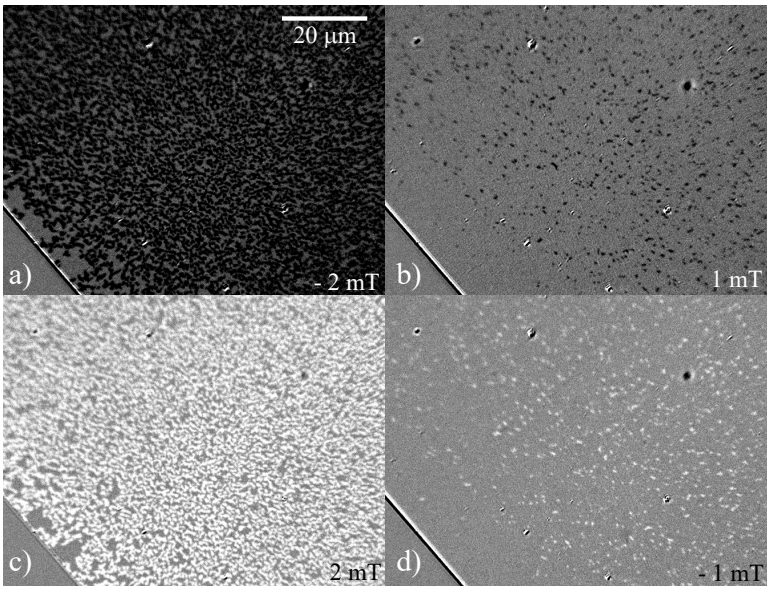

Figure 3.10: Typical stripes and skyrmion images for TM dom. sample. a-c) Differential MOKE images of black (white) stripes. b-d) Differential MOKE images of black (white) skyrmions.

In Figure 3.10 are presented examples of stripes and skyrmions magnetic textures in a TM dominated sample at 350 K. The images are obtained by subtracting a saturated reference. For this purpose, the sample is saturated in Fig. 3.10 a-b) with a positive magnetic field and a reference image is taken at the lowest magnetic field for which the film is still saturated, in order to limit the Faraday effect on the image. When further decreasing the field, black skyrmions naturally nucleate Fig. 3.10 b), and then black stripes are favoured by a negative field Fig. 3.10 a). The black stripes become denser and denser as the field reaches high negative values. The exact opposite is observed for white skyrmions: the sample is saturated with a negative magnetic field (uniform black magnetisation) and white skyrmions naturally nucleate at low enough negative field Fig. 3.10 d) with white stripes favoured by a positive magnetic field Fig. 3.10 c). For a RE dom. sample, the field sweep has to be reversed to observe domains with the same Co orientation (i.e. a negative saturation and field lowering to observe black skyrmions).

MFM and MOKE skyrmion size comparison

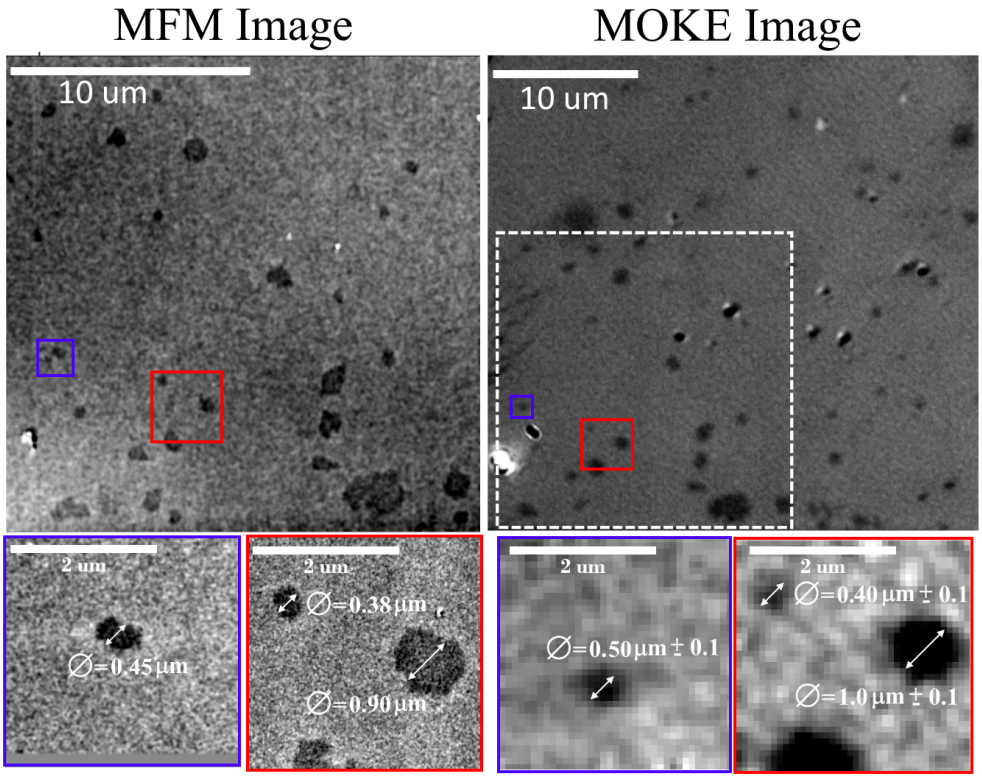

Figure 3.11: MFM and MOKE skyrmion size comparison. a) MFM image of skyrmion with their observed diameter. b) MOKE image of the same region where the same skyrmions present very equivalent diameters.

Using MOKE, we determined skyrmion radius down to the limit of the optical resolution. To verify the validity of these results, we compared the measurements taken from MOKE images with Magnetic Force Microscopy (MFM), which possesses a much better resolution. We present the comparison of the same skyrmions measured by MFM and then observed by MOKE in the Figure 3.11.

Skyrmions were nucleated and observed by MOKE, then measured by MFM, and a final image by MOKE was taken afterwards. We compare this last image with the MFM image in Figure 3.11 where the large image clearly shows that both measured regions are the same. For both techniques, images were also taken with better resolution (with the largest magnification objective for MOKE and with a smaller scanning size for MFM) and the regions are presented in blue and red for both. Skyrmions from the MFM image were measured by a simple cut along several directions to obtained an averaged size whereas the MOKE images were analysed using the analysis protocol that is discussed below.
We can observe a good agreement between the high resolution MFM technique and the MOKE images analysed by our protocol. This gives confidence in the measured size of skyrmions later presented and validates our image analysis protocol.

Skyrmion profile

Considering that we observed large skyrmions, close to T_R (so $\kappa \to 1$) we can expected a bubble-like profile rather than a compact skyrmion profile (see Sec. 3.2.3). We present computed skyrmion profile for several typical radius in Figure 3.12b.

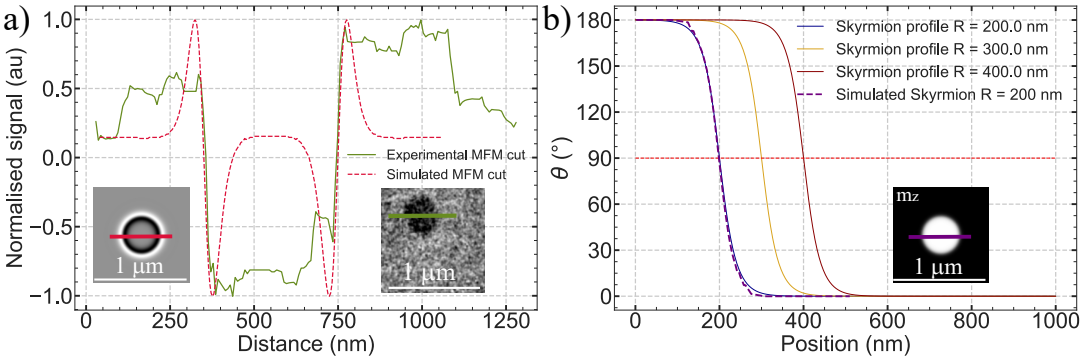

Figure 3.12: Experimental and computed skyrmion profile. a) MFM signal profile of a skyrmion (radius of 200 nm) from the experimental MFM image (green) and calculated from a Mumax3 simulation (red; calculated for the experimental measurement height of 25 nm). The insets show the respective images. b) Theoretical skyrmion θ angle profile (Eq. 3.4) for various radius, with $\Delta = 25$ nm (corresponding to parameters of the RE dom. sample). The profile in purple corresponds to the skyrmion in a).

Figure 3.12a shows MFM signal profile of a skyrmion from experiment and the MFM signal calculated for the same measurement height (25 nm) from a micromagnetic simulation. They show some important differences. This can be due to several issues. First of all, the MFM signal is noisy, even though the image has been gaussian smoothed before taking the cut it still deforms the signal. Also, the computed signal only considers the effect of the sample dipolar field on a punctual tip (only considering its height). A more elaborated computation of the MFM signal might give better results. Nonetheless, we can observe that all features of the simulated signal are observed: small signal away from the texture, positive peak followed by a negative peak and lowering of the signal in the middle of the texture with the symmetric on the other side of the profile. Because the MFM signal is not measuring the magnetisation but its dipolar field [306], the skyrmion profile can not be directly extracted from the MFM measurement without demanding calculation [307].

Following a simpler procedure, we can verify that for a simulated MFM signal comparable to the one measured, the simulated skyrmion profile does fit very well with computed profiles from eq 3.4 where the domain wall width parameter is constrained and not fitted as in most cases. This simply shows that the 360° DW ansatz for the skyrmion profile does correspond to the profile obtained from micromagnetic simulations.

Image analysis procedure

We describe here the image analysis protocol used to measure the skyrmion size. As some of the measured structures are only a few pixels wide, special care was taken to reduce artefacts as much as possible and establish a reproducible protocol. There are many different software that allow for image analysis (Gwydion or ImageJ to name a few) and we also used such software to compare with our protocol analysis, or typically for simpler analysis. With the magnification usually used in our experiments, one pixel corresponds to a square of $\approx$ 80 nm side length. This means that skyrmions with diameter of 550 nm are actually observed as 6x6 pixels structures.
We chose an arbitrary cut-off of structures below 250 nm of diameter (around 3x3 pixels) because it would be difficult to distinguish them from noise. We present the typical kind of image treatment we realised in order to measure the size of the skyrmions from our MOKE images in Figure 3.13.

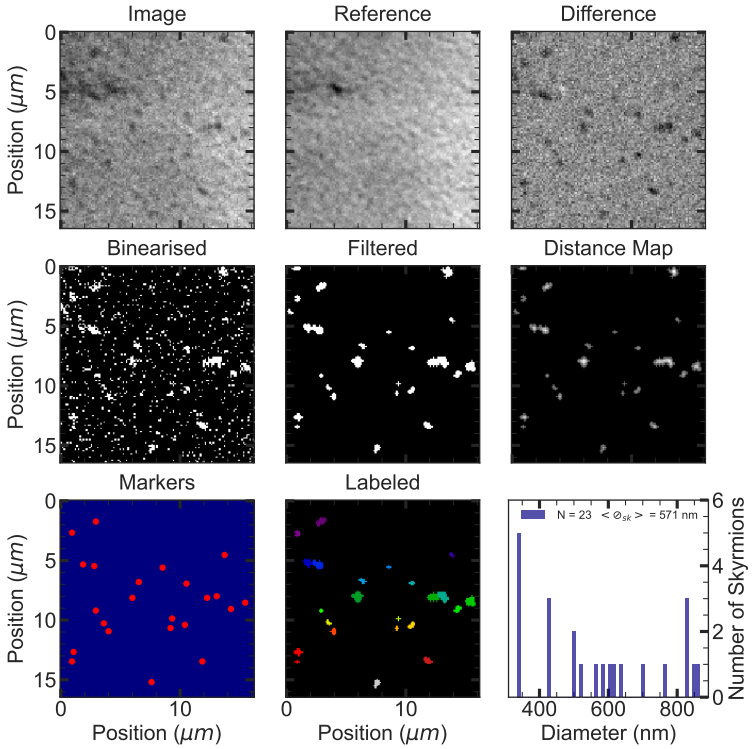

Figure 3.13: Image analysis procedure: Difference, binarization, filtering, markers and labelling.

The image analysis procedure is as follows:

- A reference image from a saturated state is taken, then skyrmions are nucleated (by changing the magnetic field or by electrical current pulses).
- A differential image is obtained and binarized with a conventional thresholding algorithm (Otsu's method implemented in the library Scikit-image [308]).
- The binarized image is then filtered by removing isolated white or black pixels. For radius determination on full images, manual cleaning of artefacts on the images (like dust) is also done.
- The distance map (converts binarized imaged to the distance image of each pixel with the background) is then taken on which a local maxima algorithm is used to determine the centre of all structures. A clear bias can be present here as a minimum distance between local maxima is defined, this distance should be taken to be larger than average size of skyrmions (but not too large to detect most skyrmions).
- The marked centre regions, is used as a seed by a watershed algorithm [309] to separate structures and label them with distinct colours. It can be noted that when skyrmions are well separated the use of a watershed algorithm is not needed and simpler isolated structure detection can be used.
- From all labelled areas, a diameter is obtained from the area by supposing a round shape (so $d = 2\sqrt{\frac{Area}{\pi}}$).

As described for the determination of the experimental phase diagram 3.15, much information can be taken from the labelled images: eccentricity, surface to perimeter ratio, image of the structure. Many quantities can be computed from these images and we will restrict our analysis to the most useful ones.

3.3.2 Skyrmion phase diagram in the two GdCo samples

3.3.2.1 Skyrmion textures in RE dom. sample

Figure 3.14 shows some typical hysteresis loop obtained for the RE dominated sample where the sign of the contrast can be observed to be reversed compared to images from Figure 3.10 (opposite domination of the sample).

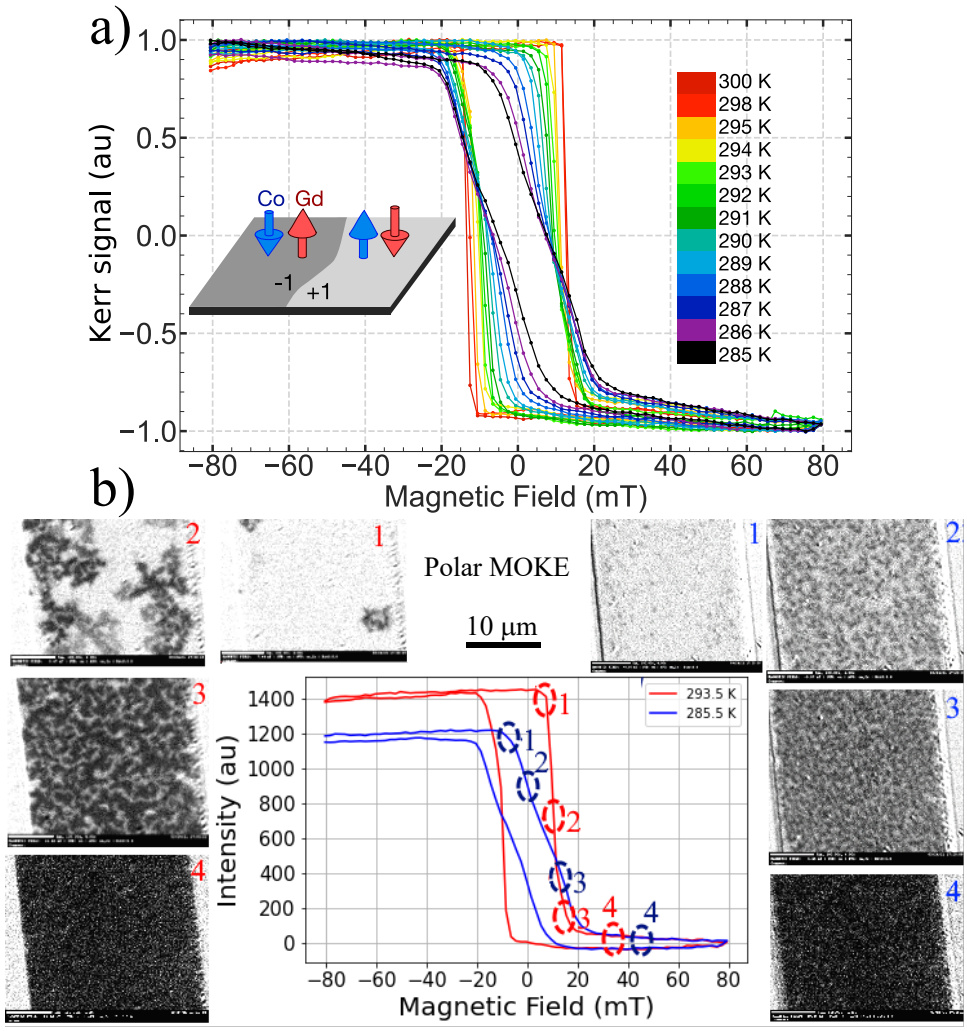

Figure 3.14: Hysteresis cycle in RE dominated sample. a) Set of hysteresis loops measured at several temperatures. The inset figure represent the orientation of both magnetic sub-lattices with respect to the Kerr contrast. b) Differential images with saturated reference background associated to MOKE hysteresis loop.

Figure 3.14a shows hysteresis loops of the RE dom. sample from 288.5 to 300 K where the transition from square to non-remnant loops is better observed. This shape of hysteresis loop is a signature of fractured magnetic domains, that are a good indication that skyrmions can be stabilised. This is better observed by decomposing the images used to obtain the hysteresis loop as presented in Figure. 3.14 b).
One can see the hysteresis loops obtained at 293.5 and 285.5K from the above figure, with the associated images recorded at each magnetic field step. It is then easily observed that the signal is higher when the sample is saturated by white magnetic domains and lower for black magnetic domains. In our configuration, and due to the RE domination of the sample, positive magnetic field, favours black magnetic domains growth, whereas white magnetic domains grow with negative field. The orientation of the Co lattice related to the MOKE contrast is shown in the inset of Figure 3.14

a). The hysteresis loop is square at 293.5 K: the coercive field H_c has to be overcome before any nucleation and propagation of magnetic domains. Because of homogeneous propagation field, the whole sample reverses on a small field range and the hysteresis loop appears square. The domain observed at this temperature are labyrinth like, which we refer as stripes in the manuscript. Then, at a slightly lower temperature of 285.5K, one can observe a clear difference of the hysteresis loop shape, that shows partial remanence at zero field. This is due to the nucleation of black magnetic domains that starts even while an opposing magnetic field is applied. The magnetic textures nucleating are believed to be skyrmions, which will be demonstrated by dynamical measurements in chapter 4. They will therefore be referred as such in the following chapter. While lowering the magnetic field, the number of skyrmions grows rapidly, and once a magnetic field is applied along the skyrmions core magnetisation, the observed magnetic texture shifts towards stripes. At high enough field the sample is then saturated by black magnetic domains.

Skyrmions close to T_R

It is already noteworthy to realise that using only experimentally measured parameters, the model presented in the previous section predicts quite accurately our observations on a large part of the phase diagram. It predicted skyrmions above 100 nm radius (which is in the range of our experimental resolution[2]) around 290 K, which is exactly what is observed experimentally.

At lower temperature we observed higher skyrmion density with increasing size (see Fig.3.21) down to the lowest temperature of our ambient sample holder (285K). Using a liquid nitrogen cryostat to explore lower temperatures, we then observed smaller magnetic textures, with the Kerr signal decreasing strongly close to TR. However, it was not possible to discern whether the sample was in-plane or was in a state of dense and very small domains. Also, Kerr contrast is lowered and Faraday effect enhanced in the cryostat which make these measurement even more challenging to analyse. We could not resolve these textures, and do not consider the MOKE signal fading to reveal the crossing of T_R that is more accurately measured by transport measurement of effective anisotropy field. T_R is observed to take place at a lower temperature around 250 K 3.1b). The fading of the MOKE contrast should be compared to the expectation from the theoretical phase diagram that predicted ever growing skyrmions when reaching T_R. This is a clear sign of the limits of the model, which only considers isolated skyrmions, and no transition to the stripe phase. We can expect that close to T_R, small magnetic textures become more favourable than a unique large skyrmion, for instance due an energy balance found by nucleating more (and smaller) skyrmion or simply to a phase transition towards stripes with a smaller periodicity close to T_R (Sec. 3.2.1.1). This is indeed what is usually observed with system brought close to T_R as seen in [310, 311, 312]. An extension of this model that would consider the transition to the stripe phase would then be a very good improvement as it could propose coherent expectations up to T_R.

The skyrmion density great increase at lower temperature, can be countered by increasing the applied magnetic field, but this is contrary to our goal to observe isolated skyrmion dynamics at room temperature and zero magnetic field. For this reason, the temperature range to study the skyrmion dynamic should remain far enough from T_R.

[2]With this setup the numerical aperture is NA=0.8 and the diffraction limit expected around 500 nm (at λ=800 nm). However, it is possible to measure the diameters of isolated skyrmions below the optical resolution, as skyrmions, even though they appear all with the same size, will show a size-dependent signal intensity. Also, the resolution of the microscope can be assessed on a sharp lithographied edge that appears as a 250 nm step.

RE dom. sample phase diagram

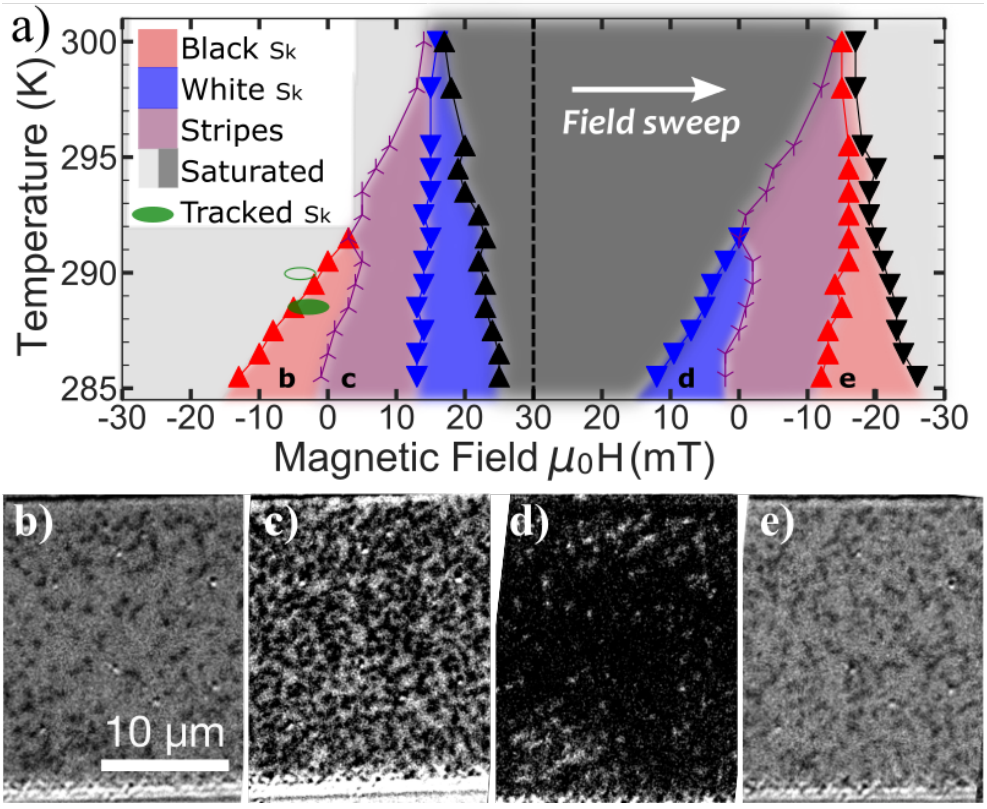

Figure 3.15: Temperature and magnetic field phase diagram of the RE dominated sample. a) Phase diagram of magnetic textures during field hysteresis loops from -30 to 30 mT and back to -30 mT. The phases and their transition fields are defined in the text. Markers define the entered region with respect to the field sweeping direction. b-e) MOKE differential images at $T = 285.5$ K and at the magnetic fields indicated in a). The region where skyrmion dynamics measurements were performed (presented in the next chapter) are displayed as green regions.

The phase diagram constructed from the images of hysteresis loops at fixed temperature (Figure 3.14) is shown in Figure 3.15. It is presented by unwrapping the magnetic field sweep and should therefore be read following the field sweep arrow depicted in the figure. The phase diagram is focused on the transition region around T_{Dc}. The images reveal different types of textures which we classify in four phases, shown in Fig. 3.15 a): saturated, black or white skyrmions (with the cobalt moment at the skyrmion core along $-\vec{z}$ or $+\vec{z}$, respectively), and stripes. Starting with a saturated state at -30 mT and increasing the field, we observe skyrmions (black dots in the MOKE image of Figure 3.15b) above a temperature-dependent nucleation field (first red triangles). Then a stripe, labyrinth-like phase develops, and becomes denser with increasing positive field 3.15c). The white stripes are then compressed into sparse white skyrmions, before reaching the full saturation of the sample. A symmetric evolution is observed along the opposite field sweep in Figure 3.15d,e, with white skyrmions naturally nucleating from an opposite saturated state, followed by a white stripe growth with positive magnetic field, up to a compression of black stripes into black skyrmions.
Finally, it can be noticed that the skyrmions compressed out of the stripe phase can actually be observed up to much higher temperature than the ones nucleating from the saturated state. Indeed, from the saturated state, skyrmions nucleate at 285.5 K at -12 mT (3.15a) but, when compressed out of stripes, skyrmion last up to -26 mT.

This is an interesting behaviour as it means that the accessible range of temperature where skyrmions are stable can be enlarged by a careful choice of field sweeps. It also explains why the tracked skyrmion region in green in 3.15 can be located in the saturated region, as these skyrmions were nucleated by current pulses and can thus survive in this region. The tracking of skyrmion is discussed in section 4.2

Comment on the phase diagram construction

The transition from skyrmions to stripes (shown as lines and symbols in Fig. 3.15a) is smooth. To distinguish them, we extract the shapes of the domains from binarized images using a watershed segmentation algorithm [309] and calculate their surface-to-perimeter ratios. A threshold is chosen to classify the textures either as stripes (with higher ratio) or skyrmions (with lower ratio). Similar results were obtained by using the eccentricity of the best-fitting ellipse (with a different threshold). This phase determination is insensitive up to some degree to the choice of binarization threshold as only the shape is relevant.

3.3.2.2 TM dom. sample

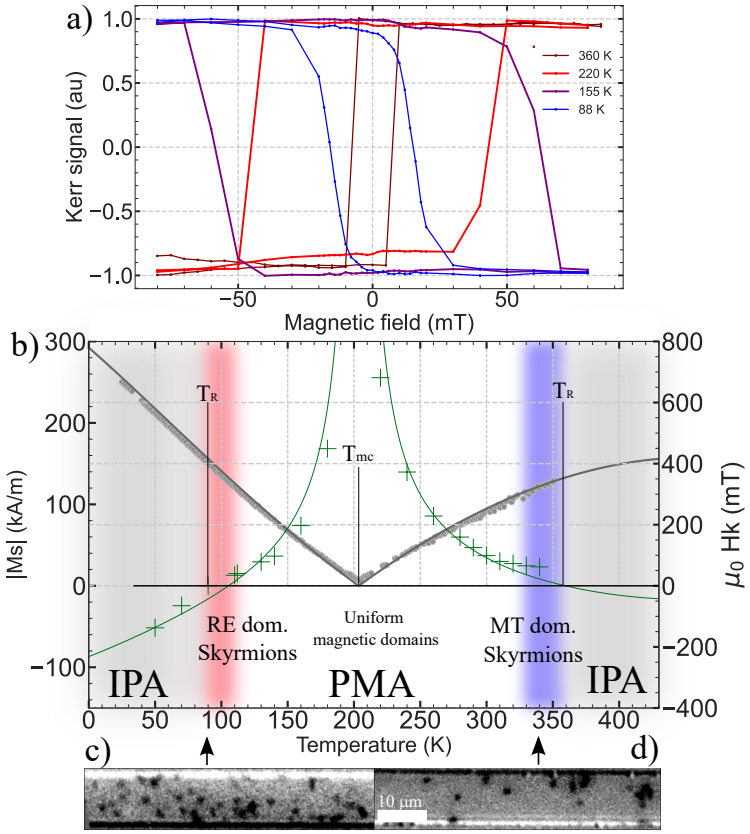

Figure 3.16: Experimental phase diagram of the TM dom. sample. a) Normalised MOKE hysteresis loop versus temperature. b) Magnetisation, effective anisotropy field and magnetic texture phases. c) MOKE differential image of RE dom. skyrmions in magnetic track at 88 K. d) MOKE differential image of MT dom. skyrmions in same magnetic track at 355 K.

Figure 3.16 shows some MOKE hysteresis loops obtained on the TM dom. sample in a), the sketch of the phase diagram of the sample in b) and typical MOKE images of skyrmions obtained at 88 K and 355 K in c). We can observe that the hysteresis loops clearly show the crossing of T_{mc} with the reversal of the Kerr signal sign between loops at 155 K and 220 K with large coercive fields.

The typical magnetic textures in the blue region of Figure 3.16b) are uniform magnetic domains. Closer to red regions, stripy magnetic textures can be observed. We can observe skyrmions in both red regions as presented in Figure 3.16 c) 88 K and d) 355 K. The loops present a more square shape in the skyrmion regions than the ones obtained for the RE dom. sample. Indeed, in this sample, only a few skyrmions nucleate naturally from the saturated state and most appeared only after the application of a small magnetic field along the skyrmion core. These skyrmions then remained stable after reversal of the field polarity. This is certainly due to the fact that the hysteresis loop were obtained far enough from T_R where skyrmion nucleation is less favoured. It also seems that we slightly underestimate the magnetic anisotropy K_u of the sample presented in Table 2.2, which is most obvious at low temperature, where the T_R is expected 20 K above our observation.

It is interesting to note the skyrmions present the same contrast in both images, which shows that the Co lattice is pointing in the same direction. Indeed, in order to nucleate skyrmions in c), we saturated the sample with a negative magnetic field, whereas to obtain skyrmions in d) we saturated the sample with a positive magnetic field. There are no obvious differences in the statics properties of the skyrmions observed at low or high temperature, and their properties seems to be mostly determined by magneto-statics energies. We can expect that the temperature can have an impact on the stability of the skyrmions, but from our observations it is still low enough at 350 K compared to the skyrmion annihilation energy barrier, as these skyrmions remained stable for hours. We will present results on the dynamical properties of skyrmions in both of these regions in the next chapter in section 4.8.1.

3.3.2.3 Comparison with theoretical model

These experimental phase diagrams can be compared to the one obtained by the model (Figs. 3.5 and 3.7). In the case of the RE dom. sample, the model predicts T_{Dc} at 283 K, where the DW energy becomes negative and so skyrmions can only be observed with an applied opposite magnetic field. The model finds skyrmions growing to observable sizes around 292 K. In the experimental phase diagram, we observe skyrmion in zero, or even positive magnetic field, from 287 to 292 K, which is quite close to the model expectations.
More generally, the behaviour observed is very consistent with expectations, namely that closer to T_R the skyrmions nucleate sooner at lower opposite field. This illustrates the fact that, as the DW energy lowers, skyrmions naturally nucleate even with an increasingly high applied magnetic field against their core.

In the case of the MT dom. sample, the theoretical phase diagram predicted skyrmions around two temperatures, 110 K and 300 K, but they were only observed around 100 K and 330 K. This suggests that the anisotropy field was slightly underestimated, as a higher anisotropy would shift these temperatures down and up, respectively. Nonetheless, the model shows a good agreement with our experimental observations. The discrepancies presented here are mostly due to lack of precision in the determination of the model parameters. These errors could be better assessed for the RE dom. sample because of repeated measurements that allowed to determine precisely the magnetic parameters and reduce their experimental error.

These observations show the quantitative predictions of the energy model, but also its limitations. The model only describes an isolated skyrmion, which limits its usefulness. For example, it does not predict the transition between skyrmions and stripes, neither takes in account the competition between nucleating a new skyrmion or enlarging a pre-existing one to satisfy long-range dipolar effects. A model considering these cases would be able to describe experimental observation with better accuracy.

3.4 Skyrmion radius versus temperature and field

3.4.1 Micromagnetic simulations

Methods

Using micromagnetic simulation parameterised for the RE dom. sample, i.e. using its magnetisation curve and experimentally determined parameters, we could replicate the features observed experimentally as well as the one from the theoretical phase diagram. We adapted MuMax3 in order to simulate a ferrimagnetic material, which is realised by defining the two antiferromagnetically coupled sub lattices separately but by taking special care to correctly compute the dipolar field of the system [250]. The procedure to simulate skyrmions consists in relaxing an ansatz Néel skyrmion until its equilibrium size is found. Figure 3.17 shows the radius of skyrmion versus temperature for several applied magnetic fields. The simulated skyrmions are equivalent to the white skyrmions from our experimental results (and so magnetic field can be considered as opposite to the one in the study of black skyrmions). The simulation considered 512×512×1 cells of 5 nm. This gives the limit of small and large skyrmions that can be simulated: skyrmions smaller than a few cells can not be resolved, and skyrmions larger than half of the simulation area will be affected by the simulation boundaries (periodic boundary conditions were used to minimise this effect).

Simulated skyrmion radius versus temperature and magnetic field

We could observe magnetic textures forming by the relaxation procedure. In Fig. 3.17, we can see that the stripe phase is observed close to T_R and that skyrmions are indeed stable in same region as the one observed experimentally. The threshold of the stripe phase is reduced with increasing applied magnetic field, i.e., the higher the magnetic field (opposite to the skyrmion core magnetisation) the lower the temperature below which skyrmions shift into stripes. Skyrmions remain stable up to the T_{mc}, but note that no thermal fluctuations (nor disorder) were added to the simulation. This means that the stability of these very small skyrmions was not assessed in the simulations, and they might be unstable at finite temperature. These simulation will be used in the next chapter as relaxed initial state for dynamical simulations of skyrmions (see section 4.4).

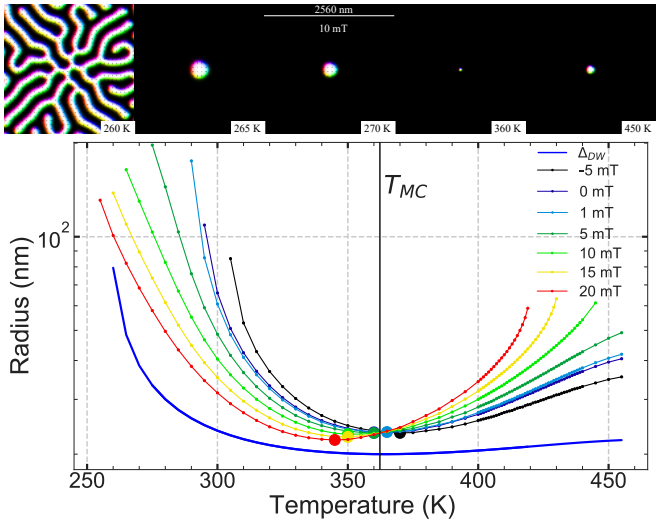

Figure 3.17: Simulated radius versus field for RE dom sample. Top: snapshots of the simulation for several temperatures at 10 mT. Bottom: evolution of the skyrmion radius (and domain wall width parameter Δ) with temperature for several applied magnetic fields.

The simulations are very consistent with our experimental observations. Indeed, the simulations reproduce the skyrmion radius divergence towards T_R and a minimum radius at T_{mc}, also seen in the simulation snapshot above Figure 3.17. Quite interestingly, it shows that the effect of the magnetic field has to be taken into account for the skyrmion size around T_{mc}. Indeed, at T_{mc} there is no magnetisation so skyrmions all have the same radius, whatever the applied magnetic field. But, depending on the direction of the field, the size of the skyrmion is reduced, or enlarged, below or above T_{mc}. This is easily understandable due to the skyrmion core magnetisation whose direction is reversed at T_{mc}.

3.4.2 Theoretical skyrmion radius

Theoretical skyrmion radius versus temperature and magnetic field

Using the theoretical phase diagrams obtained in the previous section, we present in Figure 3.18 the evolution of the radius with temperature for different fields.

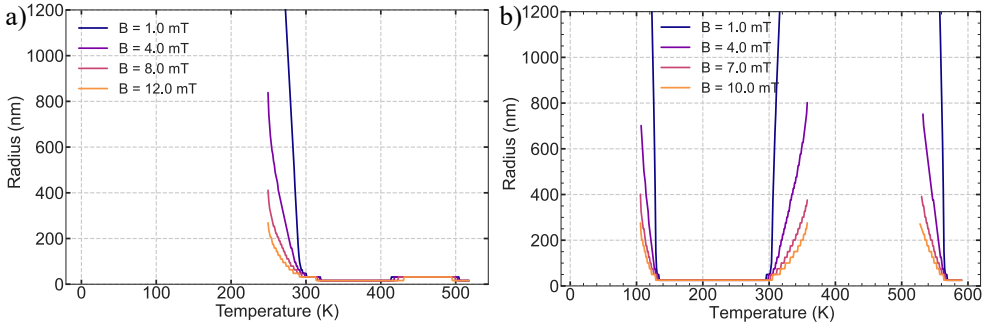

Figure 3.18: Theoretical skyrmion radius vs temperature for RE and TM dom. samples. a-b) Radius versus temperature of the RE dom. (TM dom.) sample for several magnetic field.

The skyrmion radius diverges at T_R for both samples, as one can see in Figure 3.18 a,b). The smallest radius is found at T_{mc}. Rapidly varying radius is only found close to T_{Dc} in both cases. The magnetic field is observed to compress the skyrmion radius, with a noticeable effect only for large enough skyrmions of some tens of nm. This evolution follows the one observed for simulated skyrmions in 3.17 and quantitative comparison are made later (see Sec.3.4.4).

We now present cuts of the theoretical phase diagrams in Figure 3.19 that show the evolution of the radius with magnetic field for some temperatures close to T_{Dc}.

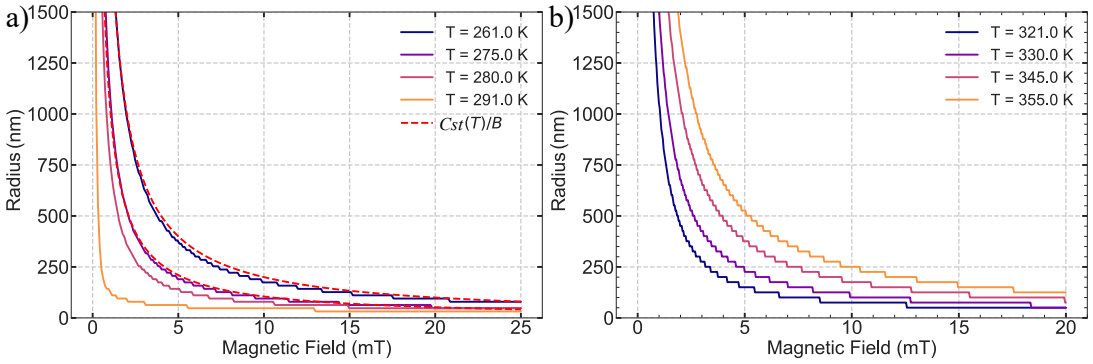

Figure 3.19: Theoretical skyrmion radius versus magnetic field for RE and TM dom.samples. a) Cuts at fixed temperature extracted from 3.5 from RE dom. sample b) Cuts at fixed temperature extracted from 3.7 from MT dom. sample

We can observe that the radius follow a law of the form $R_{eq} = \frac{Cst(T)}{B}$ where $Cts(T)$ is a constant that depends on the temperature of the sample. This behaviour is found to be the same for both modelled samples (RE and TM dom.). It can be noticed that skyrmions away from T_R (towards high temperature for RE dom. sample and lower temperature for TM dom.) are less sensitive to the field, which seems mostly due to their smaller size.

3.4.3 Experimental skyrmion radius

Radius versus temperature and magnetic field

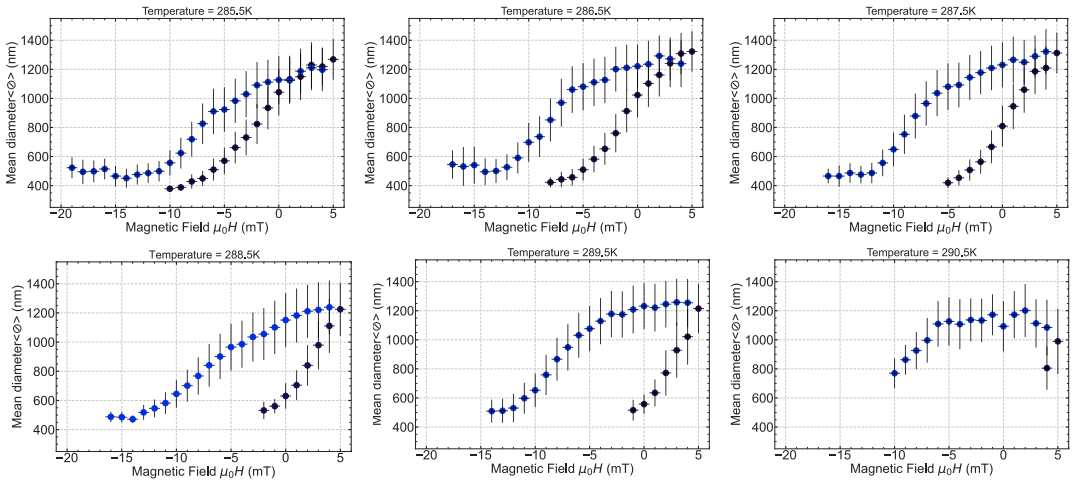

Figure 3.20: Experimental skyrmion radius with field for RE dom. sample at several temperatures. Minor hysteresis loops are performed from -30 to 5 mT and black skyrmions size are averaged on the whole image to obtain the size presented in all figures. Dark blue points are obtained for field sweep up and lighter blue for field sweep down. Measurements at 288.5 K with a different blue are highlighted because this will be the temperature of interest in the next section for skyrmion dynamics of the RE dom. sample. The errors bars represent the standard deviation of the averaged sizes.

Figure 3.20 shows the averaged diameter of skyrmions measured on the RE dom. sample, with the same overall procedure as described previously. Special care was taken to have a consistent threshold for all images, which is not straightforward, as the Faraday effect requires the use of a field-dependent threshold value. A calibration of the Faraday effect is done in order to define a field-dependent binarization threshold free of artefacts.
The measurement is done along minor hysteresis loops from -30 to 5 mT and repeated at several temperatures above and below T_{Dc}. The error bars represent the standard deviation of all the skyrmions measured on an image. The dispersion is quite large, around 300 nm for images with enough skyrmions (when only few skyrmions are visible on the image they have much similar sizes). This might be due to the proximity of T_{Dc} which gives a rather shallow energy profile of the radius, as discussed before.

The $\frac{Cts(T)}{B}$ law can be fitted when considering points from -20 to -5 mT, but skyrmions at the lowest field are usually very densely packed and their size therefore does not diverge as predicted by models for isolated skyrmions. On a range of field from -12 to -5 mT the experimental evolution of the diameter with magnetic field rather points to a linear behaviour. The hysteresis of the averaged skyrmion size (Fig 3.20) can be explained considering pinning effects. Indeed, pinning is known to deform skyrmions [313, 314, 216], but can also prevent them to reach their equilibrium size.

The pinning-free equilibrium size of the skyrmion should lay somewhere between the up and down sweeps. Due to pinning effects we can expect skyrmions to present reduced size (from pinning free) for the sweep up, and enlarged size for the sweep down.
We can also observe that the hysteretic behaviour becomes smaller closer to T_R. This might be due to the fact that the DW of these skyrmions is wider and therefore less sensitive to pinning, which might have a length scale smaller in the order of few nanometers as discussed in chapter 2.
Finally, we can see that the lower the temperature the higher the magnetic field at which skyrmions nucleate during the sweep up, or survive at the sweep down which is consistent to what was observed for the theoretical phase diagram with skyrmions closer to T_R showing larger radius for constant magnetic field compared to skyrmion further away from T_R.

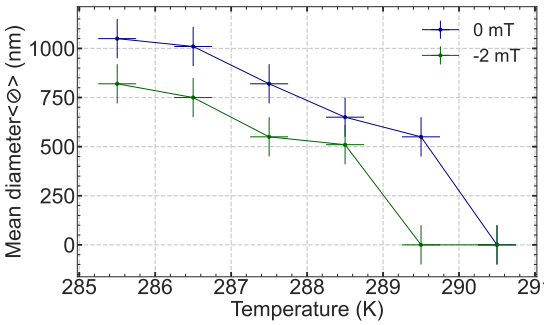

Figure 3.21: Experimental skyrmion size versus temperature. Averaged skyrmion sizes obtained from cut of sweep up from 3.20 at two fixed field of 0 and -2 mT.

Figure 3.21 shows the evolution of the skyrmion size with temperature for constant magnetic field, at 0 and -2 mT from skyrmions nucleating during field sweep up. This is consistent with model expectations that predicts smaller skyrmions for lower magnetisation, which is indeed the case for this sample with its T_{mc} around 360 K. We can see that the typical size of the skyrmions ranges between 500 nm to 1 μm in the low magnetic field range. Measurements of the skyrmions size closer to T_R are expected to show a decrease of the skyrmion size at a temperature where the system become more stable by nucleating skyrmions instead of increasing the size of pre-existing ones. Also, measurements towards T_{mc} would have been interesting to realise, with a better resolved technique like MFM for instance, in order to verify the model's predictions.

On the skyrmion stability

The theoretical model pointed to the skyrmion size as the key parameter for its stability. We could only access the experimental stability quite rudimentarily by two type of observations. One is simply to nucleate skyrmions and to see how long they survive while keeping all parameters constant. From our experiments, most skyrmions were stable on the whole time scale of our experiments, which were not extended more than a day. This is too little time to be able to conclude precisely on the stability of these skyrmions. Also, we would often perform nucleation of skyrmions at lower temperature (around 285K) and then perform experiments at higher temperature around 300 K where they would also remain stable. The temperature could even be increased further, but the issue with such experiment is due to the nature of ferrimagnets and their temperature dependant magnetisation. Heating the sample therefore induces a shrinking of the skyrmion size from which a comparison of stability at different temperature become quite difficult.

3.4.4 Experimental, theoretical and simulated radius comparison

The radius R is determined for the simulated skyrmion with the same criterion as for the theoretical model, namely it is the distance from the core to the point where $\theta(R) = \pi/2$. In the case of skyrmion measured experimentally, the threshold of the binarization is supposed to cut the contrast between dark and bright and so around the same $\theta(R) = \pi/2$ value. However, because the MOKE resolution is far below Δ, the error is not at this level of precision and rather due to the noise in the images or threshold determination.

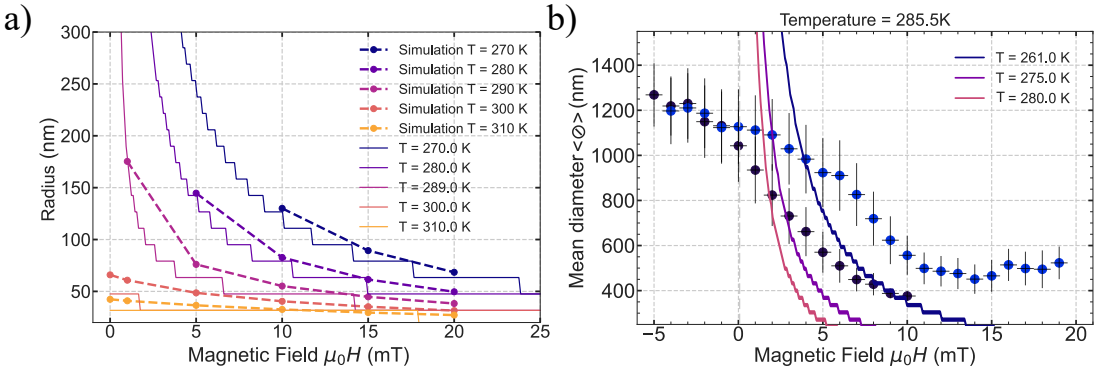

Figure 3.22: Simulated and theoretical skyrmion radius versus magnetic field. a) Cuts at fixed temperature extracted from 3.17 corresponding to RE dom. sample drawn on top of corresponding temperature of the theoretical skyrmion sizes from extracted from 3.5.

In Figure 3.22a, we superimpose the evolution of the skyrmion radius from the simulation on the one from the theoretical model for the RE dom. sample. The cut are made at several temperatures and we can observe a very good agreement between the two. There are fewer points for the simulations, especially at low temperature where the divergence of the radius is stronger. Indeed, in this region the simulations showed the skyrmions diverging rapidly (and reaching the simulation borders), disappearing or being replaced by the stripe phase. The step of magnetic field should have been much smaller to enable a precise measurement of the divergence radius and, because simulations were done for temperature sweep, we only have computed the evolution for a few magnetic field values. The good agreement between the model and the simulation is an indicator of the accuracy of the model.

In Figure 3.22b we present the experimental measurement of skyrmion diameter at 285.5 K (from Fig. 3.20) with x axis reversed. We super-impose some cut of the theoretical phase diagram of the RE dom. sample done at several temperatures. The agreement is far from satisfactory. We can see that the size of the skyrmions along the sweep up are closer to the simulated values, but only if considering a shift of around 20 K. We can therefore conclude that the theoretical model (as well as the simulations) are underestimating the observed skyrmion size. The evolution of the skyrmion size somehow resembles the same $Cts(T)/B$ law observed for theoretical (and simulated) skyrmions, with a different Cts only on a small field range.

For practical purposes, we can simply observe that the typical skyrmion radius variation with applied magnetic field on the sweep down (rather constant at all temperatures) is around 40 to 60 nm/mT for the diameter (20 to 30 nm/mT for the radius). This holds only above 0 mT up to the point where the skyrmion size is observed to be rather constant with increasing magnetic field (around 10 mT). This will be useful in the next chapter (see Sec. 4.2), where this law will be compared to the one obtained from averaged size of tracked skyrmions modified by the application of different fields.

If we try to compare with the theoretical model, one can make a linear regression on the radius with field at 280 K and focus on the intermediate region between 2 and 10 mT where the radius behaviour is away from the very rapid growth and also from the much flatter behaviour at large field. In this condition, one would obtain a linear variation of the radius around 33 nm/mT which is then quite consistent with our observations.

Finally, we can compare these results with analytical formulas for skyrmion sizes. These formulas do not consider the effect of an external magnetic field, which makes a direct comparison rather difficult. Several models were developed to find analytical expression of the skyrmion radius with material properties. This was realised for confined skyrmions in micro-pillars [144] but also for infinite film [315] and was later extended by [161] but also in a very complete study by [149]. Using the parameters of the RE dom. sample (table 2.2) and a magnetisation that corresponds to temperatures between 280 and 290 K (90 kA/m to 80 kA/m), the eq. 3.7 from [149] and eq. 3.6 from [144] yield very similar results (diameter which varies from 500 to 140 nm), especially for skyrmions larger than 200 nm. At zero field, as observed in Figure 3.21, skyrmions diameters range from 550 to 1050 nm. These formulas underestimate the observed skyrmion diameter, but we note that values computed for 280 K are rather close to our experimental observation of smallest averaged skyrmion size from 285 to 288 K (around 500 to 600 nm).

Summary

In summary, we presented the region where stable skyrmions are observed in two RETM samples with different T_{mc}. For the RE dom. sample, with a T_{mc} at 360 K, only one range of temperature, between 280-290 K, showed stable skyrmions (see Fig. 3.15), found around 30 K before the spin reorientation temperature. We focused on the beginning of the stability region where skyrmions were observed at room temperature without the application of external magnetic fields. On the TM dom. sample, with T_{mc} at 200 K, two ranges of temperature, 80-100 K, and 340 to 360 K showed stable skyrmions (see Fig. 3.16). Using an energy model for skyrmions, parameterised with experimentally determined magnetic parameters, we were able to replicate the experimental phase diagrams with a satisfying agreement (see Fig. 3.5 and Fig. 3.7). The energy model is compared with micromagnetic simulations and yields very similar skyrmion radius. The comparison with experimentally determined skyrmion radius is less satisfactory. The theoretical model predicts ever growing skyrmions towards T_R, which is not observed. This is certainly explained by the framework used for the model that only considers one isolated skyrmion and does not consider the energy of multiple skyrmions, nor the elliptical instabilities that can shift skyrmions into stripes. Also, the theoretical and simulations yield smaller skyrmions compared to the observations. The overall qualitative agreement is very good, but the quantitative one less so. The better agreement of the location of the skyrmion stable phase for the RE dom. sample compared to the TM dom. one, points to the sensitivity of the model parameterisation to obtain better quantitative comparisons.

3.5 Comparison with literature

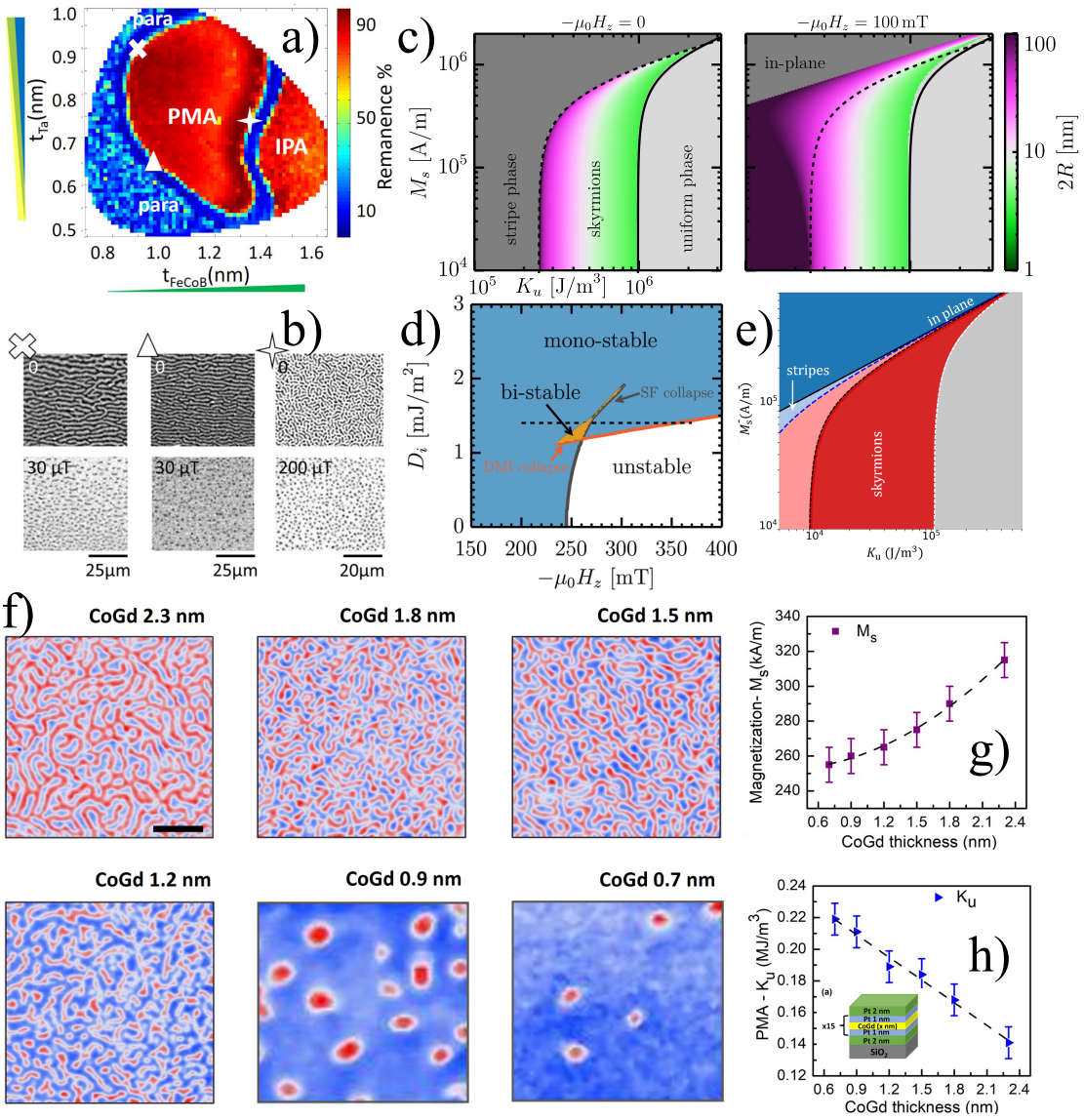

Figure 3.23: Skyrmion statics experimental and theoretical comparison with literature. a-b) Wedged CoFeB sample with magnetic textures observed at 3 locations [146]. c-d) Theoretical phase diagrams: M_s vs K_u in c) with 0 or -100 mT and D_m vs B_a in d) reproduced from [147]. e) Theoretical phase diagram: M_s vs K_u reproduced from[302] f-g-h) MFM magnetic textures observed on [Pt(1)/GdCo(t)/Pt(1)]x15 (nm) for different GdCo thickness with correspondent M_s (g) and K_u (h) reproduced from [159]. Scale bar is $1\mu m$.

To my knowledge, there are very few experimental references in the literature to compare with our phase diagrams. One diagram can be found in [157] on a multi-stack of 100 repetitions of Fe/Gd very thin layers (0.3 nm), which does sees an interesting phase diagram in field and temperature. However, the magnetisation in their system seems to be much more constant than here, as the phase diagram does not change much with temperature, where we would otherwise expect at least an increase of the magnetic field of the stripe-to-skyrmions transition at lower temperatures.
The best comparison we could find is in the article of [146] (Fig. 3.23a,b), where a wedge stack of Ta/FeCoB/TaO_x allows to see the clear switching from IPA to PMA and their relation with skyrmions statics that also appears close to the transition region.

Also, an interesting study was realised by [159] in Pt/GdCo/Pt repeated layers with variable GdCo thickness. Quite surprisingly, their sample is symmetric, with Pt on top and below the GdCo, but does present typical textures found with large DMI systems. The difference in growth of the bottom and top Pt layer might be the cause of the still sizeable DMI in their sample. Their results are shown in Fig. 3.23f-h), where we can see a similar evolution of the magnetic textures with thickness to the evolution with temperature we observed. Indeed, one can see in panel f that stripes are observed at 2.3 nm thick GdCo layer, with a transition to skyrmions between 1.2 and 0.9 nm, at room temperature, without magnetic field applied. Considering the M_s and the K_u of their samples (panels g, h), we see that the M_s increases with increasing thickness, and that the K_u lowers (consistent with interfacial magnetic anisotropy). It can then be understood that at higher thickness, the effective anisotropy is smaller. In our RE dom. sample, the effective anisotropy is lower at low temperature. So, increasing the thickness is equivalent to lowering the temperature of our sample. Thus, it makes sense that stripes are seen in thicker samples (very low anisotropy, equivalent to being below T_{D_c} in our sample) and that skyrmions appear in thinner ones (still small but positive DW energy cost). Then, the skyrmion size is smaller in the thinner sample, just like when increasing temperature in our case. We can expect that their sample crosses T_R for a large enough GdCo thickness. This study is then very comparable with our observations.

Finally, the comparison of the theoretical phase diagrams is much easier because of an extensive literature on the matter. Comparisons can be made with other models for skyrmions statics [147] or with further developments [302] of the original research behind the model we used. The main issue with these comparisons is that two variables are changing in our theoretical model, which are the effective anisotropy K_{eff} and the D_c, that can be modelled theoretically by changing K_u and D_m.

We reproduced a phase diagram from [302] in Fig. 3.23e), where the spin reorientation at high M_s and low K_u is clearly visible. In light blue is represented the region of negative DW energy where stripes are favoured and skyrmion solutions are only possible by applying a magnetic field. In the dark red region, skyrmion are found as metastable solutions, but in the light red region, elliptical instabilities of skyrmions does not guarantee a stable skyrmion solution. In the grey region, the uniform magnetic domains are energetically favoured. We can also observe in [147], with figure reproduced in Fig. 3.23 c) with the application of 100 mT a very similar phase diagram as the one from Fig. 3.23e), with the spin reorientation and the diverging skyrmion radius before the reorientation, with skyrmion size reduction towards the transition to the uniform ferromagnetic state. We see that without the application of a magnetic field, the stripe phase is favoured on a broad region. Finally, the figure 3.23 d) (also reproduced from [147]) shows the small region of skyrmion double equilibrium radius region. If we rotate this diagram by 90° counter-clockwise, with an abscissa of decreasing DMI and ordinate of increasing magnetic field, this can then be better compared to our phase diagram (Fig. 3.5 for example). Indeed, in RE dom. phase diagram, when increasing temperature D_c increases, which is equivalent to a lowering of D_m of figure 3.23 d). Then, because of the low anisotropy of our sample, the magnetic field is much lower in our case, but the region of bi-stability is also found at the very beginning of the skyrmion stable region, on a small magnetic field range, with a very thin tail at higher magnetic field.

These comparisons show a very good agreement between the phase diagram and understanding of our phase diagrams with [147] and [148, 302]. There are numerous other theoretical studies on skyrmion stability [165, 143, 166, 177, 305], with their own specificities that we can not exhaustively address here, but they do share very similar assumptions and conclusions as the two references used above.

Chapter 4

Magnetic Skyrmion Dynamics

In this chapter, we present experimental results on the skyrmions dynamics in GdCo thin films displaced by spin orbit torques (SOT) induced by electrical current pulses. We report the dynamical properties of skyrmions in the two samples studied in chapter 3, namely the RE and the TM dom. samples. We begin by presenting the method used to track skyrmions (section 4.1). Section 4.2 gathers results on the RE dom. sample and introduces the main dynamical properties observed of RETM skyrmions. These results are described and fitted using a Thiele equation based model of rigid skyrmions (section 4.3) and compared to micromagnetic simulations (section 4.4). We then discuss the different current-induced parasitic phenomena that can bias our observations in section 4.7. Finally, we compare the skyrmion dynamics between the RE and TM dom. samples in section 4.8, which shows the reversal of the skyrmion deflection across the angular compensation, demonstrating one of the interests of ferrimagnetic samples for skyrmion dynamics. A discussion on the mobility and depinning current observed in regard of the literature is attempted in section 4.9.

4.1 Method for tracking skyrmions

To measure the velocity and deflection angle θ_{sk}, the successive positions of skyrmions displaced by current pulses are followed using MOKE microscopy. This technique, whose acquisition time is a few ms, is used to observe the equilibrium position found by skyrmions after the excitation pulse.

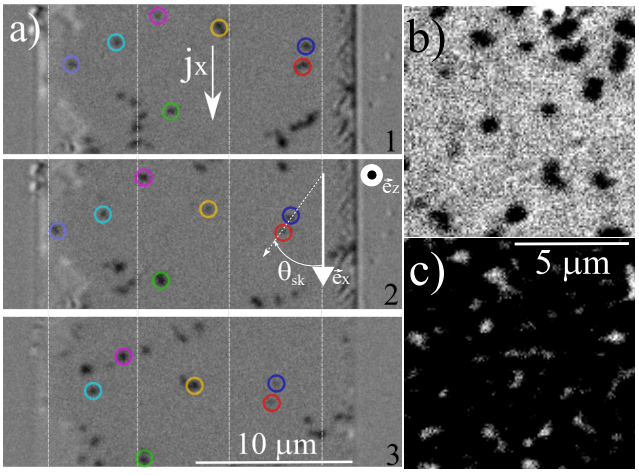

Figure 4.1: Example of skyrmion displacements under nanosecond current pulses. a) Three successive MOKE differential images separated by 10 ns current pulses of 260 GA/m^2 at -4 mT and 288.5 K. b-c) Examples of MOKE images for black and white skyrmions at 288.5 K at -1 mT and 5 mT. All images are obtained on the RE dom. sample.

Figure 4.1 presents the typically observed skyrmion displacements and images of up and down magnetisation core skyrmions (black and white MOKE contrast for RE dom. sample). In figure 4.1a), the successive positions of skyrmions are highlighted by coloured circles. Skyrmions with different sizes and shapes are observed with typical displacements around 1μm for 10 ns current pulses (100 m/s). Their displacement is along the electrical current and they present a deflection angle of around 40°. In figure 4.1 b) the two skyrmion polarities that are experimentally observed are presented.

As discussed previously in Chap. 3.3.1, MOKE microscopy is inherently limited in resolution by the diffraction limit of light. This resolution is adequate for the skyrmions we study, which have a diameter of the order of 500 nm to 1.5 μm.

As presented in section 3.3, the automated detection of isolated structures in an image is rather easy. On the other hand, the tracking of a structure over several images is not. We need to identify skyrmions from image i to i+1, which can be very difficult as the number of structures on a single image can be quite large (over 100), and the shape of skyrmions is not well preserved between successive images as, once displaced, the skyrmion relaxes in a slightly different effective anisotropy landscape. Moreover, skyrmions can be nucleated or annihilated between successive images, which adds to the complexity of the tracking. Several trials for complete automation were explored to find the correspondence between skyrmions in successive frames: using auto-correlation between images, measurements of all possible connections and statistical determination of the averaged displacement, or also k-means clustering method (an unsupervised machine learning data clustering technique). These attempts showed promising results, but their time consuming development and validation pushed us towards a method with a clearer control, in order to ensure proper data collection. In these complex conditions, we ended up developing a user interface in Python that facilitated the manual connection of skyrmions between frames, while allowing for automation as much as possible for improved reproducibility of the analysis. We present in figure 4.2 an example of the different steps of the tracking procedure.

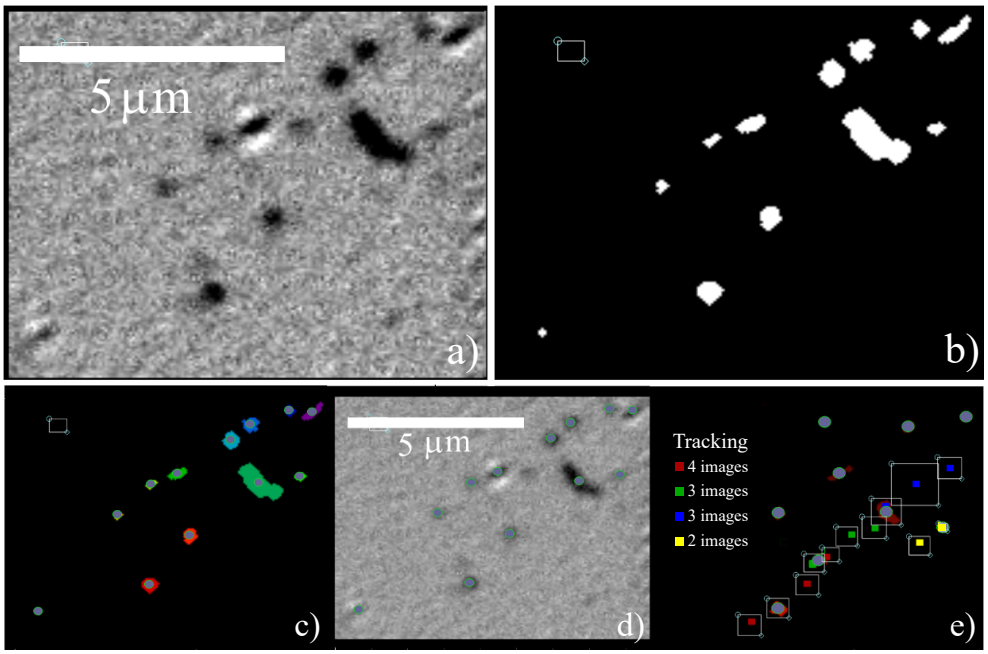

Figure 4.2: Skyrmion tracking procedure. a) Differential MOKE image. b) Binarized image. c) Isolated structure detection with clickable marker at the structure center. d) Superposition of markers from c) on image a). e) Manually connected positions for 4 skyrmions over 4 images. Different skyrmions are marked with different colours. The final image is a superposition of all tracked positions on the third image.

Figure 4.2 a) shows a differential MOKE image of a region of a magnetic track. Around 10 skyrmions are observed on this image, including a very elongated skyrmion that became much rounder in the following images. This image is then binarized (panel b). Three defects (dust), present on top of the magnetic track, are also observed in the binarized image and can be manually removed before subsequent automatic image treatment, but this is not necessary for tracking experiments as the skyrmions are manually selected. Our script then automatically detects the isolated structures (panel c), where a clickable marker is added at the structure centre. In d) we superimpose these markers on the initial image which is important to ensure before the selection of a structure that it corresponds to a skyrmion and not a defect. The user then can click on the skyrmion on several images in a sequence and follow its path. In e), we present the result of the tracking of these skyrmions where each colour corresponds to a different tracked skyrmion and the white frame to the snapshot area taken by the software for each selected skyrmion. We can see that one skyrmion survived for four images (red), two for three images (green and blue) and one for only two (yellow). The trajectories of red, green and blue skyrmions actually overlap. We then present the superposition of the tracking markers (presented on top of the third image). In conditions where the skyrmions are not dense, this method presents very little possibility to confuse skyrmions between images; however, when the skyrmions are dense (when their separation is comparable to their typical displacement), errors become probable. For this reason, we did not take measurements in the very dense skyrmion regime. The velocity is calculated from the skyrmion centre position before and after the pulse, and then averaged over successive frames to obtain its velocity.
The procedure for measuring the skyrmion dynamics consists first in choosing a temperature where skyrmions naturally nucleate at low enough magnetic field (slightly below 290 K for the RE dom. sample, for example). Then, the sample is saturated at high field which is slowly decreased down to the natural nucleation of skyrmions. Then the field of the experiment is fixed, and current pulses of gradually increasing current density are applied while monitoring the skyrmions position by MOKE. At some current density threshold, skyrmions naturally nucleate at the magnetic track edges, as observed by the appearance of new skyrmions after the current pulse. In the next chapter 5.1 we discuss in more detail different experiments to control the nucleation of skyrmions. In the tracking experiments presented in this chapter we simply used the natural nucleation of skyrmion happening at the magnetic track edges. Edges defects can act as notches that are known to favours skyrmion nucleation by currents [316].

In figure 4.3 b) we present all the initial and final position of skyrmions tracked for one set of measurements at -1, -2.5, -4 and -5.5 mT for the RE dom. sample at 288.5 K. We can see that most skyrmions are nucleated on the right side of the track. This is explained by two reasons, the first one is represented in figure 4.3 a), where the Oersted field spatial intensity is represented on top of a magnetic track. We see that for the largest current densities reached in our experiments (around 350 GA/m^2) the Oersted field at the edges is far from negligible, with values above 3mT at 1μ m from the edge. A 3 mT field along the skyrmion core is sufficient to favour stripes as seen in the sample phase diagram in Fig. 3.15. The external field applied against the skyrmion core mitigate this effect but we indeed see that the Oersted field favours up core magnetisation, i.e black skyrmions in the MOKE images of RE dom. sample. This Oersted field direction therefore determines the edge of preferential nucleation. Also, even though the Oersted field on the other side is reversed (unfavourable for nucleation), if skyrmions would nucleate there they might reach the edge of the track (and annihilate) before the end of the pulse and so disappear from the image. The Oersted field gradient effect on the skyrmion dynamics is discussed later in Sec. 4.7.3.

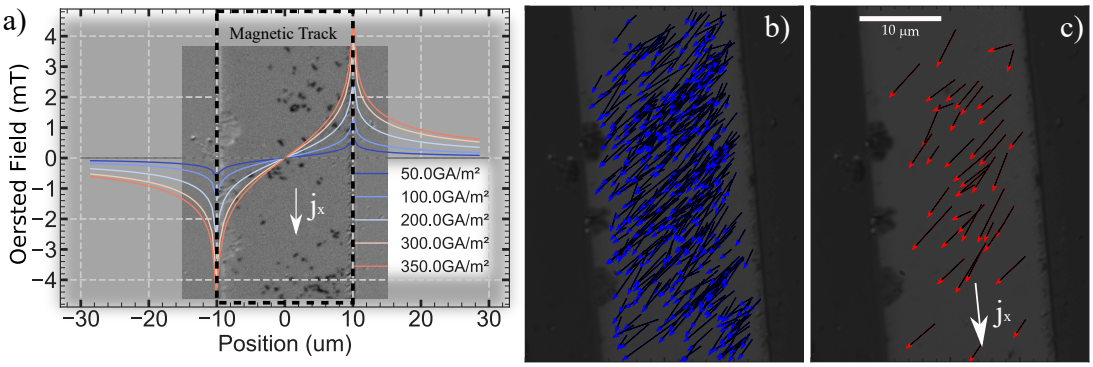

Figure 4.3: Oersted field and skyrmion nucleation. a) Out-of-plane (along $\vec{e}_z$) Oersted field across the track, for several current densities. Computed with formulas found in suppl. [125] b) Starting and ending points (origin to head of arrows) of all the skyrmions measured at 288.5K for RE dom. sample. b) Skyrmions moving with at least 70% of the recorded maximum speed (200 m/s).

Finally, we present in figure 4.3 c) skyrmions with at least 70% of the maximum speed measured from this set (200 m/s). This is done to visually verify the homogeneity of our measurement. We do see a reduction of fast skyrmions close to the top and bottom of the image, but these are believed to be mainly due to analysis bias because skyrmions are harder to follow close to the edges of the image and so we preferentially tracked skyrmion closer to the centre of the image. There is otherwise no clear inhomogeneity in the track observed directly by the positions and speed of the tracked skyrmions. Statistical analysis neither pointed to any obvious inhomogeneity.

4.2 SOT-driven skyrmion dynamics in RE dom. sample

Most of the following results are part of the work published in ref. [25].

We followed the procedure presented above to measure a large number of skyrmions in the RE dom. sample, around 800 skyrmions in two sets of measurements, one at 288.5 and one at 290 K for different applied magnetic fields. As presented in Sec. 3.4.3, the skyrmion size can be tuned by the application of a magnetic field. We then apply magnetic fields oriented against the skyrmion core to compress their size and access their size dependant dynamical properties.

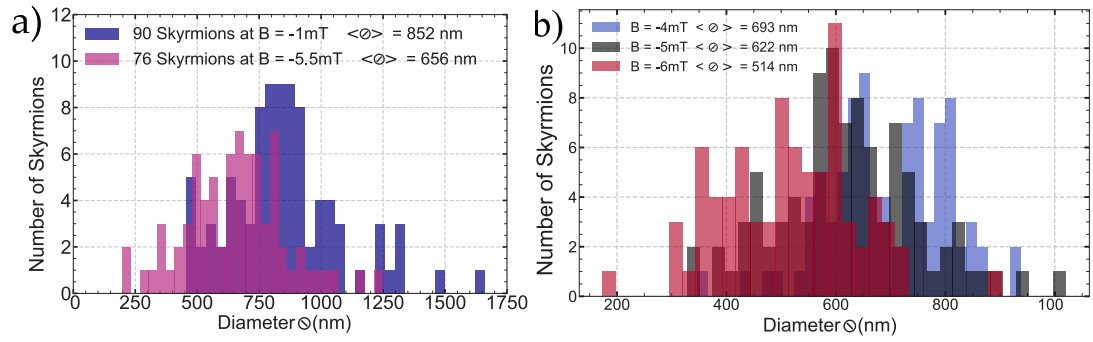

Figure 4.4: Tracked skyrmions size histograms. a) Two skyrmion size histograms out of the four magnetic fields applied for the tracking measurements at 288.5K. b) All three skyrmion size histograms of the measurements at 290 K.

As observed in the histograms in Fig. 4.4 a) at 288.5K and b) at 290 K, the skyrmion tracked present a rather large distribution of size. For example, at $B = -1$ mT, the average diameter is $\langle \varnothing \rangle = 852$ nm and the standard deviation is 230 nm. The rather large size distribution is explained by the effects of pinning inhomogeneity [314] that deforms skyrmions and modify their local equilibrium size, coupled to the very low domain-wall energy near T_R, which lead to a very shallow energy versus skyrmion size close to T_{D_c} as described in the previous chapter 3.2.2. But, nonetheless, as seen by the mean value of each histogram, the average skyrmion size is indeed observed to reduce with increasing magnetic field. The wide distribution of size is the main reason behind the need to measure a rather large number of skyrmions in order to obtain statistically meaningful quantities.

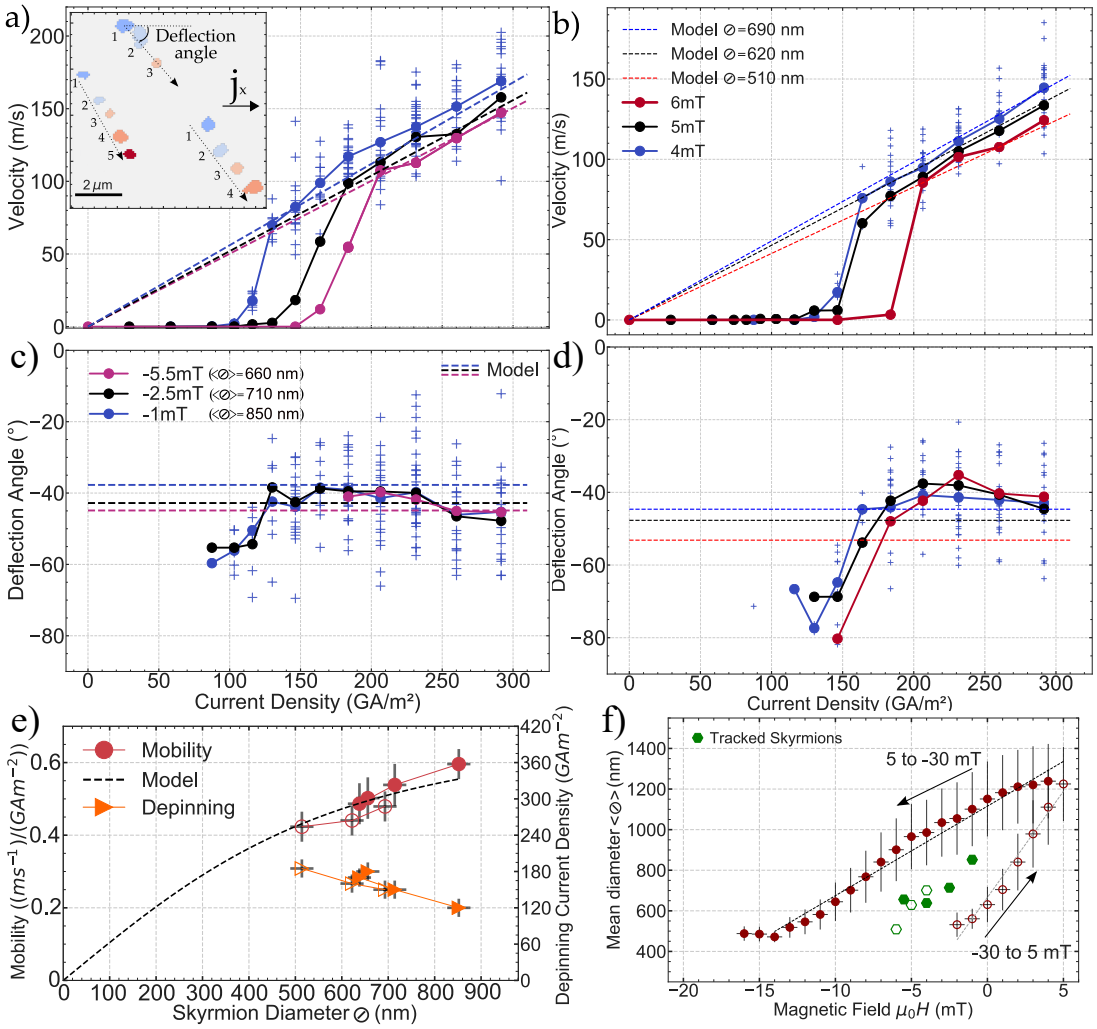

Figure 4.5: SOT skyrmion dynamics in RE dom. ferrimagnetic sample. a-d) Skyrmion velocity and deflection angle versus current density, for three different magnetic fields at 288.5 K (a,c) and 290 K (b,d). The line and circles are the mean values of all tracked skyrmions, and the crosses are the measurements for individual skyrmions (only shown for one value of field for clarity). The inset in a) shows the superposition of the binarized images after 5 successive 10-ns-long pulses of 210 GA/m^2 showing three propagating skyrmions. e) Skyrmion depinning current density and mobility versus skyrmion diameter measured at 288.5 K (filled markers) and 290 K (empty markers). The dashed lines in a-e) correspond to the values calculated by the model described in sect. 1.6.6. f) Averaged skyrmion size of tracked skyrmion measured at 288.5 K (green filled markers) and 290 K (green empty markers). Red markers are the averaged size measured at 288.5 K for minor hysteresis loop from -30 to 5 mT adapted from Fig. 3.20.

We study the current-driven skyrmion dynamics in a 20-μm-wide magnetic track.

At 288.5 and 290 K, for different magnetic fields, skyrmions positions are tracked over several images. We usually send a single 10 ns current pulse between each image. For small current densities, we apply several current pulses (5-1000) between each image to increase the skyrmion displacement up to a measurable value. The pulse repetition rate is kept very low (50 Hz) to avoid cumulative Joule heating effect (see sect. 4.7.1). We present in figure 4.5 the velocity curve and deflection angle with current density obtained for different applied magnetic field for the two sets of measurements, a-c) at 288.5 K and b-d) at 290 K.

As observed in figure 4.5 f), the averaged size of skyrmions tracked at different magnetic fields is observed to decrease with increasing magnetic field. It is interesting to plot these sizes with the ones obtained in the previous chapter (Fig. 3.20), as the sizes of the tracked skyrmions lay between the hysteresis found during the minor hysteresis loop. The origin of the hysteresis can be attributed to the effects of pinning [314, 317, 313] as discussed in section 3.4.3. It is then quite consistent to observe skyrmions nucleated by current pulse to find equilibrium sizes inside of the size hysteresis. Also, the averaged radius of tracked skyrmion varies by ≈ 34 nm/mT which is very consistent with observations of section 3.4.3.

The inset in Fig. 4.5a) shows the parallel trajectories of three black skyrmions (with Co moment along $-\vec{e}_z$) over five successive superimposed images. Note that some skyrmions disappear and are not present in the last images. Indeed, most skyrmions disappear after a few frames, and only a few cross the entire track especially beyond the region where the Oersted field is opposite to the skyrmion core.
Skyrmions move along the current direction ($\vec{e}_x$), opposite to the flow of electrons, which is coherent with the SOT and chirality given by a Pt buffer layer. The presence of SOT is confirmed by torque measurements presented in the previous chapter on magnetic properties characterisation. There is a significant deflection towards $-\vec{e}_y$, that we attribute to the gyrotropic force related to the skyrmion topology [205]. Note that it is opposite to that of a skyrmion with same cobalt core orientation in a pure cobalt film [125, 48]. Indeed, the gyrotropic deflection is expected to be proportional to the L_S of material, which is negative in this GdCo film below T_{mc}, opposite to that of a pure Co film. This property will be discussed in mode details in section 4.8.
Figs. 4.5a-b) and c-d) show the skyrmion velocity and deflection angle versus current density, J, at three values of applied magnetic field. We observe, at low J, a hopping regime of very few moving skyrmions with a badly defined deflection angle and very slow velocity. This is followed by an abrupt transition at a depinning current density J_D above which most skyrmions propagate and obey a linear velocity regime that extrapolates to zero. These skyrmions move up to 170 m/s (on average) for the largest current density of $J = 290$ GA/m^2 and $B = -1$ mT, resulting in a mobility of 0.59 ms^{-1}/GAm^{-2}.

Skyrmions display a large deflection angle of $-40° \pm 10°$ once the linear regime is reached. During the depinning regime, the angle is found to be larger. However, only a few skyrmions moved in these conditions and were mostly located near the edge of the track, which may strongly bias the measurement of the angle as skyrmions with very low deflection angle might not escape the very edge and so would not be measured. The angle seems also to increase at the largest current densities, which may be due to an effect of shape distortions [162].

The mobility and J_D are observed to vary with the applied magnetic field: the lowest $J_D = 125$ GA/m^2 and highest mobility are observed for the lowest field (-1 mT). No clear effect of the field on the deflection angle can be discerned.

We observe the lowest depinning current J_D and the highest velocity for the smallest applied magnetic field, i.e., for the largest skyrmions. The relation between the dynamic features and the magnetic field might thus be attributed to the change in skyrmion size (Fig. 4.5e). As for depinning, previous simulation studies of skyrmions pinned in granular films [318, 319] predict that the pinning threshold varies strongly with skyrmion size and attains a maximum when the diameter is comparable to the length scale of the variation of the effective anisotropy modulation. The presented data shows a strong variation of pinning with size in an amorphous film, suggesting that the conclusions of those studies may also be applied to inhomogeneous films other than multi-crystalline materials. The observed variation of J_D with diameter is compatible with a characteristic pinning length smaller than the observed diameters.

Although not directly comparable, the microscopy cross section observations of a similar material (GdFeCo) deposited in the same conditions [201] and presented in figure 2.4 showed lateral Co rich structures with a length scale around 3 nm, suggesting that the pinning length scale of this film is indeed smaller than the observed diameters. However, in [318], the increasing depinning current due to the effect of anisotropy grain is sizeable only around a ratio of 1 to 10 between skyrmion and grain size. There are no known characteristic length of disorder in the order of 50 nm in our samples. The only one found in literature are about density modulation in the order of tens of nanometer that we do not expect for very thin films as they arise from self-shadowing during deposition [233, 242].
The observed velocity and mobility are significantly higher than what has been observed in other thin films (see reference [49] for GdFeCo and, for other materials, e.g., [211, 215, 48, 212]) or compare with 1.26. As we are far from T_{ac}, this high mobility is not due to the angular compensation.
The small depinning current observed and clear linear regime are pointing to the fact that these skyrmions are observed away from the depinning regime whereas most other skyrmion propagation observations were performed below or near the pinning threshold. Another factor for the lower mobility reported in previous studies is the smaller skyrmions that were studied, which is a observed to be an important parameter in these measurements, but appears to be even more important as discussed in section 4.9.

4.3 Modelling skyrmion dynamics

The model presented in Sec. 1.6.6 can be applied to ferrimagnetic skyrmions using Wangsness effective model (see sec 2.3.1), which assumes a perfect antiparallel alignment between the sublattices.

As the effective α diverges at T_{ac} ($\alpha = L_\alpha/L_S$), it is convenient to use the always-finite L_α instead. The f, d and n parameters are unchanged as they are purely functions of the texture's morphology. We can then rewrite eqs. 1.40 as follows:

$$v_0 = -\frac{\hbar j \theta_{SHE}}{2eL_\alpha t}\frac{f}{d} \tag{4.1a}$$

$$\rho = \frac{L_S}{L_\alpha}\frac{n}{d}. \tag{4.1b}$$

This formalism successfully describes the vanishing gyrotropic deflection expected at the angular momentum compensation T_{ac} (where $L_S = 0$) [320, 49, 263]. The velocity modulus displays a maximum at T_{ac} with $|\vec{v}| \approx |v_0|(1 - \frac{1}{2}\rho^2)$.
Equation 4.1 show that L_α determines the deflection free dynamics (v_0). This explains why double magnetic lattices material with smaller L_s than ferromagnetic materials do not inherently offer faster dynamics, as L_α is comparable for both types of materials.

Their main advantage is found for the potentially reduced deflection. A two Thiele equation model, developed in the next section 4.3.1, shows that this effective approach is valid even in the case of imperfect anti-parallel alignment.

4.3.1 Double magnetic lattice Thiele based equation

A skyrmion in a double-lattice material can be described as a bound state of two skyrmions, one in each of the two antiferromagnetically-coupled magnetic lattices, described with two Thiele equations [147, 321]. This double-equation approach may also be used to model the dynamical effects due to separation between the skyrmions of each sublattice, such as transient behaviours and inertia, which appear when the coupling is weak, as in synthetic antiferromagnets [322]. Here, we describe the steady state dynamics, for which the skyrmion velocity $\mathbf{v}$ is the same in both equations (the skyrmions may still show a non-zero separation):

$$\mathbf{G}^{(1)} \times \mathbf{v} - \alpha^{(1)} D^{(1)} \mathbf{v} + \mathbf{F}^{(1)} + \mathbf{F}_{2/1} = 0 \tag{4.2a}$$

$$\mathbf{G}^{(2)} \times \mathbf{v} - \alpha^{(2)} D^{(2)} \mathbf{v} + \mathbf{F}^{(2)} + \mathbf{F}_{1/2} = 0 \tag{4.2b}$$

where the superscript (i) refers to lattice i, the parameters $\mathbf{G}^{(i)}$, $\alpha^{(i)} D^{(i)}$, and $\mathbf{F}^{(i)}$ being specific to each lattice. The additional forces $\mathbf{F}_{1/2}$ and $\mathbf{F}_{2/1}$ account for the interaction between the two lattices. These forces are analogous to a spring, and couple the two skyrmions. Whatever the skyrmion separation, the action-reaction principle requires that $\mathbf{F}_{1/2} = -\mathbf{F}_{2/1}$. Summing the two equations shows that the bound state velocity is independent of the coupling forces [147] and leads to a single Thiele equation with effective parameters $\mathbf{G}_{\text{eff}} = \mathbf{G}^{(1)} + \mathbf{G}^{(2)}$, $(\alpha D)_{\text{eff}} = \alpha^{(1)} D^{(1)} + \alpha^{(2)} D^{(2)}$, and $\mathbf{F}_{\text{eff}} = \mathbf{F}^{(1)} + \mathbf{F}^{(2)}$. For a sufficiently large coupling, the textures are similar in both lattices, but with opposite magnetization direction. Therefore $n^{(1)} = -n^{(2)} = n$ (n is odd in $\mathbf{m}$), $d^{(1)} = d^{(2)} = d$ and $f^{(1)} = f^{(2)} = f$ (d and f are even in $\mathbf{m}$) and the effective forces can be written as

$$\mathbf{G}_{\text{eff}} = \left[L_S^{(1)} - L_S^{(2)} \right] tn \; \mathbf{z} = L_S tn \; \mathbf{z} \tag{4.3a}$$

$$(\alpha D)_{\text{eff}} = \left[\alpha^{(1)} L_S^{(1)} + \alpha^{(2)} L_S^{(2)} \right] td = L_\alpha td \tag{4.3b}$$

$$\mathbf{F}_{\text{eff}} = -\frac{\hbar}{2e} \mathbf{J} \left[\theta_{\text{SHE}}^{(1)} + \theta_{\text{SHE}}^{(2)} \right] f = -\frac{\hbar}{2e} \mathbf{J} \theta_{\text{SHE}} f \tag{4.3c}$$

where right-hand sides are expressed with the effective parameters defined earlier. In the steady state, the solution is identical to the one obtained for infinite coupling with the effective parameters in the previous section. This shows that the infinite coupling approach is valid even for non-zero separation between skyrmions in the two lattices.

4.3.2 Effect of skyrmion size on Thiele parameters

The geometric parameters from equations 1.38 (n, f, d) are expected to vary greatly with the ratio of skyrmion radius and the magnetic domain wall width parameter Δ. This is particularly important near T_R where Δ becomes very large. Since n corresponds to the skyrmion topological number, it is independent of the skyrmion size.
The integral that defines f is similar to a micromagnetic Dzyaloshinskii-Moriya integral [197] and therefore involves the skyrmion chirality c ($c = \pm 1$ respectively for clockwise and counterclockwise spin rotation).
In the limit of $R \gg \Delta$, $f \to \pi^2 cR$. Since $f \to 0$ for small skyrmions, this linear variation can be used as an approximation for the full range of size. We also note its independence with Δ. The integral d is similar to the micromagnetic exchange integral [205, 321], and it is expected to scale in the same way with the skyrmion size.

For a skyrmion radius R large as compared to Δ, $d = 2\pi R/\Delta$ [208, 125].
However, as shown by Belavin and Poliakov [163], the exchange integral of a topological texture does not vanish even at infinitesimally small, and therefore, for $R \to 0$, $d \to |n|$. This implies that the dissipation does not vanish at small sizes [147]. To describe the dissipation over the full range of R, the two limits can be interpolated as

$$d \approx |n| \exp\left(-\frac{2\pi R}{|n|\Delta}\right) + \frac{2\pi R}{\Delta}. \tag{4.4}$$

The variation of these three parameters with the skyrmion radius is shown by the lines in Fig. 4.6a,b. The approximations for small and large R/Δ ratio for d and f are shown as dashed lines in Fig. 4.6. As a consequence, the mobility, which is proportional to f/d (Eq. 4.1), vanishes for small skyrmions (Fig. 4.6d), and the deflection is maximum but does not diverge (Fig. 4.6c).

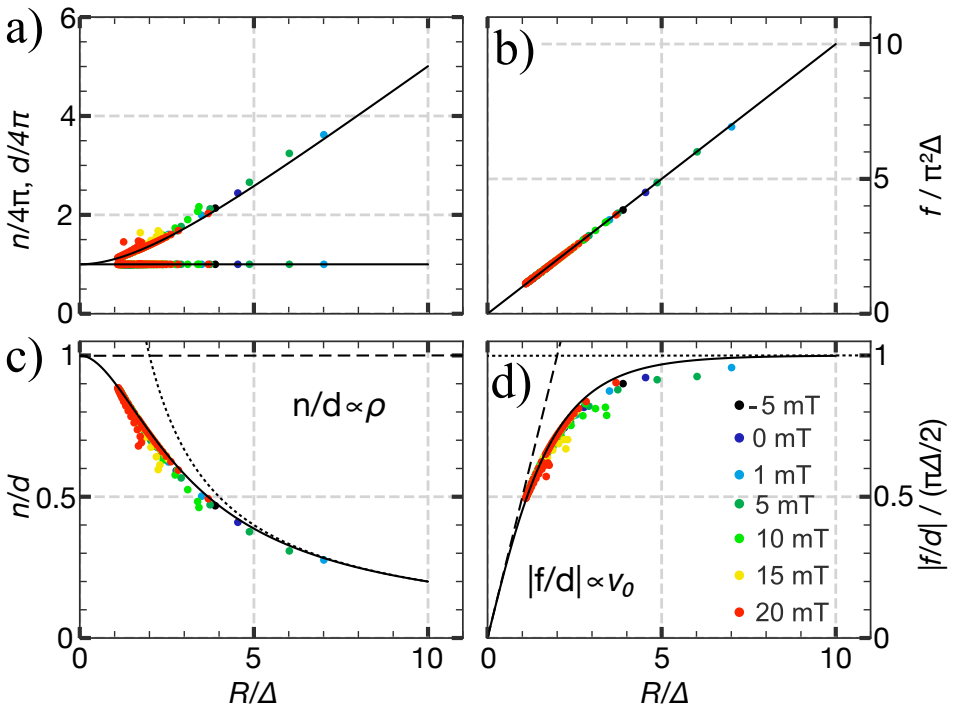

Figure 4.6: Geometric components of the Thiele parameters versus the normalized skyrmion radius (R/Δ). a) Gyrotropic n and dissipation d parameters. b) Spin Hall effect force related length f (divided by Δ so that is represented as a function of R/Δ). c) n/d, proportional to the skyrmion deflection ρ. d) f/d, proportional to the skyrmion deflectionless velocity v_0. Solid lines correspond to the analytical expressions in the text and the dots correspond to the simulations of a GdCo ferrimagnetic alloy at different fields and temperatures. In c) and d), the dashed line shows the small skyrmion limit ($n/d = 1$, $|f/d| = \pi R/2$) and the dotted line the large skyrmion limit ($n/d = 2\Delta/R$, $|f/d| = \pi\Delta/2$).

4.4 Model validation by micromagnetic simulations

We performed micromagnetic simulations of skyrmions in a GdCo thin film using MuMax^3 [323], modified to account for the specificity of ferrimagnetic films [262, 250], each lattice being described independently, and coupled with an antiferromagnetic coupling $J_{\mathrm{TM/RE}}$. We keep all parameters constant in temperature except for the sublattice magnetisation and angular momentum, calculated with the mean field model, Fig. 3.1, from which the measured magnetisation M_s is separated between both sub-lattices contribution which finally allows to compute: $L_S^{\mathrm{Co}} = M_S^{\mathrm{Co}}(T)/\gamma_{\mathrm{Co}}$, $L_S^{\mathrm{Gd}} = M_S^{\mathrm{Gd}}(T)/\gamma_{\mathrm{Gd}}$.

The parameters used for the simulations are presented in Table 4.1 and corresponds to parameters measured or extrapolated by mean-field.

	Co	Gd
g	2.22	2.00
α	0.019	0.019
M_S (MA/m)	[0.62 – 0.5]	[1.1 – 0.4]
K_u (kJ/m^3)	11.5	0
A^{ex} (pJ/m)	4.6	0
D_{m} (mJ/m^2)	0.22	0
$J_{\mathrm{TM/RE}}$ (MJ/m^3)	25	25
θ_{SHE}	0.03	0

Table 4.1: Parameters used for the micromagnetic simulations. Only the M_S and L_S of the two sublattices vary with temperature according to the mean field model (fig. 3.1). $J_{\mathrm{TM/RE}}$ is the interlattice coupling. Note that D_m is positive D_m so skyrmions move against the current.

The skyrmion mobility, and velocity ratio between v_x and v_y versus temperature and field are shown in Fig. 4.7a-b). These simulations are performed in a low current regime ($J = 100$ GA/m^2) so that the skyrmions do not deform by the SOT force.

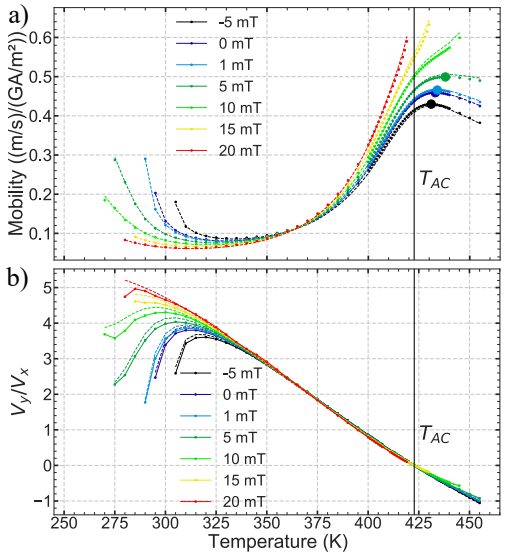

Figure 4.7: (a) Mobility $|v|/J$ versus temperature for different magnetic fields from simulations (points) and model (dashed lines). The circles represent the maximum mobility for each field. (b) deflection v_y/v_x versus temperature and field. $J = 100$ GA/m^2.

The equilibrium sizes obtained in the statics simulations (Fig. 3.17) are used to input a skyrmion with an already relaxed size for each temperature. The skyrmion is then excited by the SOT torque and its position is numerically determined. Such kind of simulation is quite sensitive to the size of the mesh used. Periodic boundary conditions were used, which is valid as the skyrmion size was much smaller than the total mesh size to ensure an isolated skyrmion dynamics. Also, the size of each cell should be chosen to be smaller than the typical displacement of the skyrmion (which can be increased by increasing the time of the excitation) to ensure correct measurement of the skyrmion displacement. Finally, there is a transient regime at the beginning of the simulation because of the effect of SOT that induces a canting of all simulated spins.

The velocity is then measured after the transient regime on an optimised simulation mesh. We observe a very good agreement between the simulation points and the lines computed from the model. A velocity maximum is observed close to T_{ac}, as predicted by the model. However, the velocity curve is more complex than a simple peak, and the maximum velocity occurs above T_{ac}.

Let us consider the effect of the radius first. In this sample T_{ac} is located very close to the peak of the magnetisation above T_{mc}. This makes the radius increasing up to T_{ac} but then it still increases for around 30 K afterwards. This means that the mobility is increasing due to T_{ac} but also due to the increasing radius (similar to what happens below T_{ac}). This effect then adds up to the lowering of angular momentum density, which can indeed shift the peak of mobility depending on the variation of L_s and R with temperature. Also, because of the rather high T_{ac}, effects from T_c starts to be present. Indeed, because L_α rapidly reduces close to T_c, which increases the mobility, this other effect broadens the mobility peak.
To conclude, the maximum observed slightly above T_{ac} is due to a combination of lowering L_α and skyrmion size evolution with temperature. The mobility minimum at T_{mc} is due to the size minimum (Fig. 3.17).

The skyrmion deflection v_y/v_x crosses zero at T_{ac} and is linear around T_{ac}. This supports the model which predicts that $v_y/v_x \propto L_S$. Far from T_{ac}, the deflection deviates from this linear relation due to the large skyrmion size, as the deflection decreases as $1/R$. The model, using no fitting parameters other than the static skyrmion diameter (obtained from simulations), is in quantitative agreement with the simulations, which confirms that the effective model used that considers infinite antiferromagnetic coupling is valid even for finite coupling.

4.5 Model comparison with experiments

In order to compare the analytical model with our experiments, we need to parameterised the model as precisely as possible. The parameters of this sample, RE dom., are presented in table 2.2.

Let us sum up the behaviour described by the model for small and large skyrmions (with respect to Δ). In the limit of small radius compared to domain wall width, the model predicts that $v_0 \propto f/d \propto R$ and that $\rho \propto n/d \to 1$ (its maximum). In the large radius limit, v_0 is independent of the R and $\rho \propto 1/R$. So the velocity is expected to increase with skyrmion size and the deflection angle to decrease. Therefore, the velocity v (Eq. 1.39b) is expected to increase and saturate with skyrmion size, while the deflection angle should be maximum and rather constant for small skyrmions and then decrease with increasing size. For a given radius, this model, which does not account for pinning, predicts a linear dependence of the velocity with current and a constant deflection angle.

The behaviour expected for the velocity is indeed observed in fig 4.5 where we observe a clear linear regime with current density after a critical current density and a reduction of the velocity with skyrmion diameter.
We can also see that the mobility $\mu = |v|/J$ presented in (Fig. 4.5e) yield a very satisfactory fit with this model, where only θ_{SHE} is used as a free parameter (its behave as a scaling factor). It yields $\theta_{\mathrm{SHE}} = 0.03$ which is in the range of the experimental values obtained from torque measurements from literature [291] but also the one we measured on this sample 2.24.

The model predictions with the constrained parameters are shown by the dashed lines in Fig. 4.5. They reproduce the size dependence of the linear velocity regime of skyrmions taken at 288.5 K and 290 K where only the averaged skyrmion size measured is inputted. Between 4.5a-c) and b-d) the magnetisation is slightly modified according to the measured magnetisation.

The predicted deflection angles are consistent with the experimental angles, but the agreement is less satisfactory, in the sense that the expected variation of deflection angle with diameter is not observed. Moreover, for the skyrmion sizes we observe ($R/\Delta = 15$), we expect the mobility variation with size to be driven only by the variation of ρ because of the large skyrmion regime. Therefore, the variation of mobility implies a variation of deflection that is not observed. This may be due to the dispersion of the measured deflection angle, which can blur the variation with size.
The model predicts the angle to be more dispersed than the velocity v for a given size distribution. The larger sensitivity of the deflection compared to the velocity is illustrated in Fig. 4.8, where we calculate (using the Thiele model) the dispersion of skyrmion velocity and deflection angle from the experimental histograms of skyrmion radius at -1mT. The ratio of standard deviation to mean value is shown in the panels. For the same radius distribution, the deflection angle indeed shows to be more dispersed which might then explain why the expected varying angle is not observed in our experimental data. Indeed, the observed effect of the skyrmion size on the velocity is rather small, and we understand here that the effect on the angle is even harder to observe.

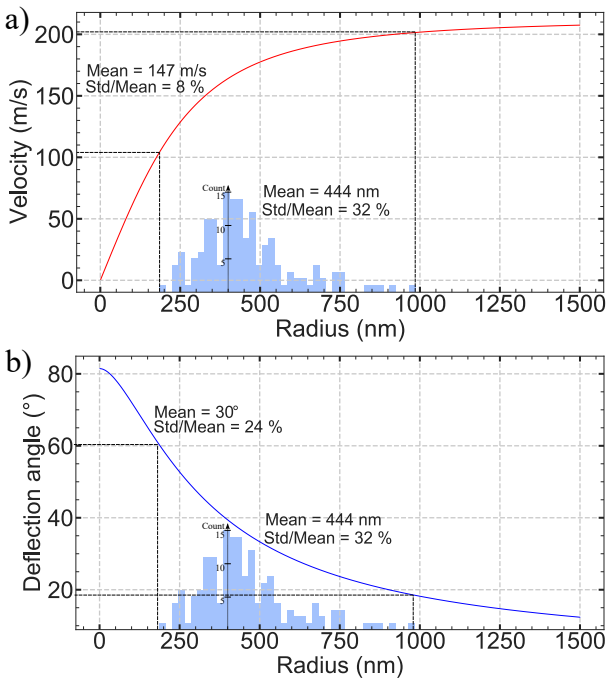

Figure 4.8: Skyrmion velocity and deflection relative distribution. Comparison of the dispersion of velocity (a) and deflection angle (b) predicted by the model from an experimental distribution of skyrmion size of $444 \pm 32\%$ ($B = -1$ mT) shown as histograms in both figures.

Another very probable cause to the slight imprecision of the model to describe our experimental measurements may be due to the effects of skyrmion-skyrmion interactions[324, 325, 210], that the model does not account for. It seen quite obvious that the skyrmion-skyrmion interaction can modify the dynamics of the skyrmions, but further micromagnetic simulations of multiple skyrmions with various densities would be interesting to test this hypothesis and obtain quantitative expectations.

Summary

In summary, we observe skyrmions in a RETM ferrimagnetic thin film, at room temperature and close to T_R with zero external magnetic field and then modified the skyrmions sizes by the application of an external magnetic field in order to study the effect of skyrmion size on their dynamical properties.
Skyrmions are driven by SOT and follow a clear linear regime after a steep depinning threshold, that decreases with the skyrmion size. The flow regime, beyond the effects of pinning, was observed, with a linear dependence of the velocity extrapolating to zero.
The mobility, its dependence on the skyrmion size, and the trajectory deflection angle were found to be in quantitative agreement with an analytical model based on the Thiele equation, with a single fitting parameter.
This shows that the rigid skyrmion model using the Thiele equation is sufficient and quantitative, as long as the skyrmion is unhindered by pinning and even for the largest current density that was applied.
In particular, the model predicts a strong reduction of mobility at smaller diameters, which is potentially a problem for scaling down skyrmion devices.

4.6 STT and SOT efficiency comparison

It should be noted now that has presented in Fig. 1.23b), our typical stack of Ta(1-3)/Pt(5)/GdCo(5-8)/Ta(3-5)/Pt(0-1) (nm) implies a non-uniform distribution of the current density between each layer. We can estimate roughly this distribution considering a model of parallel resistors where the typical resistivity of each material is obtained from the literature. This typically yields Ta(10%)/Pt(50%)/GdCo(10%)/Ta(30%) (% of current) without passivating Pt layer. This shows that we can expect a ratio around 8 between the current resulting in SOT effect (Pt and Ta) and the one resulting in STT effect (GdCo). This ratio can then be directly inputted in Fig. 1.25b) because the velocity are linear with the current density for both SOT and STT.
In conclusion, it shows that the contribution from STT can be safely neglected, even more considering the typical size of the skyrmions we observed in our sample (ranging from R=200 to 500 nm). It should be noted that the STT contribution can become rather important for very small skyrmions below 100 nm in diameter, especially in the case of thick (or conductive) magnetic material.

4.7 Parasitic current induced phenomena

The measurement presented before can be sensitive to parasitic effects related to the electrical current used. We explore the three major phenomenon with potential important implications on our measurements: the Joule heating, pulses echos, and finally the effect of the Oersted field.

4.7.1 Joule heating

High current densities may lead to significant changes in temperature due to Joule heating, which could drastically change the skyrmion properties and stability, including the direction of the gyrotropic deviation. Taking into account the temperature of the sample during the current pulse is therefore very important. For instance, it greatly changes the magnetisation of a ferrimagnetic sample .

To assess the Joule heating produced during the pulse, we studied the variation with temperature and current of the transmission coefficient (S_t), using a similar track in the same sample ($R = 470\ \Omega$). Firstly, a low current pulse (to avoid any heating) is applied for different temperature set-points and its $S_t(T)$ is measured. A linear decrease of $S_t(T)$ is observed (-0.0091 %/K, Fig. 4.9a) which is attributed to a linear increase in resistance of the sample with the set-point temperature. Then, the change of S_t due to Joule heating was measured for various pulse current densities J and pulse widths (Fig. 4.9b). Using the previous fit of $S_t(T)$ as a temperature calibration, the Joule heating can be quantified. The Joule heating is deduced and shown in Fig. 4.9c versus J for various pulse widths. For 10 ns, as used experimentally, it seems rather large (30±20 K). However, it is not large enough to cross T_{ac} (which we estimate to be about 420 K), which would, e.g., change the sign of the deflection and so drastically change the observed properties.

Also, this sizeable temperature change decrease the magnetisation of the sample during the pulse and so lower the equilibrium size of the skyrmion during its displacement. This can then have a quantitative impact on the skyrmion dynamics, but it seems quite difficult to assess such an effect due to its very small time scale. However, as presented in the two phase diagrams of 3.15 and 3.16, the magnetisation variation with increasing temperature is opposite between the two samples in the skyrmion stable regions. Therefore the potential effect of the Joule heating on the magnetisation and so skyrmion size and stability during the current pulse might then be explored by comparing both samples. For instance, a comparative study of the nucleation rate between a RE dom. or TM dom. sample might shed some light on this effect.

Finally, the characteristic time to reach a thermal steady state is computed using finite elements simulation. It shows a characteristic time scale is in the order of the μs which implies that no cumulative Joule heating is expected below the MHz repetition rate.

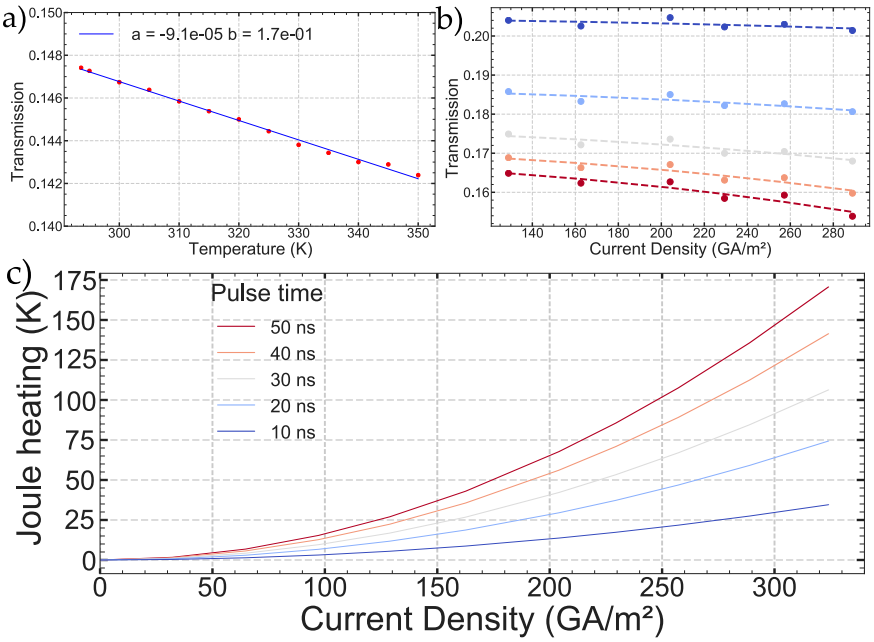

Figure 4.9: Experimentally measured Joule heating. a) Transmission coefficient S_t versus set-point temperature T. The slope of the linear fit ($S_t = aT + b$) is used as a temperature calibration. b) S_t versus J fitted with a quadratic law ($S_t(J) = cJ^2 + d$). c) Joule heating versus J calculated from the fits of a) and b), considering $\Delta T(J) = \frac{c}{a}J^2$.

4.7.2 Pulse echoes

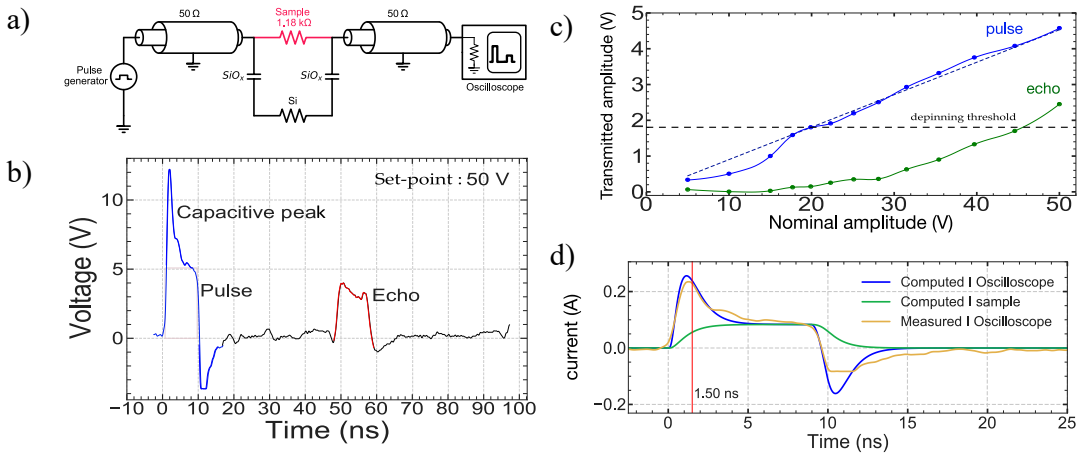

Figure 4.10: Echo and capacitives effects in magnetic tracks. a) Schematic of the experimental circuit. b) Oscilloscope trace of the transmitted signal. c) Pulse and echo amplitudes versus nominal applied voltage (non-linearity due to non-linearities of the pulser input impedance with nominal voltage). d) Calculated pulse profile (in green) and transmitted pulse profile (blue) computed using Python library PySpice where we reproduced the circuit presented in a).

The experimental circuit is shown in Fig. 4.10a. The device is modelled by a 1.18 kΩ resistor connected in series with the pulser and an oscilloscope with coaxial cables. The large connection pads (200×200 μm^2) and the doped (conductive) Si substrate, separated by 100 nm of SiOx, act as two capacitors and a resistor. The shunting of the current through the substrate is modelled by a parallel circuit.
The device is excited by short voltage pulses generated by a Picosecond Pulse Labs pulser, and the transmitted signal is measured by the oscilloscope, where it is absorbed. The oscilloscope trace shows the main pulse and an echo (Fig. 4.10b). The pulse shows capacitive peaks at the rising and fall edges due to the substrate shunting.

The current through the device is estimated from a circuit analysis made to reproduce the observed transmitted signal (Fig. 4.10d). The rise time of the current pulse through the device is computed to be 1.5 ns which is quite long and maybe due to the capacitive leakage that shunted higher frequencies. Also, the pulse width is measured around 9 ns. This suggests that the reported velocities may be underestimated by 10 %. This does not change any of our conclusions and would only increase by 10 % the fitted value for θ_{SHE} which would then be even closer to the experimental value measured.

The device represents a change in impedance of the circuit with an associated transmission coefficient of $S_{\mathrm{t}} = \frac{2Z_0}{R_{\mathrm{sample}}+Z_0}$. The reflected pulse (with 92 % amplitude) travels back to the pulser and is again partially reflected back to the sample, where it arrives 50 ns after the initial pulse, and is transmitted onwards to the oscilloscope. When the reflected pulse amplitude is lower than the depinning threshold (J_C) it will not affect the skyrmion position. However, at the largest current density, the echo is above J_C (Fig. 4.10c) and its effect was observed and corrected in the velocity reported in section 4.2. Such an effect can be avoided by several means. The first one is simply to improve the impedance matching of the magnetic track to reduce the amplitude of the reflected pulse. Otherwise, the reflection could be redirected to a 50 Ω resistor by properly timed switches (which necessitates cables with length compatible with the switches time response). Finally, an attenuator could be placed along the pulse path.

The pulse would be reduced on its way towards the sample, but the reflected pulse would then be attenuated twice and so its effect could be mitigated. This quick analysis of the electrical properties of the system shows how important is the precise design of an experiment involving electrical currents. Especially because we use very short current pulses, the rising time of the pulse of some 100 ps implies high frequency above 10GHz, where radio-frequency compliant circuits start to be necessary. For instance, current pulses below 3 ns would become too much attenuated to be useful (even in sample without capacitive leakage). This means that we can improve our sample design by taking special care of the full signal path. This implies more constraint on our designs, with shorter magnetic tracks for impedance matching and waste of space with ground plane in order to obtain good transmission lines.

4.7.3 Oersted field

The out-of-plane component of the Oersted field (B^z_{Oe}) for an infinite track can be obtained by integrating Ampère's law and is given by [15]:

$$\begin{aligned} B^z_{\mathrm{Oe}}(y) &= \frac{J\mu_0}{4\pi}\Bigg[-4(y+w/2)\arctan\left(\frac{t}{2(y+w/2)}\right) \\ &+ t\ln\left(\frac{t^2+4(y-w/2)^2}{t^2+4(y+w/2)^2}\right) \\ &+ 4(y-w/2)\arctan\left(\frac{t}{2(y-w/2)}\right)\Bigg] \end{aligned}$$

It is plotted in Fig. 4.3. B^z_{Oe} reaches 4.5 mT at highest current density explored here (350 GA/m^2), and is more than ± 1 mT on half of the 20 μm track. This could affect the skyrmions size and velocity in a way that depends on their position in the track. Indeed, B^z_{Oe} is positive on the right side of the track where the black skyrmions (with Co moment pointing down and magnetisation pointing up) are preferably nucleated.

The B^z_{Oe} shows a gradient across the track which exerts a sideways force on the skyrmion. The linearised deflection force from the Oersted field, valid for a large region centred on the track where most of the dynamics occurs, reads as [125]:

$$\vec{\boldsymbol{F}_{Oe}} = \frac{4\pi\mu_0 M_s t}{w} jhR^2 \vec{\boldsymbol{e}_y} \tag{4.5}$$

with w the width of the track, h the complete thickness and t the magnetic thickness. We neglect here the Oersted field gradient at the edge of the track, which can become invalid for narrow tracks.

The deflection force from the gyrotropic contribution is given by:

$$\vec{\boldsymbol{F}_G} = -4\pi L_s t v_x \vec{\boldsymbol{e}_y} \tag{4.6}$$

Considering typical parameters for our sample: $w = 20\mu$m, $t = 5$ nm , $h = 14$ nm, $v_x = 150$ m/s, $\gamma/2\pi = 18.3$ GHz/T, $J = 300$ GA/m^2 and $M_s = 80$ kA/m for skyrmion with 200<R<500 nm, the force due to the Oersted field is about 5% of the gyromagnetic force for large current density and large skyrmions, as shown in fig 4.11.

In order to properly take into account the effect of the radius on the gyrotropic deflection we use the expression of the model 4.1, so we can express v_x as follows:

$$v_x = \sqrt{\frac{(\frac{\hbar j \theta_{SHE}\ f}{2e L_\alpha t\ d})^2}{1+(\frac{L_s n}{L_\alpha\ d})^2}} \tag{4.7}$$

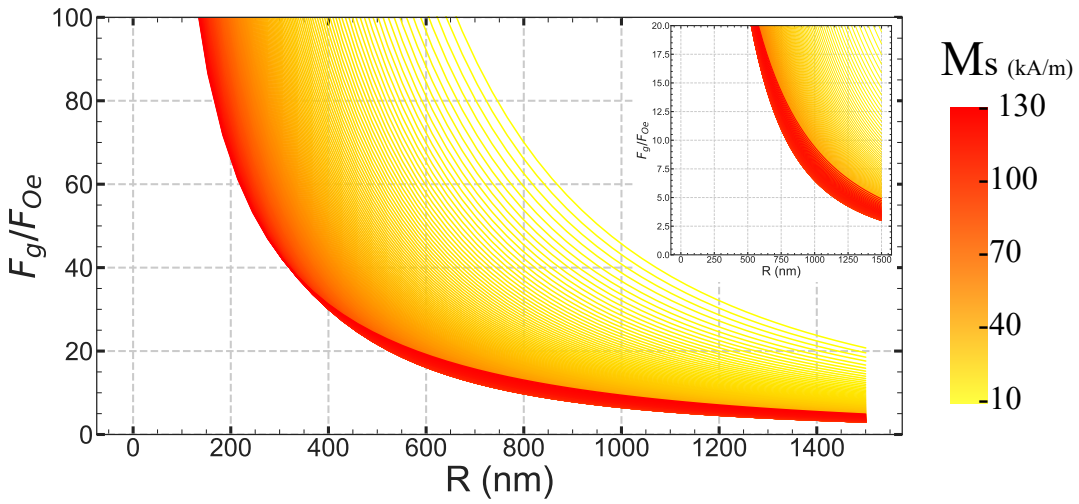

Figure 4.11: Gyrotropic on Oersted deflection contribution ratio with skyrmion size and magnetisation. The ratio between the gyrotropic and Oersted gradient contribution to the skyrmion deflection is presented for the material parameters of the RE dom. sample, considering several magnetisation that will also change the magnetic domain wall width parameter Δ. The inset shows the parameter region where the Oersted contribution can not be neglected.

We can then analytically compute the expected evolution as the gyrotropic deflection with radius, shown in figure 4.11, calculated for several values of magnetisation, considering all the other parameters to be the same as above. For large skyrmions, and so large R/Δ ratio, the contribution of the Oersted field cannot be neglected (when $F_g/F_{Oe} < 10$ in the inset). Also, the higher the magnetisation, the stronger the effect of the Oersted field, and so the lower F_g/F_{Oe} ratio. This shows that the Oersted contribution can become comparable to the gyrotropic contribution for large skyrmions with high magnetisation, especially in small magnetic tracks with high current densities.
It should be noticed that the contribution of the gyrotropic deflection and Oersted field do not depend on the same magnetic parameters:

$$\mathbf{F}_G \propto -L_s p_{Co} \vec{\boldsymbol{y}}$$

$$\mathbf{F}_{Oe} \propto M_s p_{Co} \vec{\boldsymbol{y}}$$

Therefore the Gyrotropic and Oersted gradient forces will reverse sign at respectively the angular compensation temperature and the magnetic compensation temperature. Let us consider a skyrmion with fixed polarity, with Co momentum in its core oriented along $-z$ ($p_{\mathrm{Co}} = -1$), as the "black" skyrmions in the MOKE measurements. The left panel of Table 4.2 shows the signs of the forces in this case. The force due to the Oersted field gradient is proportional to M_S, and so is along $+y$ below T_{mc} and $-y$ above it. On the other hand, the gyrotropic force depends on L_S, so it changes sign at T_{ac}. Therefore, the two forces oppose for $T < T_{mc}$ and for $T > T_{ac}$ but are in the same direction between the compensation temperatures.

4.8 Skyrmion dynamics across angular compensation

As discussed before, the models predict that the gyrotropic deflection of skyrmions changes sign at T_{ac}, which would be interesting to verify. We sum up the different signs of the deflections of skyrmion with temperature in Tab. 4.2 for the two signs of skyrmion Co core orientation (p_{Co}).

	$p_{\mathrm{Co}} < 0$				$p_{\mathrm{Co}} > 0$		
T	$T < T_{mc}$	$T_{mc} < T < T_{ac}$	$T > T_{ac}$	T	$T < T_{mc}$	$T_{mc} < T < T_{ac}$	$T > T_{ac}$
Sk_{Mcore}	$+z \odot$	$-z \otimes$	$-z \otimes$	Sk_{Mcore}	$-z \otimes$	$+z \odot$	$+z \odot$
p_{Co}	-1	-1	-1	p_{Co}	$+1$	$+1$	$+1$
F_G	$-y$	$-y$	$+y$	F_G	$+y$	$+y$	$-y$
F_{Oe}	$+y$	$-y$	$-y$	F_{Oe}	$-y$	$+y$	$+y$
L_s	$-$	$-$	$+$	L_s	$-$	$-$	$+$
M_s	$-$	$+$	$+$	M_s	$-$	$+$	$+$

Table 4.2: Comparison of the signs of the deflection forces (F_G and F_{Oe}) for a current propagating along $\vec{x}$ for $p_{Co} < 0$ (left) and $p_{Co} > 0$ (right). Sk_{Mcore} refers to the magnetisation in the core of the skyrmion. M_s and L_s are computed using [249] convention. Skyrmions that appear black in the MOKE images correspond to $p_{\mathrm{Co}} < 0$.

The temperature dependant gyrotropic deflection is a purely RETM system property. Available experimental results in ferrimagnets showed that the deflection of chiral finger-like domains is reversed at T_{ac} [263]. It was also found that the skyrmion deflection angle could be quite low in ferrimagnets even far away from compensation [49] but the effect of the angular momentum compensation on the skyrmion deflection has not yet been described.

As presented in chapter 3, the skyrmion stability region is found in ferrimagnets in a region close to T_{D_c}, located in the PMA region before the spin reorientation temperature T_R.

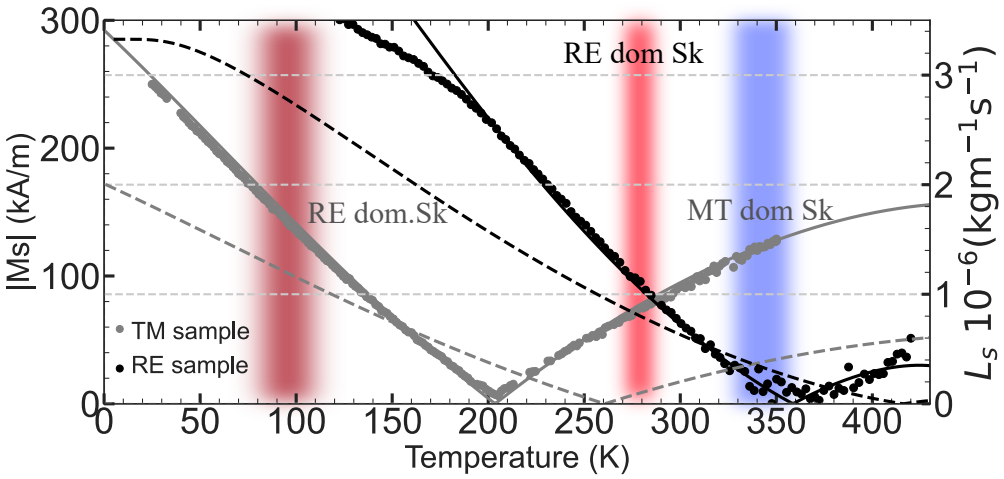

Figure 4.12: Magnetisation vs temperature for the RE and TM dom. samples. The saturation magnetisation $|M_s|$ (continuous lines) and the angular momentum $|L_s|$ (dashed lines) are presented for RE and TM dom. samples (red and blue). M_s is fitted with the mean field model. The regions where skyrmion dynamics are studied are shaded in red and blue.

We shall compare the skyrmion dynamics in the two samples described before (sect. 2.6), named again by their dominating lattice at 293 K (figure 4.12). We recall here their respective stack structures: Ta(1)/ Pt(5)/ $Gd_{0.32}Co_{0.68}$(5)/ Ta(3) (RE dominated) and Ta(3)/ Pt(5)/ $Gd_{0.3}Co_{0.7}$(8)/ Ta(5)/ Pt(1) (nm) (TM dominated). We present in Fig. 4.12 the magnetisation $|M_s|$ (measured and fitted by mean field), the angular momentum density $|L_s|$ extracted from mean field and the skyrmion stability region of both samples. We will then make two comparisons of the skyrmion dynamics, one between $L_s < 0$ and $L_s > 0$ of the TM dom. sample, and the second for $L_s < 0$ in the RE dom. sample with the $L_s > 0$ skyrmion dynamics of the TM dom. sample.

4.8.1 Skyrmion dynamics in the TM dom. sample

We tracked the skyrmion trajectories in the TM dom. sample at 90 K and 355 K, with the skyrmion velocity and deflection angle presented in Fig. 4.13. The measurements at 90 K (dark red) were obtained in a cryostat, as was a control measurement at 340 K (dark blue), realised to verify skyrmion dynamics in the TM dom. region, as the measurements presented at 355K (blue) were obtained out of the cryostat (for better resolution).

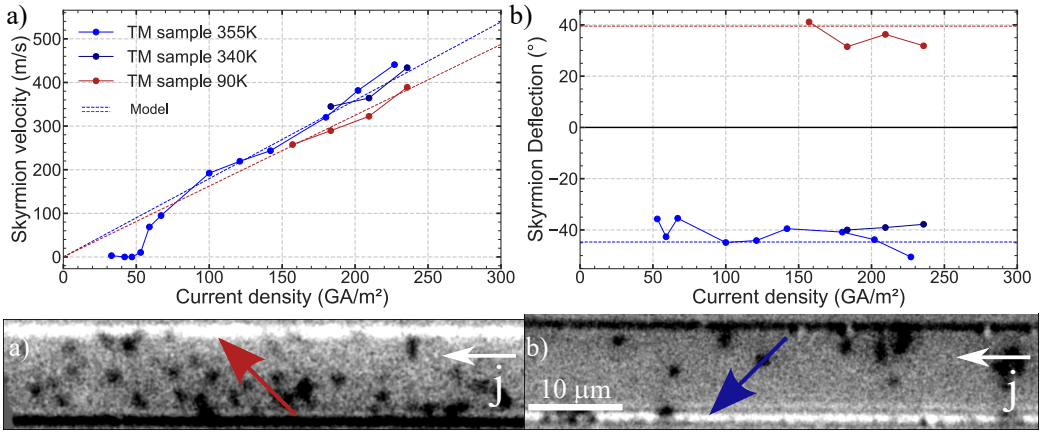

Figure 4.13: Skyrmion dynamics in TM dom. sample across T_{ac}. a) Skyrmion velocity versus current density measured at 90 K (dark red, RE dom.), 340 K (dark blue TM dom.) and 355K (blue TM dom.). b) Skyrmion deflection angle measured at the same temperatures. Dashed lines are obtained using Thiele model presented in Eq. 4.1 and parameterised with values from Tab. 3.1. c-d) Unique differential MOKE image obtained at 90 K (340 K) with typical deflection illustrated with coloured arrows.

In Fig. 4.13a, we observe a comparable skyrmion velocity between the measurement at 355 and 340 K. This confirm that the comparison with measurements at 355 K and 90 K (without and with a cryostat) can be made without concerns. The average size measured at 355K (see Fig. 4.14a) is comparable to the one measured at 90 K (we measured a 50 nm increased skyrmion diameter in this case, but this is far below our error bars, especially because the measurement in the cryostat presents poorer resolution). The velocity difference cannot then be imputed to the skyrmion size. We fully characterised the sample at 355 K, with a BLS measurement of α and γ (see Fig. 2.22) and torque measurements (see Fig.2.24) which are summed up in Tab. 3.1. We use these parameters to compute the model velocity and deflection (Eq. 4.1). θ_{SHE} is left as a free parameter, and the fit yields θ_{SHE}=0.08, which is very consistent with the experimental value (0.09) and within the error bar. The parameters of the model at 90 K were obtained using the mean field model, hence extrapolated from our measurements at higher temperature. In practice, all parameters are kept except for L_α, which is increased by 20% (from its value at 355 K) as predicted by the mean field analysis This yield a very good fitting of the measurement at 90 K, pointing towards the fact that the evolution of L_α in temperature is a critical parameter of the skyrmion dynamics. The model also agrees relatively well with the measured skyrmion deflection, as seen in Fig. 4.13b. All points show averaged values. This measurement then unambiguously demonstrates the reversal of the skyrmion deflection across the angular compensation in RETM ferrimagnets. In the two cases, special care was made to nucleate skyrmions with the same Co core orientation to ensure comparable results (which can be seen by the fact that they share the same black contrast as seen in Fig. 4.13c-d).

4.8.2 Different dynamics between TM dom. and RE dom. samples

We now compare the skyrmion dynamics between the RE dom. and TM dom. sample, so T_{ac} is not crossed due to different temperature, but to different composition. We superimpose in figure 4.14 the results of the RE dom. sample (also presented in Fig. . 4.5) and of TM dom. sample (presented previously in Fig. 4.13).

We can see in figure 4.14a) that the skyrmions tracked in both samples present very comparable sizes, and so the differences in their dynamical properties cannot be explained by skyrmion size effects. We do see in c and in the comparison in d-e) that the skyrmion deflection angle is opposite in the two samples, with similar angles of 40°. On the other hand, the samples show a very different mobility, with the TM. dom sample presenting faster skyrmions than the RE dom. sample. This very large difference in mobility, of a factor around 2, can be understood considering two differences between their structures. Firstly, the samples may present different interfacial effects, especially those due to the Ta upper layer. In the RE dom. sample this layer is only 3 nm thick and may be mostly oxidised, which implies a very low contribution from this layer to the overall SHE. In contrast, the TM sample has a thicker (5 nm) Ta layer that is protected by a 1 nm Pt capping layer, that should not be oxidised, and therefore produced a higher SHE contribution. Torque measurements on both samples are consistent with this hypothesis as seen in section 2.5.5.

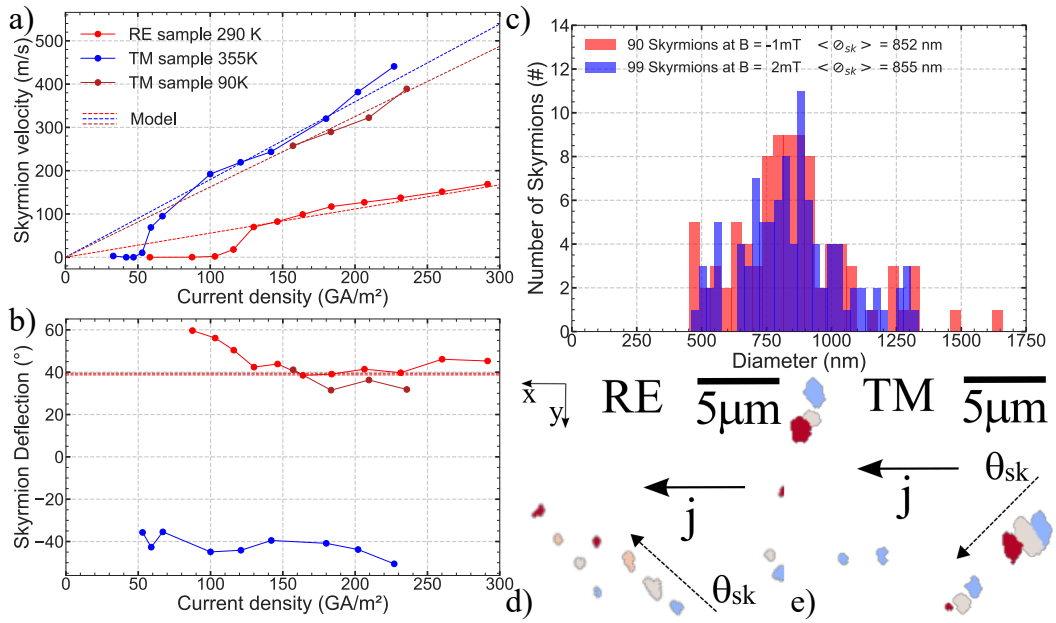

Figure 4.14: RE and TM skyrmions dynamics. a) Size histograms of tracked skyrmions for RE dom. sample (290 K) in red and TM dom. sample (355 K) in blue. b) Velocity curve with current density for both samples at -1 mT for RE dom. and 2 mT for TM dom. c) Averaged skyrmion hall angle for both samples. d-e) Superposition of 4 (3) MOKE images for typically observed skyrmion dynamics for RE (TM) dom. samples.

Secondly, the two samples have a very different angular momentum density, 4.29×10^{-7} J.s for TM dom. and 7.38×10^{-7} J.s for the RE. dom sample (obtained from the measurement of M_s and γ). Considering their respective α this yields $\frac{L_\alpha^{RE}}{L_\alpha^{TM}} \approx 1.5$. This large difference in L_α between both sample adds a contribution to the difference in velocity (larger L_α implies an overall reduction of the velocity).
This means that skyrmions dynamics obtained at a higher temperature, where L_α is reduced (see an example in Fig. 2.9), are expected to present an increased mobility.

This point seems to have been raised recently in [162] where they observed an increased velocity for dynamics at higher temperature in a ferromagnetic sample (where L_α is also supposed to reduce with increasing temperature). Their explanation also considers the change in angular momentum density (with reducing M_s when increasing temperature) but they consider that the major reason for increased velocity at higher temperature is the varying torque efficiency.

We may be surprised that we always find somehow comparable skyrmion deflection angles, but this might be simply due to the fact that we always studied skyrmions in comparable stability regions. The model does also show that the deflection angle computed in the different cases are expected to be the same.
This study would be improved with a comparison of the skyrmion dynamics at the exact same temperature of two samples with opposite domination. Optimisation of sample to make this comparison is completely achievable, and would be interesting to consolidate our observations.

4.8.3 Skyrmion deflections angle in ferrimagnets

We can observe in figure 4.15 that the skyrmion deflection angle is opposite between the RE and TM dom. sample. We can first notice that the side of nucleation is also reversed between the two samples. Looking at figure 4.15 a-b) we see that the Co lattice points down in both cases, but the magnetisation of the skyrmion core is opposite, and so is the effect of the Oersted field. So naturally, the Oersted field being along $\vec{e}_z$ at the bottom of the track, black skyrmions are nucleated from a white saturated domain in the RE dom. sample whereas black skyrmions are nucleated at the top of the track in the TM dom. sample where the Oersted field is along $-\vec{e}_z$.

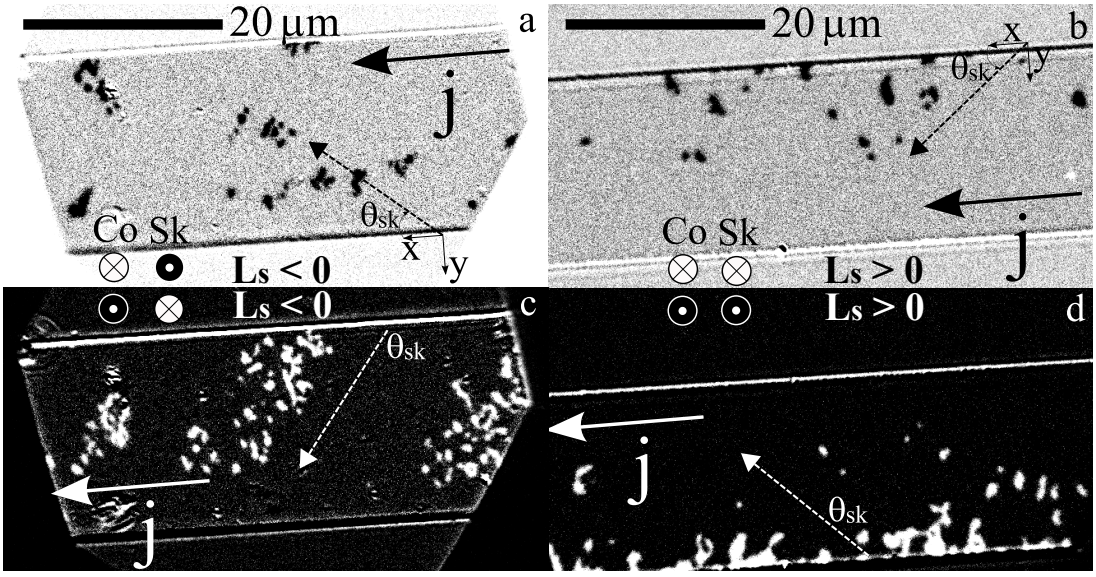

Figure 4.15: Skyrmion deflection across T_{ac}. a) Differential MOKE image of skyrmions in RE dom. sample for down Co lattice with respect to sample surface. b) In the case of down Co lattice for TM dom. sample. c) For up Co lattice in RE dom. sample. d) For up Co lattice in TM. dom sample.

It should be noted how important it is to follow the Co lattice and not the magnetisation of the skyrmion core to understand this effect, as a comparable Co orientation between the RE and TM cases corresponds to the same spin configuration, implying that one could go from one state to the other without applying any external field.

In essence, it means that starting from a), with black skyrmions in a RE dom. situation (T $< T_{mc}$), the temperature could be raised in order to cross T_{mc}, and so the magnetisation of the core of the skyrmion would reverse (if no external magnetic field is applied), and so by keeping on increasing the temperature up to T $> T_{ac}$, we would end up in situation b), with black skyrmion still, so down Co lattice, and then a reversed deflection as observe in the figure.

The reversal of the deflection between $T < T_{ac}$ and $T > T_{ac}$ is a clear experimental evidence that the angular momentum density reversal does induce a reversal of the skyrmion deflection. The theoretical expectation is then indeed observed. The following step would then be to observe the skyrmion dynamics as close as possible to T_{ac}. This requires a well optimised sample where the usually low magnetisation at T_{ac} is sufficient to stabilise skyrmions (by lowering the effective anisotropy and using long range dipolar effects). As discussed previously, this can be achieved by positioning the T_{mc} at a rather low value (<200 K) that favours larger magnetisation at T_{ac}, but also a tuned magnetic anisotropy K_u that should be scaled accordingly so skyrmions would be stable around T_{ac}.
This can be achieved by a very well designed sample directly at the step of deposition, but was not realised in this work due to time consideration of the complex optimisation needed to obtain such a precisely controlled film properties. Indeed, because of the patterning into magnetic tracks of the plain film in order to study the skyrmion dynamics, all the supplementary nano-fabrication step are going to modify the properties of the sample (always the issue of Gd migration) and so a lot of calibration of these thermally activated effects would need to be done to be able to fabricate such a sample on demand. To tackle the difficulty of the perfect control of all fabrication steps, we explored another way to fine tune the magnetic properties of our samples that we present in chapter 5 in section 5.3.

4.9 Comparison with literature

Three regimes for skyrmion motion are expected with increasing driving current: a pinning regime, where the effects of the film disorder strongly inhibits the propagation, a linear flow regime, where the skyrmion propagates with a velocity proportional to the current while conserving its shape, and a non-linear flow regime, where the skyrmion shape is deformed by the driving force.

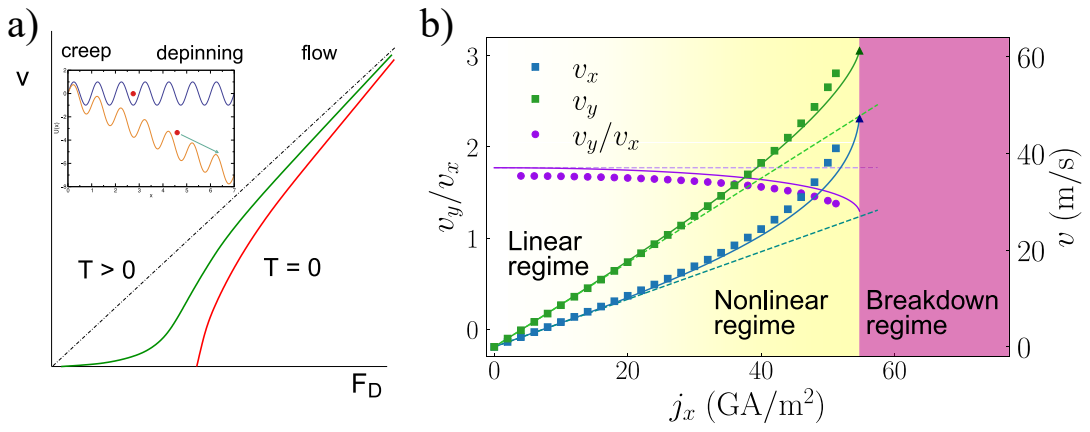

Figure 4.16: Skyrmion regimes. a) Expected skyrmion regime with increasing driving force considering pinning, adapted from [216] with inset described in the text. b) Simulated skyrmion regime in up to the deformation regime, reproduced from [288].

Fig. 4.16a) illustrates the predicted skyrmion velocity with increasing driving force. At non-zero temperature and low driving force, the skyrmion is in the creep regime with very low velocity. At a depinning threshold, the velocity increases and the skyrmion follows a depinning regime. With sufficient driving force, the skyrmion follows a linear regime [206, 207]. The inset of Fig. 4.16a) is a schematic of a sinusoidal potential, the simplest system exhibiting depinning, with the red particle pinned at $F_D = 0$, where an increasing driving force eventually overcomes the pinning potential and the particle begins to move. With such a model, the skyrmion velocity is expected to converge to the linear regime with increasing driving force.

Fig. 4.16b) on the other hand, represent simulation results of a pinning-free system, where skyrmion deformation is observed. In this regime, the elongated skyrmion present a non-linear regime with an increased velocity and reduction of deflection angle up to a breakdown at largest current density due to the annihilation of skyrmions.
This model goes beyond the simpler rigid skyrmion model (represented in dashed lines) that predicts that the velocity remains linear and the deflection angle constant with driving force. Their model shows that the deformation induced by the driving force has important effects on the skyrmion dynamics: a reduced deflection angle and increased velocity. These effects are maybe due to an increasing skyrmion size in the nonlinear regime. Other studies such as the one from Litzius et al. [162] observed experimentally and in simulations a different effect of deformation: an increased deflection angle.
This apparent contradiction might be due to different strengths of pinning and deformation, which may lead to different variations with driving force. A complete review on the effect of pinning on skyrmions offers a thorough discussion on the matter [216].

There are some general expectations to draw on the linear skyrmion regime, where analytical and numerical models [218, 288] describe the skyrmion dynamical laws and identify the main governing parameters: the current density (J and its efficiency), the skyrmion size, the material's angular momentum density (L_S) and the dissipation (α) (we describe dissipation with the more convenient parameter L_α).

As a function of skyrmion size, the velocity is expected to increase whereas the deflection should decrease. The deflection should be proportional to L_S. Because of the different regimes in which skyrmion dynamics can be observed, experimental observations agree only partially with these predictions or are incomplete.
For example, instead of being constant, the deflection has most often been observed to increase with current, eventually saturating at the highest currents [326, 48, 211, 138]. The velocity was observed to increase linearly with current in some experiments [49, 215], but often follows a shifted linear law [211, 125, 212, 162] or even a linear law but quantitatively slower than the velocity expected for the linear regime [127, 48, 138, 214].
The dependence of the deflection angle on the diameter was observed in some cases [48, 215] but not in others [214]. Also, the dependence of the velocity with diameter was found to be constant in ref. [210].

We sum up experimental skyrmion dynamics in Fig. 4.17, where we superimposed the skyrmion mobility versus the skyrmion diameter reported in the literature for several different systems. Some points present very low mobility in different conditions, for instance [138], at high current densities of TA/m^2 and [136] at less than 1 GA/m^2. For all results above the pinned regime, we notice a very high correlation between mobility and skyrmion size.

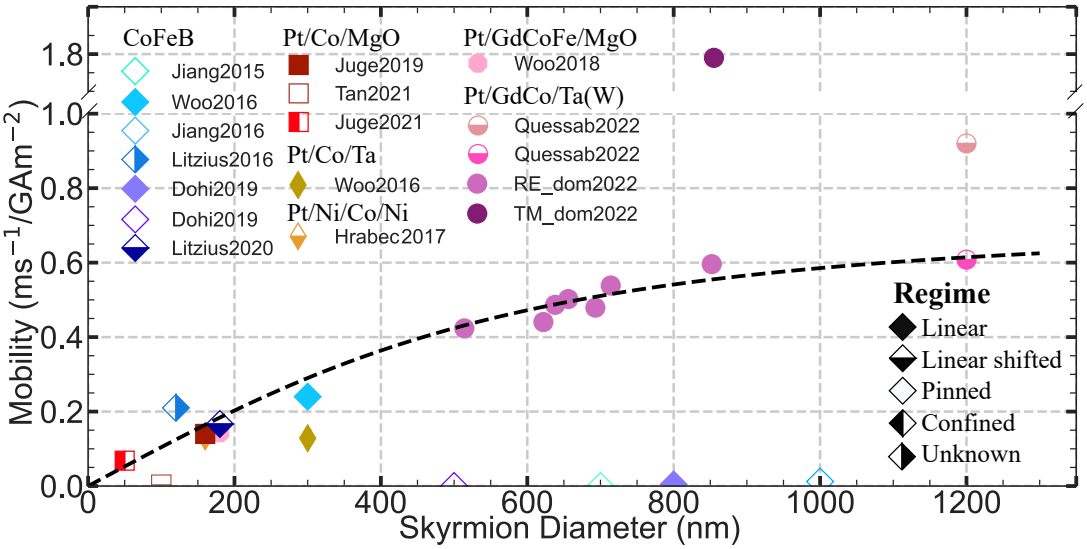

Figure 4.17: Mobility comparison with literature. Presentation of mobility versus skyrmion radius using values found in the literature. The dashed line is obtained with the rigid skyrmion model for the RE dom. sample magnetic parameters. All references: Jiang2015 [127], Woo2016 [212], Jiang2016 [48], Litzius2016 [215], Dohi2019 [138], Litzius202 [162], Juge2019 [211], Tan2021 [210], Juge2021 [26], Woo2016 [212], Hrabec2017 [125], Woo2018 [49], Quessab2022 [213]. RE-dom2022 and TM-dom2022 (at 355 K) are the data described in this chapter.

It is also quite striking to observe that the rigid skyrmion model (Eq. 4.3), parameterised with the RE dom. magnetic parameters (Tab. 2.2) gives an overall consistent description of most of these points. Let us emphasise that there is actually no reason for this to work, as the model predicts different mobility for different driving efficiencies, DW width parameter Δ, L_s, or L_α (as one expects is the case for the very different materials presented here). The fact that most mobilities points are close to the model curve in the figure is therefore only due to the critical effect of the skyrmion size compared to other parameters.
In order to better compare the mobility in all these different materials, the parameters should be normalised. First of all, the radius should be normalised by the DW width parameter Δ, and the mobility by the torque efficiency (θ_{SHE} for SOT for instance). Then only the effects of L_s and L_α would remain (see Eq. 4.3).

But two points are clearly far from the dashed curve plotted. One by Quessab et al. obtained on Pt/GdCo/W, and the second that corresponds to our TM dom. sample (at 355 K). In both cases the velocities where very high (above 400 m/s) but, in our case, the current density is much smaller which implies a larger mobility. We explained the reasons behind this much increased mobility in the TM dom. sample compared to the RE dom. one in Sec. 4.8.1.
It should also be noted that in confined skyrmion dynamics, due to the cancellation of the skyrmion deflection, higher mobility are expected, and this regime should not be compared directly with free space dynamics. This might be a cause of discrepancy in the literature, especially about the skyrmion deflection angle, as the effect of the edges can impact the observed dynamics.

Also, there are many reports of skyrmion velocity curve that display a shifted linear regime (not extrapolating to zero). In most cases, very few explanations are proposed, and often it is attributed to the effects of pinning, but as presented in Fig. 4.16a), a simple picture of pinning cannot explain this observation. The velocity should always reach a linear regime (extrapolating to zero) and should be considered in the depinning regime before. There might be some explanations of this effect, but I could not find any.

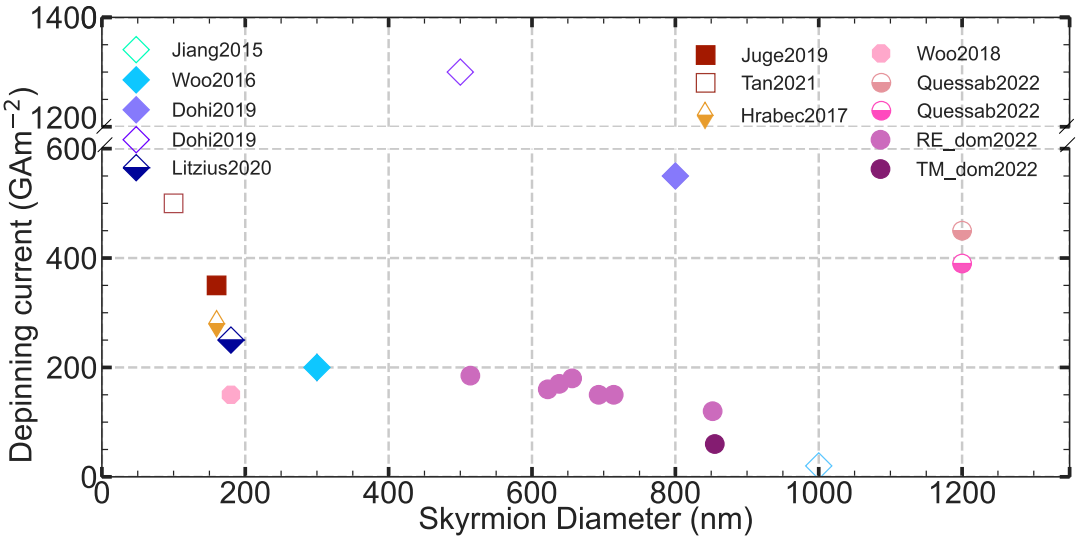

Figure 4.18: Mobility comparison with literature. Presentation of mobility versus skyrmion radius using values found in the literature. See references in figure 4.17.

We also present in Fig. 4.18 the associated depinning current thresholds (when possible) of systems presented in Fig. 4.17. It shows a clear correlation of depinning current with the skyrmion size. Only four points [138, 213] stand out, presumably due to the large current densities used. This correlation can be understood by the fact that the current threshold is expected to scale according to the ratio between the skyrmion size and pinning typical length scale [318, 319], and we can reasonably expect that this ratio does not vary much between these thin-film systems.

Both these figures show an important issue in skyrmion dynamics, that these several experimental reports seem to confirm: smaller skyrmions have lower mobility and increased pinning.

Chapter 5

Local effects on skyrmion properties

5.1 Controlled nucleation

The controlled nucleation of skyrmions remains a challenging task. Some experiments in the literature showed promising ideas that we explored. One idea is to use geometric constrictions, and the diverging current density after the constriction to favour skyrmions nucleation as reported in [127]. We tried to replicate this in many samples, in various skyrmion stability conditions, with different current densities and pulse widths. We present in figure 5.1 the typical observed behaviour.

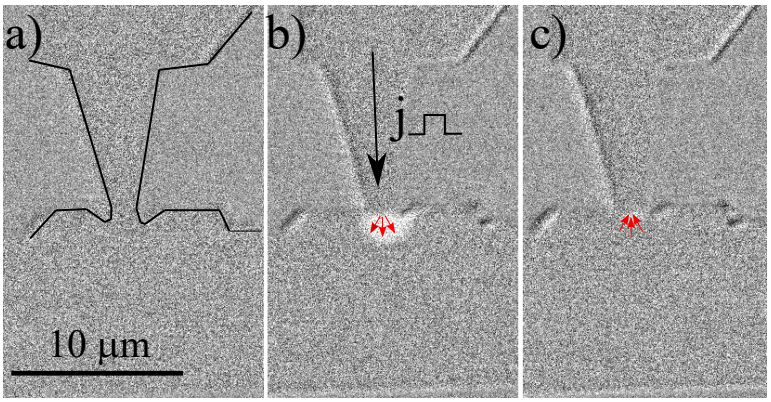

Figure 5.1: Constriction nucleation in GdCo thin film away from T_{D_c}. a) A magnetic domain (white) is brought to the opening of the constriction using magnetic field (not visible as the reference image is taken at this state). b) 5 current pulses (100 ns) around 50 GA/m^2 are applied and a round white domain grows where red arrows show the typical growth geometry. c) The round domain collapses back (red arrows) to the constriction opening.

We can see in figure 5.1 a 1μm wide constriction where a round magnetic domain grows after current pulses. The domain ends up collapsing back to its initial position a few seconds after its growth. This is due to the DW energy that increased with the domain growth and that is minimised by its collapse to a smaller straight DW in c). This could be described using the analogy with surface tension of soft mater systems like soap films. This effect has been seen in most of our trials, with sometimes the white domain growing further and stabilising, but never nucleating a magnetic skyrmion. Smaller constrictions down 0.5 μm in various geometries have also been attempted but none yielded particularly interesting or reproducible results. In samples already in a region of skyrmion stability, these constrictions enhance the skyrmion nucleation, but because skyrmions are also nucleating at edges it does not present much advantage.

We believe that this mechanism nonetheless deserves to be improved as it shows promising results and would be very convenient if capable of nucleating single skyrmions on demand. But because of the high increase in temperature induce by Joule heating, this effect seems quite challenging to master in ferrimagnetic materials where the heating has non-trivial effects on the samples properties other than thermal activation.

We also made attempts of constrictions of 1 μm width with a constriction limited to only a 1μm length, that we arranged in arrays in a 20μm wide magnetic track. We present the typically observed effect of such geometry in figure 5.2.

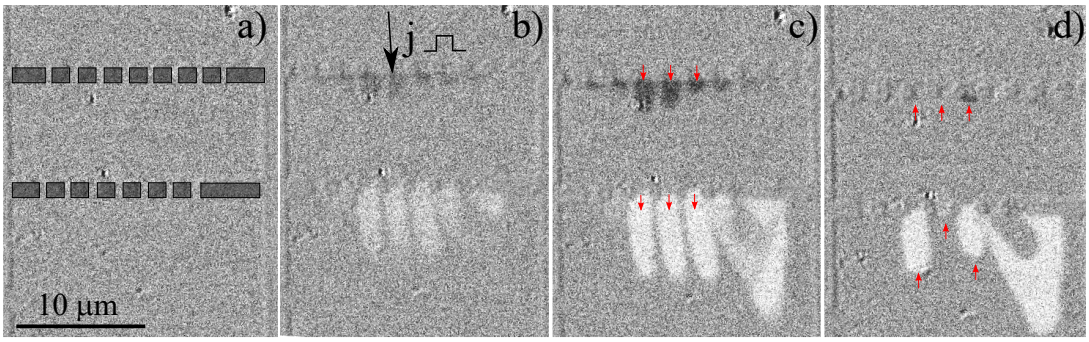

Figure 5.2: Array of constrictions. a) Sample is prepared with a white domain between the two sets of constrictions array (not visible as the reference image was taken in this state).b) 10 current pulses of 100 ns of around 200 GA/m^2 are sent and domains are growing along the current direction. c) Finger like domains after the current pulses indicated by red arrows. d) The finger are retracting (red arrows), some to the initial position of the DW, others remain pinned in intermediate positions.

In figure 5.2a) we prepare the track with a white magnetic domain located between the two arrays of constrictions. We then send 10 current pulses (100 ns) with current density around 200 GA/m^2 and see in b-c) the formation of finger-like magnetic domains at the ends of the constrictions. The effect is seen to be much larger for the white fingers (below) than for the black ones (above), with also a clear non-uniform current distribution that seems to be larger at the centre of the track than at the edges. This geometry should be completely characterised in order to be optimised as a skyrmion blowing machine. The finger domains suffer the same issues as the round domain described previously. They mostly collapse back after few seconds if the current did not made them grow enough up to a region where they can stay pinned.
We can note that these domains resembles the ones presented in [260]. This geometry of nucleation of DW can then be used to try to reproduce their results of reversing the tilt angle of finger like DWs across T_{ac}.

We studied this geometry while varying the temperature of the sample but could not obtain any remarkable results. This geometry was not explored with samples close to T_R which should be realised before making conclusion on its capabilities. The formation of finger like domains is well understood in the case of SOT dynamics as the borders of the finger should present a magnetisation profile which prevents the driving by SOT. Indeed, for magnetisation collinear with the spin polarised current of SOT, zero net torque is expected. This might be the main reason behind the observed shape.

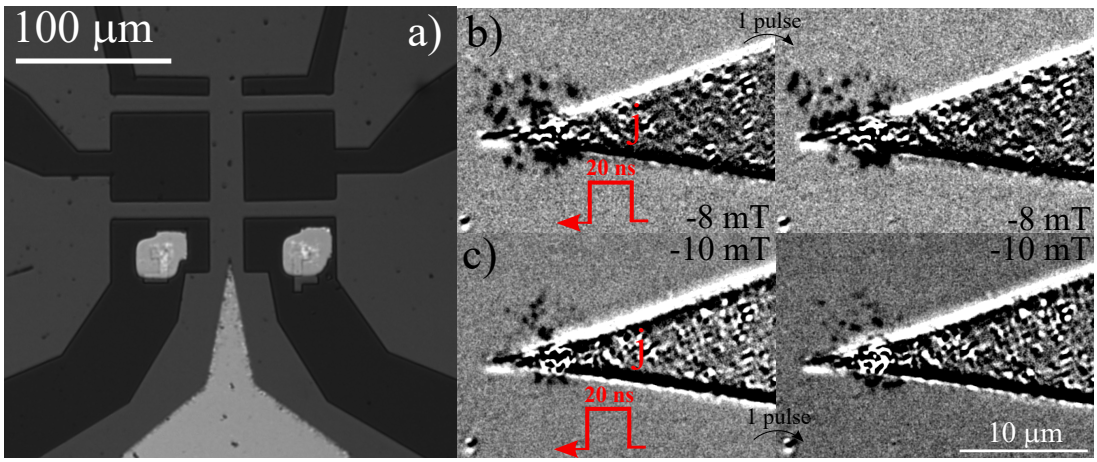

Figure 5.3: Nucleating skyrmion using a conductive tip. a) Large view of the device, with SiO_x substrate in dark grey, the magnetic track in grey, and the Al tip deposited on top of the track in light grey. The square light grey regions are due to realignment step for lithography. b) Single 20 ns current pulses is sent and skyrmion nucleate with a -8 mT magnetic field applied against their core magnetisation. The second image is taken one pulse after the first. c) Same procedure as b), but with -10 mT applied.

Finally, we also tried to inject skyrmions using conductive tip deposited on top of the magnetic track as presented in 5.3. The idea was to reproduce the promising nucleation mechanism demonstrated by Hrabec et al. [125] who used a conductive tip deposited on top of the magnetic layer. We deposited an Al tip of (50 nm) on top of the RE dom. sample. Away from T_{D_c} we could not reliably nucleate skyrmions. However, close to T_{D_c} we could use the tip to nucleate skyrmions preferentially at the tip. Unfortunately, as seen in 5.3 b-c), we could not achieve single skyrmion nucleation. On the other hand, using magnetic field, we could reduce the number of nucleated skyrmions (and remove any nucleation away from the tip). This is indeed seen between b) and c) where the slight increase of 2 mT is sufficient to reduce by half the number of skyrmions. This could be done at higher field but the smaller skyrmions were hard to observe with MOKE. This method is by far the most interesting one we tried. The effect was more reliable than the other methods, and we do believe that it would yield satisfactory results with further optimisation. One issue with this method is the degradation of the tip (e.g., damage is noticeable in the second image of c) and some optimisation of the tip would be necessary to use this technique over long period of time.

5.2 He FIB irradiation

The effect of He-FIB irradiation on the properties of magnetic thin films has been studied for a long time and have gained much interest in the study of skyrmions recently [26, 27, 28, 29, 30]. We want to use it in our samples to fine tune their magnetic properties locally and after the fabrication step. In this section, we present results on He-FIB irradiation on GdCo thin films. We present the dose studies we realised on several samples, where we disentangled the effects of FIB on the magnetic properties: shift in T_{mc} and changes of the magnetic anisotropy (K_u). We also present some preliminary results obtained with the irradiated tracks, namely: favouring skyrmion phase in a sample with uniform magnetisation, FIB induced skyrmion confinement, and finally FIB induced nucleation.

5.2.1 Evidence of effects in ferrimagnets

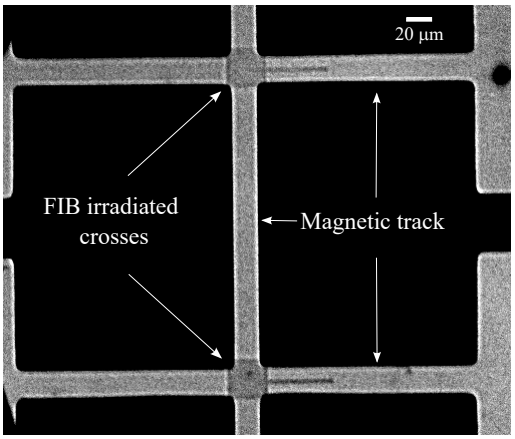

Figure 5.4: FIB irradiation of ferrimagnetic track. Optical microscope images of two He-FIB irradiated crosses. One square in the middle of the cross was irradiated, with a line going to one of the cross arm.

Let us first see the most obvious magnetic effects of the He irradiation in our samples. We irradiated a Ta(1)/Pt(5)/GdCo(5)/Ta(5) (nm) ($T_{mc} = 270$ K) sample with different doses. The sample had been patterned in crosses. Figure 5.4 shows some optical images where the irradiated region surprisingly appear very clearly (even for small dose down to 5 ions/nm^2). We observe that the reversal field is different between the irradiated and non-irradiated zones and depends on the irradiation dose. Figure 5.5 shows the reversal for a dose of 50 ions/nm^2 in a TM dom. sample (T_{mc} around 270 K) of Ta(1)/Pt(5)/GdCo(5)/Ta(5) (nm).

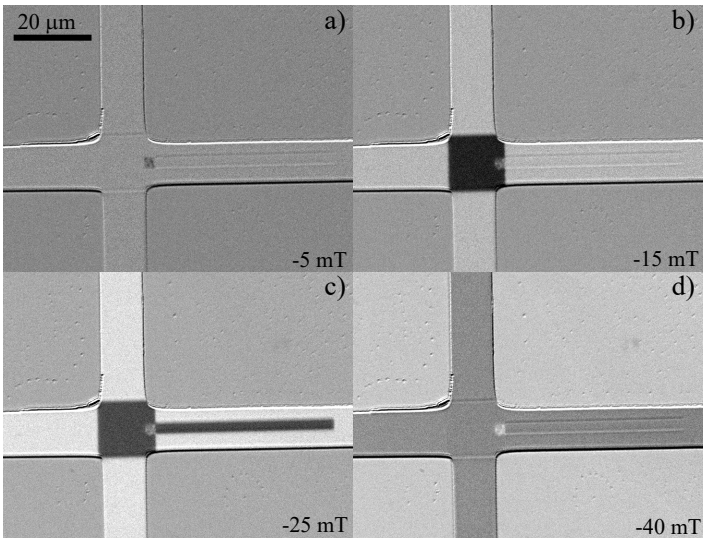

Figure 5.5: FIB irradiation induced field dependant domain reversal. A square and a line were irradiated with 50 ions/nm^2 a) After positive magnetic field saturation, the field is lowered to zero and increased to negative values. At -5 mT reversal of the twice irradiated zone. b) At -15 mT reversal of the square. c) At -25 mT reversal of the line. d) At -40 mT the rest of the sample reverses.

We can see in figure 5.5 that the reversal does not occur at the same field in irradiated areas and outside. The small square in a) was exposed to twice the 50 ions/nm^2 dose and reverses first at negative magnetic field after a saturation of the sample at positive field. Then at -15 mT the large square region reverses.

Because of the Faraday effect the whole image gets brighter and so the small square reverses from a) appears brighter. Then at -25 mT c) the irradiated line reverses. Both the square and the line has been irradiated with the same dose, but because the square touches edges, it is more likely to reverse as nucleation most often begins at edges. Then at -40 mT the rest of the sample reverses. We then present a closer look of the small square region from a) in figure 5.6.

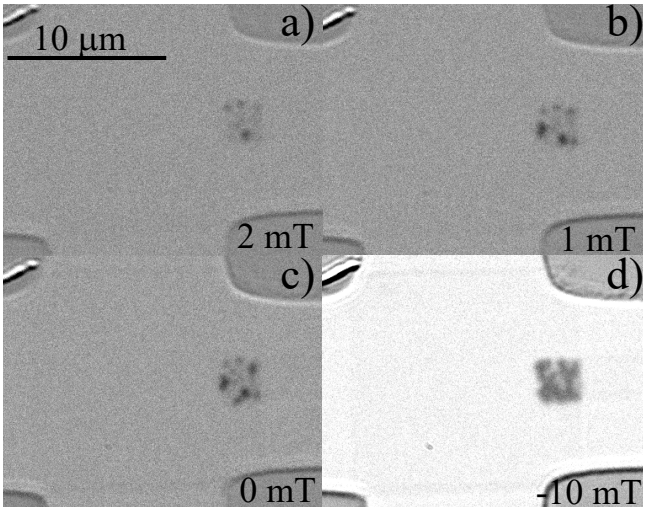

Figure 5.6: Skyrmion stabilised by FIB. a) After saturation at positive field, appearance of skyrmion like texture at 2 mT (opposed to the magnetisation core). b) More skyrmions at 1mT. c) Stable skyrmions at zero magnetic field. d) When increasing the field, stripes growth replacing skyrmions.

In figure 5.6 the zone irradiated with a dose of 100 ion/nm^2 display skyrmion like magnetic textures. From a saturated state at positive magnetic field, skyrmions naturally nucleate at 2 mT a), with a field opposed to their core magnetisation. This resembles the properties found in 3.15. While lowering the field, new skyrmions are nucleating and their contrast (size) increases. We see stable skyrmions even at zero magnetic field c). When the magnetic field is increased towards negative values (align with their core magnetisation) we see a stripe phase taking over as showed in 5.6 d). These results show that FIB can indeed be used to modify the magnetic properties of the GdCo film. The non-irradiated film shows uniform magnetic state (and thus square hysteresis loops), as does the zone irradiated with 50 ions/nm^2. At higher dose, 100 ions/nm^2, different types of magnetic textures are stabilised, the ones typically observed in low anisotropy environment, namely skyrmions and stripes. As explained before, the effective anisotropy $K_{\text{eff}} = K_u - (\mu_0 M_s^2)/2$ can be modified both by the magnetisation (M_s) and magnetic anisotropy (K_u), and so we will study the effects of irradiation on these two parameters. In other dose tests, we could see the reversal of the RE/TM domination of irradiated areas, which suggests the irradiation affects the effective composition of the sample and thus the M_S. From these measurements, we understand that the He-FIB lowers the effective Gd content and reduces the magnetic anisotropy. We then propose to explore this technique in order to favour skyrmions stabilisation.

5.2.2 He-FIB effect on T_{mc} and K_u

We made experiments on thin films of Pt/GdCo/Ta and Pt/GdCo/Ta/Pt. We realised several He-FIB dosage test to calibrate the effects of the irradiation. We could observe two distinct effects on the ferrimagnetic sample: a shift T_{mc} consistent with a lowering of the effective Gd chemical composition and a reduction of magnetic anisotropy.

We managed to disentangle these two effects by measuring the magnetisation and effective anisotropy of a specifically designed sample with multiple hall bars each irradiated with a different dose. This allowed us to obtain very consistent results as all the measurements of effective anisotropy and T_{mc} shift by AHE where obtained on the same device. The measured anisotropy of this sample versus He- FIB dose are presented in figure 5.7 a-b) and the disentangled effect on the T_{mc} and anisotropy are presented in figure 5.7 c-d) respectively.

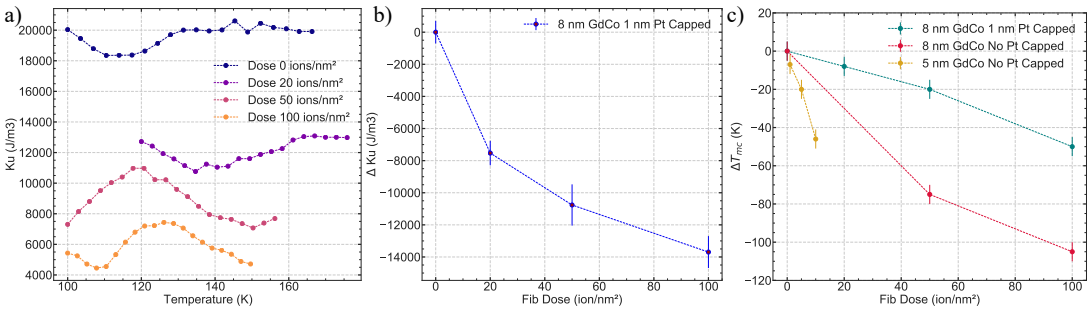

Figure 5.7: He-FIB effect on magnetic anisotropy K_u and T_{mc} in Ta/Pt/GdCo/Ta/Pt samples. a) Magnetic anisotropy K_u versus temperature on a single sample irradiated with different dosage from 0 to 100 ion /nm^2. b) ΔK_u versus He-FIB dosage. c) ΔT_{mc} shift with He-FIB dosage for different sample thicknesses and capping.

Thanks to these calibrations we can now predict the effect of He-FIB irradiation on the magnetic properties of our thin films. Using simple linear fits for the Pt capped sample, we obtain: $\Delta T_{mc} = -0.5$ K nm$^2\times$ dose and $\Delta K_u = -0.14$ kJ nm^2/m$^3\times$ dose for the dose in ions/nm^2. Another study on irradiation dose in GdFe and TbFe can be found in [30]. Different thicknesses or capping layers modify the strength of the effect, with thinner magnetic or capping layers showing larger effects on the T_{mc} shift as observed in figure 5.7d).

We can already quantitatively estimate the effect of irradiation on the M_s and K_{eff}. The shift in T_{mc} is going to modify the magnetisation at a fixed temperature, but it can be rapidly seen by computing the effect of both the shift in T_{mc} and K_u that the dominating influence on the effective anisotropy comes from the effect on the magnetic anisotropy. Using these effects, we could tune the magnetic properties of the ferrimagnetic sample using FIB irradiation, in order to drive the reorientation slightly above the T_{ac} of the ferrimagnetic sample which should then allow us to study very stable skyrmions at T_{ac}. We show the schematic of the proposed approach in fig 5.8.

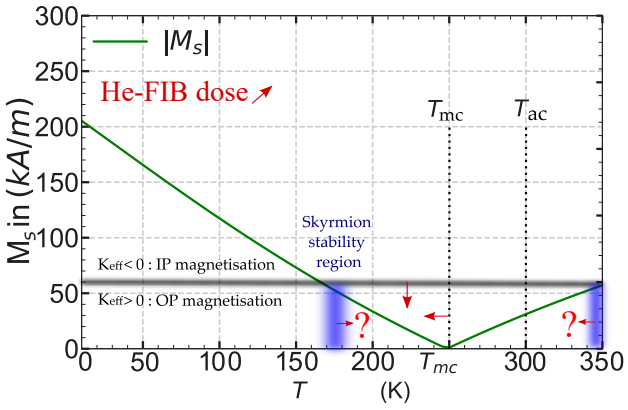

Figure 5.8: Tuning skyrmion stability by FIB. Schematic of the effect of He-FIB on the magnetic compensation and anisotropy of a ferrimagnet.

Considering, for example, a sample with $T_{mc} = 350$ K and $K_u = 20$ kJ/m^3, a dose of 100 ions/nm^2 is expect to reduce T_{mc} to around 300 K and the K_u to 4 kJ/m^3. The magnetisation at T_{ac} should become 40 kA/m, which will make an effective anisotropy just below 3kJ/m^3. where we can expect skyrmions to be stable our from previous observations (see Fig.3.1 for instance). We make a more complete analysis of this effect in the next section 5.3.

5.2.3 Confined dynamics and controlled nucleation

We present in Fig. 5.9 some results of confined skyrmion dynamics and controlled nucleation obtained on He-Fib irradiated tracks on a Ta(3)/Pt(5)/$Gd_{0.32}Co_{0.68}$/Ta(5) (nm) sample. The irradiated tracks were 1 μm wide and were irradiated with a dose of 20 ions/nm^2, and were located in a 30 μm wide patterned track.

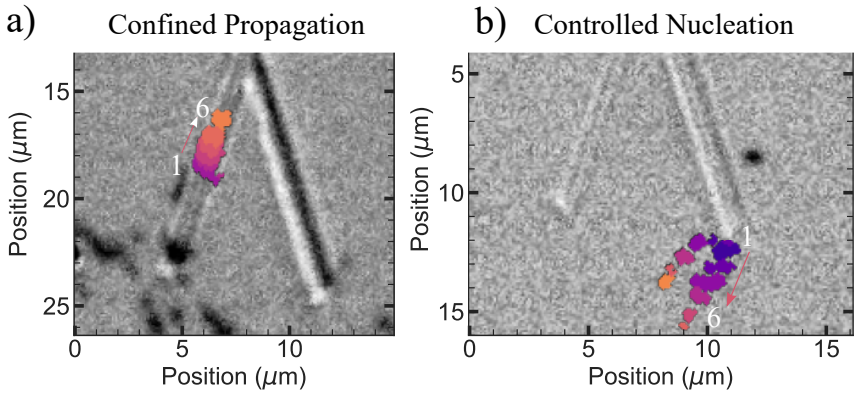

Figure 5.9: Magnetic textures confinement and nucleation in zones irradiated by He-FIB. a) He-FIB 1 μmirradiation zone confining the propagation of skyrmions. Superimposed images of the same skyrmion over several images, displaced by SOT. b) Skyrmion nucleation at the edge of an HE-FIB irradiated track. Superposition of two distinct events, where nucleation occurred at the end of the track and followed by free space skyrmion propagation.

Fig. 5.9a) shows the superposition of 6 images separated by 5 ns current pulses of ≈ 100 GA/m^2. This sample presented skyrmions naturally nucleating at edges at sufficiently large current density. Some skyrmions entered the irradiated zone and continued their propagation inside the irradiated track.
Skyrmions could only enter the irradiated zone through its end. When coming from an edge, they either followed the irradiated zone from outside or otherwise simply disappear. We can see in the figure that the skyrmion deforms inside of the irradiated zone. The shape varies along the displacement, and becomes more square or rounder depending on cases. It was clearly observed that, for a large enough current density, skyrmions confined in irradiated track geometrically oriented against their deflection would annihilate rapidly. This effect of confinement is discussed in [26].
In Fig. 5.9b) we observe the superposition of two distinct events of nucleation followed by propagation. Using magnetic field and reduced current densities, we were able to specifically nucleate skyrmions at the end of the irradiated track, without nucleation on edges of the magnetic track.

The interest of He-FIB to fine control the propagation, as well as the nucleation of skyrmion is extremely promising. We explored many different types of geometries: point like, centre or edges of track, gradients, constriction, crosses, and we have to continue this ongoing research in order to obtain quantitative results on the effect of irradiation on the skyrmion dynamics.

This effect is very promising to study the confined skyrmion regime, and offer much more control than with conventional patterning of magnetic track because of the possibility to have defect free confining edges. Very recent studies showed interesting observations of the confined dynamics of skyrmion as in [29] in CoFeB.
Also in the same material, the combination of a light irradiation of a track and larger irradiation of dots separated along the track allowed for a particularly interesting motion of skyrmion, that could be displaced from one spot to the next by electrical current pulses [27]. It has also been used to create local defect capable of nucleating skyrmion in Pt/Co sample [28] or to tune the density of skyrmion with Ga-FIB[327]. This technique has a major interest for applications as it allows to precisely engineer the landscape potential.

5.3 Optimisations for fast dynamics, low deflection, small size and high stability

We described in the section above how FIB can be used to fine tune the compensation and magnetic anisotropy of a sample. In this final section, we propose to explore our model on skyrmion dynamics, conjointly with our model of skyrmion statics, to study how the He-FIB irradiation, or tuning GdCo thickness, could be used to optimise the skyrmion properties. All the rest of this section is therefore speculative and based on our models calculations.

Let us consider a sample with T_{ac} at 293 K (T_{mc} = 245 K) from which we model the magnetisation curve by the mean field model. We consider here, for simplicity, that the FIB only shifts the magnetisation curve (and thus T_{mc} and T_{ac}) and reduces K_u with the relations found in section 5.2.2. We use the typical exchange and D_s measured on our GdCo thin films (A^{ex}=4.6 pJ/m and D_s= 1.1 pJ/m).
The magnetic anisotropy is taken for t= 8nm to be K_u=16.7 kJ/m^3. The current density J=300 GA/m^2, and $\theta_{SHE} = 0.09$. In ferrimagnets, because α and γ vary with temperature, we used comparison with BLS measurements and mean field to fix the values of α_{Gd},γ_{Gd}, α_{Co}, γ_{Co} (see Tab. 4.1).

Note that the results of the analysis presented in this section would need to be adapted before using them in a a real sample, as it is based on a model of the skyrmion statics that underestimate the skyrmion size by more than a factor of two, as we saw before (see section 3.4.4).

Optimisation by He-FIB irradiation

Numerous observations can be extracted from the plots in figure 5.10. Let us first describe the plots for the zero dose. The radius in Fig. 5.10a) is rather small on the whole temperature range; it only increases towards T_R below 200 K, and slightly along the magnetisation dome above T_{mc}. The skyrmion energy barrier, in b), is larger for the largest skyrmions. The velocity, in c), shows two peaks. One close to T_{ac} and a second one around the skyrmion radius maximum.

The deflection angle in d) is observed to be zero at T_{ac} and rather large away from T_{ac}. Then, we can see that at the lowest shown dose of 10 ions/nm^2, a spin reorientation is created at two T_R on both side of the magnetisation maximum above T_{mc} (visible for instance with the diverging radius). The reorientation temperatures change with dose because K_u reduces with increasing dose, and its evolution above or below T_{mc} is non-trivial as the compensation itself is shifting.

The shift of T_{ac} (represented by dashed lines) is considered to be the same as the one of T_{mc}. In order to suppress skyrmion deflection, the region of skyrmion stability has to be driven towards T_{ac}. This region was observed, by MOKE, as a region with naturally nucleating skyrmions, in a temperature range coinciding with their fast radius increase (see Fig. 3.15 and Fig. 3.5 for instance).
We see that for a dose of 80 ions/nm^2, that T_{ac} becomes almost superimposed with T_R. We can therefore expect that a slightly smaller dose (60-70 ions/nm^2) allows the observation of stable skyrmions at T_{ac}. The irradiation also reduces T_{ac} (from 293 K to 260 K at this dose). However, a T_{ac} close to room temperature could be obtained by designing a sample with a slightly higher initial T_{ac}. With an initial T_{mc} at 275 K, (T_{ac} at 320 K), the T_{ac} of an irradiated sample at 70 ions/nm^2 would lay around 290 K. We can note that the increasing dose also increases the computed skyrmion radius because of the lowering of K_u. This large increase in radius also drives the increasing skyrmion stability and overall velocity, while also reducing the deflection.

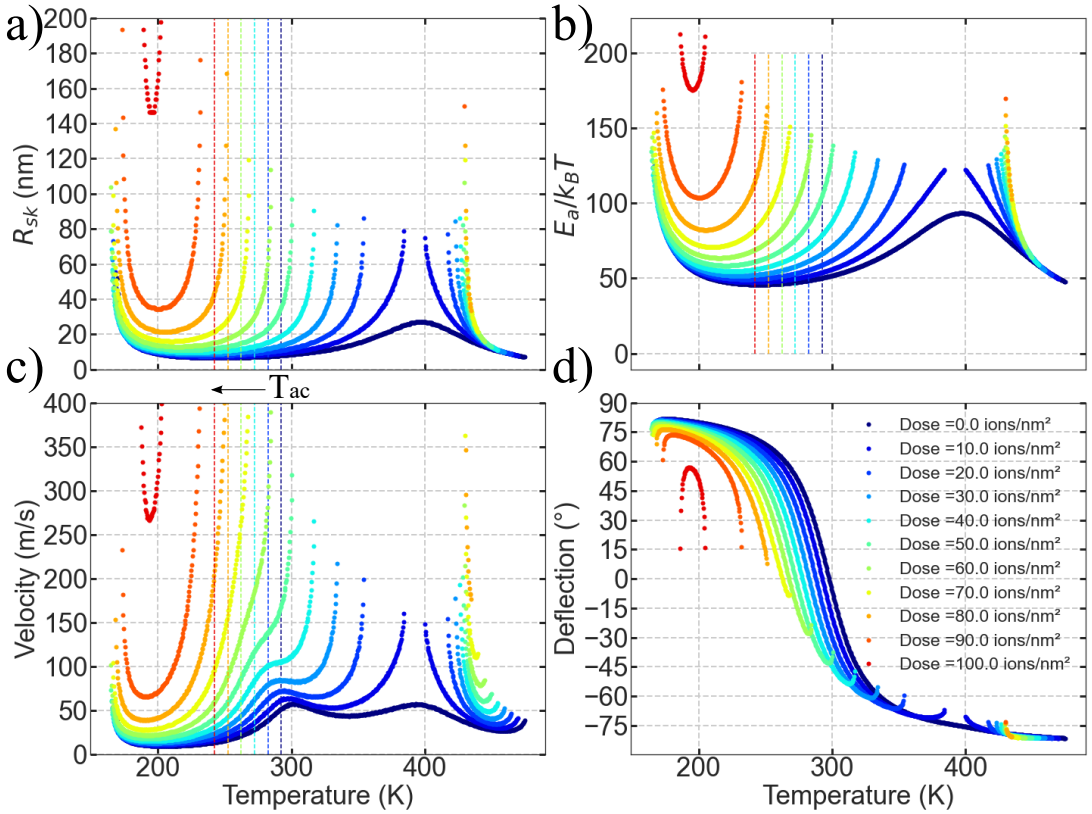

Figure 5.10: Calculations for optimisation by He-FIB of skyrmion properties in GdCo. a) Skyrmion radius with temperature for different He-FIB doses. b) Corresponding skyrmion energy barrier compared to k_BT at 293 K. c) Corresponding skyrmion velocity. d) Corresponding skyrmion deflection. Dashed line shows the location of T_{ac} for some doses.

Optimisation of GdCo thickness

Let us finally describe the optimisation of the sample directly at the deposition stage. We will now consider that the thickness of the sample can be modified without changing the magnetisation curve, nor the T_{ac} location. This is similar to what was experimentally realised in Sec. 2.18. K_u is computed to vary accordingly to the linear law described in Sec. 2.18 and the current density kept constant at J=300 GA/m^2. All parameters are otherwise the same as above.

In figure 5.11 we present the different key parameters to optimise the properties of skyrmion. We can see that the increasing thickness increases T_R and thus reduces the temperature range in which skyrmions can be observed. This is due to a decreasing K_u with thickness, which makes the the sample in-plane at lower magnetisation. Also, the variation of thickness displaces the region where the radius rapidly increases with temperature, which we have seen is where skyrmions are observed experimentally (sect. 3.3.2.3). This is very useful as it allows to use the film thickness to host skyrmions at T_{ac}; for example, for a sample with $T_{ac} = 293$ K, a thickness of 8.5 nm leads to easily nucleated skyrmions at T_{ac}. Then, by monitoring the major velocity peak at T_{ac}, we observe a non-trivial feature (Fig. 5.11 c).

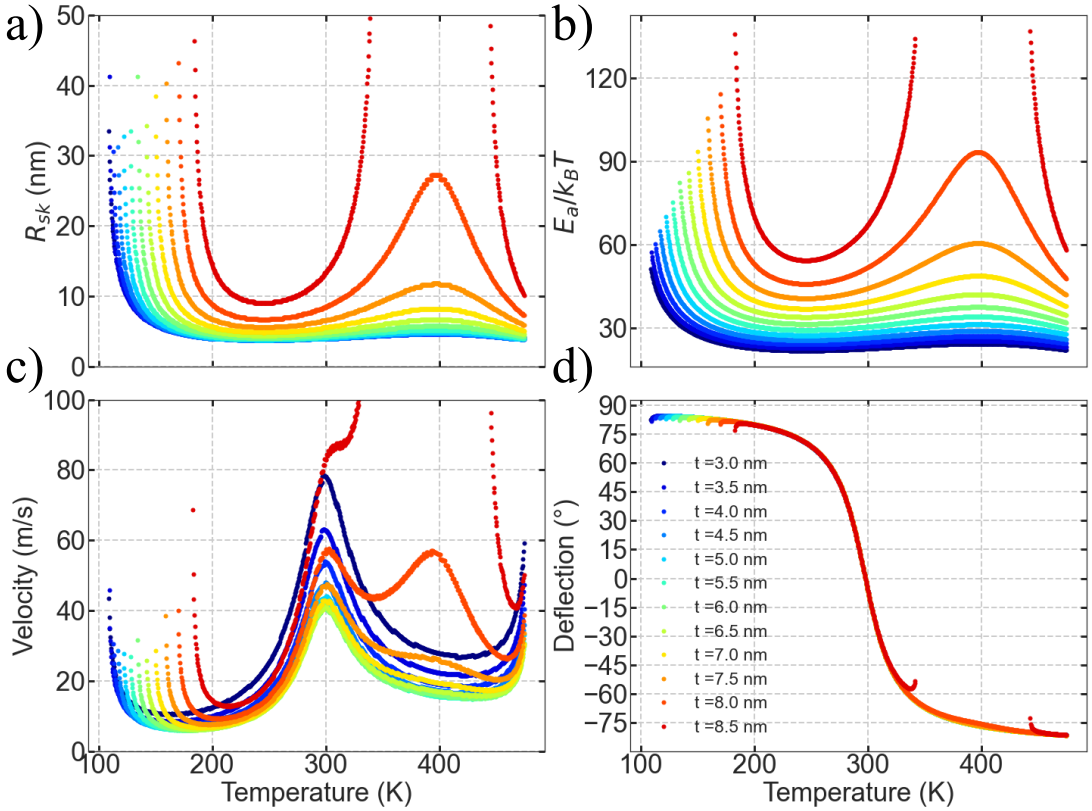

Figure 5.11: Optimisation of GdCo thickness for optimal skyrmion properties . a) Skyrmion radius with temperature for different magnetic layer thickness. b) Corresponding skyrmion energy barrier compared to k_BT at 293 K. c) Corresponding skyrmion velocity. d) Corresponding skyrmion deflection.

We see very fast dynamics for $t = 3$ nm, which become slower for increasing thickness up to 6 nm, and then increasing again with thickness. This effect is not related to the skyrmion size, but comes from a stronger SOT in thinner layers (at constant current density). Indeed, the deflection-less velocity (v_0) in eq. 4.1 is inversely proportional to t. This is equivalent to an increasing efficiency of the torque on the skyrmion (same amount of spin polarised current but less volume of skyrmion to displace) which therefore largely increases the resulting velocity. Nonetheless, the velocity is observed to be maximum at 8.5 nm because T_R is close to T_{ac} and so the large increase of skyrmion radius drives the increase of velocity conjointly with the reduction of the deflection. The double peak of velocity observed at 8 nm is also due to a skyrmion size effect. Finally, we can observe that the deflection angle is very comparable for all thicknesses because it is mostly sensitive to the skyrmion radius that only differs largely between all curves close to T_R. Again, at largest thicknesses (and smaller K_u) the skyrmion radius is increased as well as the stability.

Summary

These last two exploratory studies show two ways to optimise our samples. We can see that small skyrmions with high velocities are only expected for very thin samples, where the efficiency of the spin current is enhanced. Otherwise, the velocity scales with the skyrmion radius and so skyrmions both small and fast are difficult to obtain. This is also the case for the skyrmion stability. It increases with lowering of the anisotropy, but mostly with increasing skyrmion radius. On the other hand, we only found one way to reduce the deflection, which is to displace skyrmions at T_{ac}. Therefore, it seems that the best compromise for stable and fast skyrmions is to tune T_R close to T_{ac}.
This allows to obtain very stable skyrmions with reduced deflection and highest velocity, with the drawback of the larger skyrmion radius. A compromise between velocity and size seems unavoidable. Another approach for the issue of deflection is found in the confined skyrmion regime, but then necessitates very stable skyrmions to avoid their annihilation on track edges. We discussed how to tune a Pt/GdCo/Ta sample properties either at the fabrication step by changing the GdCo thickness or by a post processing using FIB irradiation.
We can finally note that the effect of FIB can also be used to create a region of preferable nucleation of skyrmions on a track (like a small dot optimised to be close to T_R) that can then be sent by current pulses towards areas with different magnetic properties. This technique can therefore induce a diversity of magnetic properties on a single sample, which is clearly a huge advantage that can be used for applications.

Conclusion

In this thesis manuscript, I presented my work on the static as well as the dynamical properties of skyrmions in thin films of GdCo RETM ferrimagnets.

After a reminder of useful concepts in **chapter 1**, I present RETM properties, in **chapter 2**. Emphasis was placed on the use of heavy metal buffer layers (Pt and Ta) to engineer the magnetic properties of ferrimagnetic layer, such as the magnetic anisotropy, DMI and SHE, favourable to stabilise and move skyrmions by current.

The magnetisation of RETMs depends strongly on temperature. For this reason, the stability and size of skyrmions are very sensitive to temperature, as well as to applied magnetic field. I was able, as presented in **chapter 3**, to obtain precise (H, T) phase diagram of skyrmions in GdCo samples. Focus was made on the part where skyrmions can be stable without any external magnetic field, which is located at the edge of their temperature stability region. Using an analytical energy model to account for the skyrmion stability, I could replicate with good agreement the experimentally observed phase diagrams, with the model fully constrained by experimental measurements of the samples magnetic properties. This allowed me to point out to the key parameters of skyrmion stabilisation, with the interplay of DMI and long range dipolar field, and to obtain a precise understanding of the temperature dependant skyrmion stability in RETM films. I also studied the skyrmion size dependence with magnetic field and temperature and showed that both models and simulations underestimate this size but, nonetheless, give a consistent qualitative description and a rather correct dependence of the size with magnetic field.

I then studied the displacement under current of skyrmions in GdCo films and, in particular, the effect of skyrmion size on the mobility of large skyrmions (compared to the DW width parameter) in **chapter 4**. I could evidence the transition from a pinned regime to a linear velocity regime with increasing current density in the experiments. The skyrmion deflection angle was measured to be independent of the skyrmion velocity. The linear regime is also very accurately described by a rigid skyrmion model using the Thiele formalism. Finally, I demonstrated the reversal of the skyrmion deflection angle by crossing the angular compensation, either by changing the temperature on one single sample, or by comparing two samples with different Gd composition. The reversal of the skyrmion deflection angle is also perfectly described by our model and shows the interest of the tunability of RETM systems for the study of skyrmions. The quantitative agreement between experiments and the model, which was well constrained by experimental measurements of the samples magnetic parameters, validates the rigid skyrmion approximation and the use of Wangness effective parameters, even for finite antiferromagnetic exchange coupling.

In **chapter 5** I described an ongoing study on the fine tuning of the GdCo by He-FIB irradiation. I could disentangle the effects of the irradiation on the magnetic anisotropy and magnetisation of GdCo samples with different thickness and capping.

I was able to use this knowledge to stabilise skyrmions in samples that otherwise show saturated magnetic states, but also to confine the dynamics of skyrmions in an irradiated track. Irradiation also showed very promising results for controlled skyrmion nucleation. This work aims at favouring the stabilisation of skyrmions close to T_{ac} in order to precisely characterise the reversal of the skyrmion deflection, and hopefully to observe a complete inhibition of the skyrmion deflection in large magnetic tracks.

Perspectives

There are many different directions in which this work can be continued. I believe that it would be particularly interesting to study the skyrmion nucleation by electrical current pulses and how it changes with RE or TM domination of the RETM material. Indeed, we can expect that the large temperature increase generated by the pulse plays a major role in the nucleation of skyrmions, especially around defects. But, because the magnetisation of the ferrimagnet depends so strongly on temperature, the nucleation process should differ drastically between samples of opposite RE/TM domination. As a matter of fact, for a RE dominated skyrmion stability region, the magnetisation will reduce when increasing temperature (current density or pulse width) which should drive the system away from T_R, and so reducing the size of the nucleated skyrmion. On the other hand, for a TM dominated skyrmion stability region, increasing the temperature drives the system closer to T_R where larger skyrmions should nucleate. We can therefore expect that in both cases, for a given temperature distance to T_R, only a restricted range of current density can nucleate skyrmions, with major differences between the two cases. The temperature increase during the current pulse might reduce (RE dom.) or increase (TM dom.) the skyrmion size during the pulse and so completely modify their dynamical properties; in MOKE, the skyrmion size during their displacement is not accessible but only their successive equilibrium size. An exact calculation of all the time scales at play in this mechanism is needed first to obtain some general expectations and time resolved experiments in STXM with also a better size resolution should be envisioned.
Also, I think that the study of skyrmions in RETM samples with a higher resolution technique (like MFM or synchrotron related techniques (XPEEM or again STXM)) is quite necessary to study their properties closer to T_{mc}. It would be rather interesting to verify the expected skyrmion radius dependence with temperature predicted by the model and the simulations, to nucleate skyrmions close to T_R and to gradually change the temperature towards T_{mc} while monitoring the skyrmions size.

Finally, I believe that more proofs of concept of skyrmion devices should be developed using RETM materials, because their extreme tunability is an undeniable advantage compared to ferromagnetic or SAF samples. Indeed, we can explore the phase space of the magnetic system with much ease compared to these other systems, and therefore, using RETM to optimise potential devices appears as a much efficient way to make skyrmions application readily available.

Publications and Collaborations

I had minor contributions to the following articles, which were part of the work of the group's previous PhD student, Eloi Haltz:

- E. Haltz, L. Berges et al. *Measurement of the tilt of a moving domain wall shows precession-free dynamics in compensated ferrimagnets.* Scientific Reports ,Vol. 10. No. 1 (2020), p. 16292. [262]

- Eloi Haltz, L. Berges et al. *Domain wall dynamics in antiferromagnetically coupled double-lattice systems.* Physical Review B ,Vol. 103. No. 1 (2021), p. 014444. [250]

- E. Haltz, L. Berges et al. *Quantitative analysis of spin wave dynamics in ferrimagnets across compensation points.* Physical Review B ,Vol. 105. No. 10 (2022), p. 104414. [265]

I have made an important contribution to the following article:

- S. Krishnia, L. Berges et al. *Spin-Orbit Coupling in Single-Layer Ferrimagnets: Direct Ob- servation of Spin-Orbit Torques and Chiral Spin Textures.* Physical Review Applied ,Vol. 16. No. 2 (2021), p. 024040. [201]

The work I developed in Section 4.2 on the skyrmion size dependant mobility in the linear velocity regime was published in the following article, of which I am the first author, with little contributions on the model derivation:

- L. Berges et al. *Size-dependent mobility of skyrmions beyond pinning in ferrimagnetic GdCo thin films.* Physical Review B ,Vol. 106. No. 14 (2022), p. 144408. [25]

An article is in preparation to publish our results on the reversal of the skyrmion deflection across the angular compensation presented in Section 4.8.

I had the opportunity to present my work myself in several national and international conferences, but also my coworkers could present it:

- Intermag 2021 (virtual conference), *Spin Orbit Torque Dynamics of Magnetic Skyrmions in GdCo Ferrimagnetic Thin-Films*, oral communication, presented by me.

- Louis Néel , Obernai 2022, *Ferrimagnetic Skyrmions driven by Spin-Orbit Torque in GdCo Thin-Films* , oral communication, presented by me.

- JEMS 2022, Warsaw, *Ferrimagnetic skyrmions in GdCo* , presented by João Sampaio.

- MMM 2022, Minneapolis. *Reversal of skyrmion topological deflection across the angular compensation in GdCo ferrimagnetic thin-film*, presented by Stanislas Rohart.

During my PhD, I collaborated with two teams, for which I fabricated and prepared thin films.

- I fabricated, nano-patterned and characterised sample for the PMTeQ group of Laura Thevenard and Catherine Gourdon at Institut des Nanosciences de Paris (Université de la Sorbonne). They study the coupling of acoustic waves with the magnetisation, by reversing the magnetisation by surface acoustic excitation for instance, and want to use the tunable gyromagnetic ratio of ferrimagnets to explore how the coupling evolves with temperature for instance. This work is financed by the ANR project ACAF.

- I also fabricated, nano-patterned and characterised sample for the S2QT group of Vincent Jacques at Laboratoire Charles Coulomb (Université de Montpellier). Our samples were studied in this group with NV microscopy, where the sensitivity to spin-waves fluctuations of this technique showed a temperature dependant relaxation time of the nitrogen vacancy centre.

Bibliography

[1] T. Skyrme. "A non-linear field theory". *Proceedings of the Royal Society of London. Series A. Mathematical and Physical Sciences* ,Vol. 260. No. 1300 (1961), pp. 127–138. DOI: 10.1098/rspa.1961.0018.

[2] T. Skyrme. "A unified field theory of mesons and baryons". *Nuclear Physics* ,Vol. 31 (1962), pp. 556–569. DOI: 10.1016/0029-5582(62)90775-7.

[3] N. Manton and P. Sutcliffe. *Topological Solitons Cambridge Monographs on Mathematical Physics*. Cambridge University Press, 2004. DOI: 10.2277/0521838363.

[4] N. Zabusky and M. Porter. "Soliton". *Scholarpedia* ,Vol. 5. No. 8 (2010), p. 2068. DOI: 10.4249/scholarpedia.2068.

[5] G. Griffiths and W. Schiesser. "Linear and nonlinear waves". *Scholarpedia* ,Vol. 4. No. 7 (2009), p. 4308. DOI: 10.4249/scholarpedia.4308.

[6] A. Scott. *Encyclopedia of nonlinear science*. Routledge, 2006.

[7] G. S. Adkins, C. R. Nappi, and E. Witten. "Static properties of nucleons in the Skyrme model". *Nuclear Physics B* ,Vol. 228. No. 3 (1983), pp. 552–566. DOI: 10.1016/0550-3213(83)90559-X.

[8] B. Piette, B. Schroers, and W. Zakrzewski. "Dynamics of baby Skyrmions". *Nuclear Physics B* ,Vol. 439. No. 1-2 (1995), pp. 205–235. DOI: 10.1016/0550-3213(95)00011-G.

[9] A. Bogdanov and D Yablonskiui. "Thermodynamically stable "vortices" in magnetically ordered crystals. The mixed state of magnets". *Sov. Phys. JETP* ,Vol. 68 (1989), p. 101.

[10] G. Holzwarth and B. Schwesinger. "Baryons in the Skyrme model". *Reports on Progress in Physics* ,Vol. 49. No. 8 (1986), pp. 825–871. DOI: 10.1088/0034-4885/49/8/001.

[11] S. Mu¨hlbauer, B. Binz, F. Jonietz, et al. "Skyrmion Lattice in a Chiral Magnet". *Science* ,Vol. 323. No. 5916 (2009), pp. 915–919. DOI: 10.1126/science.1166767.

[12] I. Dzyaloshinsky. "A thermodynamic theory of "weak" ferromagnetism of antiferromagnetics". *Journal of Physics and Chemistry of Solids* ,Vol. 4. No. 4 (1958), pp. 241–255. DOI: 10.1016/0022-3697(58)90076-3.

[13] T. Moriya. "Anisotropic Superexchange Interaction and Weak Ferromagnetism". *Physical Review* ,Vol. 120. No. 1 (1960), pp. 91–98. DOI: 10.1103/PhysRev.120.91.

[14] A. N. Bogdanov and U. K. Rößler. "Chiral Symmetry Breaking in Magnetic Thin Films and Multilayers". *Physical Review Letters* ,Vol. 87. No. 3 (2001), p. 037203. DOI: 10.1103/PhysRevLett.87.037203.

[15] A. Fert, N. Reyren, and V. Cros. "Magnetic skyrmions: advances in physics and potential applications". *Nature Reviews Materials* ,Vol. 2. No. 7 (2017), p. 17031. DOI: 10.1038/natrevmats.2017.31.

[16] B. Göbel, I. Mertig, and O. A. Tretiakov. "Beyond skyrmions: Review and perspectives of alternative magnetic quasiparticles". *Physics Reports* ,Vol. 895 (2021), pp. 1–28. DOI: 10.1016/j.physrep.2020.10.001.

[17] C. Kooy and U. Enz. "Experimental and theroretical study of the domain configuration in thin layers of BaFe12O19". *Philips Research Reports* ,Vol. 15. No. 388 (1960), pp. 7–29. DOI: 10.1038/157799a0.

[18] F. A. de Jonge and W. F. Druyvesteyn. "Calculations and Experiments Related to the Magnetostatics of Bubble Domains". *Advances in Solid State Physics*. Elsevier, 1972, pp. 531–597. DOI: 10.1016/B978-0-08-017285-9.50017-X.

[19] A. Malozemoff and J. Slonczewski. *Magnetic Domain Walls in Bubble Materials*. Elsevier, 1979. DOI: 10.1016/C2013-0-06998-8.

[20] A. H. Eschenfelder. *Magnetic Bubble Technology*. Vol. 14. Springer Series in Solid-State Sciences. Berlin, Heidelberg: Springer Berlin Heidelberg, 1980. DOI: 10.1007/978-3-642-96549-4.

[21] S. Heinze, K. von Bergmann, M. Menzel, et al. "Spontaneous atomic-scale magnetic skyrmion lattice in two dimensions". *Nature Physics* ,Vol. 7. No. 9 (2011), pp. 713–718. DOI: 10.1038/nphys2045.

[22] P. Hansen, C. Clausen, G. Much, et al. "Magnetic and magneto-optical properties of rare-earth transition-metal alloys containing Gd, Tb, Fe, Co". *Journal of Applied Physics* ,Vol. 66. No. 2 (1989), pp. 756–767. DOI: 10.1063/1.343551.

[23] P. Gambardella and I. M. Miron. "Current-induced spin–orbit torques". *Philosophical Transactions of the Royal Society A: Mathematical, Physical and Engineering Sciences* ,Vol. 369. No. 1948 (2011), pp. 3175–3197. DOI: 10.1098/rsta.2010.0336.

[24] A. Manchon, J. Železný, I. M. Miron, et al. "Current-induced spin-orbit torques in ferromagnetic and antiferromagnetic systems". *Reviews of Modern Physics* ,Vol. 91. No. 3 (2019), p. 035004. DOI: 10.1103/RevModPhys.91.035004.

[25] L. Berges, E. Haltz, S. Panigrahy, et al. "Size-dependent mobility of skyrmions beyond pinning in ferrimagnetic GdCo thin films". *Physical Review B* ,Vol. 106. No. 14 (2022), p. 144408. DOI: 10.1103/PhysRevB.106.144408.

[26] R. Juge, K. Bairagi, K. G. Rana, et al. "Helium Ions Put Magnetic Skyrmions on the Track". *Nano Letters* ,Vol. 21. No. 7 (2021), pp. 2989–2996. DOI: 10.1021/acs.nanolett.1c00136.

[27] L.-M. Kern, B. Pfau, V. Deinhart, et al. "Deterministic Generation and Guided Motion of Magnetic Skyrmions by Focused He + -Ion Irradiation". *Nano Letters* ,Vol. 22. No. 10 (2022), pp. 4028–4035. DOI: 10.1021/acs.nanolett.2c00670.

[28] K. Fallon, S. Hughes, K. Zeissler, et al. "Controlled Individual Skyrmion Nucleation at Artificial Defects Formed by Ion Irradiation". *Small* ,Vol. 16. No. 13 (2020), p. 1907450. DOI: 10.1002/smll.201907450.

[29] V. Ahrens, L. Gnoli, D. Giuliano, et al. "Skyrmion velocities in FIB irradiated W/CoFeB/MgO thin films". *AIP Advances* ,Vol. 12. No. 3 (2022), p. 035325. DOI: 10.1063/9.0000287.

[30] M. Krupinski, J. Hintermayr, P. Sobieszczyk, et al. "Control of magnetic properties in ferrimagnetic GdFe and TbFe thin films by He+ and Ne+ irradiation". *Physical Review Materials* ,Vol. 5. No. 2 (2021), p. 024405. DOI: 10.1103/PhysRevMaterials.5.024405.

[31] D. Reinsel, J. Gantz, and J. Rydning. "The Digitization of the World - From Edge to Core". *International Data Corporation* No. November (2018). DOI: US44413318.

[32] A. Andrae and T. Edler. "On Global Electricity Usage of Communication Technology: Trends to 2030". *Challenges* ,Vol. 6. No. 1 (2015), pp. 117–157. DOI: 10.3390/challe6010117.

[33] M. N. Baibich, J. M. Broto, A. Fert, et al. "Giant Magnetoresistance of (001)Fe/(001)Cr Magnetic Superlattices". *Physical Review Letters* ,Vol. 61. No. 21 (1988), pp. 2472–2475. DOI: 10.1103/PhysRevLett.61.2472.

[34] G. Binasch, P. Grünberg, F. Saurenbach, et al. "Enhanced magnetoresistance in layered magnetic structures with antiferromagnetic interlayer exchange". *Physical Review B* ,Vol. 39. No. 7 (1989), pp. 4828–4830. DOI: 10.1103/PhysRevB.39.4828.

[35] N. D. Rizzo, D. Houssameddine, J. Janesky, et al. "A Fully Functional 64 Mb DDR3 ST-MRAM Built on 90 nm CMOS Technology". *IEEE Transactions on Magnetics* ,Vol. 49. No. 7 (2013), pp. 4441–4446. DOI: 10.1109/TMAG.2013.2243133.

[36] S. S. P. Parkin. "Data in the Fast Lanes of Racetrack Memory". *Scientific American* ,Vol. 300. No. 6 (2009), pp. 76–81. DOI: 10.1038/scientificamerican0609-76.

[37] W. Kang, B. Wu, X. Chen, et al. "A Comparative Cross-layer Study on Racetrack Memories". *ACM Journal on Emerging Technologies in Computing Systems* ,Vol. 16. No. 1 (2020), pp. 1–17. DOI: 10.1145/3333336.

[38] R. Blasing, A. A. Khan, P. C. Filippou, et al. "Magnetic Racetrack Memory: From Physics to the Cusp of Applications Within a Decade". *Proceedings of the IEEE* ,Vol. 108. No. 8 (2020), pp. 1303–1321. DOI: 10.1109/JPROC.2020.2975719.

[39] G. Yu, P. Upadhyaya, Q. Shao, et al. "Room-Temperature Skyrmion Shift Device for Memory Application". *Nano Letters* ,Vol. 17. No. 1 (2017), pp. 261–268. DOI: 10.1021/acs.nanolett.6b04010.

[40] D. Zhu, w. Kang, S. Li, et al. "Skyrmion Racetrack Memory With Random Information Update/Deletion/Insertion". *IEEE Transactions on Electron Devices* ,Vol. 65. No. 1 (2018), pp. 87–95. DOI: 10.1109/TED.2017.2769672.

[41] D. Kumar, T. Jin, R. Sbiaa, et al. "Domain wall memory: Physics, materials, and devices". *Physics Reports* ,Vol. 958 (2022), pp. 1–35. DOI: 10.1016/j.physrep.2022.02.001.

[42] X. Zhang, Y. Zhou, K. Mee Song, et al. "Skyrmion-electronics: writing, deleting, reading and processing magnetic skyrmions toward spintronic applications". *Journal of Physics: Condensed Matter* ,Vol. 32. No. 14 (2020), p. 143001. DOI: 10.1088/1361-648X/ab5488.

[43] S. Zhang, A. A. Baker, S. Komineas, et al. "Topological computation based on direct magnetic logic communication". *Scientific Reports* ,Vol. 5. No. 1 (2015), p. 15773. DOI: 10.1038/srep15773.

[44] M. Chauwin, X. Hu, F. Garcia-Sanchez, et al. "Skyrmion Logic System for Large-Scale Reversible Computation". *Physical Review Applied* ,Vol. 12. No. 6 (2019), p. 064053. DOI: 10.1103/PhysRevApplied.12.064053.

[45] M. Song, M. G. Park, S. Ko, et al. "Logic Device Based on Skyrmion Annihilation". *IEEE Transactions on Electron Devices* ,Vol. 68. No. 4 (2021), pp. 1939–1943. DOI: 10.1109/TED.2021.3055157.

[46] J. Zázvorka, F. Jakobs, D. Heinze, et al. "Thermal skyrmion diffusion used in a reshuffler device". *Nature Nanotechnology* ,Vol. 14. No. 7 (2019), pp. 658–661. DOI: 10.1038/s41565-019-0436-8.

[47] K. M. Song, J.-S. Jeong, B. Pan, et al. "Skyrmion-based artificial synapses for neuromorphic computing". *Nature Electronics* ,Vol. 3. No. 3 (2020), pp. 148–155. DOI: 10.1038/s41928-020-0385-0.

[48] W. Jiang, X. Zhang, G. Yu, et al. "Direct observation of the skyrmion Hall effect". *Nature Physics* ,Vol. 13. No. 2 (2017), pp. 162–169. DOI: 10.1038/nphys3883.

[49] S. Woo, K. M. Song, X. Zhang, et al. "Current-driven dynamics and inhibition of the skyrmion Hall effect of ferrimagnetic skyrmions in GdFeCo films". *Nature Communications* ,Vol. 9. No. 1 (2018), p. 959. DOI: 10.1038/s41467-018-03378-7.

[50] L. Caretta, M. Mann, F. Büttner, et al. "Fast current-driven domain walls and small skyrmions in a compensated ferrimagnet". *Nature Nanotechnology* ,Vol. 13. No. 12 (2018), pp. 1154–1160. DOI: 10.1038/s41565-018-0255-3.

[51] G. Sala and P. Gambardella. "Ferrimagnetic Dynamics Induced by Spin-Orbit Torques". *Advanced Materials Interfaces* ,Vol. 2201622. No. 1 (2022), p. 2201622. DOI: 10.1002/admi.202201622.

[52] J. Zhou and J. Chen. "Prospect of Spintronics in Neuromorphic Computing". *Advanced Electronic Materials* ,Vol. 7. No. 9 (2021), p. 2100465. DOI: 10.1002/aelm.202100465.

[53] C. Navau and J. Sort. "Exploiting random phenomena in magnetic materials for data security, logics, and neuromorphic computing: Challenges and prospects". *APL Materials* ,Vol. 9. No. 7 (2021), p. 070903. DOI: 10.1063/5.0055400.

[54] Y. Ma and M. Rho. "Recent progress on dense nuclear matter in skyrmion approaches". *Science China Physics, Mechanics & Astronomy* ,Vol. 60. No. 3 (2017), p. 032001. DOI: 10.1007/s11433-016-0497-2.

[55] M. Rho and I. Zahed. *The Multifaceted Skyrmion Chap1*. 2nd. World Scientific, 2016. DOI: 10.1142/9710.

[56] L De Broglie. "Institut international de physique Solvay (1928). Electrons et photons: rapports et discussions du cinquième Conseil de physique tenu à Bruxelles du 24 au 29 octobre 1927". *Solvay Conference*. 1927, pp. 133–142.

[57] L. de Broglie. "L'interprétation de la mécanique ondulatoire". *Journal de Physique et le Radium* ,Vol. 20. No. 12 (1959), pp. 963–979. DOI: 10.1051/jphysrad:019590020012096300.

[58] H. Freistadt. "The Causal Formulation of Quantum Mechanics of Particles (the Theory of De Broglie, Bohm and Takabayasi)". *Il Nuovo Cimento* ,Vol. 5. No. S1 (1957), pp. 1–70. DOI: 10.1007/BF02744313.

[59] D. J. Bohm and B. J. Hiley. "The de Broglie pilot wave theory and the further development of new insights arising out of it". *Foundations of Physics* ,Vol. 12. No. 10 (1982), pp. 1001–1016. DOI: 10.1007/BF01889273.

[60] S. Colin, T. Durt, and R. Willox. "L. de Broglie's double solution program: 90 Years later". *Annales de la Fondation Louis de Broglie* ,Vol. 42. No. 1 (2017), pp. 19–71. DOI: 10.48550/arXiv.1703.06158.

[61] A. Bocdanov and A. Hubert. "The Properties of Isolated Magnetic Vortices". *physica status solidi (b)* ,Vol. 186. No. 2 (1994), pp. 527–543. DOI: 10.1002/pssb.2221860223.

[62] R. G. Elias. "Solitons magnétiques et transitions topologiques". PhD thesis. Université d'Aix-Marseille, 2013.

[63] E. Fradkin. *Field Theories of Condensed Matter Physics*. Cambridge University Press, 2013. DOI: 10.1017/CBO9781139015509.

[64] T. Weidig. "The baby Skyrme models and their multi-skyrmions". *Nonlinearity* ,Vol. 12. No. 6 (1999), pp. 1489–1503. DOI: 10.1088/0951-7715/12/6/303.

[65] I. S. Aranson and L. Kramer. "The world of the complex Ginzburg-Landau equation". *Reviews of Modern Physics* ,Vol. 74. No. 1 (2002), pp. 99–143. DOI: 10.1103/RevModPhys.74.99.

[66] N. Akhmediev and A. Ankiewicz. *Solitons of the Complex Ginzburg—Landau Equation*. Vol. 25. 1. 2001, pp. 311–341. DOI: 10.1007/978-3-540-44582-1_12.

[67] S.-Z. Lin and S. Hayami. "Ginzburg-Landau theory for skyrmions in inversion-symmetric magnets with competing interactions". *Physical Review B* ,Vol. 93. No. 6 (2016), p. 064430. DOI: 10.1103/PhysRevB.93.064430.

[68] A. Yurov and V. Yurov. "The Landau-Lifshitz Equation, the NLS, and the Magnetic Rogue Wave as a By-Product of Two Colliding Regular "Positons"". *Symmetry* ,Vol. 10. No. 4 (2018), p. 82. DOI: 10.3390/sym10040082.

[69] D. Urzagasti, D. Laroze, M. G. Clerc, et al. "Breather soliton solutions in a parametrically driven magnetic wire". *EPL (Europhysics Letters)* ,Vol. 104. No. 4 (2013), p. 40001. DOI: 10.1209/0295-5075/104/40001.

[70] A. N. Bogdanov and C. Panagopoulos. "Physical foundations and basic properties of magnetic skyrmions". *Nature Reviews Physics* ,Vol. 2. No. 9 (2020), pp. 492–498. DOI: 10.1038/s42254-020-0203-7.

[71] M. Ryutova. "Magnetic Solitons". *Journal of Experimental and Theoretical Physics* ,Vol. 127. No. 5 (2018), pp. 912–921. DOI: 10.1134/S1063776118110183.

[72] A. Hubert and S. Schaffert. *Magnetic Domains*. Berlin, Heidelberg: Springer Berlin Heidelberg, 1998. DOI: 10.1007/978-3-540-85054-0.

[73] J. McCord. "Progress in magnetic domain observation by advanced magneto-optical microscopy". *Journal of Physics D: Applied Physics* ,Vol. 48. No. 33 (2015), p. 333001. DOI: 10.1088/0022-3727/48/33/333001.

[74] W. Heisenberg. "Mehrkorperproblem und Resonanz in der Quantenmechanik". *Zeitschrift fur Physik* ,Vol. 38. No. 6-7 (1926), pp. 411–426. DOI: 10.1007/BF01397160.

[75] P. Dirac. "On the theory of quantum mechanics". *Proceedings of the Royal Society of London. Series A, Containing Papers of a Mathematical and Physical Character* ,Vol. 112. No. 762 (1926), pp. 661–677. DOI: 10.1098/rspa.1926.0133.

[76] R. Stuart and W. Marshall. "Direct Exchange in Ferromagnets". *Physical Review* ,Vol. 120. No. 2 (1960), pp. 353–357. DOI: 10.1103/PhysRev.120.353.

[77] S. Blundell. *Magnetism in Condensed Matter*. Oxford Master Series in Physics, 2001.

[78] J. B. Goodenough. "Theory of the role of covalence in the perovskite-type manganites [La,M(II)]MnO3". *Physical Review* ,Vol. 100. No. 2 (1955), pp. 564–573. DOI: 10.1103/PhysRev.100.564.

[79] J. Kanamori. "Theory of the Magnetic Properties of Ferrous and Cobaltous Oxides, I". *Progress of Theoretical Physics* ,Vol. 17. No. 2 (1957), pp. 177–196. DOI: 10.1143/PTP.17.177.

[80] J. Goodenough. "Goodenough-Kanamori rule". *Scholarpedia* ,Vol. 3. No. 10 (2008), p. 7382. DOI: 10.4249/scholarpedia.7382.

[81] M. A. Ruderman and C. Kittel. "Indirect Exchange Coupling of Nuclear Magnetic Moments by Conduction Electrons". *Physical Review* ,Vol. 96. No. 1 (1954), pp. 99–102. DOI: 10.1103/PhysRev.96.99.

[82] T. Kasuya. "A Theory of Metallic Ferro- and Antiferromagnetism on Zener's Model". *Progress of Theoretical Physics* ,Vol. 16. No. 1 (1956), pp. 45–57. DOI: 10.1143/PTP.16.45.

[83] K. Yosida. "Magnetic Properties of Cu-Mn Alloys". *Physical Review* ,Vol. 106. No. 5 (1957), pp. 893–898. DOI: 10.1103/PhysRev.106.893.

[84] S. S. P. Parkin. "Systematic variation of the strength and oscillation period of indirect magnetic exchange coupling through the 3 d , 4 d , and 5 d transition metals". *Physical Review Letters* ,Vol. 67. No. 25 (1991), pp. 3598–3601. DOI: 10.1103/PhysRevLett.67.3598.

[85] I. A. Campbell. "Indirect exchange for rare earths in metals". *Journal of Physics F: Metal Physics* ,Vol. 2. No. 3 (1972), pp. L47–L50. DOI: 10.1088/0305-4608/2/3/004.

[86] A. Thiaville, S. Rohart, É. Jué, et al. "Dynamics of Dzyaloshinskii domain walls in ultrathin magnetic films". *EPL (Europhysics Letters)* ,Vol. 100. No. 5 (2012), p. 57002. DOI: 10.1209/0295-5075/100/57002.

[87] H. Yang, A. Thiaville, S. Rohart, et al. "Anatomy of Dzyaloshinskii-Moriya Interaction at Co/Pt Interfaces". *Physical Review Letters* ,Vol. 115. No. 26 (2015), p. 267210. DOI: 10.1103/PhysRevLett.115.267210.

[88] H. T. Nembach, J. M. Shaw, M. Weiler, et al. "Linear relation between Heisenberg exchange and interfacial Dzyaloshinskii–Moriya interaction in metal films". *Nature Physics* ,Vol. 11. No. 10 (2015), pp. 825–829. DOI: 10.1038/nphys3418.

[89] A. Belabbes, G. Bihlmayer, F. Bechstedt, et al. "Hund's Rule-Driven Dzyaloshinskii-Moriya Interaction at 3d-5d Interfaces". *Physical Review Letters* ,Vol. 117. No. 24 (2016), p. 247202. DOI: 10.1103/PhysRevLett.117.247202.

[90] X. Ma, G. Yu, C. Tang, et al. "Interfacial Dzyaloshinskii-Moriya Interaction: Effect of 5d Band Filling and Correlation with Spin Mixing Conductance". *Physical Review Letters* ,Vol. 120. No. 15 (2018), p. 157204. DOI: 10.1103/PhysRevLett.120.157204.

[91] K. Shahbazi, J.-V. Kim, H. T. Nembach, et al. "Domain-wall motion and interfacial Dzyaloshinskii-Moriya interactions in Pt/Co/Ir(tIr)/Ta multilayers". *Physical Review B* ,Vol. 99. No. 9 (2019), p. 094409. DOI: 10.1103/PhysRevB.99.094409.

[92] N Nakajima, T Koide, T Shidara, et al. "Perpendicular Magnetic Anisotropy Caused by Interfacial Hybridization via Enhanced Orbital Moment in Co/Pt Multilayers: Magnetic Circular X-Ray Dichroism Study". *Physical Review Letters* ,Vol. 81. No. 23 (1998), pp. 5229–5232. DOI: 10.1103/PhysRevLett.81.5229.

[93] I. G. Rau, S. Baumann, S. Rusponi, et al. "Reaching the magnetic anisotropy limit of a 3 d metal atom". *Science* ,Vol. 344. No. 6187 (2014), pp. 988–992. DOI: 10.1126/science.1252841.

[94] D. Mergel, H. Heitmann, and P. Hansen. "Pseudocrystalline model of the magnetic anisotropy in amorphous rare-earth–transition-metal thin films". *Physical Review B* ,Vol. 47. No. 2 (1993), pp. 882–891. DOI: 10.1103/PhysRevB.47.882.

[95] M. T. Johnson, P. J. H. Bloemen, F. J. A. den Broeder, et al. "Magnetic anisotropy in metallic multilayers". *Reports on Progress in Physics* ,Vol. 59. No. 11 (1996), pp. 1409–1458. DOI: 10.1088/0034-4885/59/11/002.

[96] B. Rodmacq, A. Manchon, C. Ducruet, et al. "Influence of thermal annealing on the perpendicular magnetic anisotropy of Pt/Co/AlOx trilayers". *Physical Review B* ,Vol. 79. No. 2 (2009), p. 024423. DOI: 10.1103/PhysRevB.79.024423.

[97] F. den Broeder, W. Hoving, and P. Bloemen. "Magnetic anisotropy of multilayers". *Journal of Magnetism and Magnetic Materials* ,Vol. 93. No. C (1991), pp. 562–570. DOI: 10.1016/0304-8853(91)90404-X.

[98] S. Tandon, M. Beleggia, Y. Zhu, et al. "On the computation of the demagnetization tensor for uniformly magnetized particles of arbitrary shape. Part I: Analytical approach". *Journal of Magnetism and Magnetic Materials* ,Vol. 271. No. 1 (2004), pp. 9–26. DOI: 10.1016/j.jmmm.2003.09.011.

[99] J. M. Winter. "Bloch Wall Excitation. Application to Nuclear Resonance in a Bloch Wall". *Physical Review* ,Vol. 124. No. 2 (1961), pp. 452–459. DOI: 10.1103/PhysRev.124.452.

[100] S. Tarasenko, A. Stankiewicz, V. Tarasenko, et al. "Bloch wall dynamics in ultrathin ferromagnetic films". *Journal of Magnetism and Magnetic Materials* ,Vol. 189. No. 1 (1998), pp. 19–24. DOI: 10.1016/S0304-8853(98)00230-3.

[101] I. Lemesh, F. Büttner, and G. S. D. Beach. "Accurate model of the stripe domain phase of perpendicularly magnetized multilayers". *Physical Review B* ,Vol. 95. No. 17 (2017), p. 174423. DOI: 10.1103/PhysRevB.95.174423.

[102] A. Bogdanov and A. Hubert. "Thermodynamically stable magnetic vortex states in magnetic crystals". *Journal of Magnetism and Magnetic Materials* ,Vol. 138. No. 3 (1994), pp. 255–269. DOI: 10.1016/0304-8853(94)90046-9.

[103] J. Lucassen, M. J. Meijer, O. Kurnosikov, et al. "Tuning Magnetic Chirality by Dipolar Interactions". *Physical Review Letters* ,Vol. 123. No. 15 (2019), p. 157201. DOI: 10.1103/PhysRevLett.123.157201.

[104] S. Paul, S. Haldar, S. von Malottki, et al. "Role of higher-order exchange interactions for skyrmion stability". *Nature Communications* ,Vol. 11. No. 1 (2020), p. 4756. DOI: 10.1038/s41467-020-18473-x.

[105] M. Gutzeit, S. Haldar, S. Meyer, et al. "Trends of higher-order exchange interactions in transition metal trilayers". *Physical Review B* ,Vol. 104. No. 2 (2021), p. 024420. DOI: 10.1103/PhysRevB.104.024420.

[106] J.-V. Kim and J. Mulkers. "On quantifying the topological charge in micromagnetics using a lattice-based approach". *IOP SciNotes* ,Vol. 1. No. 2 (2020), p. 025211. DOI: 10.1088/2633-1357/abad0c.

[107] S. Rohart, J. Miltat, and A. Thiaville. "Path to collapse for an isolated Néel skyrmion". *Physical Review B* ,Vol. 93. No. 21 (2016), p. 214412. DOI: 10.1103/PhysRevB.93.214412.

[108] L. Camosi, N. Rougemaille, O. Fruchart, et al. "Micromagnetics of antiskyrmions in ultrathin films". *Physical Review B* ,Vol. 97. No. 13 (2018), p. 134404. DOI: 10.1103/PhysRevB.97.134404.

[109] M. Hoffmann, B. Zimmermann, G. P. Müller, et al. "Antiskyrmions stabilized at interfaces by anisotropic Dzyaloshinskii-Moriya interactions". *Nature Communications* ,Vol. 8. No. 1 (2017), p. 308. DOI: 10.1038/s41467-017-00313-0.

[110] A. K. Nayak, V. Kumar, T. Ma, et al. "Magnetic antiskyrmions above room temperature in tetragonal Heusler materials". *Nature* ,Vol. 548. No. 7669 (2017), pp. 561–566. DOI: 10.1038/nature23466.

[111] L. Camosi, S. Rohart, O. Fruchart, et al. "Anisotropic Dzyaloshinskii-Moriya interaction in ultrathin epitaxial Au/Co/W(110)". *Physical Review B* ,Vol. 95. No. 21 (2017), p. 214422. DOI: 10.1103/PhysRevB.95.214422.

[112] T. Devolder, D. Rontani, S. Petit-Watelot, et al. “Chaos in Magnetic Nanocontact Vortex Oscillators”. *Physical Review Letters* ,Vol. 123. No. 14 (2019), p. 147701. DOI: 10.1103/PhysRevLett.123.147701.

[113] J. Torrejon, M. Riou, F. A. Araujo, et al. “Neuromorphic computing with nanoscale spintronic oscillators”. *Nature* ,Vol. 547. No. 7664 (2017), pp. 428–431. DOI: 10.1038/nature23011.

[114] C. Phatak, O. Heinonen, M. De Graef, et al. “Nanoscale Skyrmions in a Nonchiral Metallic Multiferroic: Ni 2 MnGa”. *Nano Letters* ,Vol. 16. No. 7 (2016), pp. 4141–4148. DOI: 10.1021/acs.nanolett.6b01011.

[115] P. J. Grundy, D. C. Hothersall, G. A Jones, et al. *The Formation and Structure of Cylindrical Magnetic Domains in Thin Cobalt Crystals*. Vol. 9. 79. De Gruyter, 1972, pp. 79–88. DOI: 10.1515/9783112472682-006.

[116] Youtube. *52-bit magnetic bubble chip : www.youtube.com/watch?v=0rqPmjmQOxw*. 1971. DOI: None.

[117] M. H. Kryder and H. L. Hu. “Bubble Dynamics in Amorphous Magnetic Materials”. Vol. 213. July 2008. 1974, pp. 213–216. DOI: 10.1063/1.2947319.

[118] G. P. Vella-Coleiro, A. Rosencwaig, and W. J. Tabor. “Dynamic Properties of "Hard" Magnetic Bubbles”. *Physical Review Letters* ,Vol. 29. No. 14 (1972), pp. 949–952. DOI: 10.1103/PhysRevLett.29.949.

[119] D. C. Bullock. “The Effect of a Constant In-Plane Magnetic Field on Magnetic Bubble Translation in”. *Magnetism and Magnetic Materials — 1973: Nineteenth Annual Conference*. Vol. 232. 18. ASCE, 1974, pp. 232–236. DOI: 10.1063/1.2947324.

[120] X. Z. Yu, Y. Tokunaga, Y. Kaneko, et al. “Biskyrmion states and their current-driven motion in a layered manganite”. *Nature Communications* ,Vol. 5. No. 1 (2014), p. 3198. DOI: 10.1038/ncomms4198.

[121] Y. Tu. “Determination of Magnetization of Micromagnetic Wall in Bubble Domains by Direct Minimization”. *Journal of Applied Physics* ,Vol. 42. No. 13 (1971), pp. 5704–5709. DOI: 10.1063/1.1660002.

[122] W. J. DeBonte. “Properties of thick-walled cylindrical magnetic domains in uniaxial platelets”. *Journal of Applied Physics* ,Vol. 44. No. 4 (1973), pp. 1793–1797. DOI: 10.1063/1.1662450.

[123] W. Legrand. “Crafting magnetic skyrmions at room temperature: size, stability and dynamics in multilayers”. PhD thesis. Université Paris Saclay, 2019. DOI: tel-02145619.

[124] J. Choi, J. Wu, C. Won, et al. “Magnetic Bubble Domain Phase at the Spin Reorientation Transition of Ultrathin Fe/Ni/Cu(001) Film”. *Physical Review Letters* ,Vol. 98. No. 20 (2007), p. 207205. DOI: 10.1103/PhysRevLett.98.207205.

[125] A. Hrabec, J. Sampaio, M. Belmeguenai, et al. “Current-induced skyrmion generation and dynamics in symmetric bilayers”. *Nature Communications* ,Vol. 8. No. 1 (2017), p. 15765. DOI: 10.1038/ncomms15765.

[126] F. N. Rybakov, A. Pervishko, O. Eriksson, et al. “Antichiral ferromagnetism”. *Physical Review B* ,Vol. 104. No. 2 (2021), p. L020406. DOI: 10.1103/PhysRevB.104.L020406.

[127] W. Jiang, P. Upadhyaya, W. Zhang, et al. “Blowing magnetic skyrmion bubbles”. *Science* ,Vol. 349. No. 6245 (2015), pp. 283–286. DOI: 10.1126/science.aaa1442.

[128] X. Z. Yu, Y Onose, N Kanazawa, et al. “Real-space observation of a two-dimensional skyrmion crystal”. *Nature* ,Vol. 465. No. 7300 (2010), pp. 901–904. DOI: 10.1038/nature09124.

[129] X. Z. Yu, N. Kanazawa, Y. Onose, et al. “Near room-temperature formation of a skyrmion crystal in thin-films of the helimagnet FeGe”. *Nature Materials* ,Vol. 10. No. 2 (2011), pp. 106–109. DOI: 10.1038/nmat2916.

[130] F. Jonietz, S. Mühlbauer, C. Pfleiderer, et al. “Spin Transfer Torques in MnSi at Ultralow Current Densities”. *Science* ,Vol. 330. No. 6011 (2010), pp. 1648–1651. DOI: 10.1126/science.1195709.

[131] X. Yu, N. Kanazawa, W. Zhang, et al. "Skyrmion flow near room temperature in an ultralow current density". *Nature Communications* ,Vol. 3. No. 1 (2012), p. 988. DOI: 10.1038/ncomms1990.

[132] H. S. Park, X. Yu, S. Aizawa, et al. "Observation of the magnetic flux and three-dimensional structure of skyrmion lattices by electron holography". *Nature Nanotechnology* ,Vol. 9. No. 5 (2014), pp. 337–342. DOI: 10.1038/nnano.2014.52.

[133] M. T. Birch, D. Cortés-Ortuño, L. A. Turnbull, et al. "Real-space imaging of confined magnetic skyrmion tubes". *Nature Communications* ,Vol. 11. No. 1 (2020), p. 1726. DOI: 10.1038/s41467-020-15474-8.

[134] T. A. Moore, I. M. Miron, G. Gaudin, et al. "High domain wall velocities induced by current in ultrathin Pt/Co/AlOx wires with perpendicular magnetic anisotropy". *Applied Physics Letters* ,Vol. 93. No. 26 (2008), p. 262504. DOI: 10.1063/1.3062855.

[135] N. Romming, C. Hanneken, M. Menzel, et al. "Writing and Deleting Single Magnetic Skyrmions". *Science* ,Vol. 341. No. 6146 (2013), pp. 636–639. DOI: 10.1126/science.1240573.

[136] G. Chen, A. Mascaraque, A. T. N'Diaye, et al. "Room temperature skyrmion ground state stabilized through interlayer exchange coupling". *Applied Physics Letters* ,Vol. 106. No. 24 (2015), p. 242404. DOI: 10.1063/1.4922726.

[137] O. Boulle, J. Vogel, H. Yang, et al. "Room-temperature chiral magnetic skyrmions in ultrathin magnetic nanostructures". *Nature Nanotechnology* ,Vol. 11. No. 5 (2016), pp. 449–454. DOI: 10.1038/nnano.2015.315.

[138] T. Dohi, S. DuttaGupta, S. Fukami, et al. "Formation and current-induced motion of synthetic antiferromagnetic skyrmion bubbles". *Nature Communications* ,Vol. 10. No. 1 (2019), p. 5153. DOI: 10.1038/s41467-019-13182-6.

[139] W. Münzer, A. Neubauer, T. Adams, et al. "Skyrmion lattice in the doped semiconductor Fe1-xCoxSi". *Physical Review B* ,Vol. 81. No. 4 (2010), p. 041203. DOI: 10.1103/PhysRevB.81.041203.

[140] N. Kanazawa, S. Seki, and Y. Tokura. "Noncentrosymmetric Magnets Hosting Magnetic Skyrmions". *Advanced Materials* ,Vol. 29. No. 25 (2017), p. 1603227. DOI: 10.1002/adma.201603227.

[141] Y. Tokura and N. Kanazawa. "Magnetic Skyrmion Materials". *Chemical Reviews* ,Vol. 121. No. 5 (2021), pp. 2857–2897. DOI: 10.1021/acs.chemrev.0c00297.

[142] N. Romming, A. Kubetzka, C. Hanneken, et al. "Field-Dependent Size and Shape of Single Magnetic Skyrmions". *Physical Review Letters* ,Vol. 114. No. 17 (2015), p. 177203. DOI: 10.1103/PhysRevLett.114.177203.

[143] A. O. Leonov, T. L. Monchesky, N. Romming, et al. "The properties of isolated chiral skyrmions in thin magnetic films". *New Journal of Physics* ,Vol. 18. No. 6 (2016), p. 065003. DOI: 10.1088/1367-2630/18/6/065003.

[144] S Rohart and A Thiaville. "Skyrmion confinement in ultrathin film nanostructures in the presence of Dzyaloshinskii-Moriya interaction". *Physical Review B* ,Vol. 88. No. 18 (2013), p. 184422. DOI: 10.1103/PhysRevB.88.184422.

[145] K. G. Rana, A. Finco, F. Fabre, et al. "Room-Temperature Skyrmions at Zero Field in Exchange-Biased Ultrathin Films". *Physical Review Applied* ,Vol. 13. No. 4 (2020), p. 044079. DOI: 10.1103/PhysRevApplied.13.044079.

[146] T. Srivastava, W. Lim, I. Joumard, et al. "Mapping different skyrmion phases in double wedges of Ta/FeCoB/TaOx trilayers". *Physical Review B* ,Vol. 100. No. 22 (2019), p. 220401. DOI: 10.1103/PhysRevB.100.220401.

[147] F. Büttner, I. Lemesh, and G. S. D. Beach. "Theory of isolated magnetic skyrmions: From fundamentals to room temperature applications". *Scientific Reports* ,Vol. 8. No. 1 (2018), p. 4464. DOI: 10.1038/s41598-018-22242-8.

[148] A. Bernand-Mantel, L. Camosi, A. Wartelle, et al. "The skyrmion-bubble transition in a ferromagnetic thin film". *SciPost Physics* ,Vol. 4. No. 5 (2018), p. 027. DOI: 10.21468/SciPostPhys.4.5.027.

[149] X. S. Wang, H. Y. Yuan, and X. R. Wang. "A theory on skyrmion size". *Communications Physics* ,Vol. 1. No. 1 (2018), p. 31. DOI: 10.1038/s42005-018-0029-0.

[150] C. Jin, C. Song, J. Wang, et al. "Dynamics of antiferromagnetic skyrmion driven by the spin Hall effect". *Applied Physics Letters* ,Vol. 109. No. 18 (2016), p. 182404. DOI: 10.1063/1.4967006.

[151] W. Legrand, D. Maccariello, F. Ajejas, et al. "Room-temperature stabilization of antiferromagnetic skyrmions in synthetic antiferromagnets". *Nature Materials* ,Vol. 19. No. 1 (2020), pp. 34–42. DOI: 10.1038/s41563-019-0468-3.

[152] A.-O. Mandru, O. Yıldırım, R. Tomasello, et al. "Coexistence of distinct skyrmion phases observed in hybrid ferromagnetic/ferrimagnetic multilayers". *Nature Communications* ,Vol. 11. No. 1 (2020), p. 6365. DOI: 10.1038/s41467-020-20025-2.

[153] W. Legrand, N. Ronceray, N. Reyren, et al. "Modeling the Shape of Axisymmetric Skyrmions in Magnetic Multilayers". *Physical Review Applied* ,Vol. 10. No. 6 (2018), p. 064042. DOI: 10.1103/PhysRevApplied.10.064042.

[154] W. Legrand, J.-Y. Chauleau, D. Maccariello, et al. "Hybrid chiral domain walls and skyrmions in magnetic multilayers". *Science Advances* ,Vol. 4. No. 7 (2018). DOI: 10.1126/sciadv.aat0415.

[155] K. Chen, D. Lott, A. Philippi-Kobs, et al. "Observation of compact ferrimagnetic skyrmions in DyCo 3 film". *Nanoscale* ,Vol. 12. No. 35 (2020), pp. 18137–18143. DOI: 10.1039/D0NR02947E.

[156] H. Wu, F. Groß, B. Dai, et al. "Ferrimagnetic Skyrmions in Topological Insulator/Ferrimagnet Heterostructures". *Advanced Materials* ,Vol. 32. No. 34 (2020), p. 2003380. DOI: 10.1002/adma.202003380.

[157] M. H. Seaberg, B. Holladay, S. A. Montoya, et al. "Spontaneous fluctuations in a magnetic Fe/Gd skyrmion lattice". *Physical Review Research* ,Vol. 3. No. 3 (2021), p. 033249. DOI: 10.1103/PhysRevResearch.3.033249.

[158] J. Brandão, D. A. Dugato, M. V. Puydinger dos Santos, et al. "Evolution of Zero-Field Ferrimagnetic Domains and Skyrmions in Exchange-Coupled Pt/CoGd/Pt Confined Nanostructures: Implications for Antiferromagnetic Devices". *ACS Applied Nano Materials* ,Vol. 2. No. 12 (2019), pp. 7532–7539. DOI: 10.1021/acsanm.9b01593.

[159] J. Brandão, D. Dugato, M. Puydinger dos Santos, et al. "Tuning isolated zero-field skyrmions and spin spirals at room-temperature in synthetic ferrimagnetic multilayers". *Applied Surface Science* ,Vol. 585. No. February (2022), p. 152598. DOI: 10.1016/j.apsusc.2022.152598.

[160] H.-B. Braun. "Fluctuations and instabilities of ferromagnetic domain-wall pairs in an external magnetic field". *Physical Review B* ,Vol. 50. No. 22 (1994), pp. 16485–16500. DOI: 10.1103/PhysRevB.50.16485.

[161] R. Tomasello, K. Y. Guslienko, M. Ricci, et al. "Origin of temperature and field dependence of magnetic skyrmion size in ultrathin nanodots". *Physical Review B* ,Vol. 97. No. 6 (2018), p. 060402. DOI: 10.1103/PhysRevB.97.060402.

[162] K. Litzius, J. Leliaert, P. Bassirian, et al. "The role of temperature and drive current in skyrmion dynamics". *Nature Electronics* ,Vol. 3. No. 1 (2020), pp. 30–36. DOI: 10.1038/s41928-019-0359-2.

[163] A. Belavin and A. Polyakov. "Metastable states of two-dimensional isotropic ferromagnets". *JETP Letter* ,Vol. 22. No. 10 (1975), pp. 245–248.

[164] J. A. Cape and G. W. Lehman. "Magnetic Domain Structures in Thin Uniaxial Plates with Perpendicular Easy Axis". *Journal of Applied Physics* ,Vol. 42. No. 13 (1971), pp. 5732–5756. DOI: 10.1063/1.1660007.

[165] L. Ranno and M. A. Moro. "Design Rules for DMI-Stabilised Skyrmions" (2021), pp. 1–12. DOI: 10.48550/arXiv.2107.00767.

[166] N. S. Kiselev, A. N. Bogdanov, R. Schäfer, et al. "Chiral skyrmions in thin magnetic films: new objects for magnetic storage technologies?" *Journal of Physics D: Applied Physics* ,Vol. 44. No. 39 (2011), p. 392001. DOI: 10.1088/0022-3727/44/39/392001.

[167] U. K. Rößler, A. N. Bogdanov, and C. Pfleiderer. "Spontaneous skyrmion ground states in magnetic metals". *Nature* ,Vol. 442. No. 7104 (2006), pp. 797–801. DOI: 10.1038/nature05056.

[168] V. G. Bar'yakhtar and B. A. Ivanov. "The Landau-Lifshitz equation: 80 years of history, advances, and prospects". *Low Temperature Physics* ,Vol. 41. No. 9 (2015), pp. 663–669. DOI: 10.1063/1.4931649.

[169] M. A. W. Schoen, D. Thonig, M. L. Schneider, et al. "Ultra-low magnetic damping of a metallic ferromagnet". *Nature Physics* ,Vol. 12. No. 9 (2016), pp. 839–842. DOI: 10.1038/nphys3770.

[170] S. Azzawi, A. T. Hindmarch, and D. Atkinson. "Magnetic damping phenomena in ferromagnetic thin-films and multilayers". *Journal of Physics D: Applied Physics* ,Vol. 50. No. 47 (2017), p. 473001. DOI: 10.1088/1361-6463/aa8dad.

[171] B. H. Kamel. *Spin Dynamics in Confined Magnetic Structures III*. Ed. by B. Hillebrands and A. Thiaville. Vol. 101. Topics in Applied Physics. Springer Berlin Heidelberg, 2006. DOI: 10.1007/b12462.

[172] H. Suhl. "Theory of the magnetic damping constant". *IEEE Transactions on Magnetics* ,Vol. 34. No. 4 (1998), pp. 1834–1838. DOI: 10.1109/20.706720.

[173] J.-V. Kim, F. Garcia-Sanchez, J. Sampaio, et al. "Breathing modes of confined skyrmions in ultrathin magnetic dots". *Physical Review B* ,Vol. 90. No. 6 (2014), p. 064410. DOI: 10.1103/PhysRevB.90.064410.

[174] M. Lonsky and A. Hoffmann. "Coupled skyrmion breathing modes in synthetic ferri- and antiferromagnets". *Physical Review B* ,Vol. 102. No. 10 (2020), p. 104403. DOI: 10.1103/PhysRevB.102.104403.

[175] L. Desplat, D. Suess, J.-V. Kim, et al. "Thermal stability of metastable magnetic skyrmions: Entropic narrowing and significance of internal eigenmodes". *Physical Review B* ,Vol. 98. No. 13 (2018), p. 134407. DOI: 10.1103/PhysRevB.98.134407.

[176] M. Mochizuki. "Spin-Wave Modes and Their Intense Excitation Effects in Skyrmion Crystals". *Physical Review Letters* ,Vol. 108. No. 1 (2012), p. 017601. DOI: 10.1103/PhysRevLett.108.017601.

[177] A. S. Varentcova, S. von Malottki, M. N. Potkina, et al. "Toward room-temperature nanoscale skyrmions in ultrathin films". *npj Computational Materials* ,Vol. 6. No. 1 (2020), p. 193. DOI: 10.1038/s41524-020-00453-w.

[178] L. Berger. "Low-field magnetoresistance and domain drag in ferromagnets". *Journal of Applied Physics* ,Vol. 49. No. 3 (1978), pp. 2156–2161. DOI: 10.1063/1.324716.

[179] L. Berger. "Domain drag effect in the presence of variable magnetic field or variable transport current". *Journal of Applied Physics* ,Vol. 50. No. B3 (1979), pp. 2137–2139. DOI: 10.1063/1.327083.

[180] P. P. Freitas and L. Berger. "Observation of s - d exchange force between domain walls and electric current in very thin Permalloy films". *Journal of Applied Physics* ,Vol. 57. No. 4 (1985), pp. 1266–1269. DOI: 10.1063/1.334524.

[181] W. J. Carr. "Propagation of magnetic domain walls by a self-induced current distribution". *Journal of Applied Physics* ,Vol. 45. No. 1 (1974), pp. 394–396. DOI: 10.1063/1.1662991.

[182] D. Partin, M. Karnezos, L. DeMenezes, et al. "Nonuniform current distribution in the neighborhood of a ferromagnetic domain wall in cobalt at 4.2 K". *Journal of Applied Physics* ,Vol. 45. No. 4 (1974), pp. 1852–1859. DOI: 10.1063/1.1663503.

[183] J. Slonczewski. "Current-driven excitation of magnetic multilayers". *Journal of Magnetism and Magnetic Materials* ,Vol. 159. No. 1-2 (1996), pp. L1–L7. DOI: 10.1016/0304-8853(96)00062-5.

[184] L Berger. "Emission of spin waves by a magnetic multilayer traversed by a current". *Physical Review B* ,Vol. 54. No. 13 (1996), pp. 9353–9358.

[185] D. Ralph and M. Stiles. "Spin transfer torques". *Journal of Magnetism and Magnetic Materials* ,Vol. 320. No. 7 (2008), pp. 1190–1216. DOI: 10.1016/j.jmmm.2007.12.019.

[186] K.-W. Moon, C. Kim, J. Yoon, et al. "A spin torque meter with magnetic facet domains". *Nature Communications* ,Vol. 9. No. 1 (2018), p. 3788. DOI: 10.1038/s41467-018-06223-z.

[187] A. Brataas, A. D. Kent, and H. Ohno. "Current-induced torques in magnetic materials". *Nature Materials* ,Vol. 11. No. 5 (2012), pp. 372–381. DOI: 10.1038/nmat3311.

[188] A. Thiaville, Y. Nakatani, J. Miltat, et al. "Micromagnetic understanding of current-driven domain wall motion in patterned nanowires". *Europhysics Letters (EPL)* ,Vol. 69. No. 6 (2005), pp. 990–996. DOI: 10.1209/epl/i2004-10452-6.

[189] K. Tanabe and J.-i. Ohe. "Spin-Motive Force in Ferromagnetic and Ferrimagnetic Materials". *Journal of the Physical Society of Japan* ,Vol. 90. No. 8 (2021), p. 081011. DOI: 10.7566/JPSJ.90.081011.

[190] T. Schulz, R. Ritz, A. Bauer, et al. "Emergent electrodynamics of skyrmions in a chiral magnet". *Nature Physics* ,Vol. 8. No. 4 (2012), pp. 301–304. DOI: 10.1038/nphys2231.

[191] N. Nagaosa and Y. Tokura. "Topological properties and dynamics of magnetic skyrmions". *Nature Nanotechnology* ,Vol. 8. No. 12 (2013), pp. 899–911. DOI: 10.1038/nnano.2013.243.

[192] J. Sinova, S. O. Valenzuela, J. Wunderlich, et al. "Spin Hall effects". *Reviews of Modern Physics* ,Vol. 87. No. 4 (2015), pp. 1213–1260. DOI: 10.1103/RevModPhys.87.1213.

[193] V. Edelstein. "Spin polarization of conduction electrons induced by electric current in two-dimensional asymmetric electron systems". *Solid State Communications* ,Vol. 73. No. 3 (1990), pp. 233–235. DOI: 10.1016/0038-1098(90)90963-C.

[194] V. V. Bel'kov and S. D. Ganichev. "Magneto-gyrotropic effects in semiconductor quantum wells". *Semiconductor Science and Technology* ,Vol. 23. No. 11 (2008), p. 114003. DOI: 10.1088/0268-1242/23/11/114003.

[195] A. Manchon, H. C. Koo, J. Nitta, et al. "New perspectives for Rashba spin–orbit coupling". *Nature Materials* ,Vol. 14. No. 9 (2015), pp. 871–882. DOI: 10.1038/nmat4360.

[196] A. Soumyanarayanan, N. Reyren, A. Fert, et al. "Emergent phenomena induced by spin–orbit coupling at surfaces and interfaces". *Nature* ,Vol. 539. No. 7630 (2016), pp. 509–517. DOI: 10.1038/nature19820.

[197] F. Hellman, A. Hoffmann, Y. Tserkovnyak, et al. "Interface-induced phenomena in magnetism". *Reviews of Modern Physics* ,Vol. 89. No. 2 (2017), p. 025006. DOI: 10.1103/RevModPhys.89.025006.

[198] R. Liu, K. Gupta, Z. Yuan, et al. "Calculating the spin memory loss at Cu|metal interfaces from first principles". *Physical Review B* ,Vol. 106. No. 1 (2022), p. 014401. DOI: 10.1103/PhysRevB.106.014401.

[199] K. Gupta, R. J. Wesselink, R. Liu, et al. "Disorder Dependence of Interface Spin Memory Loss". *Physical Review Letters* ,Vol. 124. No. 8 (2020), p. 087702. DOI: 10.1103/PhysRevLett.124.087702.

[200] R. Ramaswamy, J. M. Lee, K. Cai, et al. "Recent advances in spin-orbit torques: Moving towards device applications". *Applied Physics Reviews* ,Vol. 5. No. 3 (2018), p. 031107. DOI: 10.1063/1.5041793.

[201] S. Krishnia, E. Haltz, L. Berges, et al. "Spin-Orbit Coupling in Single-Layer Ferrimagnets: Direct Observation of Spin-Orbit Torques and Chiral Spin Textures". *Physical Review Applied* ,Vol. 16. No. 2 (2021), p. 024040. DOI: 10.1103/PhysRevApplied.16.024040.

[202] S. Lee, M.-G. Kang, D. Go, et al. "Efficient conversion of orbital Hall current to spin current for spin-orbit torque switching". *Communications Physics* ,Vol. 4. No. 1 (2021), p. 234. DOI: 10.1038/s42005-021-00737-7.

[203] L. Salemi and P. M. Oppeneer. "First-principles theory of intrinsic spin and orbital Hall and Nernst effects in metallic monoatomic crystals" (2022), pp. 1–12.

[204] A. A. Thiele. "Steady-State Motion of Magnetic Domains". *Physical Review Letters* ,Vol. 30. No. 6 (1973), pp. 230–233. DOI: 10.1103/PhysRevLett.30.230.

[205] A. A. Thiele. "Applications of the gyrocoupling vector and dissipation dyadic in the dynamics of magnetic domains". *Journal of Applied Physics* ,Vol. 45. No. 1 (1974), pp. 377–393. DOI: 10.1063/1.1662989.

[206] R. Tomasello, E. Martinez, R. Zivieri, et al. "A strategy for the design of skyrmion racetrack memories". *Scientific Reports* ,Vol. 4. No. 1 (2015), p. 6784. DOI: 10.1038/srep06784.

[207] F. Büttner, C. Moutafis, M. Schneider, et al. "Dynamics and inertia of skyrmionic spin structures". *Nature Physics* ,Vol. 11. No. 3 (2015), pp. 225–228. DOI: 10.1038/nphys3234.

[208] J. Sampaio, V. Cros, S. Rohart, et al. "Nucleation, stability and current-induced motion of isolated magnetic skyrmions in nanostructures". *Nature Nanotechnology* ,Vol. 8. No. 11 (2013), pp. 839–844. DOI: 10.1038/nnano.2013.210.

[209] D.-H. Kim, D.-H. Kim, K.-J. Kim, et al. "The dynamics of a domain wall in ferrimagnets driven by spin-transfer torque". *Journal of Magnetism and Magnetic Materials* ,Vol. 514. No. June (2020), p. 167237. DOI: 10.1016/j.jmmm.2020.167237.

[210] A. K. C. Tan, P. Ho, J. Lourembam, et al. "Visualizing the strongly reshaped skyrmion Hall effect in multilayer wire devices". *Nature Communications* ,Vol. 12. No. 1 (2021), p. 4252. DOI: 10.1038/s41467-021-24114-8.

[211] R. Juge, S.-G. Je, D. D. S. Chaves, et al. "Current-Driven Skyrmion Dynamics and Drive-Dependent Skyrmion Hall Effect in an Ultrathin Film". *Physical Review Applied* ,Vol. 12. No. 4 (2019), p. 044007. DOI: 10.1103/PhysRevApplied.12.044007.

[212] S. Woo, K. Litzius, B. Krüger, et al. "Observation of room-temperature magnetic skyrmions and their current-driven dynamics in ultrathin metallic ferromagnets". *Nature Materials* ,Vol. 15. No. 5 (2016), pp. 501–506. DOI: 10.1038/nmat4593.

[213] Y. Quessab, J.-W. Xu, E. Cogulu, et al. "Zero-Field Nucleation and Fast Motion of Skyrmions Induced by Nanosecond Current Pulses in a Ferrimagnetic Thin Film". *Nano Letters* ,Vol. 22. No. 15 (2022), pp. 6091–6097. DOI: 10.1021/acs.nanolett.2c01038.

[214] K. Zeissler, S. Finizio, C. Barton, et al. "Diameter-independent skyrmion Hall angle observed in chiral magnetic multilayers". *Nature Communications* ,Vol. 11. No. 1 (2020), p. 428. DOI: 10.1038/s41467-019-14232-9.

[215] K. Litzius, I. Lemesh, B. Krüger, et al. "Skyrmion Hall effect revealed by direct time-resolved X-ray microscopy". *Nature Physics* ,Vol. 13. No. 2 (2017), pp. 170–175. DOI: 10.1038/nphys4000.

[216] C. Reichhardt, C. J. O. Reichhardt, and M. V. Milosevic. "Statics and Dynamics of Skyrmions Interacting with Pinning: A Review" (2021). DOI: 10.48550/arXiv.2102.10464.

[217] E. E. Ferrero, L. Foini, T. Giamarchi, et al. "Creep Motion of Elastic Interfaces Driven in a Disordered Landscape". *Annual Review of Condensed Matter Physics* ,Vol. 12. No. 1 (2021), pp. 111–134. DOI: 10.1146/annurev-conmatphys-031119-050725.

[218] C. Reichhardt and C. J. Olson Reichhardt. "Noise fluctuations and drive dependence of the skyrmion Hall effect in disordered systems". *New Journal of Physics* ,Vol. 18. No. 9 (2016), p. 095005. DOI: 10.1088/1367-2630/18/9/095005.

[219] J. Xia, X. Zhang, M. Ezawa, et al. "Dynamics of an elliptical ferromagnetic skyrmion driven by the spin–orbit torque". *Applied Physics Letters* ,Vol. 116. No. 2 (2020), p. 022407. DOI: 10.1063/1.5132915.

[220] E. Haltz, R. Weil, J. Sampaio, et al. "Deviations from bulk behavior in TbFe(Co) thin films: Interfaces contribution in the biased composition". *Physical Review Materials* ,Vol. 2. No. 10 (2018), p. 104410. DOI: 10.1103/PhysRevMaterials.2.104410.

[221] E Haltz. "Domain wall dynamics driven by spin-current in ferrimagnetic alloys". PhD thesis. Université Paris Saclay, 2019. DOI: tel-02903018.

[222] R. Streubel, C. Lambert, N. Kent, et al. "Experimental Evidence of Chiral Ferrimagnetism in Amorphous GdCo Films". *Advanced Materials* ,Vol. 30. No. 27 (2018), p. 1800199. DOI: 10.1002/adma.201800199.

[223] G. Hamaoui, N. Horny, Z. Hua, et al. “Electronic contribution in heat transfer at metal-semiconductor and metal silicide-semiconductor interfaces”. *Scientific Reports* ,Vol. 8. No. 1 (2018), p. 11352. DOI: 10.1038/s41598-018-29505-4.

[224] J. J. Senkevich, T. Karabacak, D.-L. Bae, et al. “Formation of body-centered-cubic tantalum via sputtering on low-κ dielectrics at low temperatures”. *Journal of Vacuum Science & Technology B: Microelectronics and Nanometer Structures* ,Vol. 24. No. 2 (2006), p. 534. DOI: 10.1116/1.2166860.

[225] J. Huang, H. Zhong, X. Xia, et al. “Phase equilibrium of the Gd–Fe–Co system at 873K”. *Journal of Alloys and Compounds* ,Vol. 471. No. 1-2 (2009), pp. 74–77. DOI: 10.1016/j.jallcom.2008.03.065.

[226] P. F. Carcia. “Perpendicular magnetic anisotropy in Pd/Co and Pt/Co thin-film layered structures”. *Journal of Applied Physics* ,Vol. 63. No. 10 (1988), pp. 5066–5073. DOI: 10.1063/1.340404.

[227] S. Bandiera, R. R. Sousa, B. B. Rodmacq, et al. “Asymmetric Interfacial Perpendicular Magnetic Anisotropy in Pt/Co/Pt Trilayers”. *IEEE Magnetics Letters* ,Vol. 2 (2011), pp. 3000504–3000504. DOI: 10.1109/LMAG.2011.2174032.

[228] M. Belmeguenai, J.-P. Adam, Y. Roussigné, et al. “Interfacial Dzyaloshinskii-Moriya interaction in perpendicularly magnetized Pt/Co/AlOx ultrathin films measured by Brillouin light spectroscopy”. *Physical Review B* ,Vol. 91. No. 18 (2015), p. 180405. DOI: 10.1103/PhysRevB.91.180405.

[229] T. Tanaka, H. Kontani, M. Naito, et al. “Intrinsic spin Hall effect and orbital Hall effect in 4d and 5d transition metals”. *Physical Review B* ,Vol. 77. No. 16 (2008), p. 165117. DOI: 10.1103/PhysRevB.77.165117.

[230] R. C. Taylor and A. Gangulee. “Magnetization and magnetic anisotropy in evaporated GdCo amorphous films”. *Journal of Applied Physics* ,Vol. 47. No. 10 (1976), pp. 4666–4668. DOI: 10.1063/1.322397.

[231] S. R. Herd. “TEM observation on the source of perpendicular anisotropy in amorphous GdCo(O2)”. *Physica Status Solidi (a)* ,Vol. 44. No. 1 (1977), pp. 363–380. DOI: 10.1002/pssa.2210440139.

[232] S. R. Herd. “Phase separation as source of perpendicular anisotropy in amorphous GdCo”. *Journal of Applied Physics* ,Vol. 49. No. 3 (1978), pp. 1744–1746. DOI: 10.1063/1.324854.

[233] S. R. Herd. “On the nature of perpendicular anisotropy in sputtered GdCo thin films”. *Journal of Applied Physics* ,Vol. 50. No. B3 (1979), pp. 1645–1647. DOI: 10.1063/1.327224.

[234] S. Tsunashima, S. Masui, T. Kobayashi, et al. “Magneto-optic Kerr effect of amorphous Gd–Fe–Co films”. *Journal of Applied Physics* ,Vol. 53. No. 11 (1982), pp. 8175–8177. DOI: 10.1063/1.330283.

[235] W. Meiklejohn, F. Luborsky, and P. Frischmann. “On the origin of KU in amorphous RE-TM magnetooptic recording materials”. *IEEE Transactions on Magnetics* ,Vol. 23. No. 5 (1987), pp. 2272–2274. DOI: 10.1109/TMAG.1987.1065652.

[236] H. Fu, M. Mansuripur, and P. Meystre. “Generic source of perpendicular anisotropy in amorphous rare-earth–transition-metal films”. *Physical Review Letters* ,Vol. 66. No. 8 (1991), pp. 1086–1089. DOI: 10.1103/PhysRevLett.66.1086.

[237] K. Ueda, A. J. Tan, and G. S. D. Beach. “Effect of annealing on magnetic properties in ferrimagnetic GdCo alloy films with bulk perpendicular magnetic anisotropy”. *AIP Advances* ,Vol. 8. No. 12 (2018), p. 125204. DOI: 10.1063/1.5054164.

[238] N. Duc, T. Hien, D. Givord, et al. “Exchange interactions in rare earth—transition metal compounds”. *Journal of Magnetism and Magnetic Materials* ,Vol. 124. No. 3 (1993), pp. 305–311. DOI: 10.1016/0304-8853(93)90131-K.

[239] C. J. Raub and S. Gmünd. “Handbook of Magnetic Materials Vol. 12”. *Journal of Alloys and Compounds* ,Vol. 312. No. 1-2 (2000), p. 331. DOI: 10.1016/S0925-8388(00)01037-9.

[240] F. E. Luborsky. “Kinetics for changes in anisotropy, coercivity, and argon content of transition metal-rare earth films”. *Journal of Applied Physics* ,Vol. 57. No. 8 (1985), pp. 3592–3594. DOI: 10.1063/1.335016.

[241] M. H. Kryder. “Magneto-optic recording technology”. *Journal of Applied Physics* ,Vol. 57. No. 8 (1985), pp. 3913–3918. DOI: 10.1063/1.334915.

[242] H. J. Leamy and A. G. Dirks. “Microstructure and magnetism in amorphous rare-earth–transition-metal thin films. I. Microstructure”. *Journal of Applied Physics* ,Vol. 49. No. 6 (1978), pp. 3430–3438. DOI: 10.1063/1.325249.

[243] N Bergeard. “Matériaux magnétiques pour l’étude de la dynamique de l’aimantation”. PhD thesis. Université Paris Sud - Paris XI, 2010. DOI: tel-00657018.

[244] B. Zegaou, N. Benkhettou, D. Rached, et al. “Electronic structure of GdX2 (X=Fe, Co and Ni) intermetallic compounds studied by the GGA+U method”. *Computational Materials Science* ,Vol. 87 (2014), pp. 172–177. DOI: 10.1016/j.commatsci.2014.02.005.

[245] S. Lee and K. Kim. “Comparative study of optical and magneto-optical properties and electronic structure of ferrimagnetic GdFe2 and GdCo2”. *Solid State Communications* ,Vol. 118. No. 5 (2001), pp. 269–272. DOI: 10.1016/S0038-1098(01)00074-6.

[246] R. C. Taylor and A Gangulee. “Magnetic Properties of 3d transition meltals in the amorphous ternary alloys”. *Physical Review B* ,Vol. 22. No. 3 (1980), pp. 1320–1326. DOI: 10.1103/PhysRevB.22.1320.

[247] E. Burzo, L. Chioncel, R. Tetean, et al. “On the R 5d band polarization in rare-earth–transition metal compounds”. *Journal of Physics: Condensed Matter* ,Vol. 23. No. 2 (2011), p. 026001. DOI: 10.1088/0953-8984/23/2/026001.

[248] J. J. Rhyne and A. E. Clark. “Magnetic Anisotropy of Terbium and Dysprosium”. *Journal of Applied Physics* ,Vol. 38. No. 3 (1967), pp. 1379–1380. DOI: 10.1063/1.1709631.

[249] R. K. Wangsness. “Sublattice Effects in Magnetic Resonance”. *Physical Review* ,Vol. 91. No. 5 (1953), pp. 1085–1091. DOI: 10.1103/PhysRev.91.1085.

[250] E. Haltz, S. Krishnia, L. Berges, et al. “Domain wall dynamics in antiferromagnetically coupled double-lattice systems”. *Physical Review B* ,Vol. 103. No. 1 (2021), p. 014444. DOI: 10.1103/PhysRevB.103.014444.

[251] P. Weiss. “L’hypothèse du champ moléculaire et la propriété ferromagnétique”. *Journal de Physique Théorique et Appliquée* ,Vol. 6. No. 1 (1907), pp. 661–690. DOI: 10.1051/jphystap:019070060066100.

[252] P. Weiss. “Sur la rationalité des rapports des moments magnétiques moléculaires et le magnéton”. *Le Radium* ,Vol. 8. No. 8 (1911), pp. 301–307. DOI: 10.1051/radium:0191100808030101.

[253] P. Weiss. “Sur la nature du champ moléculaire”. *Annales de Physique* ,Vol. 9. No. 1 (1914), pp. 134–162. DOI: 10.1051/anphys/191409010134.

[254] P. W. Anderson. “Generalizations of the Weiss Molecular Field Theory of Antiferromagnetism”. *Physical Review* ,Vol. 79. No. 4 (1950), pp. 705–710. DOI: 10.1103/PhysRev.79.705.

[255] M. D. Kuz’min, Y. Skourski, D. Eckert, et al. “Pin reorientation in high magnetic fields and the Co-Gd exchange field in GdCo5”. *Physical Review B* ,Vol. 70. No. 17 (2004), p. 172412. DOI: 10.1103/PhysRevB.70.172412.

[256] N. Duc and D. Givord. “Exchange interactions in amorphous GdCo alloys”. *Journal of Magnetism and Magnetic Materials* ,Vol. 157-158 (1996), pp. 169–170. DOI: 10.1016/0304-8853(96)01092-X.

[257] T. Imagawa, S. Narishige, and M. Hanazono. “Magnetic Properties of Co-Based Amorphous Films”. *IEEE Translation Journal on Magnetics in Japan* ,Vol. 2. No. 5 (1987), pp. 471–472. DOI: 10.1109/TJMJ.1987.4549495.

[258] R. Hasegawa. “Static bubble domain properties of amorphous Gd-Co films”. *Vacuum* ,Vol. 25. No. 2 (1975), p. 87. DOI: 10.1016/0042-207X(75)91359-7.

[259] M. Mansuripur and M. Ruane. "Mean-field analysis of amorphous rare earth-transition metal alloys for thermomagnetic recording". *IEEE Transactions on Magnetics* ,Vol. 22. No. 1 (1986), pp. 33–43. DOI: 10.1109/TMAG.1986.1064266.

[260] Y. Hirata, D.-H. Kim, T. Okuno, et al. "Correlation between compensation temperatures of magnetization and angular momentum in GdFeCo ferrimagnets". *Physical Review B* ,Vol. 97. No. 22 (2018), p. 220403. DOI: 10.1103/PhysRevB.97.220403.

[261] K.-J. Kim, S. K. Kim, Y. Hirata, et al. "Fast domain wall motion in the vicinity of the angular momentum compensation temperature of ferrimagnets". *Nature Materials* ,Vol. 16. No. 12 (2017), pp. 1187–1192. DOI: 10.1038/nmat4990.

[262] E. Haltz, J. Sampaio, S. Krishnia, et al. "Measurement of the tilt of a moving domain wall shows precession-free dynamics in compensated ferrimagnets". *Scientific Reports* ,Vol. 10. No. 1 (2020), p. 16292. DOI: 10.1038/s41598-020-73049-5.

[263] Y. Hirata, D.-H. Kim, S. K. Kim, et al. "Vanishing skyrmion Hall effect at the angular momentum compensation temperature of a ferrimagnet". *Nature Nanotechnology* ,Vol. 14. No. 3 (2019), pp. 232–236. DOI: 10.1038/s41565-018-0345-2.

[264] M. Binder, A. Weber, O. Mosendz, et al. "Magnetization dynamics of the ferrimagnet CoGd near the compensation of magnetization and angular momentum". *Physical Review B* ,Vol. 74. No. 13 (2006), p. 134404. DOI: 10.1103/PhysRevB.74.134404.

[265] E. Haltz, J. Sampaio, S. Krishnia, et al. "Quantitative analysis of spin wave dynamics in ferrimagnets across compensation points". *Physical Review B* ,Vol. 105. No. 10 (2022), p. 104414. DOI: 10.1103/PhysRevB.105.104414.

[266] O. Isnard, Y. Skourski, L. V. B. Diop, et al. "High magnetic field study of the Gd-Co exchange interactions in GdCo 12 B 6". *Journal of Applied Physics* ,Vol. 111. No. 9 (2012), p. 093916. DOI: 10.1063/1.4710995.

[267] P. Tils, M. Loewenhaupt, K. Buschow, et al. "Intersublattice exchange coupling in Gd–Mn compounds studied by INS". *Journal of Alloys and Compounds* ,Vol. 279. No. 2 (1998), pp. 123–126. DOI: 10.1016/S0925-8388(98)00688-4.

[268] M. Abou Ghantous, A. Khater, V. Ashokan, et al. "Sublattice magnetizations of ultrathin alloy [Co1-cGdc]n nanojunctions between Co leads using the combined effective field theory and mean field theory methods". *Journal of Applied Physics* ,Vol. 113. No. 9 (2013), p. 094303. DOI: 10.1063/1.4794316.

[269] M. Elkenany, S. Aly, and S. Yehia. "Magnetothermal properties and magnetocaloric effect in transition Metal-Rich Gd-Co and Gd-Fe amorphous alloys". *Cryogenics* ,Vol. 123. No. March (2022), p. 103439. DOI: 10.1016/j.cryogenics.2022.103439.

[270] A. Svalov, O. Adanakova, V. Vas'kovskiy, et al. "Thickness dependence of magnetic properties of thin amorphous ferrimagnetic rare earth–transition metal multilayers". *Journal of Magnetism and Magnetic Materials* ,Vol. 459 (2018), pp. 57–60. DOI: 10.1016/j.jmmm.2017.12.050.

[271] L. Huai-Shan, Z. Zhuong-Wu, D. Mei-Zhen, et al. "Molecular field theory analysis of rare earth-transition metal compounds RnTm". *Journal of Magnetism and Magnetic Materials* ,Vol. 75. No. 1-2 (1988), pp. 159–164. DOI: 10.1016/0304-8853(88)90135-7.

[272] S. Aly. "A mean-field study on the thermo-magnetic properties of GdxCo1-x amorphous alloys (0.16<x<0.25)". *Journal of Magnetism and Magnetic Materials* ,Vol. 232. No. 3 (2001), pp. 168–174. DOI: 10.1016/S0304-8853(01)00254-2.

[273] A. Gerber, A. Milner, A. Finkler, et al. "Correlation between the extraordinary Hall effect and resistivity". *Physical Review B* ,Vol. 69. No. 22 (2004), p. 224403. DOI: 10.1103/PhysRevB.69.224403.

[274] J. A. González, J. P. Andrés, M. A. Arranz, et al. "Electrical resistivity and interdiffusion in Gd1-xCox/Co multilayers". *Journal of Applied Physics* ,Vol. 92. No. 2 (2002), pp. 914–919. DOI: 10.1063/1.1488248.

[275] M. Waldermar. "Evidence for Coulomb interaction effect in the low-temperature resistivity of amorphous GdCo3 films". *Journal of Magnetism and Magnetic Materials* ,Vol. 82. No. 1 (1989), pp. 118–124. DOI: 10.1016/0304-8853(89)90071-1.

[276] A. Zarefy, L. Lechevallier, R. Lardé, et al. "Influence of Co layer thickness on the structural and magnetic properties of (Pt/CotCo)3/Pt/IrMn multilayers". *Journal of Physics D: Applied Physics* ,Vol. 43. No. 21 (2010), p. 215004. DOI: 10.1088/0022-3727/43/21/215004.

[277] R. Wood. "Exact Solution for a Stoner–Wohlfarth Particle in an Applied Field and a New Approximation for the Energy Barrier". *IEEE Transactions on Magnetics* ,Vol. 45. No. 1 (2009), pp. 100–103. DOI: 10.1109/TMAG.2008.2006286.

[278] T. J. Kools, M. C. van Gurp, B. Koopmans, et al. "Magnetostatics of Room Temperature Compensated Co/Gd/Co/Gd-based Synthetic Ferrimagnets" (2022), pp. 1–8.

[279] W.-Y. Kim, H. K. Gweon, K.-J. Lee, et al. "Correlation between interfacial Dzyaloshinskii–Moriya interaction and interfacial magnetic anisotropy of Pt/Co/MgO structures". *Applied Physics Express* ,Vol. 12. No. 5 (2019), p. 053007. DOI: 10.7567/1882-0786/ab181c.

[280] X. Chen, C. Feng, Z. Long Wu, et al. "Interfacial oxygen migration and its effect on the magnetic anisotropy in Pt/Co/MgO/Pt films". *Applied Physics Letters* ,Vol. 104. No. 5 (2014), p. 052413. DOI: 10.1063/1.4864184.

[281] V. G. Harris, K. D. Aylesworth, B. N. Das, et al. "Structural origins of magnetic anisotropy in sputtered amorphous Tb-Fe films". *Physical Review Letters* ,Vol. 69. No. 13 (1992), pp. 1939–1942. DOI: 10.1103/PhysRevLett.69.1939.

[282] K. Umadevi, S. Bysakh, J. A. Chelvane, et al. "Tailoring magnetic anisotropy in Tb–Fe–Co thin films by rapid thermal annealing". *Journal of Alloys and Compounds* ,Vol. 663 (2016), pp. 430–435. DOI: 10.1016/j.jallcom.2015.12.127.

[283] M. D. Kuz'min and A. K. Zvezdin. "Full magnetization process of 3d-4f hard magnetic materials in ultrahigh magnetic fields (an example: RFe11Ti)". *Journal of Applied Physics* ,Vol. 83. No. 6 (1998), pp. 3239–3249. DOI: 10.1063/1.367091.

[284] R Verhoef, R. Radwański, and J. Franse. "Strength of the rare-earth-transition-metal exchange coupling in hard magnetic materials, an experimental approach based on high-field magnetisation measurements: Application to Er2Fe14B". *Journal of Magnetism and Magnetic Materials* ,Vol. 89. No. 1-2 (1990), pp. 176–184. DOI: 10.1016/0304-8853(90)90723-4.

[285] R. Radwański, X. Zhong, F. de Boer, et al. "Study of magnetic interactions in ferrimagnetic systems in the Amsterdam high-field installation". *Physica B: Condensed Matter* ,Vol. 164. No. 1-2 (1990), pp. 131–138. DOI: 10.1016/0921-4526(90)90070-B.

[286] C. E. Patrick, S. Kumar, K. Götze, et al. "Field-induced canting of magnetic moments in GdCo 5 at finite temperature: first-principles calculations and high-field measurements". *Journal of Physics: Condensed Matter* ,Vol. 30. No. 32 (2018), 32LT01. DOI: 10.1088/1361-648X/aad029.

[287] A. E. Clark and E. Callen. "Néel Ferrimagnets in Large Magnetic Fields". *Journal of Applied Physics* ,Vol. 39. No. 13 (1968), pp. 5972–5982. DOI: 10.1063/1.1656100.

[288] Z. Chen, X. Zhang, Y. Zhou, et al. "Skyrmion Dynamics in the Presence of Deformation". *Physical Review Applied* ,Vol. 17. No. 1 (2022), p. L011002. DOI: 10.1103/PhysRevApplied.17.L011002.

[289] A. Chanda, J. E. Shoup, N. Schulz, et al. "Tunable competing magnetic anisotropies and spin reconfigurations in ferrimagnetic Fe100-xGdx alloy films". *Physical Review B* ,Vol. 104. No. 9 (2021), p. 094404. DOI: 10.1103/PhysRevB.104.094404.

[290] J. Becker, A. Tsukamoto, A. Kirilyuk, et al. "Ultrafast Magnetism of a Ferrimagnet across the Spin-Flop Transition in High Magnetic Fields". *Physical Review Letters* ,Vol. 118. No. 11 (2017), pp. 1–5. DOI: 10.1103/PhysRevLett.118.117203.

[291] M. Hayashi, J. Kim, M. Yamanouchi, et al. "Quantitative characterization of the spin-orbit torque using harmonic Hall voltage measurements". *Physical Review B* ,Vol. 89. No. 14 (2014), p. 144425. DOI: 10.1103/PhysRevB.89.144425.

[292] S. Krishnia, Y. Sassi, F. Ajejas, et al. "Large interfacial Rashba interaction and giant spin-orbit torques in atomically thin metallic heterostructures" (2022), pp. 1–6.

[293] D.-H. Kim, M. Haruta, H.-W. Ko, et al. "Bulk Dzyaloshinskii–Moriya interaction in amorphous ferrimagnetic alloys". *Nature Materials* ,Vol. 18. No. 7 (2019), pp. 685–690. DOI: 10.1038/s41563-019-0380-x.

[294] T Katayama, K Hasegawa, K Kawanishi, et al. "Annealing effects on magnetic properties of amorphous GdCo, GdFe, and GdCoMo films". *Journal of Applied Physics* ,Vol. 49. No. 3 (1978), pp. 1759–1761. DOI: 10.1063/1.324859.

[295] Y. Quessab, J. Xu, M. G. Morshed, et al. "Interplay between Spin-Orbit Torques and Dzyaloshinskii-Moriya Interactions in Ferrimagnetic Amorphous Alloys". *Advanced Science* ,Vol. 8. No. 18 (2021), p. 2100481. DOI: 10.1002/advs.202100481.

[296] C. Eyrich, A. Zamani, W. Huttema, et al. "Effects of substitution on the exchange stiffness and magnetization of Co films". *Physical Review B* ,Vol. 90. No. 23 (2014), p. 235408. DOI: 10.1103/PhysRevB.90.235408.

[297] G. G. Scott. "Review of Gyromagnetic Ratio Experiments". *Reviews of Modern Physics* ,Vol. 34. No. 1 (1962), pp. 102–109. DOI: 10.1103/RevModPhys.34.102.

[298] T. Devolder, P.-H. Ducrot, J.-P. Adam, et al. "Damping of Co x Fe 80-x B 20 ultrathin films with perpendicular magnetic anisotropy". *Applied Physics Letters* ,Vol. 102. No. 2 (2013), p. 022407. DOI: 10.1063/1.4775684.

[299] C. Vittoria, P. Lubitz, and V. Ritz. "Magnetic properties of amorphous and crystalline GdFe 2". *Journal of Applied Physics* ,Vol. 49. No. 9 (1978), pp. 4908–4917. DOI: 10.1063/1.325525.

[300] A. A. Thiele. "The Theory of Cylindrical Magnetic Domains". *Bell System Technical Journal* ,Vol. 48. No. 10 (1969), pp. 3287–3335. DOI: 10.1002/j.1538-7305.1969.tb01747.x.

[301] C.-E. Fillion, J. Fischer, R. Kumar, et al. "Gate-controlled skyrmion and domain wall chirality". *Nature Communications* ,Vol. 13. No. 1 (2022), p. 5257. DOI: 10.1038/s41467-022-32959-w.

[302] A. Bernand-Mantel, C. B. Muratov, and T. M. Simon. "Unraveling the role of dipolar versus Dzyaloshinskii-Moriya interactions in stabilizing compact magnetic skyrmions". *Physical Review B* ,Vol. 101. No. 4 (2020), p. 045416. DOI: 10.1103/PhysRevB.101.045416.

[303] C. Tannous and J. Gieraltowski. "Magnetic domain walls and the relaxation method". *Computational Materials Science* ,Vol. 42. No. 1 (2008), pp. 1–7. DOI: 10.1016/j.commatsci.2007.05.019.

[304] S. von Malottki, P. F. Bessarab, S. Haldar, et al. "Skyrmion lifetime in ultrathin films". *Physical Review B* ,Vol. 99. No. 6 (2019), p. 060409. DOI: 10.1103/PhysRevB.99.060409.

[305] S. A. Montoya, S. Couture, J. J. Chess, et al. "Tailoring magnetic energies to form dipole skyrmions and skyrmion lattices". *Physical Review B* ,Vol. 95. No. 2 (2017), p. 024415. DOI: 10.1103/PhysRevB.95.024415.

[306] R. D. Gomez, T. V. Luu, A. O. Pak, et al. "Domain configurations of nanostructured Permalloy elements". *Journal of Applied Physics* ,Vol. 85. No. 8 (1999), pp. 6163–6165. DOI: 10.1063/1.370030.

[307] J. M. Garcia, A. Thiaville, J. Miltat, et al. "Quantitative interpretation of magnetic force microscopy images from soft patterned elements". *Applied Physics Letters* ,Vol. 79. No. 5 (2001), pp. 656–658. DOI: 10.1063/1.1389512.

[308] S. Van der Walt, J. L. Schönberger, J. Nunez-Iglesias, et al. "scikit-image: image processing in Python". *PeerJ* ,Vol. 2 (2014), e453. DOI: 10.7717/peerj.453.

[309] A. Kornilov and I. Safonov. "An Overview of Watershed Algorithm Implementations in Open Source Libraries". *Journal of Imaging* ,Vol. 4. No. 10 (2018), p. 123. DOI: 10.3390/jimaging4100123.

[310] C. Won, Y. Z. Wu, J. Choi, et al. "Magnetic stripe melting at the spin reorientation transition in Fe/Ni/Cu(001)". *Physical Review B* ,Vol. 71. No. 22 (2005), p. 224429. DOI: 10.1103/PhysRevB.71.224429.

[311] Y. Z. Wu, C. Won, A. Scholl, et al. "Magnetic Stripe Domains in Coupled Magnetic Sandwiches". *Physical Review Letters* ,Vol. 93. No. 11 (2004), p. 117205. DOI: 10.1103/PhysRevLett.93.117205.

[312] L. Sun, J. H. Liang, X. Xiao, et al. "Magnetic stripe domains of [Pt/Co/Cu] 10 multilayer near spin reorientation transition". *AIP Advances* ,Vol. 6. No. 5 (2016), p. 056109. DOI: 10.1063/1.4943360.

[313] K. Zeissler, M. Mruczkiewicz, S. Finizio, et al. "Pinning and hysteresis in the field dependent diameter evolution of skyrmions in Pt/Co/Ir superlattice stacks". *Scientific Reports* ,Vol. 7. No. 1 (2017), p. 15125. DOI: 10.1038/s41598-017-15262-3.

[314] I. Gross, W. Akhtar, A. Hrabec, et al. "Skyrmion morphology in ultrathin magnetic films". *Physical Review Materials* ,Vol. 2. No. 2 (2018), p. 024406. DOI: 10.1103/PhysRevMaterials.2.024406.

[315] J. Barker and O. A. Tretiakov. "Static and Dynamical Properties of Antiferromagnetic Skyrmions in the Presence of Applied Current and Temperature". *Physical Review Letters* ,Vol. 116. No. 14 (2016), p. 147203. DOI: 10.1103/PhysRevLett.116.147203.

[316] J. Iwasaki, M. Mochizuki, and N. Nagaosa. "Current-induced skyrmion dynamics in constricted geometries". *Nature Nanotechnology* ,Vol. 8. No. 10 (2013), pp. 742–747. DOI: 10.1038/nnano.2013.176.

[317] R. Juge, S.-G. G. Je, D. de Souza Chaves, et al. "Magnetic skyrmions in confined geometries: Effect of the magnetic field and the disorder". *Journal of Magnetism and Magnetic Materials* ,Vol. 455 (2018), pp. 3–8. DOI: 10.1016/j.jmmm.2017.10.030.

[318] W. Legrand, D. Maccariello, N. Reyren, et al. "Room-Temperature Current-Induced Generation and Motion of sub-100 nm Skyrmions". *Nano Letters* ,Vol. 17. No. 4 (2017), pp. 2703–2712. DOI: 10.1021/acs.nanolett.7b00649.

[319] A. Salimath, A. Abbout, A. Brataas, et al. "Current-driven skyrmion depinning in magnetic granular films". *Physical Review B* ,Vol. 99. No. 10 (2019), p. 104416. DOI: 10.1103/PhysRevB.99.104416.

[320] X. Zhang, Y. Zhou, and M. Ezawa. "Magnetic bilayer-skyrmions without skyrmion Hall effect". *Nature Communications* ,Vol. 7. No. 1 (2016), p. 10293. DOI: 10.1038/ncomms10293.

[321] H. Vakili, J.-W. Xu, W. Zhou, et al. "Skyrmionics—Computing and memory technologies based on topological excitations in magnets". *Journal of Applied Physics* ,Vol. 130. No. 7 (2021), p. 070908. DOI: 10.1063/5.0046950.

[322] S. Panigrahy, S. Mallick, J. Sampaio, et al. "Skyrmion inertia in synthetic antiferromagnets". *Physical Review B* ,Vol. 106. No. 14 (2022), p. 144405. DOI: 10.1103/PhysRevB.106.144405.

[323] A. Vansteenkiste, J. Leliaert, M. Dvornik, et al. "The design and verification of MuMax3". *AIP Advances* ,Vol. 4. No. 10 (2014), p. 107133. DOI: 10.1063/1.4899186.

[324] D Capic, D. A. Garanin, and E. M. Chudnovsky. "Skyrmion–skyrmion interaction in a magnetic film". *Journal of Physics: Condensed Matter* ,Vol. 32. No. 41 (2020), p. 415803. DOI: 10.1088/1361-648X/ab9bc8.

[325] R. Brearton, G. van der Laan, and T. Hesjedal. "Magnetic skyrmion interactions in the micromagnetic framework". *Physical Review B* ,Vol. 101. No. 13 (2020), p. 134422. DOI: 10.1103/PhysRevB.101.134422.

[326] G. Yu, P. Upadhyaya, X. Li, et al. "Room-Temperature Creation and Spin–Orbit Torque Manipulation of Skyrmions in Thin Films with Engineered Asymmetry". *Nano Letters* ,Vol. 16. No. 3 (2016), pp. 1981–1988. DOI: 10.1021/acs.nanolett.5b05257.

[327] Y. Hu, S. Zhang, Y. Zhu, et al. "Precise Tuning of Skyrmion Density in a Controllable Manner by Ion Irradiation". *ACS Applied Materials & Interfaces* ,Vol. 14. No. 29 (2022), pp. 34011–34019. DOI: 10.1021/acsami.2c07268.